



MAX-PLANCK-GESELLSCHAFT



# Hydrogen Bonds and Electrostatic Environment of Radical Intermediates in Ribonucleotide Reductase Ia

Dissertation  
for the award of the degree  
"Doctor rerum naturalium"  
Division of Mathematics and Natural Sciences  
of the  
Georg-August-University Göttingen

Submitted by  
Thomas U. Nick  
from Bensheim

Göttingen, May 2015

Thesis Committee:

Professor Dr. Marina Bennati (Reviewer)

Institute for Organic and Biomolecular Chemistry, Georg August University, Göttingen

&

Electron Spin Resonance Spectroscopy Group, Max Planck Institute for Biophysical Chemistry

Professor Bert de Groot, Ph. D. (2<sup>nd</sup> Reviewer)

Computational Biomolecular Dynamics Group, Max Planck Institute for Biophysical Chemistry

Professor Dr. Adam Lange

Department of Molecular Biophysics, Leibniz-Institute for Molecular Pharmacology, Berlin

Examination Board Member:

Professor Dr. Marina Bennati and Professor Bert de Groot, Ph. D.

Prof. Dr. Claudia Höbartner, Institute for Organic and Biomolecular Chemistry, Georg August University, Göttingen

Prof. Dr. Markus Zweckstetter, Research Group Protein Structure Determination using NMR, Max Planck Institute for Biophysical Chemistry

Prof. Dr. Kai Tittmann, Dept. of Molecular Enzymology, Georg August University, Göttingen

Date of the oral examination: 29 June 2015

---

*“Die Neugier steht immer an erster Stelle eines Problems, das gelöst werden will”*

*- Galileo Galilei*

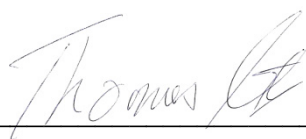
*To my Father*

---

## DECLARATION

I hereby declare that this thesis has been written independently and with no other sources and aids than quoted.

Signed: \_\_\_\_\_

A handwritten signature in cursive script, appearing to read "Thomas U. Nick", written over a horizontal line.

Date: 17.05.2015

Thomas U. Nick, Dipl. Chem.  
Göttingen

## ABSTRACT

Ribonucleotide reductase connects the RNA and the DNA world via strictly controlled radical chemistry that reduces all four essential ribonucleotides to deoxyribonucleotides. In RNR Ia, the starting point is the  $\mu$ -oxo diiron cofactor, where a “stable” tyrosine radical ( $Y_{122}\bullet$ ) is formed from a nearby tyrosine in the  $\beta$  subunit. Successive studies showed that  $Y_{356}\bullet(\beta)$ ,  $Y_{731}\bullet(\alpha)$  and  $Y_{730}\bullet(\alpha)$  are intermediate steps of an intersubunit radical pathway, before a putative catalytic cysteine radical ( $C_{439}\bullet$ ) is formed in the  $\alpha$  subunit. Conformational gating hinders the direct observation of these transient radicals. A well-characterized mutation strategy by site-specific incorporation of the unnatural 3-amino-tyrosine ( $NH_2Y$ ) was successfully used to omit conformational gating. To analyze electrostatic effects and hydrogen (H) bond networks, all three Ys ( $Y_{356}$ ,  $Y_{731}$  &  $Y_{730}$ ) were successively mutated. Seminal studies revealed an exceptional difference between the tyrosine radicals formed within the radical propagation and the  $Y_{122}\bullet$  at its beginning. The stepwise oxidation and reduction of these amino acid radicals is directly linked to a proton-coupled electron transfer (PCET). Therefore, the investigation of electrostatics and H bonds is fundamental to understand this important process in biology.

Pulsed 263-GHz EPR spectroscopy as well as ENDOR spectroscopy delivered insight based on closely characterized mutation approaches into the electronic and H bond structure of the  $NH_2Ys\bullet$ . It could be shown that an electropositive surrounding of moderate to strong H bonds are a common feature in  $\alpha$  and  $\beta$  subunits. In the  $\alpha$  subunit, double mutant approaches delivered insight into the effect of the removal of an H bond donor on the radical transfer efficiency and supported the assignment of the ENDOR studies. Deuteron nuclei ( $^2H$ ) ENDOR spectroscopy revealed 2, 1 and 0 H bonds perpendicular to the ring plane of  $NH_2Y_{730}\bullet$ ,  $NH_2Y_{731}\bullet$  and  $NH_2Y_{356}\bullet$ , which is consistent with a “ $\pi$ -stacking” between  $Y_{731}$  and  $Y_{730}$ . Three structural DFT models for  $NH_2Y_{731}\bullet$  based on optimized crystal structures have been discussed in terms of H bonds and environment. A perpendicular strong H bond (1.6 Å) and a weak H bond ( $\geq 1.9$  Å) was consistent with the electrostatics observed at  $NH_2Y_{731}\bullet$ .  $NH_2Y_{356}\bullet$  showed the lowest  $g_x$  value, typical for a polar electrostatic environment. Due to the limited structural data, no active model of  $NH_2Y_{356}\bullet$  could be obtained. The possible influences on the  $g_x$  value were discussed based on small model DFT calculations. Experimentally, one weak to moderate H bond ( $1.9\pm 0.1$  Å) could be resolved in the forward radical transfer to a wild type- $\beta$   $Y_{356}\bullet$  environment using a different mutation strategy. DFT models consistent with the obtained  $g$  values proposed another weak H bond ( $> 2.1$  Å). All moderate H bonds found at residue  $\beta$ -356 were in-plane of the tyrosine  $\pi$  system. Overall, this illustrates that different H bond networks in the  $\alpha$  and  $\beta$  subunit are used to promote this long proton-coupled redox chain.

---

## ACKNOWLEDGEMENTS

I would like to express my deep gratitude to my supervisor Professor Marina Bennati for giving me the opportunity to sit on the shoulder of giants and start this amazingly developing project. With Marina's delight to discuss new turns and outcomes, it has been a pleasure to engage new challenges. A working atmosphere with direct discussions on so many different topics as in this group cannot be taken for granted.

My thesis committee members have accompanied me along the way and dedicated time and discussions to the project. For this I would like to thank Professor Bert de Groot and Professor Adam Lange.

Thanks to Isabel Bejenke and Dr. Müge Kasanmascheff for being so enthusiastic about taking the ribonucleotide reductase torch further for our group. The discussions with you have sparked my interest day in and day out. I will take a bit more time now to enjoy your ideas. The whole EPR group has a good part in what was my time here in Göttingen. I would especially like to thank Dr. Tomislav Argirević for setting the foundation for my research. Furthermore, my gratitude goes to Dr. Igor Tkach for all the help on the way, for scientific insight into 'why we do things the way we do them.' and for helping to troubleshoot most of the problems with the instruments. Roberto Rizzato, I am grateful for working with you and you were an asset to my interests when our paths crossed. To Nikolay, Guoquan, Monika and Gitta, I am grateful for all the little discussions and help. Finally, thanks to Karin Halbmaier, my office mate, for always having an open ear and for bearing with me during my stay. I thank everyone who spent time reading parts of my thesis, especially Müge and Karin. This whole project would not have been possible, however, without my collaborators, foremost from the Stubbe lab. I would like to thank Professor JoAnne Stubbe for the trust invested in this collaboration and for the fruitful discussions and ideas also in writing the recent paper. I thank Dr. Ellen Minnihan for the introduction to such nice colleagues as Wankyu Lee and Kanchana Ravichandran. Wankyu, the discussion with you was an enriching, both scientifically and personally. Kanchana, I will not forget the night when we decided how to proceed and how the discussion went. Thanks for your input and contributions throughout the second part of my thesis. Sometimes I wished the distances would have been a bit shorter.

To our collaborator Professor Frank Neese, I would like to express my gratitude for the brief but crucial discussions. In addition, I would like to thank Dr. Simone Kossmann for bringing the DFT part up to date with the large models discussed in this thesis.

Lastly, I would like to thank my family and friends for their unfailing support and optimism. I am especially thankful to Katharina, who helped me through all the ups and downs.

# CONTENTS

1 INTRODUCTION	1
1.1 Ribonucleotide Reductases: Bridging the RNA and DNA World	1
1.2 Diverse Classes of Ribonucleotide Reductases	2
1.3 Differences and Similarities of <i>Escherichia Coli</i> and Eukaryotic RNRs	4
1.4 <i>Escherichia Coli</i> RNR Ia	6
1.4.1 Structural Basis of the Radical Transfer	6
1.4.2 Unnatural Amino Acids to Study the Radical Translocation	9
1.4.3 Experiments on the $\alpha_2\beta_2$ RNR Complex	11
1.4.4 Proton Coupled Electron Transfer	13
1.4.5 Rates and Thermodynamics during PCET	16
1.4.6 PCET through the Interface of the Subunits	17
1.5 EPR Spectroscopy for PCET Pathways	19
1.5.1 Overview	19
1.5.2 High-Field ENDOR and EPR in other PCET systems	20
1.5.3 High-Field ENDOR and EPR in RNR	21
1.6 Motivation of the Work	26
2 THEORETICAL BACKGROUND	28
2.1 Spin Hamiltonian and Magnetic Interactions	28
2.1.1 The Zeeman Contribution	30
2.1.2 Anisotropic $g$ Tensors in Organic Radicals: The Spin-Orbit Contribution	31
2.1.3 Hyperfine Interaction	33
2.1.4 Dipolar Interaction	35
2.1.5 Quadrupole Interaction	36
2.1.6 Analytical Treatment of the Spin Hamiltonian	36
2.2 High-Field Spectroscopy for Small Hyperfine Couplings	38
2.2.1 Detection of Hyperfine Interaction	38
2.2.2 Nuclei Accessible in Hyperfine Spectroscopy	39
2.2.3 Mims-ENDOR Spectroscopy	40
2.2.4 Comparison to other Hyperfine Detection Methods	43
2.2.5 Hyperfine Tensors and Origin	45
2.3 Density Functional Theory: Limitations and Advantages	47
2.3.1 Explaining Tendency within the Functionals	48
2.3.2 Dispersion Correction	49
2.3.3 Basis Sets	51
2.3.4 Effective Hamiltonian and Perturbation Theory for DFT	52
2.4 Proton Coupled Electron Transfer	54
2.4.1 Electron Transfer	54
2.4.2 Expansion to an Electron Coupled Proton Transfer	57
2.4.3 Water Participation in ET and PCET	62

3 MATERIALS AND METHODS	63
3.1 Materials	63
3.2 Sample Preparation	64
3.3 X/Q-Band Spectroscopy	66
3.4 W-Band Spectroscopy	66
3.5 263 GHz Spectroscopy and Calibration	66
3.6 Density Functional Theory Calculations	71
3.6.1 Set-up of the Models	71
3.6.2 Geometry Optimizations	71
3.6.3 EPR Calculations	72
4 3-AMINO TYROSINE RADICAL INTERMEDIATES	73
4.1 Electrostatic Environment of 3-Amino Tyrosines in the $\alpha$ Subunit	74
4.1.1 263 GHz Spectra of $\text{NH}_2\text{Y}_{730}\bullet$	74
4.1.2 263 GHz Spectra of $\text{NH}_2\text{Y}_{731}\bullet$	77
4.1.3 Comparing Simulation Parameters from 263 GHz EPR and 94 GHz EPR Spectra	80
4.2 ENDOR Spectroscopy of $\text{NH}_2\text{Y}_{731}\bullet$ Compared to $\text{NH}_2\text{Y}_{730}\bullet$ in the $\alpha$ Subunit	81
4.2.1 ENDOR on $\text{NH}_2\text{Y}_{731}\bullet$	81
4.2.2 Direction of the H bond Observed at $\text{NH}_2\text{Y}_{731}\bullet$	83
4.3 Removal of one H Bond Partner by Double Mutants	87
4.3.1 The Concept of the Double Mutant Study	87
4.3.2 Kinetic Characterization of $\text{NH}_2\text{Y}_{731}/\text{Y}_{730}\text{F}$ and $\text{NH}_2\text{Y}_{730}/\text{C}_{439}\text{A}$	88
4.3.3 Structural Comparison of $\text{NH}_2\text{Y}_{731}\bullet/\text{Y}_{730}\text{F}$ and $\text{NH}_2\text{Y}_{730}\bullet/\text{C}_{439}\text{A}$ with their Single Mutants	89
4.3.4 Electrostatic Environment and Conformer State: Comparison of the Radicals formed in Double Mutants and Single Mutants	92
4.3.5 Assignment of the H Bond Donors by ENDOR spectra of the Double Mutants.	95
4.4 Comparing Structural Models from DFT with EPR parameters	98
4.5 Discussion of the PCET in the $\alpha$ Subunit with $\text{NH}_2\text{Ys}\bullet$	105
4.6 High-Field EPR Spectra of $\text{NH}_2\text{Y}_{356}\bullet$ in the $\beta$ Subunit	110
4.6.1 EPR Spectra of $\text{NH}_2\text{Y}_{356}\bullet$ for Several Reaction Times	110
4.6.2 Polarity around $\text{NH}_2\text{Y}_{356}\bullet$ from 263 GHz and 94 GHz Spectra	111
4.6.3 H bond interactions at $\text{NH}_2\text{Y}_{356}\bullet$	114
4.6.4 Modeling $\text{NH}_2\text{Ys}\bullet$ by DFT Calculations Considering One Amino-Acid	115
4.7 Discussion of the $\beta$ - $\text{NH}_2\text{Y}_{356}\bullet$ Radical Intermediate	125



5	2,3,5-F <sub>3</sub> Y <sub>122</sub> • TO GENERATE Y• INTERMEDIATES IN THE PCET	127
5.1	Introduction of a New Rate Limiting Step to Generate Y <sub>356</sub> •	127
5.2	Multifrequency EPR Characterization of 2,3,5-F <sub>3</sub> Y <sub>122</sub> •	130
5.3	Characterization by Forward PCET Y• Formed with 2,3,5-F <sub>3</sub> Y <sub>122</sub> •	135
5.3.1	Electrostatic Environment	135
5.3.2	Assignment of the Pathway Radical by the Diagonal Distance to 2,3,5-F <sub>3</sub> Y <sub>122</sub> •	139
5.3.3	Mims ENDOR of Forward Radical Transfer to Y <sub>356</sub> •	140
5.3.4	Direction of the H Bond	142
5.3.5	Y <sub>356</sub> • H bond Length	144
5.4	Equilibrium PCET Radical Y <sub>356</sub> • formed during Reverse PCET	146
5.4.1	Multifrequency Characterization	146
5.4.2	Mims ENDOR of Y <sub>356</sub> • using Wild Type $\alpha$	149
5.5	Discussion	155
5.5.1	Removing the Conformational Gating by 2,3,5-F <sub>3</sub> Y	155
5.5.2	Comparison between Y <sub>356</sub> • and NH <sub>2</sub> Y <sub>356</sub> • Forward PCET Radical Intermediates	155
5.5.3	Y <sub>356</sub> • in Forward and Reverse PCET	157
5.5.4	Mechanistic Implications	159
6	CONCLUSION	162
6.1	NH <sub>2</sub> Y• Intermediates Investigated in the $\alpha$ Subunit	162
6.2	NH <sub>2</sub> Y• and Y• Intermediates Investigated in the $\beta$ Subunit	164
6.3	Outlook	165
7	REFERENCES	167
8	APPENDICES	190

---

## LIST OF TABLES

1-1: HF couplings of tyrosine to exchangeable intermolecular deuterons for two examples.....	24
1-2: The $g$ values as a function of the environment are tabulated for $\text{NH}_2\text{Ys}\bullet$ and $\text{Ys}\bullet$ .....	25
4-1: Parameters of the simulation for 263-GHz and 94-GHz EPR spectra for $\text{NH}_2\text{Y}_{731}\bullet$ and $\text{NH}_2\text{Y}_{730}\bullet$ .....	80
4-2: Simulation parameters for the $^2\text{H}$ ENDOR spectra of $\text{ND}_2\text{Y}_{731}\bullet$ .....	86
4-3: Kinetics of $\text{NH}_2\text{Y}\bullet$ formation for $\alpha_2$ mutants.....	88
4-4: Parameters obtained from the double mutant $\text{NH}_2\text{Y}_{730}\bullet/\text{C}_{439}\text{A}$ and $\text{NH}_2\text{Y}_{731}\bullet/\text{Y}_{730}\text{F}$ EPR spectra.....	94
4-5: Summary of $g$ values and C- $\beta$ HF couplings of $\text{NH}_2\text{Y}\bullet$ at residues 730, 731, 356. ....	101
4-6: Summary of EPR parameters for the H bond to $\text{NH}_2\text{Y}_{731}\bullet$ .....	104
4-7: Summary of $g$ values and HF couplings observed in the EPR spectrum of $\text{NH}_2\text{Y}_{356}\bullet$ .....	114
4-8: Summary of EPR parameters for the exchangeable protons at $\text{NH}_2\text{Y}_{356}\bullet$ .....	115
4-9: EPR parameters from DFT of $\text{NH}_2\text{Y}\bullet$ in water model C .....	123
5-1: Summary of obtained $g$ values, C- $\beta$ HF couplings, and $^{19}\text{F}$ HF couplings .....	133
5-2: Pathway radical observed with $\beta_2$ -2,3,5- $\text{F}_3\text{Y}_{122}:\alpha_2\text{-Y}_{731}\text{F}$ simulation parameters and comparison to Yokoyama et al. ....	137
5-3: Simulation parameters of the unknown H bond donor to $\text{Y}_{356}\bullet$ .....	144
5-4: Small DFT model using a $\text{Y}\bullet$ and two waters scanning the distance of a distant of the second water (wat2). ....	145
5-5: Simulation parameters of the pathway radical observed with $\beta_2$ -2,3,5- $\text{F}_3\text{-Y}_{122}$ and wild type $\alpha_2$ in comparison to $\text{Y}_{356}\bullet$ formed with $\beta_2\text{-NO}_2\text{-Y}_{122}:\alpha_2\text{-wt}$ .....	147
5-6: Comparison between experimental and calculated $g$ values and, number and distances of H bonds .....	154

## LIST OF FIGURES

1-1: Chemical reaction catalyzed by RNRs. ....	2
1-2: Classification of RNRs based on their metallocofactor to activate C• at the nucleotide reduction site.....	3
1-3: Similarities between the different RNR I $\alpha$ subunit structures from four organisms. ....	5
1-4: Crystal structure of the $\alpha_2$ dimer of <i>E. coli</i> RNR Ia. ....	7
1-5: <i>E. coli</i> RNR $\alpha_2\beta_2$ docking model.....	8
1-6: Unnatural amino acids which could be incorporated into RNR. ....	10
1-7: Overlay of crystal structures of NH <sub>2</sub> Y <sub>730</sub> , NH <sub>2</sub> Y <sub>731</sub> and wt- $\alpha_2$ . ....	11
1-8: Diagonal distances of the active complex obtained with radical traps. ....	12
1-9: PCET pathways between two Y radicals.....	13
1-10: Working model of the PCET between the subunits $\alpha$ and $\beta$ of RNR Ia.....	14
1-11: Redox peak potential changes relative to Y <sub>122</sub> . ....	17
1-12: Electrostatic and local structural information found for $\alpha$ -RNR. ....	18
1-13: The <sup>2</sup> H Mims ENDOR spectra of two states of Y <sub>D</sub> • from photosystem II ..... 21	21
1-14: High-field EPR and ENDOR spectra combined with DFT calculations derive a structural model of the active structure of NH <sub>2</sub> Y <sub>730</sub> • ..... 23	23
2-1: Typical energies in Hz of electron and nuclear spin interactions from microwave frequencies between X band and W band..... 30	30
2-2: Illustration of the spin-orbit coupling and effects on the <i>g</i> value. .... 33	33
2-3: Spin polarization mechanism in an aromatic CH-fragment. .... 34	34
2-4: Dipolar coupling between two spins A and B in the magnetic field B <sub>0</sub> . .... 35	35
2-5: Energy levels in two spin systems at a certain orientation in the weak coupling ( $A \ll \omega_1$ ) case..... 38	38
2-6: Nuclear spins coupled to a NH <sub>2</sub> Y•..... 39	39
2-7: Gain in ENDOR resolution for organic radicals ( $S=1/2$ ) with increasing Zeeman field B <sub>0</sub> and microwave frequency $\nu$ . .... 40	40
2-8: Mims ENDOR sequence for the detection of small HF couplings. .... 41	41
2-9: Illustrative picture of the pattern created in the preparation sequence. .... 42	42
2-10: Mims hole functions in dependence of the interpulse delay $\tau$ . .... 43	43
2-11: Comparison of Davies ENDOR and pulsed ELDOR-detected NMR..... 45	45
2-12: Hyperfine powder patterns for different ratios of $a_{\text{iso}}$ to $T$ ..... 46	46
2-13: Dissociation curve of H <sub>2</sub> <sup>+</sup> ..... 49	49
2-14: Dispersion correction for two argon atoms..... 50	50
2-15: Two geometry-optimized phenoxy/phenol structures..... 51	51
2-16: Comparison between Slater type $\phi_{1s}^{\text{STO}}(r)$ orbital and Gaussian type orbitals ..... 52	52

2-17: Cross section of the free energy surface along a nuclear reaction coordinate $Q$ for ET. .....	55
2-18: Distance dependence between acceptor and donor of an activationless electron tunneling.....	56
2-19: Extension from ET to a PCET .....	59
2-20: Adiabatic potential along the transferring hydrogen coordinate.....	61
3-1: Comparison of CW 263-GHz EPR spectra of $Mn^{2+}$ (in CaO, 0.02%) at room temperature with and without linearization. ....	68
3-2: Linearization improvement compared in CW 263 GHz EPR measurements. ....	69
3-3: Pulsed-EPR spectrum of the $\beta_2$ - $Y_{122}\bullet$ as calibration standard.....	70
4-1: 263-GHz echo detected spectrum of $Y_{730}NH_2\bullet$ .....	75
4-2: Ring dihedral $\theta_{C\beta}$ comparison of the DFT/EPR model and the $NH_2Y_{730}$ crystal structure.....	76
4-3: 263-GHz echo detected spectrum of $Y_{730}ND_2\bullet$ and simulation. ....	77
4-4: 263-GHz ESE spectrum $ND_2Y_{731}\bullet$ .....	79
4-5: 263-GHz ESE spectrum obtained from $ND_2Y_{731}\bullet$ and $NH_2Y_{731}\bullet$ with a reaction time of 18 s and 2 min, respectively.....	79
4-6: 94-GHz EPR spectra and their simulations of $ND_2Y$ s intermediates in $\alpha$ .....	81
4-7: 94-GHz $^2H$ Mims ENDOR spectra at $B_{  g_y}$ of trapped $NH_2Y$ s• intermediates in $\alpha$ .....	83
4-8: Orientation selective $^2H$ Mims ENDOR spectrum of $ND_2Y_{731}\bullet$ .....	85
4-9: Kinetics of $NH_2Y\bullet$ formation in $\alpha_2$ - $NH_2Y_{731}/Y_{730}F$ : $\beta_2$ -wt (A) or $\alpha_2$ - $NH_2Y_{730}/C_{439}A$ : $\beta_2$ - wt (B) with CDP and ATP by SF Vis spectroscopy.....	88
4-10: 34-GHz distance measurements between $NH_2Y_{731}\bullet$ and $Y_{122}\bullet$ in the $\alpha_2$ - $NH_2Y_{731}/Y_{730}F$ double mutant at 5 K. ....	90
4-11: 34-GHz distance measurements between $NH_2Y_{730}\bullet$ and $Y_{122}\bullet$ in the $\alpha_2$ - $NH_2Y_{730}/C_{439}A$ double mutant.....	92
4-12: 94-GHz ESE spectra of $NH_2Y_{730}\bullet/C_{439}A$ and $NH_2Y_{731}\bullet/Y_{730}F$ compared to the corresponding single mutants. ....	94
4-13: 263-GHz EPR spectra of $NH_2Y_{730}\bullet/C_{439}A$ and $NH_2Y_{731}\bullet/Y_{730}F$ compared to their corresponding single mutants. ....	95
4-14: $^2H$ Mims ENDOR spectrum of the double mutants .....	96
4-15: Orientation-selective $^2H$ Mims ENDOR for $NH_2Y_{731}\bullet/Y_{730}F$ .....	98
4-16: Central part of the DFT geometry optimized $NH_2Y_{731}\bullet$ models.....	100
4-17: X-ray structures including water molecules in $\alpha$ subunit. ....	100
4-18: Ring dihedrals $\theta_{C\beta}$ of the crystal structure compared to models 1, 2 and 3 considered for $NH_2Y_{731}\bullet$ and $Y_{731}\bullet$ .....	102
4-19: Comparison of DFT models and H bond orientation from ENDOR simulation parameters in their respective molecular frame. ....	103

4-20: Energy diagram for the PCET in $\alpha$ .....	108
4-21: H bond environment of $Y_{730}\bullet$ .....	109
4-22: 94 GHz-Echo detected spectra of $NH_2Y_{356}\bullet$ recorded at different freezing time points during the reaction.....	111
4-23: 263-GHz EPR spectra of $ND_2Y_{356}\bullet$ measured at three reaction time points.....	113
4-24: 94 and 263-GHz EPR spectra of $NH_2Y_{356}\bullet$ and simulation.....	113
4-25: $^2H$ ENDOR spectrum of $NH_2Y_{356}\bullet$ quenched at 10 s compared with simulation.....	115
4-26: Dihedral scan over the ring dihedral.....	118
4-27: Dihedral scan over the H bond dihedral.....	120
4-28: DFT models of different H bonding situations at a $NH_2Y\bullet$ .....	122
4-29: DFT model demonstrating the effect of positive charges ( $Mg^{2+}$ ) in the surrounding of the phenoxy nucleus.....	125
5-1: Reduction redox potentials are shown along the PCET in mV relative to the oxidation of $Y_{122}\bullet \rightarrow Y_{122}\bullet + e^- + H^+$ .....	129
5-2: EPR spectra of $2,3,5-F_3Y_{122}\bullet$ at different frequencies (9, 94 and 263 GHz).....	132
5-3: DFT model of $2,3,5-F_3Y_{122}\bullet$ .....	134
5-4: 94-GHz EPR spectrum of PCET radical formed with $\beta_2-2,3,5-F_3Y_{122}:\alpha_2-Y_{731}F$ in deuterated buffer.....	136
5-5: 34-GHz EPR spectrum of the PCET radical formed with $\beta_2-2,3,5-F_3Y_{122}:\alpha_2-Y_{731}F$ in deuterated buffer.....	137
5-6: Comparison between radical formed from $\beta_2-2,3,5-F_3Y_{122}:\alpha_2-Y_{731}F$ in $H_2O$ and $D_2O$ .....	138
5-7: 34-GHz diagonal distance measurement with the pathway radical produced by $\beta_2-2,3,5-F_3Y_{122}:\alpha_2-Y_{731}F$ .....	140
5-8: $^2H$ ENDOR of $Y_{356}\bullet$ with $\alpha(Y_{731}F)$ .....	141
5-9: Orientation selective $^2H$ ENDOR of $Y_{356}\bullet$ with $\alpha-Y_{731}F$ .....	143
5-10: DFT model of a $Y\bullet$ with one water molecule.....	144
5-11: EPR spectra and simulation of the pathway radicals using $\beta_2-2,3,5-F_3Y_{122}:\alpha_2$ -wt at two frequencies.....	147
5-12: Comparison between an $H_2O$ and a $D_2O$ spectra of the $Y_{356}\bullet$ formed $\beta_2-2,3,5-F_3Y_{122}:\alpha_2$ -wt.....	149
5-13: $^2H$ ENDOR of $Y_{356}\bullet$ with wild type $\alpha$ .....	150
5-14: Comparison of $Y_{356}\bullet$ with wild type $\alpha$ in protonated and deuterated buffer.....	152
5-15: Biomimetic systems of H bonded tyrosine analogs linked to a photosensitizer.....	160
5-16: Dependence of the estimated PCET rate constant on the proton donor-acceptor distance $d_{O-N}$ .....	161

---

## LIST OF ABBREVIATIONS AND ACRONYMS

§	section
A	Alanine
A	hyperfine coupling coupling value
$a_{iso}$	isotropic hyperfine coupling value
C(•)	cysteine (radical)
cf.	confer
DFT	density functional theory
Dopa	( <i>S</i> )-2-Amino-3-(3,4-dihydroxyphenyl) propanoic acid
E. coli	Escherichia coli
ELDOR	electron-electron nuclear double resonance
ENDOR	electron nuclear double resonance
EPR	electron paramagnetic resonance
ET	electron transfer
Exp.	experimental
HAT	hydrogen atom transfer
H bond	hydrogen bond
HF	hyperfine
MW	microwave frequency
(d)NDP	(2'-deoxy)nucleotide diphosphate (nucleotide = A, adenosine; G, guanosine; T, thymidine; U, uridine; C, cytidine)
NH <sub>2</sub> Y(•)	3-amino tyrosine (radical)
PAS	principle axis system
p.	page
P	phosphate
PDB ID	protein database identification code
PELDOR	pulsed electron-electron double resonance
ref.	reference
RF	radio frequency
PS	photosystem
PT	proton transfer
RMSD	root mean square deviation
RNR	ribonucleotide reductase
RT	radical transfer (translocation)
SRT	shot repetition time (delay between two pulse sequences)
S/N	signal to noise ratio
SPP	shots per point

T	temperature
$T_{\perp/\parallel}$	orthogonal/parallel anisotropic hyperfine coupling
$T_1$	spin-lattice relaxation time
$T_2$	spin-spin relaxation time
UAA	unnatural amino acid
wt	wild type
XRD	X-ray crystal structure diffraction
Y(•)	l-tyrosine (radical)
$g_e$	2.002329304, g-factor
$\nu_{1H}$	142.63 MHz, $^1H$ Larmor frequency ( $B_0=3.35$ T)
$\nu_{2H}$	21.895 MHz, $^2H$ Larmor frequency ( $B_0=3.35$ T)
$\nu_{19F}$	134.16 MHz·T <sup>-1</sup> , $^{19}F$ Larmor frequency ( $B_0=3.35$ T)
$\gamma_e$	-1.760 s·T <sup>-1</sup> , gyromagnetic ratio for an electron ( $g\mu_e/\hbar$ )

---

## LIST OF APPENDICES

1:	Previous EPR Results for $\text{NH}_2\text{Y}^\bullet$ .....	191
2:	Appendix to Chapter 4 ( $\text{NH}_2\text{Y}_{730/731}^\bullet$ ) .....	192
3:	Appendix to Chapter 4 ( $\text{NH}_2\text{Y}_{356}^\bullet$ ) .....	198
4:	Appendix to Chapter 5 .....	200
5:	CV .....	201



# 1 INTRODUCTION

## RIBONUCLEOTIDE REDUCTASES

Decades after their discovery, Ribonucleotide Reductases (RNRs) remain at the frontier of science in diverse disciplines. With the first tyrosine radical ever found in an enzyme,<sup>1</sup> RNRs opened up a complete new field of radical enzymes.<sup>2, 3</sup> Regarding oxygen storage and transformation, the RNR cofactor structure has sparked interest in atomistic molecular mechanisms.<sup>4</sup> Furthermore, orally administered compounds targeting ribonucleotide reductases were found useful in cancer therapy.<sup>5</sup> Therefore, a short overview of this class of essential enzymes for higher life forms is given.<sup>6,7</sup>

### 1.1 Ribonucleotide Reductases: Bridging the RNA and DNA World

With the evolution from RNA to DNA, the necessity to form deoxyribonucleotides from ribonucleotides—under the retention of configuration—fostered the need for a specialized radical enzyme, the ribonucleotide reductase.<sup>8</sup> This enzyme is entirely responsible for providing 2'-deoxyribonucleotides (as dNPDs or dNTPs) from all four ribonucleotides (as NPDs or NTPs; Figure 1-1);<sup>9</sup> thereby it plays a strictly controlled central metabolic role in regulation of DNA precursors.<sup>10,11</sup> Depending on the target organism, this essential role has been used successfully for anticancer, antibacterial and antiviral therapies.<sup>12-15</sup>

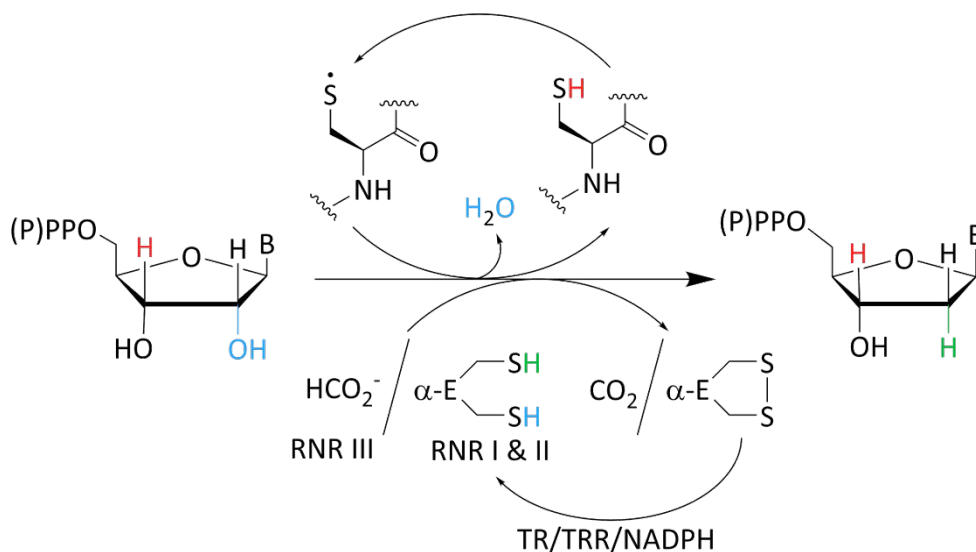


Figure 1-1: Chemical reaction catalyzed by RNRs. The 3' hydrogen (marked red) abstraction leads to the irreversible loss of the 2' hydroxyl (marked blue) in the form of water.<sup>16-18</sup> The reaction is catalyzed by a bound cysteine radical (C•).<sup>19</sup> The C• is initially formed by several radical precursors as shown in Figure 1-2. Proton(s) and two electrons of two neighboring thiols (RNR I and II) or from formate (RNR III) reduce the nucleotide. For RNR I and II the rereduction is performed by thioreoxin (TR) coupled to thioredoxin reductase (TRR) using NADPH as cofactor.<sup>2</sup>

## 1.2 Diverse Classes of Ribonucleotide Reductases

RNRs are divided into three enzyme classes. From the evolutionary view point, the different classes of RNRs can be linked to the change from a reducing to an oxidizing atmosphere. The different classes of RNRs are connected to aerobic and anaerobic life forms. In all classes a cysteine radical is proposed to induce a 3' abstraction on the nucleotide side, as illustrated in Figure 1-1. Hence, this radical has to be generated. The three classes of RNR can be distinguished by their cysteine radical generation, see Figure 1-2.<sup>8</sup> The cysteine radical is located on the tip of a loop within a structurally conserved ten-stranded  $\alpha/\beta$  barrel protein, the  $\alpha$  subunit.<sup>20-22</sup> The structural motive belongs to the super family of glycyl radical enzymes.<sup>23,24</sup> RNR class III indeed produces a glycyl radical by an activase. This additional enzyme utilizes iron sulfur chemistry ( $\text{Fe}_4\text{S}_4^{+/2+}$ ) in a complex with S-adenosylmethionin.<sup>3,20,25-27</sup> Glycyl radicals are oxygen sensitive; therefore RNR III works strictly under anaerobic conditions. Here the catalytic cycle is closed by a chemically simple formate as reductant, supporting the idea that class III is closely related to the ancient form of RNRs.<sup>6</sup>

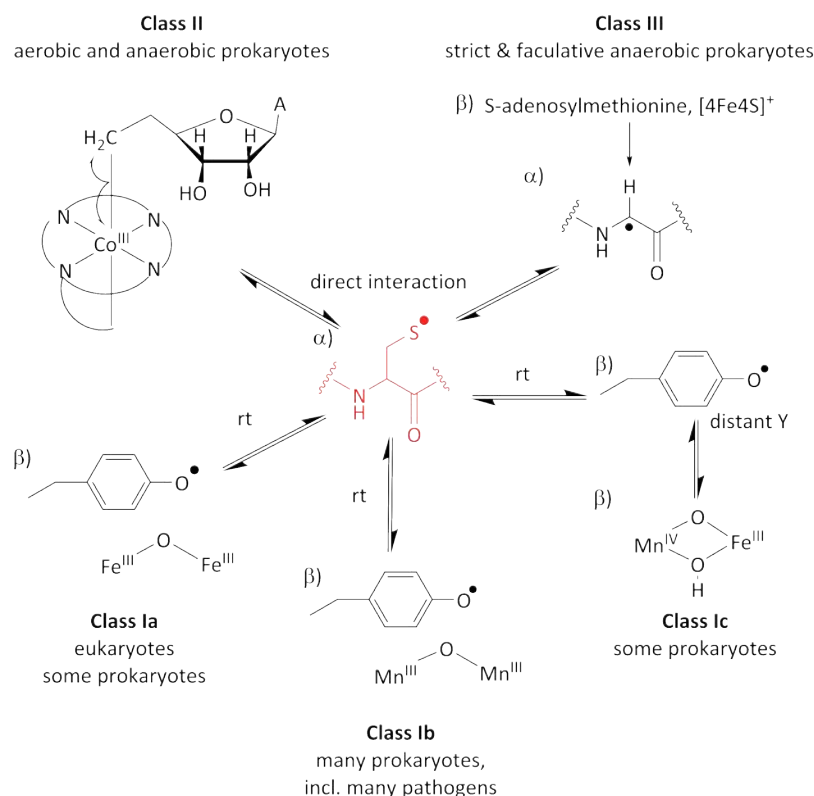


Figure 1-2: Classification of RNRs based on their metal cofactor to activate  $C^\bullet$  at the nucleotide reduction site. The respective location of the cofactors is denoted by  $\alpha$  or  $\beta$ . Adapted from reference.<sup>28</sup> The interaction between cofactor and active site is either direct or over a radical transfer (RT, see Section §1.4, p.6).

Class II RNRs can tolerate oxygen, but are also independent from oxygen. They are activated by a radical cofactor formed from adenosylcobalamin and have been found to include the only functional monomeric RNRs.<sup>21</sup> RNR class II and III proteins are common in bacteria and archaea, but rare in eukaryotes.<sup>29</sup> A comparison of the  $\alpha/\beta$  barrel has found a higher structural similarity between RNR II and RNR I compared to RNR III. The root mean square deviation (RMSD) increases from 1.0 Å to 1.7-1.8 Å (based on 70  $C_{as}$ ).<sup>20-22</sup>

Class I RNR's are common in eukaryotes and rare in bacteria and archaea.<sup>29,30</sup> This class I harbors an  $\mu$ -oxo-di-metallo cofactor, which induces a tyrosine radical ( $Y^\bullet$ ) in the  $\beta$  subunit.<sup>27,31-33</sup>

Depending on the environmental conditions, one RNR class can be better suited than another, as in anaerobic conditions RNR III, iron limiting or facultative oxygen supply conditions RNR II and in aerobic oxygen rich environments RNR I.<sup>8</sup> Therefore, often several enzymes are found in an individual organism, as in *Escherichia coli* (*E. coli*).

The class I RNRs are further divided into three subclasses: (i) class Ia harbors an  $\text{Fe}^{\text{III}}_2$  site, (ii) RNR Ib has a  $\text{Mn}^{\text{III}}_2$  cofactor and (iii) RNR Ic has a mixed  $\text{Mn}^{\text{IV}}$  and  $\text{Fe}^{\text{III}}$   $\mu$ -oxo- $\mu$ -hydroxy complex. Despite the huge diversity of RNRs, some structural aspects are highly conserved, for instance, the nucleotide reduction mechanism, the activity and the specificity binding site.<sup>33-35</sup> It is noteworthy that the location of the glycy radical (RNR III), 5'-deoxyadenosyl radical (RNR II) and two tyrosines (RNR I) occupy the same structural space in all RNRs. RNR Ia and Ib form a  $\text{Y}\bullet$  in direct vicinity to the metal cofactor,<sup>20-22</sup> whereas RNR Ic forms a  $\text{Y}\bullet$  in  $\beta$  under a similar radical propagation mechanism.<sup>36-38</sup> In RNR Ib, however, the formation is dependent on a cosubstrate (NrdI).<sup>32, 39, 40</sup> Whereas for RNR Ia and Ic the active state resembles an  $\alpha_2:\beta_2$  complex,<sup>33, 41</sup> RNR Ib shows a variety of active encounters.<sup>42</sup> All class I enzymes must transfer the electron from the  $\alpha$  to the  $\beta$  subunit. This radical translocation and its mechanism based on putatively conserved radical intermediates within RNR Ia (cf. §1.4, p. 6) is still part of ongoing research and studied within this thesis.<sup>22,</sup>

38, 43-49

### 1.3 Differences and Similarities of *Escherichia Coli* and Eukaryotic RNRs

This thesis focuses on the prototypical RNR Ia from *E.coli*. However, class Ia is most prominently found in eukaryotic organisms.<sup>29</sup> RNR structures of yeast, mice and humans have been studied.<sup>50</sup> Therefore, structural differences and similarities should be mentioned. The  $\alpha$  subunits of several RNRs can be compared based on existing crystal structures (Figure 1.3).

Although the sequence homology of approximately 27%, is quite small, the RMSD of *E. coli* RNR structure is small compared to that of eukaryotic RNR.<sup>50</sup> For example, the differences in all common  $\text{C}_\alpha$  positions between *E. coli* and human RNR is  $1.3 \text{ \AA}^{50}$  and to yeast it is  $1.7 \text{ \AA}^{50}$ . Moreover, conserved residues, which are intended to take part in the radical translocation, allocate the same structural space for all found class I  $\alpha$  structures (cf. Figure 1-3). In *E. coli* RNR Ia numbering, they are  $\text{Y}_{730}$  and  $\text{Y}_{731}$  (dark gray in Figure 1-3).

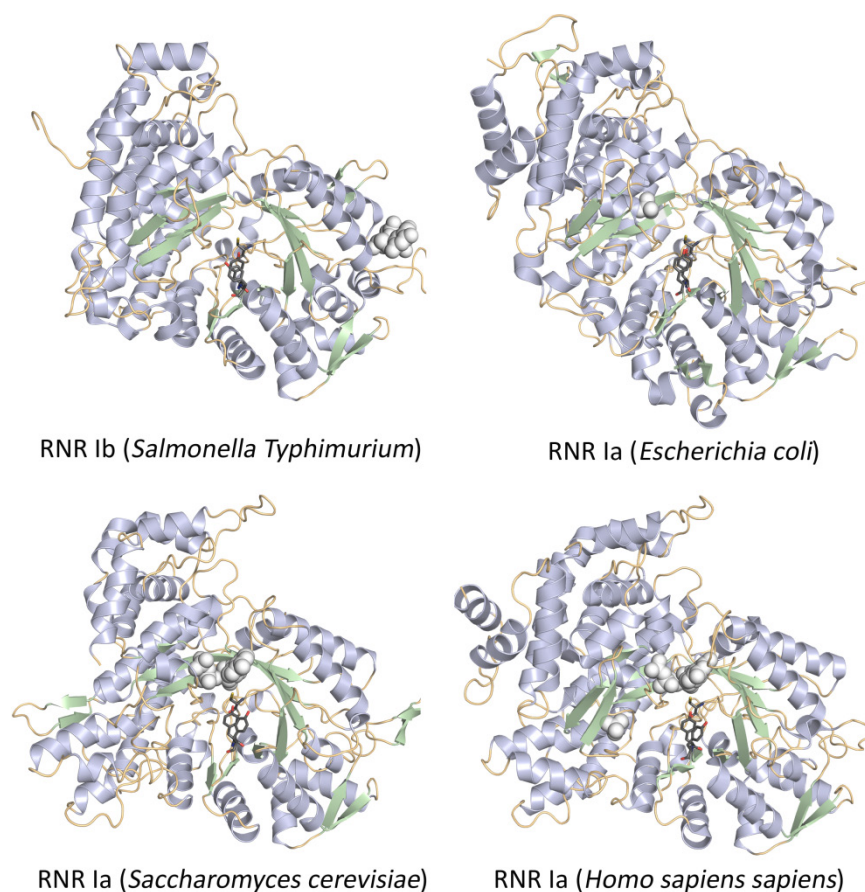


Figure 1-3: Similarities between the different RNR I  $\alpha$  subunit structures from four organisms. Important conserved residues (Y-Y-C) for the radical transfer are shown in dark gray. The occupancy of the nucleotide reduction side or the effector side is shown in white spheres. The crystal structures used can be found in the protein data base under PDB ID: 1PEQ, 2X0X, 3S87 and 3HND left to right, up to down.<sup>38, 43, 44, 50, 51</sup>

Comparing eukaryotic RNR  $\beta$  subunits to *E. coli*, several differences were found: the so-called stable  $Y\bullet$  (Figure 1-2) has been found to be far more accessible in eukaryotes compared to the prokaryotic structure.<sup>52, 53</sup> This also had implications on the electron paramagnetic resonance (EPR) spectra of this radical site. The  $Y\bullet$  in eukaryotic RNRs is hydrogen (H) bonded, whereas that of *E. coli* is isolated; however, both are expected to be in a hydrophobic environment (cf. Figure 1-5, inset).<sup>54, 55</sup> The structural differences to *E. coli* in the  $\beta$  subunit are larger. For example, based on the C- $\alpha$  overlay 389 atoms fit between the hp53R2 dimer and the *E. coli* (1PFR) structure with an r.m.s. deviation of 1.67 Å.<sup>53</sup> The  $\alpha_2/\beta_2$  subunit interaction is weak with a  $K_d$  of 0.4-0.5  $\mu\text{M}$ <sup>56-59</sup> in pro- and eukaryotic RNR Ia. So far, no structure of the active state could be found in any RNR.

In the following part of the chapter, the current knowledge and the aim of this thesis is further defined.

## 1.4 Escherichia Coli RNR Ia

### 1.4.1 Structural Basis of the Radical Transfer

#### 1.4.1.1 The Tertiary and Quaternary Structure

To understand the activity of RNR Ia enzymes, several features have to be considered. Two diferrous sites are located in the obligate dimeric  $\beta_2$  subunit with 87 kDa.<sup>46,60</sup> The  $\beta_2$  subunit forms the  $\mu$ -oxo-diferric  $Y^\bullet$  cofactor using molecular oxygen.<sup>60</sup> UV-vis spectroscopy has shown that this tyrosine cofactor is remarkable in terms of stability.  $Y_{122}^\bullet$  is exceptionally stable with a half-life of  $t_{1/2} \approx 14$  d at 4 °C,<sup>61</sup> whereas tyrosine radicals in solution are reduced within  $\mu$ s.<sup>62</sup> The crystal structure of the oxidized form revealed that  $Y_{122}$  is 10 Å away from the surface and embedded in a closed hydrophobic region.<sup>46</sup> EPR crystal studies showed only a slight tilt ( $\approx 3^\circ$  ring dihedral) of  $Y_{122}^\bullet$  after reduction.<sup>63</sup> On the other hand, stability of the radical implies that the  $\beta$  subunit is able to trigger catalysis in  $\alpha$  over a long reaction time.

Due to its central role in DNA synthesis and repair, the enzyme has to be tightly regulated. Beside the regulation in transcription,<sup>64</sup> the subunit interaction controls the formation of the  $\alpha_2/\beta_2$  active complex. This is regulated by the large  $\alpha_2$  dimer, with 172 kDa (Figure 1-4). Binding of ATP and dATP in the activity site increases and reduces the activity, respectively. Furthermore, allosteric control insures for the four different substrates (S= CDP, ADP, GDP, UDP) by nucleotide binding to the effector site (E= ATP, dGTP, TTP and dATP) a balanced pool of dNTPs. Overall, the binding of nucleotides intensifies the inter subunit binding by a factor of 2-8.<sup>56,59</sup> Moreover, the equilibrium between the active  $\alpha_2\beta_2$  complex and the inactive  $\alpha_4\beta_4$  is regulated by the activity site.<sup>65</sup>

The active complex envisioned *in silico* based on shape complementary of the individual subunits  $\alpha_2$ <sup>22,66,67</sup> and  $\beta_2$ <sup>46,63,68</sup> is shown in Figure 1-5. The inactive ( $\alpha_4\beta_4$ ) complex has been characterized by low-resolution methods such as cryo-EM<sup>69,70</sup> and small angle X-ray scattering data.<sup>71</sup> Interestingly, the distance between the substrate binding site and the  $Y_{122}^\bullet$  increases from about 40 Å to 55 Å between the active to the inactive form based on these models.<sup>65</sup> This regulatory process, however, tells us nothing about how this distance can be overcome to form the catalytic  $C^\bullet$ .

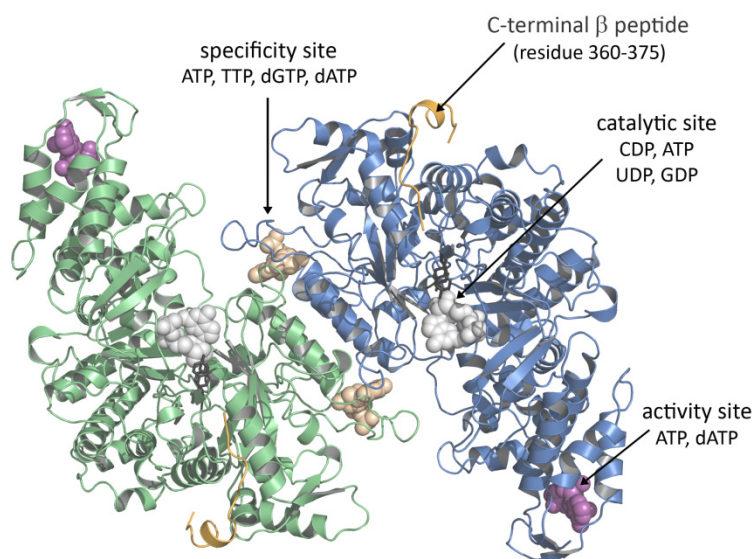


Figure 1-4: Crystal structure of the  $\alpha_2$  dimer of *E. coli* RNR Ia. The  $\alpha_2$  (green and blue) has three nucleotide binding sites. A catalytic site (GDP in white) with the nearby catalytic C<sub>439</sub>, a specificity site (TTP in ecru).<sup>22</sup> An activity site harbors an ATP substitute (PDB ID 3R1R) as highlighted in purple.<sup>66</sup> The obtained crystals required all the presence of a 15 amino acid C-terminal  $\beta$  peptide (orange).

#### 1.4.1.2 The Proposal of the Radical Translocation Pathway

In the docking model, as mentioned in the previous section, a rigid  $\alpha/\beta$  barrel structure interacts with a buried Y<sub>122</sub><sup>•</sup>.<sup>22,46</sup> Ridged-body docking models could not further reduce this distance between Y<sub>122</sub><sup>•</sup> and the catalytic site.<sup>22</sup> This *in silico* model implied a radical transfer (RT) over 38 Å. Uhlin and Eklund concluded in 1994, that a long-range radical transfer takes place to overcome the distance between Y<sub>122</sub><sup>•</sup> and nucleotide reduction side.<sup>22,72</sup> The proposal of an electron transfer (ET) over more than 35 Å was unprecedented at that time.<sup>2</sup> Four residues were suggested to form radical intermediates as W<sub>48</sub> and Y<sub>356</sub> in  $\beta$ , whereas Y<sub>731</sub> and Y<sub>730</sub> were assigned to take part in this RT in  $\alpha$  (cf. Figure 1-5 left).

The participation of  $\beta$ -W<sub>48</sub> in RT was suggested based on two arguments. First, it is a strictly conserved residue at the interface. Second, W<sub>48</sub> was in a local environment similar to a W in cytochrome c oxidase, where W<sup>+</sup><sup>•</sup> has been found as an intermediate.<sup>72</sup> However, no experimental evidence has been shown for the participation of W<sub>48</sub><sup>+</sup><sup>•</sup> in the ET of RNR up to today.<sup>73,74</sup>

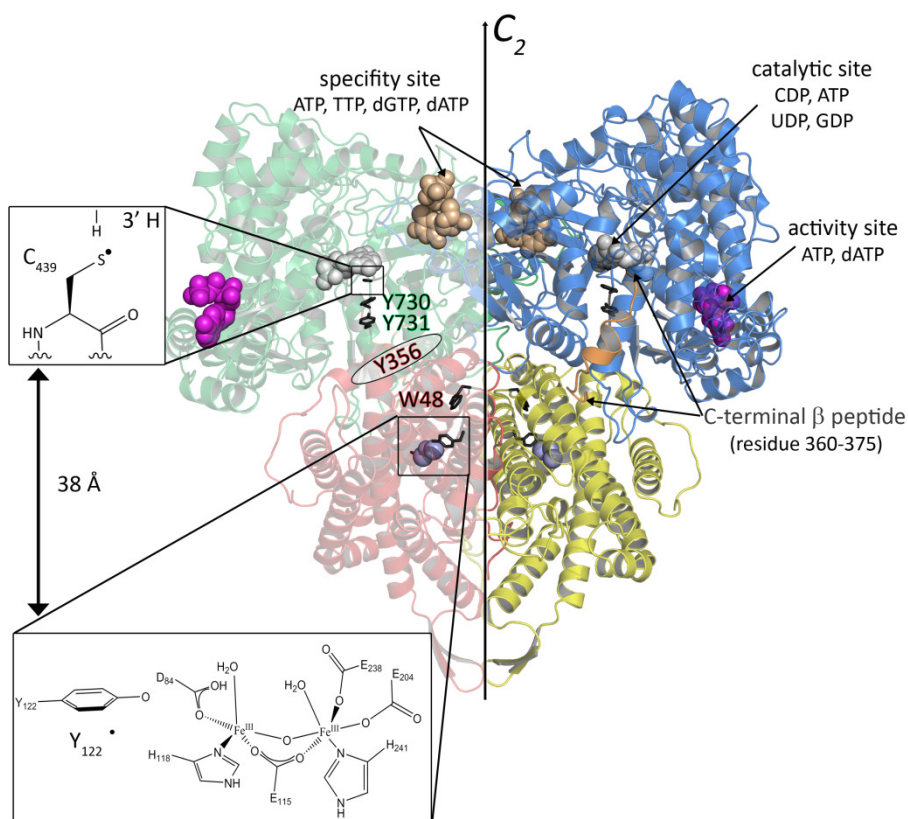


Figure 1-5: *E. coli* RNR  $\alpha_2\beta_2$  docking model.<sup>22</sup> The  $\beta_2$  subunit (red and yellow) harbors the diferric  $Y_{122}\bullet$  cofactor (large inset).<sup>46</sup> The  $\alpha_2$  dimer (green and blue) has the catalytic side (GDP in white) with the nearby catalytic  $C_{439}\bullet$  (small inset).<sup>22</sup> The distance in this model between  $\beta$ - $Y_{122}$  and  $\alpha$ - $C_{439}$  is 38 Å. Strictly conserved residues along the radical translocation pathway are shown in black. 32 C terminal residues are not observed due to thermal lability including  $\beta_2$ - $Y_{356}$  (marked with an ellipsoid).

Despite the absence of structural information (Figure 1-5), residue  $\beta$ - $Y_{356}$  was proposed to form a  $Y\bullet^{75}$  and bridge the gap between  $\beta_2$  and  $\alpha_2$  subunits. Seminal studies demonstrated that, although binding of the subunits is not perturbed,  $Y_{356}F$  mutation renders the protein inactive.<sup>45,56</sup> In  $\alpha_2$ , the phenylalanine mutants of  $Y_{730}$  and  $Y_{731}$  were revealed to be inactive,<sup>47</sup> although the inter-subunit binding and crystal structures of the mutant were unperturbed.<sup>47</sup> Despite the success in assigning putative intermediates, the detection of radicals along the pathway remained elusive. A slow conformational step has been postulated as the main reason for the absence of pathway radicals in the wild type (wt) enzyme and mutants mentioned so far.<sup>34,47,76</sup>



## 1.4.2 Unnatural Amino Acids to Study the Radical Translocation

In RNR Ia, two things have to be considered in studies of the RT: local structural or kinetic changes. First, RNR has an apparent half-site reactivity,<sup>77</sup> but the active model is completely symmetric. Half-site reactivity is otherwise known from pseudo-symmetric molecular machines like the photosystem II (PS II).<sup>78,79</sup> In RNR both half-sites are proposed to be active successively.<sup>41,76</sup> A slow conformational arrangement occurs before the first  $\alpha/\beta$  RT takes place and the second conformational step during or after product formation, but before the other half-site is triggered.<sup>80</sup> This clearly complicates a stepwise investigation of the formed intermediates. The radical transfer and nucleotide reduction steps are not directly observable.<sup>18,76</sup> Therefore, unnatural amino acids (UAA) were incorporated into *E. coli* RNR.

### 1.4.2.1 Evidence for the Active Role of $\beta$ -Y<sub>356</sub>

First experimental evidence for an active role of  $\beta$ -Y<sub>356</sub> within RT was obtained by turnover studies with unnatural amino acids. Catalytic rates changed by changing the redox potential (compared to  $Y \rightarrow Y^\bullet + e^- + H^+$ ) and the pK<sub>a</sub> at position 356.<sup>81-83</sup> F<sub>n</sub>Y's and 4-NH<sub>2</sub>-phenylalanine (Figure 1-6 B) were incorporated at this position. It could be shown that redox potential differences from -50 to 50 mV are tolerated without loss of activity. When the pH of the buffer was changed stepwise at redox potential differences above 120 mV, only 30% of wt activity was observed. The differences in pK<sub>a</sub> values also revealed that RNR does not require a protonated tyrosine at 356 to be active. These studies suggested that a proton transport (PT) is not a prerequisite for ET from and to Y<sub>356</sub>.<sup>82,83</sup>

Notably, this was the first indication that in the  $\beta$  subunit, due to the higher pK<sub>a</sub> of tyrosines, the proton travels orthogonally to the ET. Here a strongly conserved E<sub>350</sub> in  $\beta$  has been proposed to be involved.<sup>82,83</sup> Mutation of  $\beta$ <sub>2</sub>-E<sub>350</sub> to alanine leads to a catalytically inactive enzyme, despite the ability to bind  $\alpha$ <sub>2</sub>.<sup>45</sup>

### 1.4.2.2 Observation of Radical Intermediates

Three main procedures were developed to introduce a new rate limiting step in RNR and to observe radical intermediates.<sup>41</sup> First, an unnatural amino acid (Figure 1-6, 2&3) was incorporated to reduce the electron potential. This method can be applied to all RT pathway residues. Second, the potential of Y<sub>122</sub> can be increased by introduction of an unnatural amino acid.<sup>28,84</sup> This method will be discussed in Chapter 5 in more detail. Furthermore, a

radical can be produced via photoexcitation, for instance with a Re(I) complex.<sup>85,86</sup> This complex is apolar and can alter the local environment at the interface.<sup>85,86</sup>

Introducing more stable radical intermediates to form radical “sinks” or “traps” could be performed site selectively in various ways.<sup>41</sup> The first example is the incorporation of (*S*)-2-Amino-3-(3,4-dihydroxyphenyl) propanoic acid (Dopa) as unnatural amino acid. It has a 260 mV lower reduction potential compared with tyrosine under similar conditions. Hence, incorporated for Y<sub>356</sub>-β<sub>2</sub> the protein becomes inactive, but a radical can be observed at Dopa<sub>356</sub>-β<sub>2</sub> after reaction with excess substrate, effector and α<sub>2</sub> (single turnover conditions).<sup>87</sup>

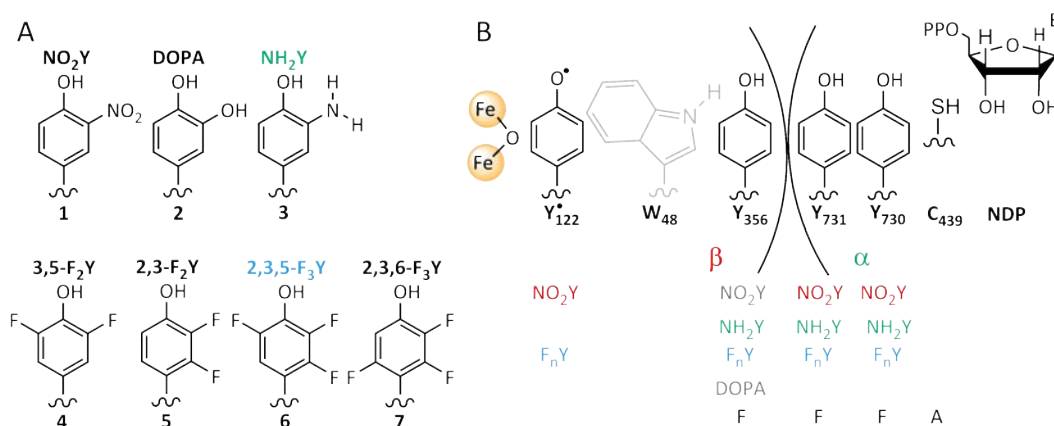


Figure 1-6: Unnatural amino acids (UAA), which could be incorporated into RNR. A) UAA 1, 3-7 have been incorporated by the AMBER Stop codon *in vivo* nonsense suppression.<sup>88</sup> UAA 1, 2, and 4-7 have been incorporated in position 356 of β<sub>2</sub> by expressed protein ligation.<sup>89</sup> B) Positions within the pathway where UAA have been incorporated by the AMBER stop codon (in color) and protein ligation (in gray). Phenylalanine (F) or alanine (A) are shown in black incorporated by site specific mutagenesis. As summarized in ref. <sup>41</sup>.

The second example stabilizes the radical on the pathway and still allows residual activity of the mutant protein complex with 3–12%.<sup>44,67</sup> Additionally, the pK<sub>a</sub> is nearly identical to that of Y.<sup>44</sup> 3-Amino tyrosine (NH<sub>2</sub>Y) is 190 mV easier to oxidize to its corresponding radical (NH<sub>2</sub>Y•) than Y based on the peak potentials.<sup>90</sup> Under single turnover conditions it competitively “traps” the radical along the pathway.<sup>91</sup> Here crystal structures of α<sub>2</sub> revealed an undisturbed environment for the NH<sub>2</sub>Y incorporation at 731 and 730, as displayed in Figure 1-7.<sup>67</sup> These mutants were incorporated at all pathway tyrosine residues, as summarized in Figure 1-6. Kinetic studies revealed that the radical formation is kinetically competent compared to the overall rate of wt RNR of 2-10 s<sup>-1</sup>.<sup>76</sup> The biphasic behavior of all

radical formations was assigned to a conformational step. This step is prior to radical formation, thus between  $Y_{122}$  and  $Y_{356}$ .<sup>28, 44, 67</sup> After formation of the radicals in ~30–40% yield, they are stable up to several minutes.<sup>67, 92</sup> This offered the possibility for their spectroscopical (§1.4.3 §1.5 and Chapter 4) and biochemical investigation.

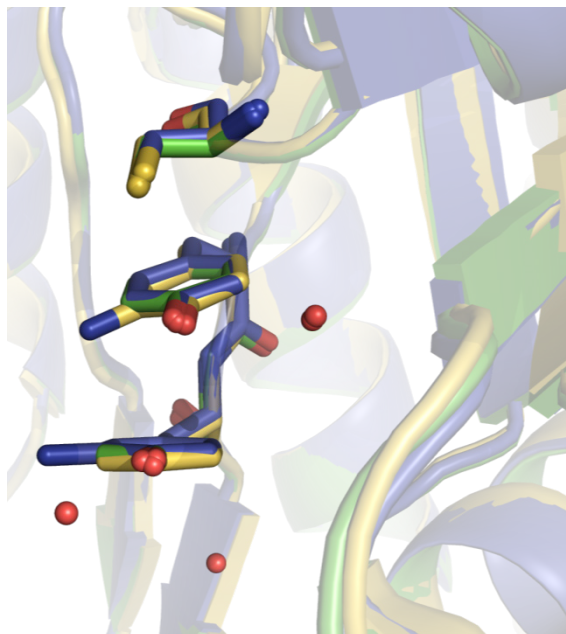


Figure 1-7: Overlay of crystal structures of  $NH_2Y_{730}$  (yellow),  $NH_2Y_{731}$  (blue) and  $wt-\alpha_2$  (green). Three RT pathway residues are shown as sticks and oxygen nuclei of water molecules in red spheres.<sup>67</sup>

### 1.4.3 Experiments on the $\alpha_2\beta_2$ RNR Complex

The first experimental evidence of the “active” complex was obtained from pulsed EPR spectroscopy of radical pairs.<sup>80</sup> The coupling between radical pairs can be measured by pulsed electron double resonance (PELDOR) spectroscopy and a distance can be assigned (see Section §2.1.4, p.35). After observation that both  $\beta$  subunits carry a  $Y_{122}$ <sup>93</sup> the half-site reactivity<sup>77</sup> was used to measure the distance between  $\beta$ - $Y_{122}\bullet$  and radicals in  $\beta$  or  $\alpha$ , as shown in Figure 1-8A.<sup>80</sup> First, in a PELDOR experiment with solely wild type enzyme only one distance from  $Y_{122}\bullet$ - $Y_{122}\bullet$  could be observed.<sup>76</sup> Then a nucleotide analog inhibitor forming a stable radical in  $\alpha$  was used. A diagonal distance of  $48\pm 1$  Å was obtained.

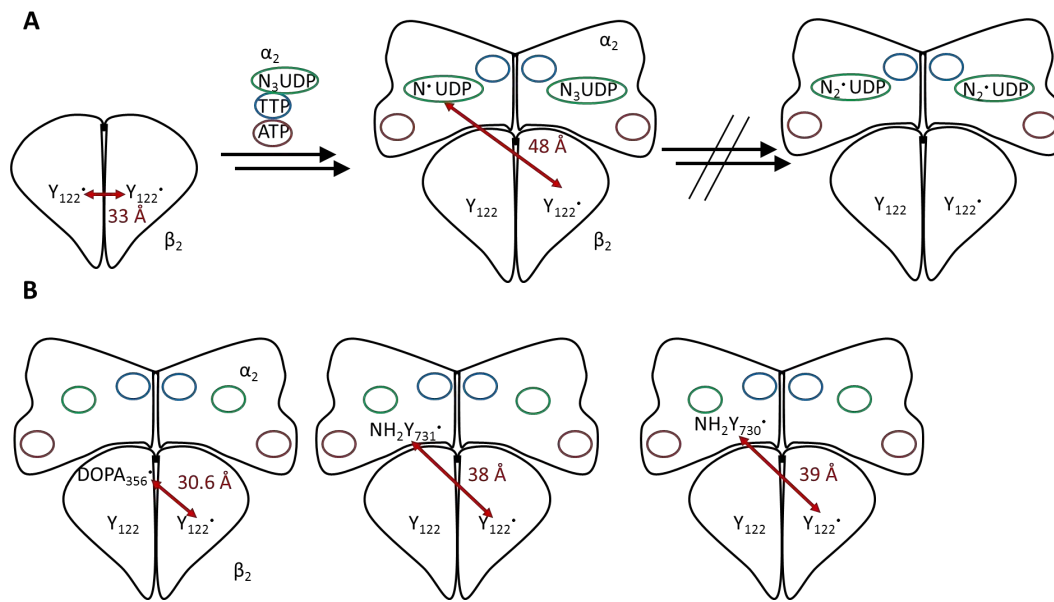


Figure 1-8: Diagonal distances of the active complex obtained with radical traps. A) PELDOR on  $\beta_2$  revealed two  $Y_{122}^{\bullet}$  in  $\beta_2$ . Under reaction conditions with the substrate inhibitor 2'-azido-2'-deoxyuridine-5'-diphosphate only two distances are observed, 48 Å and 33 Å. B) In three consecutive reactions with three  $\beta_2/\alpha_2$  mutants diagonal distances gave the first experimental evidence for the proposed radical intermediates. All distances supported the docking model.

Successive work also measured diagonal distances to  $Dopa_{356}^{\bullet}$  and  $NH_2Y^{\bullet}$  at all suggested RT Y positions (Figure 1-8B).<sup>28, 41, 65</sup> All distances supported the docking model. The “active”  $\alpha_2\beta_2$  complex is meanwhile generally accepted.<sup>28, 41, 65</sup> These PELDOR studies were equally important as the first experimental evidence of radical intermediates between the subunits bridging the interface. And therefore they demonstrated the long distance electron transfer. Recently, the same distance to  $Y_{356}^{\bullet}$  has been determined in the millisecond time scale (8 ms) using another UAA ( $NO_2Y_{122}^{\bullet}$ ) approach discussed in §1.4.5 (p.16).<sup>84</sup>

The “active” complex was only observed during the lifetime of a metastable transient radical ( $NH_2Y_{730}^{\bullet}$ ) formed in  $\alpha$ .<sup>69</sup> Using this mutant, it had been demonstrated that in the “active” complex the subunit interaction increases by a kinetic factor of  $\sim 10^4$ .<sup>69</sup> This information along the interface could identify binding principles, which might be intercepted by inhibitors. Finding specialized inhibitors in RNRs is still an ongoing process.<sup>15</sup> For instance  $\beta$ -peptides mimicking the C-terminal region of  $\beta_2$  (see Figure 1-4) or nucleotide inhibitors operate at the interface.<sup>13, 15</sup> Structural information might improve these inhibitors. Currently, a 32 Å resolution structure of the “active” complex is available from cryo-electron microscopy reconstruction.<sup>69</sup>

### 1.4.4 Proton-Coupled Electron Transfer

All radical transfer intermediates shown so far are amino acids. During each nucleotide turnover, they oxidize reversibly within the turnover rate of RNR ( $2\text{-}10\text{ s}^{-1}$ ).<sup>76</sup> Under physiological conditions, reversible oxidation requires release of a proton to an acceptor concomitant with oxidation. Otherwise, high energy intermediates are formed. More specifically, for tyrosines the difference between a stepwise transfer and a concerted proton electron transfer (CPET) is 540 mV in redox potential.<sup>94</sup> A strong acidic ( $\text{Y-OH}^+\bullet$ ) transition state would be formed in a stepwise transfer, as illustrated in the parallelogram in Figure 1-9. To avoid high energy intermediates a variety of individual proton coupled electron transfer (PCET) steps are linked to the nature of the RNR radical enzyme.<sup>17</sup> Studying individual PCET steps can be a paradigm to understand common principles, which control this fundamental process. Basic principles among PCET processes in biology are still hardly defined including but not limited to: photosynthesis, respiration and nitrogen fixation.<sup>95-97</sup>

In RNR several amino acid oxidations take place over an unprecedented length.<sup>41, 94, 98</sup> Here nearly every combination of possible PCETs has been discussed. The differences in mechanism should be briefly described in terms of forward radical transfer toward the active site (forward PCET). A recent proposal of the PCET mechanism in RNR is shown in Figure 1-10.<sup>41</sup>

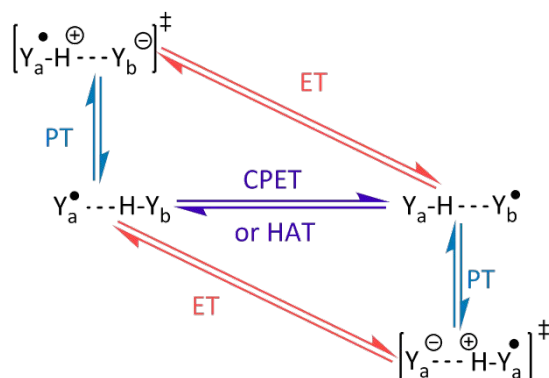


Figure 1-9: PCET pathways between two Y radicals. An electron transfer (ET) and a proton transfer lead successively to charge separated transition states (double dagger). A concerted proton coupled electron transfer (CPET) avoids these states. A hydrogen atom transfer (HAT) is a special case of CPET in which the proton and the electron are transferred to the same orbital.

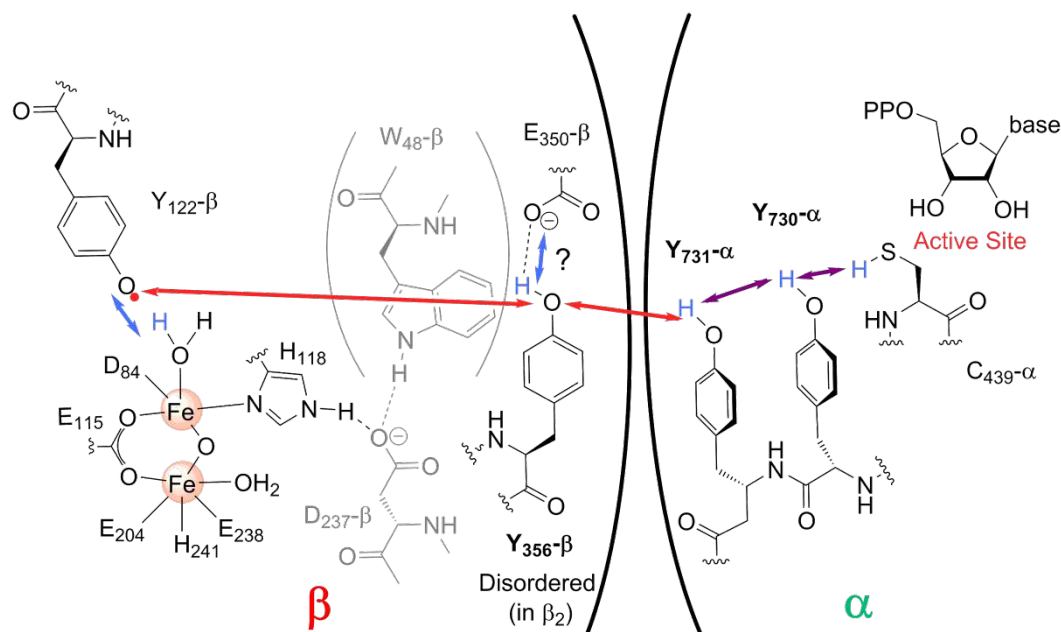


Figure 1-10: Working model of the PCET between the subunits  $\alpha$  and  $\beta$  of RNR Ia. The conserved residues participating in the radical translocation are shown. Coupled protons (blue) to this electron transfer move collinearly (purple arrow) in  $\alpha$  or orthogonally (blue arrow) in  $\beta$  to the electron transfer (red arrow) direction.  $W_{48}$  and  $D_{237}$  are shown in gray because there is no evidence for their participation in PCET between the subunits.

$Y_{122}^{\bullet}$  and  $Y_{356}^{\bullet}$  are reduced based on the current model (Figure 1-10) by a long range electron transfer and a short range proton transfer. The direction of ET and PT is different for the  $Y_{122}^{\bullet}$  and  $Y_{356}^{\bullet}$  redox reaction this is coined a bidirectional PCET. This step is strongly linked to the intrinsic quantum mechanical nature of the proton and electron movement. Electrons with their light mass can travel over large distances (in biology up to 20 Å),<sup>99, 100</sup> whereas PTs are limited to short distances (< 1 Å).<sup>94, 101</sup> Experimentally, exponential distance decay parameters have been estimated with  $\beta_{ET} = -1-1.4 \text{ \AA}^{-1}$  and  $\beta_{PT} \approx -27 \text{ \AA}^{-1}$ <sup>100-103</sup> for ET and PT, respectively (see §2.4.1 p.54). The different nature of these transfers is also the background for a recent finding.  $Y_{122}^{\bullet}$  is first activated by a proton transfer from an iron cofactor ligand, only then does the electron transfer (most probably to  $Y_{356}^{\bullet}$ ) take place.<sup>104, 105</sup>

The proton acceptor for  $\beta$ - $Y_{356}^{\bullet}$  has been proposed to be  $\beta$ - $E_{350}$ .<sup>45</sup> The assignment of  $E_{350}$  as proton acceptor, however, is still elusive. Experimental evidence is absent for participation of any of the conserved glutamates within  $\beta$ . It is generally accepted that the

electron to reduce  $\beta\text{-Y}_{356}\bullet$  comes from  $\alpha\text{-Y}_{731}$ .<sup>41</sup> The proton acceptor of  $\alpha\text{-Y}_{731}$ , however, is again undefined.

The adiabatic CPET between  $\alpha\text{-Y}_{730}$  to  $\alpha\text{-Y}_{731}\bullet$  is generally postulated, represented by a purple arrow in Figure 1-9 and Figure 1-10.<sup>41, 94, 106, 107</sup> Spectroscopic evidence is still missing. A prerequisite for this CPET is a parallel displaced “ $\pi$ -stacking”<sup>108</sup> between  $\alpha\text{-Y}_{730}$  and  $\alpha\text{-Y}_{731}\bullet$  (cf. Theory §2.4.2, p.57).<sup>107, 109</sup> Open questions remain, because some crystal structures showing either a T-shaped “ $\pi$ -stacking” (see Figure 1-3) or even distant conformations between the reduced  $\alpha\text{-Y}_{731}$  and  $\alpha\text{-Y}_{730}$  amino acids (see Figure 1-12B). Moreover, it is still not clear if the proton travels as hydrogen atom (HAT)<sup>107</sup> or if the electron interacts with the  $\pi$  system of the nearby aromat (CPET).<sup>106, 110</sup> The former is often defined as a transfer from and to the same acceptor orbital.<sup>95</sup> The CPET case describes the process in which the proton and the electron travel to two different acceptor orbitals (cf. §2.4.2.1).<sup>95</sup> Common pitfalls in the assignment and term discussion are explicitly stated in a recent review.<sup>111</sup> Additionally, it is unclear if a water can participate in this transfer steps,<sup>106</sup> or which hydrogen bond (H bond) interactions can modulate the PCET (cf. water in Figure 1-7).<sup>107</sup>

The interaction between  $\alpha\text{-Y}_{730}$  and  $\alpha\text{-C}_{439}$  has been questioned to occur over an additional water species that generates a double PCET step.<sup>112</sup> This has been postulated based on a QM/MM study. Results from EPR and density functional theory (DFT) a postulated direct transfer above, as discussed in §1.5.3. Here the authors assigned the proton acceptor of  $\alpha\text{-Y}_{730}$  to  $\alpha\text{-Y}_{731}$  and  $\alpha\text{-C}_{439}$ , for forward and reverse radical transfer, respectively. The central difficulty is to find, locate and finally to assign interactions within the PCET. Our approach is to use the still spectroscopically observable stabilized radical state and resolve the interaction of protons in the environment after each PCET step, as introduced in §1.5 (p.19).

In most discussions of mechanism, calculations have always played a central role. Siegbahn et al. have demonstrated that the mechanism of PCET can be investigated without prior knowledge of the complete surrounding.<sup>107</sup> Therefore various studies investigated the transfer between  $\text{Y}_{731}$  and  $\text{Y}_{730}$  solely by modeling a dipeptide<sup>†</sup>.<sup>106, 113</sup> However, already in

---

<sup>†</sup> The models were set up with and without an intervening water molecule present between the two Ys.

1998 Siegbahn clearly stated that at least the H bond interaction has to be known in order to obtain an accurate model, which is in part the scope of this thesis.<sup>107</sup>

Beside the proximity, energetics play a major role in PCET reactions. For short electron transfers (14 Å) it has been calculated that endogenous transfer steps of 450 mV can be overcome.<sup>99</sup> At  $10^2 \text{ s}^{-1}$ , the rates remained within the range observed in RNR.<sup>99</sup> In RNR, an endogenous step of more than 150 mV has been theoretically found for the forward radical transfer between Y<sub>730</sub> and C<sub>439</sub> in  $\alpha$ .<sup>110</sup> If the potential is not the rate limiting factor in electron transfers, how does RNR then control the remarkable specificity of its PCET? In RNR, a change in one residue renders the whole electron transfer inactive as discussed before.

ET rates in oxidoreductases are typically faster than observed in RNR with a catalytic rate of 2-10 per s.<sup>99,100</sup> These ETs are reported to be in the order of  $\mu\text{s}$ .<sup>99</sup> Therefore it was interesting to investigate which fast processes are hidden under the slow conformational step(s). Fast rates as  $10^5 \text{ s}^{-1}$  could be found for the PCET within  $\alpha$  by photo activation, using a deprotonated UAA tyrosine analog (2,3,5-F<sub>3</sub>Y) at residue  $\beta$ -356.<sup>86,114</sup>

#### 1.4.5 Rates and Thermodynamics during PCET

The discussion of PCET energetics is usually either based on bond dissociation energies (BDE)<sup>2</sup> or redox potentials.<sup>41</sup> The former can lay out the general picture of an endogenous forward PCET. BDE of PhO-H, RS-H, and HOCH<sub>2</sub>-H are  $\sim 86$ , 91, and 94 kcal·mol<sup>-1</sup>, respectively.<sup>115,116</sup> The redox potential discussion tries to consider not only the solution redox potential, but also the potential in the individual protein environments. Initial studies could show that the pK<sub>a</sub>s are within one subunit similar at Y<sub>731</sub> and Y<sub>730</sub>.<sup>117,118</sup> Only Y<sub>122</sub> has a  $>1.5$  units larger pK<sub>a</sub> shift compared to the three on pathway tyrosines.<sup>118,119</sup> Therefore it was postulated that by incorporation of different tyrosine analogs the redox potential could be estimated over the whole pathway. Up to now, studies have reported two major indications. Both use mutants, which increase the oxidation potential of Y<sub>122</sub>, to omit the conformational gating, as shown on the left side of Figure 1-11. When 2,3,5-F<sub>3</sub>Y<sub>122</sub> is incorporated, Y<sub>356</sub>• is formed first up to 50% in the ms time scale, then it reduced to 25% in comparison with 2,3,5-F<sub>3</sub>Y<sub>122</sub>•.<sup>28,120</sup> Therefore it was suggested that the 2,3,5-F<sub>3</sub>Y<sub>122</sub> has a similar redox potential as Y<sub>356</sub> for radical formation (cf. Chapter 5). Furthermore studies incorporating NO<sub>2</sub>Y<sub>122</sub> could demonstrate, that Y<sub>356</sub>• is formed in equilibrium in a ratio of



10:1:1 with  $Y_{731}^{\bullet}$  and  $Y_{730}^{\bullet}$ .<sup>84</sup> This equilibrium can be interpreted thermodynamically. The following redox potentials are obtained relative to  $Y_{122}$ , as shown in Figure 1-11.<sup>41</sup> However, there is evidence for a non-Nernstian behavior between  $Y_{122}$  and  $Y_{356}$  positions.<sup>28,41</sup> This is suggestive for a conformational gating step present between these  $Y$ 's.<sup>28,41</sup> Additionally, the peak potentials reported here are under revision.<sup>15, 22</sup> Reversible redox potentials are reported for the 3,5- $F_2$ - $Y$  up to now.<sup>28, 41, 121, 122</sup>

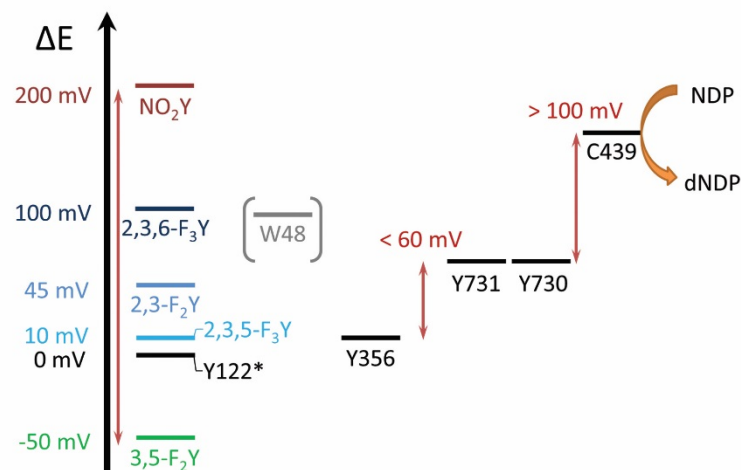


Figure 1-11: Redox peak potential changes relative to  $Y_{122}$ .<sup>41,110</sup> The potentials are evaluated for the reaction  $Y \rightarrow Y^{\bullet} + e^{-} + H^{+}$ . Local  $pK_a$  considerations have been taken into account for the UAA in position  $\beta$ -122.<sup>41</sup>

#### 1.4.6 PCET through the Interface of the Subunits

Information of the interaction between  $\alpha$ - $Y_{731}$  and  $\beta$ - $Y_{356}$  is essential to understand the function of this enzyme class. The information from the individual crystal structures should be briefly summarized. As already mentioned, the C-terminal tail is unstructured in the  $\beta$  dimer, however it becomes ordered in the active state as PELDOR data and NMR work has revealed.<sup>43,123</sup> From an electrostatic point of view, the sequence of the C-terminal  $\beta$  tail reveals the presence of three negatively charged amino acids but zero positively charged ones. A plot of the expected electrostatic potential of an individual  $\alpha$  at the interface to  $\beta$  is shown in Figure 1-12A. Thus not only the nucleotide binding site, but also the larger region is dominated by positive electrostatic charges.

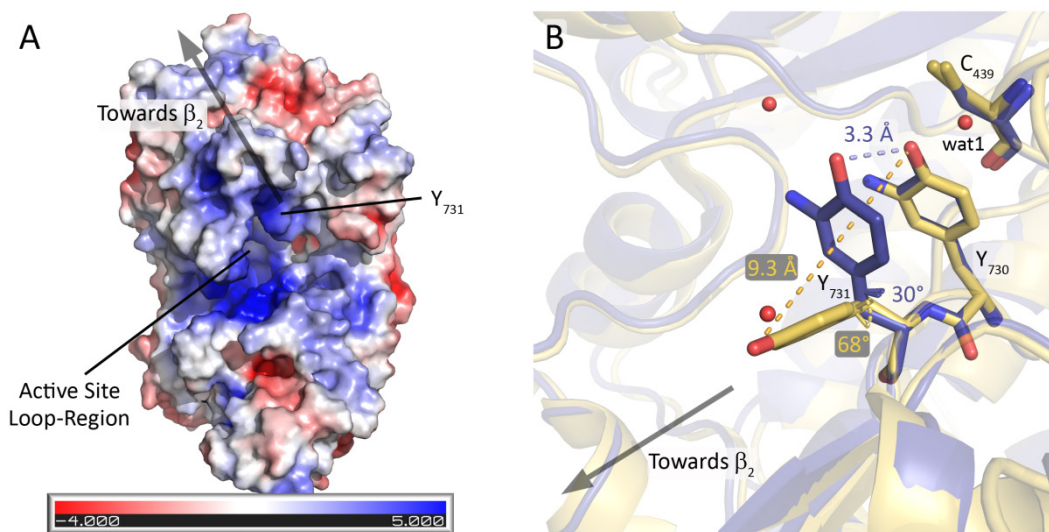


Figure 1-12: Electrostatic and local structural information found for  $\alpha$ -RNR. A) Electrostatic surface potentials were calculated using the program APBS<sup>124</sup> with the nonlinear Poisson–Boltzmann equation and contoured at -4 to 5 kT/e. A dielectricity of water ( $\epsilon=80$ ) and  $\epsilon=4$  for wt protein  $\alpha$  subunit was used.<sup>67</sup> B) The crystal structure of  $\text{NH}_2\text{Y}_{731}$  (blue, PDB ID 2XO5) is compared to the third monomer of  $\text{NH}_2\text{Y}_{730}$  (yellow, PDB ID 2XO4). The O-O distance in Å and the ring dihedral is given.<sup>67</sup>

The ET rate decays with distance. Considering this, the distance of the ET is limited to insure a selective transfer step across the interface (see Theory §2.4, p.54).<sup>99</sup> The current proposed step of 33 Å between  $\beta_2\text{-Y}_{122}$  and  $\alpha_2\text{-Y}_{731}$  is long, even including the  $\beta_2\text{-Y}_{356}$  intermediate.<sup>125</sup> However, a flexibility present in one monomer of the X-ray structure shows  $\text{Y}_{731}$  changing its conformation and distance to  $\text{NH}_2\text{Y}_{730}$  by 6 Å (Figure 1-12B). A conformational change at  $\beta\text{-Y}_{356}$  cannot be excluded and could also reduce the distances for an individual PCET steps. Conformational changes could be too fast to be observed even using rapid freeze quench (>5 ms)<sup>126</sup> techniques or other spectroscopic assays (>10 ms).<sup>127</sup> However, a conformational change at a Y has been reported by infrared (IR) spectroscopy in  $\beta$ .<sup>128</sup> They compared the non-oxidized to the oxidized state within minutes reaction time.<sup>128</sup> IR spectroscopy normally need well characterized ring dihedrals and backbone dihedrals in order to assign IR shifts precisely (cf. Figure 1-12B).<sup>129-131</sup> Barry et al. propose based on their Y,T di-peptide model<sup>129-131</sup> a conformational change of  $\text{Y}_{122}\bullet$ ;<sup>128</sup> however, the apparent contradiction between the ring dihedral from EPR spectral simulation ( $43^\circ$ )<sup>132</sup> and their assigned ring dihedral ( $80^\circ$ ) is currently not resolved.<sup>133</sup> Generally, information on ring dihedrals within the PCET of RNR is reported only at one additional position. The ring dihedral of  $\text{NH}_2\text{Y}_{730}\bullet$  was assigned by EPR spectroscopy (see next section).<sup>134</sup> Spectroscopic

investigation in frozen solution and in the second time scale can deliver complementary information to interpret results on a common foundation.

## 1.5 EPR Spectroscopy for PCET Pathways

### 1.5.1 Overview

EPR spectroscopy on biomolecules is an elegant way to study selectively active sites around radicals and paramagnetic ions. Radicals and paramagnetic ions have an unpaired electron, which can be probed in a magnetic field ( $B_0$ ). Pulsed EPR techniques like double resonance techniques can meanwhile routinely be applied. One example is PELDOR (§1.4.3, p.11) spectroscopy, which delivers structural information based on the magnetic interaction between two unpaired electron spins. Another technique, Electron nuclear double resonance (ENDOR) spectroscopy, can be applied to retrieve structural information if an electron spin interacts with a nuclear spin (hyperfine interaction), i.e., protons of H bonds around a  $Y\bullet$ .

EPR techniques brought valuable insight into PCET systems in general<sup>135-138</sup> and particularly to RNR.<sup>41, 139</sup> EPR spectroscopy applied in combination with UAA is able to characterize trapped radicals in the “active” RNR complex.<sup>41, 44</sup> Radical intermediates (i.e.,  $NH_2Y\bullet$ ) were assigned in the PCET of RNR for the first time.<sup>43, 44</sup>

EPR spectra provide information about the radical species observed, for instance the resolved  $^{14}N$  hyperfine (HF) coupling in  $NH_2Y\bullet$ .<sup>134</sup> In organic radicals (as  $Y\bullet$  and  $NH_2Y\bullet$ ) only at high-field ( $> 3$  T) another interaction becomes resolved the  $g$  tensor. This  $g$  tensor is often essential for the identification of the organic radical species.<sup>140</sup> In the principle axis system, the  $g$  tensor has three  $g$  values ( $g_x$ ,  $g_y$  and  $g_z$ ). The orientations of the principle axis are directly connected to the molecular frame (cf. Figure 1-14A).  $g$  Values can be viewed as an electronic finger print of a radical species. At high accuracy, however, they are also a function of the oxygen spin density population (see §2.1.2, p.31). Therefore they are affected by electrostatic interactions in the surrounding of the phenoxy oxygen. In  $\pi$  radicals as tyrosines especially  $g_x$  and  $g_y$  values are affected by local electrostatics as charges or protons around the phenoxy oxygen nuclei.<sup>141-146</sup>

In biomolecules with several paramagnetic species as in the PS II or RNR it is often necessary to selectively probe one paramagnetic species. The literature shows

examples for the separation of EPR spectra at very high fields ( $> 9$  mT),<sup>147</sup> by relaxation filtering<sup>148</sup> or by advanced pulsed methods.<sup>149</sup> A general procedure cannot be given, because the paramagnetic species, their surrounding and their relaxation properties have to be considered. In RNR,  $Y_{122}\bullet$  is always present in samples investigating PCET radical intermediates (cf. §1.4.3, p.11). However,  $Y_{122}\bullet$  has a short spin lattice relaxation  $T_1$  due to the interaction to the ferric diiron site in its vicinity.<sup>55, 150, 151</sup> Therefore the contribution of  $Y_{122}\bullet$  in the EPR spectra could be efficiently removed at elevated temperatures (70 K) in combination with pulsed EPR spectroscopy.<sup>55, 148, 152</sup>

### 1.5.2 High-Field ENDOR and EPR in Other PCET systems

The effect of electrostatic interaction on the  $g$  value can depend on an H bond distance to a  $Y\bullet$  as reported experimentally in a recent publication by Chatterjee *et al.*<sup>153</sup> Here the authors could demonstrate that the combination of high-field ENDOR and EPR can bring unprecedented spectroscopic evidence for a PT from  $Y_D\bullet$  in PS II. In this study, a proton transfer could be demonstrated between a cold temperature state (7 K, “tensed”) and an elevated temperature state (70 K, “relaxed”) by ENDOR spectroscopy (the study is illustrated in Figure 1-13). The hyperfine (HF) interaction decreases from the “tensed” to the “relaxed” state according to the dipolar coupling strength of the nuclei spin and the electron spin (see §2.1.4, p.35). The dependence on the H bond distance is clearly visible in this example. By contrast, the  $g_x$  value increases by 1 ppt concomitant with the increase in H bond length of 0.25 Å. This is in agreement with the reduction of electrostatics and has been predicted by DFT calculations before for  $Y_S\bullet$ .<sup>143, 154</sup>

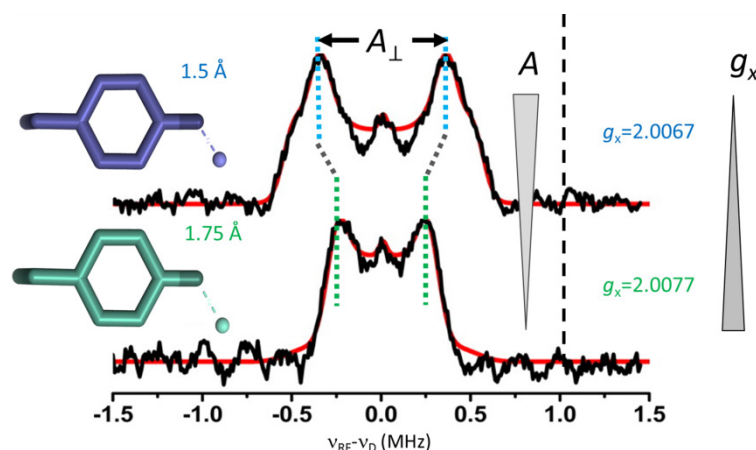


Figure 1-13: The  $^2\text{H}$  Mims ENDOR spectra of two states of  $\text{Y}_\text{D}\bullet$  from photosystem II in  $\text{D}_2\text{O}$  buffer are shown. The  $\text{Y}_\text{D}\bullet$  (7 K, blue, upper spectrum) low temperature state has a short H bond, a larger (deuterium) HF coupling, and a lower  $g$  value as the  $\text{Y}_\text{D}\bullet$  (70 K, green, lower spectrum) at higher temperatures. Adapted from ref. 153.

### 1.5.3 High-Field ENDOR and EPR in RNR

In the last sections, it could be shown that incorporated  $\text{NH}_2\text{Y}$ 's are useful to observe the radical in the “active” complex. Section §1.4.4 (p. 13) highlighted the need for a well-defined H bond network in order to calculate energetic landscapes via for instance DFT. Hyperfine (HF) interactions from intermolecular protons or deuterons can be probed precisely by modern high-field ENDOR spectroscopy. Thus information about H bonds can be derived. Additionally, the electrostatic interaction can be investigated by high-field EPR spectroscopy. The investigation on  $\text{NH}_2\text{Y}\bullet$  intermediates at residues  $\beta$ -356,  $\alpha$ -730 and 731 was started by T. Argirević in our research group.<sup>92, 110, 134</sup>

At  $\text{NH}_2\text{Y}_{730}\bullet$  it was demonstrated that at higher field/frequencies the principal  $g$  values can be partially resolved at 94 GHz and fully resolved beyond  $\approx 180$  GHz, as shown in Figure 1-14A.<sup>92</sup> Below the spectrum, the individual principal axis orientation of the  $\text{NH}_2\text{Y}\bullet$   $\mathbf{g}$  tensor toward the magnetic field are shown. Orientations can be selectively probed, if the excitation bandwidth of the pulse is much smaller than the spectral width of the EPR line.<sup>†</sup> Orientation selection in combination with high-field ENDOR was employed. In this case, T. Argirević could assign three intermolecular HF couplings as highlighted in Figure 1-14B (yellow, red and blue) in a  $^2\text{H}$  Mims ENDOR spectrum. With the aid of a DFT

<sup>†</sup> And hyperfine couplings can be neglected in size. (cf. §2.1.3).

structures HF couplings obtained from  $\text{NH}_2\text{Y}_{730}\bullet$  were assigned to three protons in the surrounding. The assignment is illustrated by red, blue and yellow dotted lines between the oxygen ( $\text{O}-\text{Y}_{731}\bullet$ ) and the individual H bond donor nuclei in Figure 1-14C.

The tensor shape found in  $\text{NH}_2\text{Y}_{730}\bullet$  for the nearly perpendicular H bonds (red and blue, Figure 1-14 B&C)<sup>110</sup> has not been described before by orientations selective ENDOR on  $\text{Ys}\bullet$ . Several other orientation selective HF spectroscopy studies were performed (a selection is summarized in Table 1-1). One has investigated the yeast RNR  $\text{Y}_{122}$  analog.<sup>55</sup> Where  $\text{Y}_{122}\bullet$  is not H bonded, its yeast counterpart ( $\text{Y}_{127}\bullet$ ) has an H bond with a distance of 1.8 Å and the O-H vector is nearly collinear to  $g_x$ .<sup>55</sup> The H bond of  $\text{Y}_D\bullet$  is also within the ring and its direction is displayed in Figure 1-13.<sup>155</sup> It is noteworthy that for these H bonds nearly within the ring plane the HF coupling were described by a dipolar tensor shape (§2.2.5, p.45). Interestingly, this seems to be independent of the estimated distance.<sup>153</sup>

By contrast, the study of  $\text{NH}_2\text{Y}_{730}\bullet$  showed a tensor, in which the so-called Fermi contact interaction plays a role. This can be seen in Figure 1-14B, by an increase of isotropic coupling ( $a_{\text{iso}}$ ). Such couplings cannot be explained by simple point dipolar interaction approximations. Therefore quantum chemical calculations have shown to be useful. A joint EPR and DFT structural representation of the active state could be obtained. It linked the information of the inactive crystal structure to the active state observed via these mutants.<sup>110</sup>

In a multi-frequency EPR investigation in  $\text{H}_2\text{O}$  and  $\text{D}_2\text{O}$  buffer Argirević assigned  $g$  values and HF couplings for all three  $\text{NH}_2\text{Ys}\bullet$  (Table 1-2, p.25 and Table A. 1, p.191). Results showed at least one stronger perpendicular  $^2\text{H}$ -HF coupling to  $\text{NH}_2\text{Y}_{731}\bullet$  as to  $\text{NH}_2\text{Y}_{730}\bullet$ .<sup>92</sup> Controversially, the  $g$  values were identical between  $\text{NH}_2\text{Y}_{730}\bullet$  and  $\text{NH}_2\text{Y}_{731}\bullet$  (Table 1-2, bottom), although different ENDOR spectra indicated a change in the environment. In order to resolve this, 263 GHz spectra were recorded in all three  $\text{NH}_2\text{Ys}\bullet$  in this thesis.

Furthermore Argirević reported the highest electrostatic interaction at  $\beta\text{-NH}_2\text{Y}_{356}\bullet$ , but did not investigate the local structure of this mutant (cf. §1.4.1.1). Notably, ENDOR at  $\text{NH}_2\text{Y}_{356}\bullet$  is more challenging, because  $\text{Y}_{122}\bullet$  content per  $\beta_2$  in all studied mutants is reduced by a factor of 2. Moreover, the  $\text{NH}_2\text{Y}_{356}\bullet$  radical yield is reported to be  $\approx 38\%$ , which is lower than reported for  $\text{NH}_2\text{Y}_{730}\bullet$  or  $\text{NH}_2\text{Y}_{731}\bullet$  with  $\approx 50\%$ .<sup>67</sup>

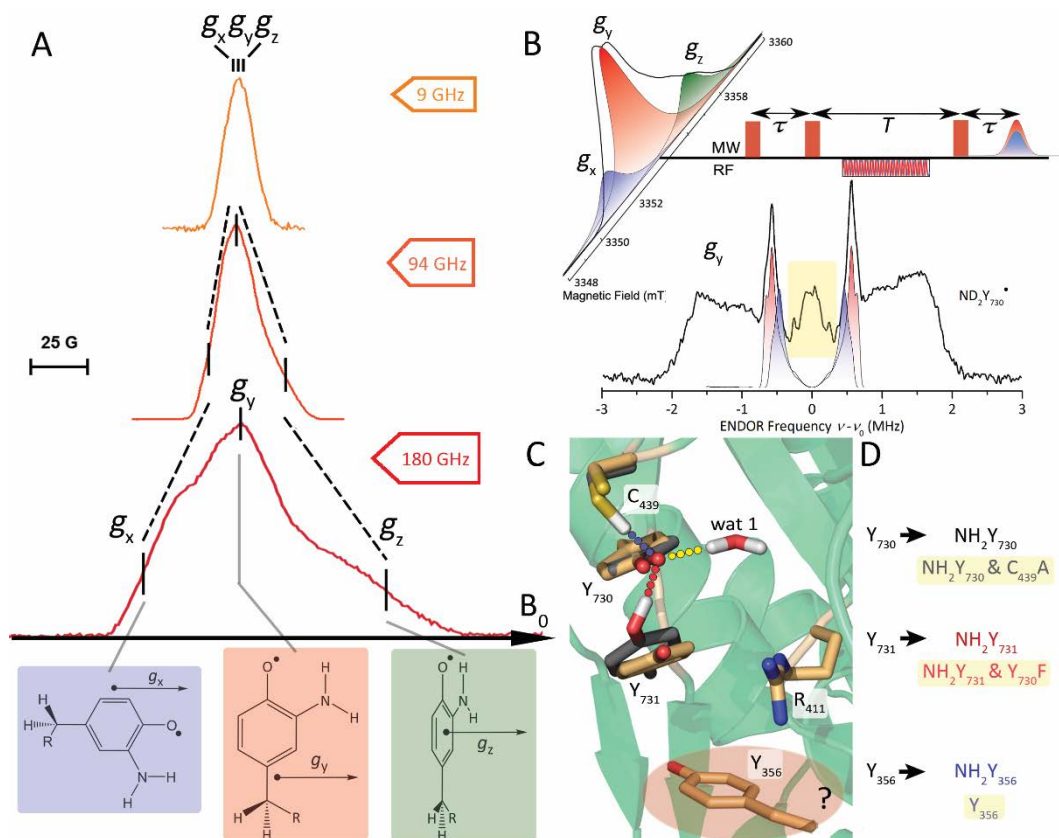


Figure 1-14: High-field EPR and ENDOR spectra combined with DFT calculations derive a structural model of the active structure of  $\text{NH}_2\text{Y}_{730}\bullet$  in the PCET of RNR.A) Multi-frequency EPR characterization of  $\text{NH}_2\text{Y}_{730}\bullet$ . The  $g$  values are not resolved at 9 GHz (orange), but have a contribution to the line shape at 94 GHz and are resolved at 180 GHz (red). Adapted from ref. 92. Each  $g$  value ( $g_x$ ,  $g_y$ ,  $g_z$ ) corresponds to an orientation of the molecule in the magnetic field. B) If the spectral width of the absorption signal is larger than the excite width of a microwave pulse (MW), then a single orientation can be excited. Three excitation bandwidths along a 94 GHz spectrum are shown in blue, red and green. By applying a Mims ENDOR sequence  $^2\text{H}$  couplings can be probed for each molecular orientation. In  $\text{NH}_2\text{Y}_{730}\bullet$  three contributions beside the amino deuterons were found. A weak H bond in the ring plane (yellow), a weak to moderate perpendicular H bond (blue) and a moderate perpendicular H bond (red) C) These couplings were interpreted with an DFT structure and an “active” state model (gray) has been formulated with 0.2 to 0.6 Å shorter H bond distances than found in the crystal structure (golden sticks, green cartoon). D) By exchanging successively the Y residues by  $\text{NH}_2\text{Y}$ s each position could be probed. The additional double mutants prepared for the present investigation of this thesis are highlighted in yellow.

1.5.3.1 Electrostatic Effect of H Bonds on the  $g$  Value

In order to understand the effect of electrostatic interaction from H bonds on  $g$  values of  $\text{NH}_2\text{Y}\bullet$ s (Table 1-2 left) several DFT models were set up.<sup>110</sup> The effect from an isolated  $\text{NH}_2\text{Y}$  over one H bond to two H bonds was successively studied by models. In the DFT models the  $g_x$  value decreases by about 0.5 ppt per weak to moderate H bond (2.0 to 1.8 Å). The  $g_x$  value increases taking the second sphere into account in this case by 0.3 ppt (entry 4 and 5). Interestingly, if the electrostatics of the second sphere are considered the removal of the weak H bond (2.0 Å) changes the  $g$  value only by 0.2 ppt. The effect of the second shell is likely a consequence of the polarization of the surrounding and steric effects. Notably, the calculations did not treat any continuum polarization or gauge origin correction. Hence, the uncertainty was estimated with 0.5 ppt for these models. However, most DFT uncertainties are systematic shifts. Therefore, it is reasonable to compare relative changes within the models.<sup>110</sup>

Table 1-1: HF couplings of tyrosine to exchangeable intermolecular deuterons (D) for two examples. The results of  $\text{Y}_\text{D}\bullet^{153,155}$  and the  $\text{Y}_{127}\bullet$  analog of yeast RNR ( $\text{Y}_{127}$ )<sup>55</sup> are shown. The corresponding proton couplings are shown in parenthesis.

	$A_x$ [MHz]	$A_y$ [MHz]	$A_z$ [MHz]	Euler angles $\alpha, \beta, \gamma$ [°]	$Q_x$ [MHz]	$Q_y$ [MHz]	$Q_z$ [MHz]
$\text{Y}_\text{D}\bullet\text{-D}$ 1.49 Å	-0.68 (-4.41)	-0.91 (-5.93)	1.59 (10.34)	0, 90, 108 0, 90, 126	-0.074	-0.066	0.14
$\text{Y}_\text{D}\bullet\text{-D}$ 1.75 Å	-0.48 (-3.10)	-0.58 (-3.79)	1.06 (6.88)	0, 90, 120 0, 90, 142	-0.07	-0.04	0.11
$\text{Y}_{127}\bullet\text{-D}$ 1.8 Å	-0.6 (-4)	-0.6 (-4)	1.2 (7.8)	0, 110, 155 0, 110, 155	-0.02	-0.06	0.08
$\text{Y}_\text{D}\bullet\text{-D}^{155}$ 1.84 Å	-0.51	1.10	-0.59	-26, 16, -9 -48, 30, 29	-0.09	-0.15	-0.06

a) The Euler angles are defined in respect to the principal axis frame of the  $\mathbf{g}$  tensor ( $\mathbf{A} \rightarrow \mathbf{g}$ ). A positive rotation is anti-clockwise.  $A_z$  and  $Q_z$  are defined as largest values.

For  $\text{Y}\bullet$  several high-field EPR studies are reported with various H bond environments (Table 1-2 right). Here the change from zero to one and to two moderate H bonds decreases the  $g_x$  value by  $\approx 1.4$  ppt and 1.0 ppt, respectively. A strong H bond, defined here with a length between 1.5-1.6 Å, leads to a decrease of about  $\approx 2.4$  ppt. Three H bonds around a tyrosine have only been reported by DFT calculations for functional essential  $\text{Y}_\text{Z}\bullet$  in PS II.<sup>156</sup> This theoretical value is in agreement with the change of more than 1 ppt per moderate H bond.



Table 1-2: The  $g$  values as a function of the environment are tabulated for  $\text{NH}_2\text{Y}_s\bullet$  and  $\text{Y}_s\bullet$ . The  $g$  values decrease with an increase of H bond interactions in number and/or strength. Left: For  $\text{NH}_2\text{Y}_s$  it has been demonstrated by DFT model calculations.<sup>110</sup> Right: For tyrosines several H bond situations have been found experimentally so far. Three H bonds to a  $\text{Y}\bullet$  have only been reported by DFT calculations.

$\text{NH}_2\text{Y}\bullet$ DFT models	$g_x$	$g_y$	$g_z$	No.	Experimental $\text{Y}_s\bullet$	$g_x$	$g_y$	$g_z$
Free $\text{NH}_2\text{Y}\bullet^a$	2.0061	2.0045	2.0022	1	Isolated $\text{Y}_{122}\bullet^d$	2.00912	2.00457	2.00225
$\text{Y}_{731}^a + \text{NH}_2\text{Y}_{730}\bullet$ (1 H bond: 1.77 Å)	2.0055	2.0044	2.0020	2	1 H bond (>1.9 Å) $\text{Y}_D\bullet$	2.0075 <sup>e</sup>	2.0044 <sup>e</sup>	2.0022 <sup>e</sup>
				2'	$\text{Y}_{122}\bullet$ in eukaryotes <sup>g</sup>	2.0076-2.0077	2.0043-2.0044	2.0022-2.0023
$\text{Y}_{731} + \text{NH}_2\text{Y}_{730}\bullet + \text{C}_{439}$ (2 H bonds: 1.77/2.03 Å)	2.0050	2.0040	2.0018	3	1 H bond ( $\approx$ 1.5-1.6 Å)	2.00673 <sup>h</sup> 2.0066 <sup>i</sup>	2.00453 <sup>h</sup> 2.0041 <sup>i</sup>	2.00232 <sup>h</sup> 2.0021 <sup>i</sup>
$\text{Y}_{731} + \text{NH}_2\text{Y}_{730}\bullet + \text{C}_{439} + \text{Wat1}$ (3 H bonds: 1.80/2.04/1.78 Å)	2.0046	2.0039	2.0017	4	2 H bonds (1x 1.6 Å)	2.00661 <sup>j</sup> 2.00621 <sup>k</sup>	2.00418 <sup>j</sup> 2.00418 <sup>k</sup>	2.00244 <sup>j</sup> 2.00212 <sup>k</sup>
Model including second sphere <sup>b</sup>	2.0049	2.0041	2.0018	5	3 H bonds $\text{Y}_z\bullet$ (1.6 Å, 2x 1.8 Å)	2.0055 <sup>l</sup>	2.0043 <sup>l</sup>	2.0023 <sup>l</sup>
Model including second sphere (without WAT1) <sup>c</sup>	2.0051	2.0041	2.0019	6				
From simulations of the experiment								
$\alpha_2\text{-NH}_2\text{Y}_{730}\bullet^m$	2.0052	2.0042	2.0022	7				
$\alpha_2\text{-NH}_2\text{Y}_{731}\bullet^m$	2.0052	2.0042	2.0022	8				
$\beta_2\text{-NH}_2\text{Y}_{356}\bullet^m$	2.0050	2.0041	2.0021	9				

a) 2-amino-4-methyl-phenol radical (2-AMPR) model; b,c) All residues within 5 Å in the surrounding of  $\text{NH}_2\text{Y}_{730}\bullet$  have been modeled with (b, model 4) and without (c, model 6) WAT 1.<sup>110</sup> d) Taken from ref. 157. e) Median value of several  $\text{Y}_D\bullet$  organisms reviewed in 136. f, h) Taken for the relaxed and tensed state from ref. 153. g) Values reported for yeast,<sup>55</sup> mouse<sup>158</sup> and HSV1<sup>159</sup>  $\text{Y}_{122}\bullet$  RNR corresponding amino acid. i) H bonded Y radical in prostaglandin H-Synthetase from ref. 160 j,k)  $\gamma$ -irradiated L-Y-HCl crystal with two H bonds from ref. 161 l) DFT study of  $\text{Y}_z\bullet$  in the S2 state of photosystem II, ref. 156 m) The values are taken from ref. 134 and 92.

### 1.5.3.2 Investigation of the PCET in $\alpha$ with H Bond and Electrostatic Information from $\text{NH}_2\text{Y}_{730}\bullet$

Detailed DFT models could be set up that considered the proposed H bond interactions, as illustrated in Figure 1-14C. Taking into account all H bond interactions and a large model size, a more reliable energetic representation of the PCET in  $\alpha$  could be calculated. The necessary electrostatic information and minimum model size from the successive models for  $\text{NH}_2\text{Y}_{730}\bullet$  were also considered (Table 1-2). The model was expanded to the radical positioned at residue 731, to calculate the PCET transition state between the  $\text{Y}_{731}\bullet$  and  $\text{Y}_{730}\bullet$ . However, the H bond environment at  $\text{Y}_{731}\bullet$  was not considered here.<sup>110</sup>

The assignment of H bonds at  $\text{NH}_2\text{Y}_{731}\bullet$  in agreement with the observed polarity at this site is a core focus of my thesis. It has still to be understood if two H bonds also cause the observed polarity at this site. Two double mutants ( $\alpha\text{-NH}_2\text{Y}_{730}/\text{C}_{439}\text{A}$  and  $\alpha\text{-NH}_2\text{Y}_{731}/\text{Y}_{730}\text{F}$ ) have been characterized to test the assignments made in Figure 1-14D (see §4.3, p. 87).

## 1.6 Motivation of the Work

Before unnatural amino acids (UAA) could be incorporated, it was possible to study any of the detailed chemistry of the PCET in RNR. The incorporation of UAA is an expanding field and many more expansions of the genetic code<sup>162-164</sup> but also organisms<sup>165</sup> adapted to the UAA incorporation have been or will be developed. The development of these methods as well as the identification of its advantages and shortcomings is important.<sup>84, 120, 134, 166</sup> Here, I have the chance to explore the utility for EPR of a  $\text{NH}_2\text{Y}$  as a competitive radical trap for an interesting and still not understood PCET.<sup>41</sup> It requires three tyrosine stepping stones over a distance of more than 35 Å. This is an ideal test case to compare these three  $\text{NH}_2\text{Y}\bullet$  with each other and relate the findings to their function in the forward PCET.

## CHAPTER 4:

The assignment and the active state model, as shown in Figure 1-14C, should be spectroscopically tested.

- Is the difference in H bonding geometries between  $\text{NH}_2\text{Y}_{730}\bullet$  and  $\text{NH}_2\text{Y}_{731}\bullet$  resolvable by pulsed 263 GHz EPR spectroscopy?<sup>92</sup>
- Can double mutations be used to test these interactions?
- Can flexibility of  $\alpha\text{-Y}_{731}$ , postulated based on different conformers in X-ray structures, be observed by high-resolution 263 GHz spectra of  $\text{NH}_2\text{Y}_{731}$ ?
- Are interactions from  $\beta\text{-Y}_{356}$  to  $\alpha\text{-NH}_2\text{Y}_{731}\bullet$  and from  $\alpha\text{-Y}_{731}$  to  $\beta\text{-NH}_2\text{Y}_{356}\bullet$  observable?

## CHAPTER 5:

In the second part of the thesis, another approach was used to circumvent conformational gating by the incorporation of  $\beta\text{-2,3,5-F}_3\text{Y}_{122}$  forming  $\beta\text{-2,3,5-F}_3\text{Y}_{122}\bullet$ .<sup>28, 120</sup>

This recently developed radical species has to be characterized by high-field EPR to clarify:

- Is conformeric state and the  $g$  value of  $\beta\text{-2,3,5-F}_3\text{Y}_{122}\bullet$  unperturbed compared to  $\beta(\text{wt})\text{-Y}_{122}\bullet$ ?

This  $\beta\text{-2,3,5-F}_3\text{Y}_{122}\bullet$  combined with a PCET blockade mutant ( $\alpha\text{-Y}_{731}\text{F}$ ) can be used to study a forward PCET.  $\beta\text{-Y}_{356}\bullet$  could be formed.<sup>28, 84</sup>

- The number, distance and orientation of H bonds to  $\beta\text{-Y}_{356}\bullet$  can give evidence for the type of PCET mechanism present at this position.

## 2 THEORETICAL BACKGROUND

Tyrosines and UAA neutral radicals are studied in this thesis. From the EPR point of view, they resemble organic radicals with light first and second row elements of the periodic table. This theory chapter will therefore be restricted paramagnetic systems with an electron spin  $S = 1/2$ . Pulse EPR offers a variety of techniques to probe different interactions of the electron spin with its environment. Long-range interactions as the dipole-dipole coupling between two electron spins are studied routinely with PELDOR. Local interactions can be probed by ENDOR or other suitable HF detecting methods (§2.2). Changes in the CO bond charge distribution and influence on the spin density population can be studied as shown in the introduction.

The different sizes of these magnetic interactions can be effectively evaluated in the framework of the spin Hamiltonian (§2.1). EPR DFT calculations (§2.3) and EPR simulations use these effective Hamiltonians.<sup>167-169</sup>

### 2.1 Spin Hamiltonian and Magnetic Interactions

The energies within the EPR treatment are generally small compared to the other terms of the electronic Hamiltonian. Therefore they can be often separated in the static spin Hamiltonian (2-1). This form of Hamiltonian describes magnetic resonance behavior without going into physical details.<sup>170,171</sup> They were constructed to describe the interaction

influencing magnetic resonance spectra. Therefore specific properties of the system have often to be related to these observables by quantum mechanical calculations (cf. §2.3.4. p. 52).<sup>167</sup> The introduction to the spin Hamiltonian is described in several textbooks.<sup>170-172</sup>

For an organic radical the typical contributions for this effective Hamiltonian are:

$$\hat{\mathcal{H}}_0 = \hat{\mathcal{H}}_{\text{EZ}} + \hat{\mathcal{H}}_{\text{NZ}} + \hat{\mathcal{H}}_{\text{HF}} + \hat{\mathcal{H}}_{\text{NQ}} \quad (2-1)$$

The contributing terms are:

The electron Zeeman interaction  $\hat{\mathcal{H}}_{\text{EZ}}$ ,

the nuclear Zeeman interaction  $\hat{\mathcal{H}}_{\text{NZ}}$ ,

the hyperfine couplings between the electron spin and the nuclear spins  $\hat{\mathcal{H}}_{\text{HF}}$  and

the nuclear quadrupole interaction  $\hat{\mathcal{H}}_{\text{NQ}}$  for spins with a nuclear spin quantum number  $I > 1/2$ .

Several contributions of the spin Hamiltonian have been neglected here, either because the typical line broadening in EPR is larger than their contribution or due to the restriction to organic radicals with  $S=1/2$  systems.

For all these contributions a separate treatment can be performed, if the contributions are clearly separated in energy from each other. To visualize this, Figure 2-1 shows the relative sizes of these contributions at low- and high-field.

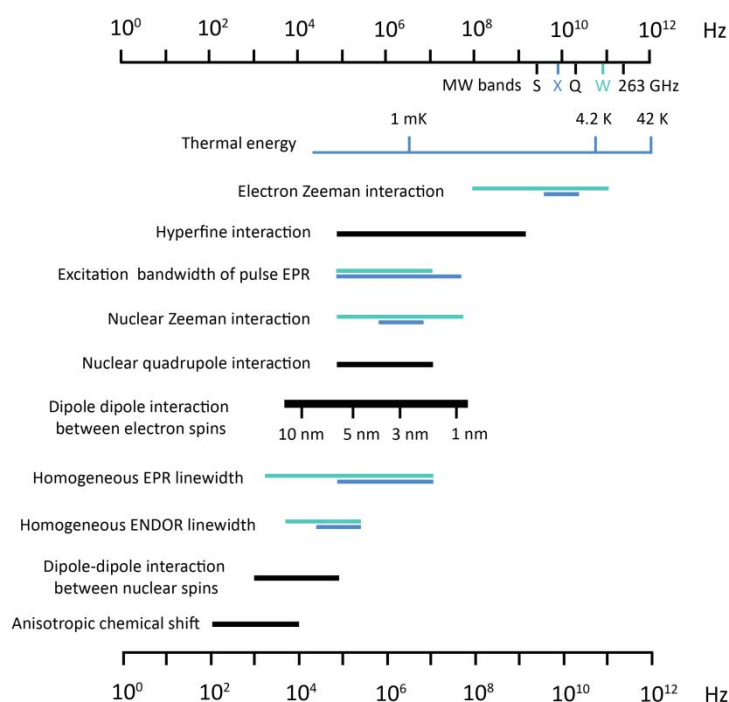


Figure 2-1: Typical energies in Hz of electron and nuclear spin interactions from microwave (MW) frequencies between X band (blue) and W band (green). The temperature scale is in Boltzman energy (kT). Adapted from ref. 172.

### 2.1.1 The Zeeman Contribution

The Zeeman interaction is the sole directly field dependent contribution for the nuclei and the electron. The energy of this quantity can be expressed in terms of the spin Hamiltonian for a free electron as:

$$\hat{\mathcal{H}}_{EZ} = g_e \mu_B \vec{S} \cdot \vec{B}_0 \quad (2-2)$$

Where  $g_e$  is the g-factor of the free electron (2.002319.) and  $\mu_B$  is the Bohr magneton. If the magnetic field is large and defined along the z-direction, the Hamiltonian simplifies to:

$$\hat{\mathcal{H}}_{EZ} = g_e \mu_B S_z B_0 \quad (2-3)$$

For an  $S = 1/2$  system the two states are separated by the energy given by:

$$\Delta E = g_e \mu_B B_0 \quad (2-4)$$

The energy difference  $\Delta E$  between two nuclear spin states can be written in an analog equation as:

$$\Delta E = g_n \mu_n B_0 \quad (2-5)$$

Where  $g_n$  is the nuclear g-factor and  $\mu_n$  the nuclear magnetic moment. The combination of both energy splittings (Equations 2-3 & 2-4) with the field is illustrated in Figure 2-5 (p.38). The difference in  $\Delta E$  between nuclear Zeeman and electron Zeeman term, originates from the difference in mass of the two particles. For example, the proton and electron magnetic moments are compared in following equation:

$$\mu_p = \frac{e}{2m_p} \hbar \text{ versus } \mu_e = \frac{e}{2m_e} \hbar \quad (2-6)$$

### 2.1.2 Anisotropic $\mathbf{g}$ Tensors in Organic Radicals: The Spin-Orbit Contribution

Approaching a real system, a resonance is seldom defined exactly at the value of the free electron. To explain the deviation several effects have to be taken into account. Some are small like the relativistic mass correction; a particularly large one is the spin-orbit coupling. For the later contribution, an effective g value has been introduced that satisfies the resonance condition  $h\nu = g_e \mu_B B_0$ . This value is orientation dependent and forms a 3x3 matrix, which is diagonalizable; it is commonly called  $\mathbf{g}$  tensor. The Hamiltonian as a function of orbital angular momentum  $\mathbf{L}$  is<sup>§</sup>

$$\hat{\mathcal{H}}_{\text{EZ(L)}} + \hat{\mathcal{H}}_{\text{LS}} = g_e \mu_B \tilde{\mathbf{B}}_0 (\mathbf{L} + g_e \hat{\mathbf{S}}_z) + \lambda \tilde{\mathbf{L}}\mathbf{S}. \quad (2-7)$$

Whereas  $\hat{\mathcal{H}}_{\text{LS}}$  is the spin-orbital interaction with the spin-orbit coupling constant  $\lambda$ . For organic radicals with nuclei with small atomic number  $Z$ , the second order perturbation treatment is a good approximation, obtaining<sup>171, 173</sup>

$$\mathbf{g} = g_e \mathbf{1} + 2\lambda \mathbf{\Lambda}, \quad (2-8)$$

where  $\mathbf{\Lambda}$  is a symmetric tensor, with elements defined by Eq. (2-9).

$$\Lambda_{ij} = \sum_{n \neq 0} \frac{\langle \psi_0 | L_i | \psi_n \rangle \langle \psi_0 | L_j | \psi_n \rangle}{\varepsilon_0 - \varepsilon_n} \quad (2-9)$$

The electronic wave function of the single occupied ground state is  $\psi_0$ ; it has the energy  $\varepsilon_0$ . Any other state  $n$  has the wave function  $\psi_n$  and the energy  $\varepsilon_n$ .

With this angular momentum contribution, the g values differ depending on the spin-orbit coupling of the individual nuclei bearing a part of the free electron ( $|\psi|^2 \neq 0$ ). A

<sup>§</sup> Bold letters numbers are indicate a matrix or a tensor and  $\tilde{\mathbf{B}}_0$  is the transposed form of  $\mathbf{B}_0$

relation taking into account the relative spin density population  $\rho_{\pi}^O$  of the individual nucleus can be formulated for instance for oxygen. In Ys• the oxygen atom is the sole nucleus with a high spin-orbit coupling and orbitals contributing strongly to the single occupied orbital. It has in this organic radical not only the highest spin-orbit coupling  $\lambda_{\text{nuclei}}$  with  $\lambda_O = 151 \text{ cm}^{-1}$  ( $\lambda_N = 76 \text{ cm}^{-1}$ ,  $\lambda_C = 28 \text{ cm}^{-1}$ ). Notably,  $^{19}\text{F}$  also has a high spin-orbit coupling with  $\lambda_F = 270 \text{ cm}^{-1}$  (§5.2). However, the spin density population of oxygen is larger compared to all other individual atoms in tyrosines and their analogs. Thus Eq. (2-10) has a substantial influence on the small spin-orbit-couplings resolved here. Due to the geometry of the individual orbitals (cf. Figure 2-2A) not all orbitals can mix. The in-plane contribution of closest lying non-bonding  $p_y$  orbital in is denoted by  $c_{nby}^2$ . The mixing is governed by the orbital angular momentum as shown in Figure 2-2B. Electrostatic effects are by far not as strong as in ligand field complexes. Small charge dependent differences, however, can be realized. The effect on the frontier orbitals is illustrated in Figure 2-2C-D.<sup>140</sup>

$$g_{SO,x}(O) = \frac{2\lambda_O \rho_{\pi}^O c_{nby}^2}{\epsilon_0 - \epsilon_{nb}} \quad (2-10)$$

For interactions along the  $p_z$  orbital as perpendicular H bonds, partial covalent bond character of the interaction can be assumed based on the increasing Fermi contact interaction.<sup>110</sup> In protonated organic radicals, it could be shown that protonation leads to a lower participation of the high lying non-bonding orbital.<sup>174</sup> Therefore, lower lying HOMOs contribute to the spin-orbit coupling. The energy difference between the excited state and lower lying HOMOs increases, which reduces the spin-orbit coupling along  $g_x$  and  $g_y$ . The  $g_{x,y}$  value decreases to a slightly larger extent than for H bonds along the non-bonding orbital.<sup>154, 174, 175</sup>

For the organic radicals investigated in this thesis, the differences are small. Differences can still be resolved, however, by considering the proportionality of the g-factor with magnetic field  $B_0$ . Taking the resonance condition into account, the difference in the field spectrum is

$$\Delta B = \frac{h\nu}{\mu_B} \left( \frac{1}{g_1} - \frac{1}{g_2} \right) \quad (2-11)$$

Thus the separation of the signals scales with the used microwave frequency.



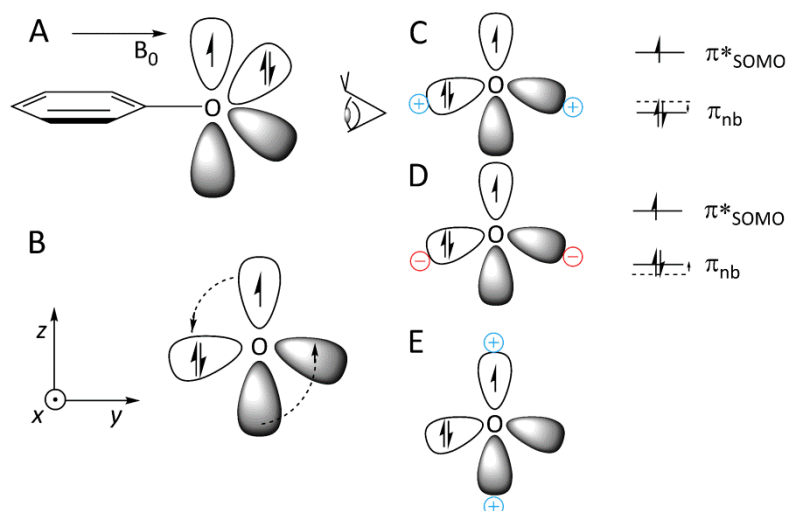


Figure 2-2: Illustration of the spin-orbit coupling and effects on the  $g$  value. In a tyrosyl radical observed along the C-O bond (A) the effect of the orbital angular momentum  $L$  is shown (B). The mixture of the non-bonding orbital and the antibonding SOMO increase the  $g_x$  value. C and D) For the non-bonding orbital, the electrostatic effects can be considered. A positive charge will stabilize the orbital and a negative charge will lead to an energy increase. E) Interactions along the SOMO cannot be treated electrostatically anymore. Adapted in part from ref. 140.

### 2.1.3 Hyperfine Interaction

To understand the factors that govern the hyperfine (HF) interaction, it is typically separated into two contributions

$$\hat{\mathcal{H}}_{\text{HF}} = \hat{\mathcal{H}}_{\text{FC}} + \hat{\mathcal{H}}_{\text{DD, HF}} = a_{\text{iso}} \tilde{\mathbf{S}} \mathbf{I} + \tilde{\mathbf{S}} \mathbf{T}_{\text{Dip}} \mathbf{I}. \quad (2-12)$$

For the Fermi contact interaction  $\hat{\mathcal{H}}_{\text{FC}}$  the probability density function  $|\psi_0(r)|^2$  of the electron density at the nucleus ( $r=0$ ) is considered. Thus, this is a spherical isotropic value and therefore the  $a_{\text{iso}}$  is defined as isotropic part of the hyperfine interaction.<sup>172</sup>

$$a_{\text{iso}} = -\frac{2\mu_0}{3\hbar} g_e \mu_e g_n \mu_n |\psi_0(0)|^2 \quad (2-13)$$

Strictly defined, only s orbitals have electron density at the nucleus; however a polarization mechanism is defined explaining how higher angular momentum orbitals (p, d and f) can contribute to the spin density at  $r=0$ .<sup>167</sup>

A coupling of protons in plane of the aromatic systems has been described by McConnell.<sup>176</sup> Assuming that a partially singly occupied molecular orbital (SOMO) of nucleus C is hybridized with the bonding orbitals as shown in Figure 2-3, the energetic degeneracy forces parallel spins in near environment of these spins based on the Hund's rules. In the bonding

orbital the states are occupied following the Pauli principle. Therefore the spin far away from nucleus C is oriented antiparallel to the SOMO spin. This is a polarization mechanism of the electron spin at the nucleus. For protons this spin has s orbital character; thus the spin density is negative at the nucleus H.<sup>171, 176-178</sup> For in-plane H bonds the polarization mechanism is weakly contributing to the HF interaction, whereas for perpendicular H bonds a similar polarization mechanism applies as for covalently bond protons (Figure 2-3 C&D).

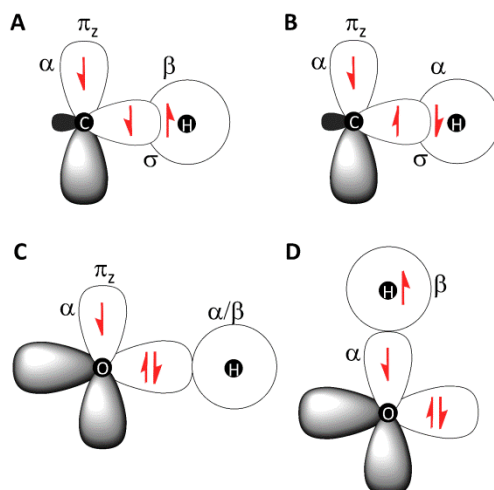


Figure 2-3: Spin polarization mechanism in an aromatic CH-fragment. The proton orbital cannot directly interact with the electron spin in the  $p_z$  orbital. Correlation energy description point out that the energy of case A is lower than case B in a magnetic field along the z axis. For an H bond within the ring plane a polarization is weak C, along the oxygen  $p_z$  orbital polarization is a non-neglectable contribution.<sup>110</sup>

After the consideration of spin density at the nucleus and polarization, the second contribution to the HF interaction is the dipole-dipole interaction between the electron and the nucleus in distance  $r$ . It is given by<sup>172</sup>

$$\hat{\mathcal{H}}_{\text{DD, HF}} = -\frac{\mu_0}{2\hbar} g_e \mu_e g_n \mu_n \left( \frac{\tilde{\mathbf{I}}\mathbf{S}}{r^3} - \frac{\tilde{\mathbf{I}}\tilde{\mathbf{r}}\tilde{\mathbf{S}}\tilde{\mathbf{r}}}{r^5} \right) \quad (2-14)$$

The integration over the spatial electron distribution result in the following anisotropic dipolar Hamiltonian (2-15).

$$\hat{\mathcal{H}}_{\text{DD, HF}} = \mathbf{S}\tilde{\mathbf{T}}_{\text{Dip}}\mathbf{I} \quad (2-15)$$

$\mathbf{T}_{\text{Dip}}$  is a traceless symmetric 3x3 matrix of the ground state wave function with the elements:

$$T_{ij, \text{Dip}} = -\frac{\mu_0}{2\hbar} g_e \mu_e g_n \mu_n \psi_0 \left| \frac{3r_i r_j - \delta_{ij}}{r^5} \right| \psi_0 \quad (2-16)$$

In which,  $\delta_{ij}$  is the Kronecker symbol ( $\delta_{ij}=0$  for  $i \neq j$  and  $\delta_{ij}=1$  for  $i=j$ ). The diagonal elements of the matrix in a principle axis system (PAS) are often defined as  $-T_{\perp}, -T_{\perp}$  and  $T_{\parallel}$ .

The equation can be simplified, considering a  $^1\text{H}$  in hydrogen bond distance  $r$  to an oxygen, i.e., of a tyrosine within a range of  $2.5 \text{ \AA}$ . For the proton the predominantly dipolar contribution scales with spin density population of the oxygen  $\rho_{\text{O}}$  and thus the single electron contribution on the oxygen. In the point dipole approximation the Eq. (2-16) can be then approximated with Eq.(2-17).

$$r = \sqrt[3]{\frac{\mu_0 g_e \mu_e g_n \mu_n \cdot \rho_{\text{O}}}{4\pi \cdot T_{\perp}}}$$

$$\text{For } ^2\text{H: } r = \sqrt[3]{\frac{11.86 \cdot \rho_{\text{O}}}{T_{\perp}}} \quad (2-17)$$

### 2.1.4 Dipolar Interaction

As in the nuclear to electron spin case the dipolar interaction between an electron spin and a second electron spin leads to a detectable dipolar frequency. Within this thesis the exchange contribution ( $J$  coupling) as scalar contribution is neglectable, because long-range distances are probed, thus Eq. (2-18) is obtained for  $\theta=90^\circ$ . The angle  $\theta$  is defined between the magnetic field and the interspin vector with the length  $r_{\text{AB}}$  as shown in Figure 2-4. Solving for the distance and assuming a  $g$  value of organic radicals near the value of the free electron it can be further simplified (2-19).

$$v_{\perp} = -\frac{\mu_0 \mu_e^2 g_A g_B}{4\pi \hbar r_{\text{AB}}^3} (3\cos^2 90^\circ - 1) \quad (2-18)$$

$$r_{\text{AB}}[\text{nm}] \cong \sqrt[3]{\frac{52.29[\text{MHz}]}{v_{\perp}[\text{MHz}]}} \quad (2-19)$$

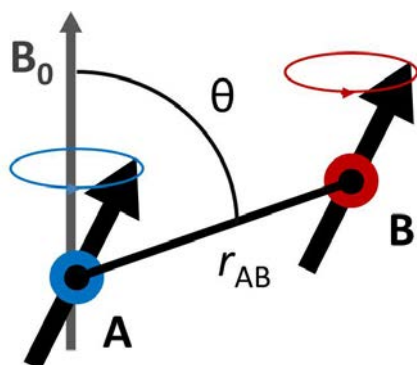


Figure 2-4: Dipolar coupling between two spins A and B in the magnetic field  $B_0$ . The coupling is dependent on the distance  $r_{(\text{A-B})}$  and the angle  $\theta$  between the magnetic field and the inter spin vector.

### 2.1.5 Quadrupole Interaction

Nuclear spins with  $I \geq 1$  are distinguished by a non-spherical charge distribution described by an electrical quadrupole moment  $Q$ <sup>172, 173</sup> with the Hamilton operator  $\hat{\mathcal{H}}_{\text{NQ}}$

$$\hat{\mathcal{H}}_{\text{NQ}} = \sum_{k; I_k > 1/2} \tilde{\mathbf{I}}_k \mathbf{Q}_k \mathbf{I}_k \quad (2-20)$$

The matrix of  $\mathbf{Q}$  is a traceless 3x3 matrix in its PAS, and can therefore, be written as:

$$\hat{\mathcal{H}}_{\text{NQ}} = Q_x I_x^2 + Q_y I_y^2 + Q_z I_z^2 = \frac{e q Q}{4I(2I-1)\hbar} \left[ (3I_z^2 - I(I+1)^2) + \eta (I_x^2 - I_y^2) \right] \quad (2-21)$$

with the asymmetry parameter  $\eta = (Q_x - Q_y) / Q_z$  for  $|Q_x| \leq |Q_y| \leq |Q_z|$  and  $0 \leq \eta \leq 1$ . The elementary charge is  $e$  and  $q$  is the electric field gradient. Consequently, the quadrupole interaction  $\hat{\mathcal{H}}_{\text{NQ}}$  can be solved in the molecular frame through knowledge of  $Q_z = e^2 q Q / (2I(2I-1)\hbar)$  and  $\eta$  as well as the three Euler angles in respect to the  $\mathbf{g}$  tensor in the PAS.

### 2.1.6 Analytical Treatment of the Spin Hamiltonian

To demonstrate the analytical solutions for the hyperfine interactions a model system with  $S = 1/2$  and a nucleus with a spin of  $I = 1/2$  will be discussed. Additionally, an isotropic  $\mathbf{g}$  tensor and an anisotropic hyperfine interaction are presumed. Thus, the static Hamiltonian in the PAS can then be written as<sup>179</sup>:

$$\begin{aligned} \hat{\mathcal{H}}_0 &= \omega_S S_z + \omega_I I_z + \tilde{\mathbf{S}} \mathbf{A} \mathbf{I} \\ &\approx \omega_S S_z + \omega_I I_z + A S_z I_z + B_x S_z I_x + B_y S_z I_y \end{aligned} \quad (2-22)$$

The resonance frequency of precession in angular frequency units is the Larmor frequency with  $\omega_S$  and  $\omega_I$  for electron spin and the nuclear spin, respectively. Here the approximated Hamiltonian includes the high-field approximation ( $\omega_S \gg |\mathbf{A}|$ ). In this case, terms with  $S_x$  and  $S_y$ , called non-secular terms, can be neglected. The non-secular terms of the HF interaction are still treated with  $A = A_{zz}$ ,  $B_x = A_{zx}$  and  $B_y = A_{zy}$  described as pseudo-secular hyperfine couplings of the  $\mathbf{A}$  matrix in the PAS of the  $\mathbf{g}$  tensor. The coordinate system for the nucleus spin can be transformed from the  $x$ -axis to the  $xz$ -plane, to simplify the non-secular terms to  $B = (B_x^2 + B_y^2)^{1/2}$  only dependent on  $S_z$ .<sup>179</sup>

To set it all in the rotating frame the electron Zeeman frequency is substituted by the resonance offset ( $\Omega_s = \omega_s - \omega_{mw}$ ), where  $\omega_{mw}$  is the microwave frequency. The combined transformation and substitution displays  $\hat{\mathcal{H}}_0$  as follows

$$\hat{\mathcal{H}}_0 \approx \Omega_s S_z + \omega_I I_z + A S_z I_z + B_x S_z I_x \quad (2-23)$$

with given spin matrices the diagonalized form of the Hamiltonian results to<sup>179</sup>

$$\hat{\mathcal{H}}_0 = \begin{bmatrix} \left( \frac{\omega_s}{2} + \frac{\omega_I}{2} + \frac{A}{4} \right) & \frac{B}{4} & 0 & 0 \\ \frac{B}{4} & \left( \frac{\omega_s}{2} - \frac{\omega_I}{2} - \frac{A}{4} \right) & 0 & 0 \\ 0 & 0 & \left( -\frac{\omega_s}{2} + \frac{\omega_I}{2} - \frac{A}{4} \right) & -\frac{B}{4} \\ 0 & 0 & -\frac{B}{4} & \left( -\frac{\omega_s}{2} - \frac{\omega_I}{2} + \frac{A}{4} \right) \end{bmatrix} \quad (2-24)$$

The corresponding eigenvalues of the Hamiltonian in nuclear frequencies can be obtained with:

$$\omega_{\beta/\alpha} = |\omega_{1 \rightarrow 2/3 \rightarrow 4}| = \sqrt{\left( \omega_I \pm \frac{A}{4} \right)^2 + \frac{B^2}{4}} \quad (2-25)$$

The frequencies  $\omega_{\beta/\alpha}$  are given for the NMR transitions  $1 \rightarrow 2$  and  $3 \rightarrow 4$  for the two spin manifolds  $\alpha$  and  $\beta$ , as shown in Figure 2-5A. Within the high-field approximation the B term is neglectable, as long as  $\omega_I \ll \omega_s$ . This has been fulfilled throughout this thesis at frequencies of  $\omega_s/2\pi \geq 94$  GHz, except for the <sup>19</sup>F HF couplings of 2,3,5-F<sub>3</sub>Y• (§5.3, p.135).

To consider the interaction of the electron spin with  $I=1$  nuclei like <sup>2</sup>H ( $I=1$ ), the resonance conditions change. Within the high-field limit the resonances  $\omega_{sq}$  (see Figure 2-5B) of the allowed transitions are given by<sup>179</sup>:

$$\omega_{sq} = \left| \frac{A_i}{2} \pm \omega_i \pm \frac{3}{2} Q_i \right| \quad (2-26)$$

With these approximations one finally arrives at the energy level diagram shown in Figure 2-5 for two cases typical cases within this thesis.

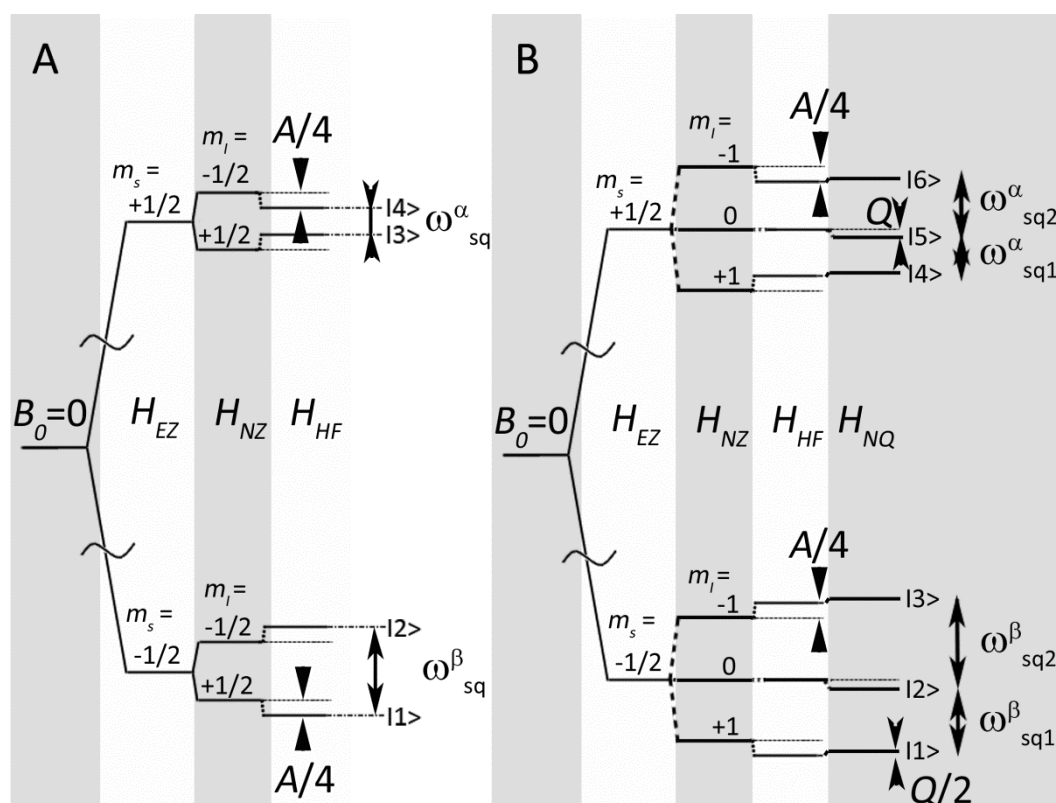


Figure 2-5: Energy levels in two spin systems at a certain orientation in the weak coupling ( $A \ll \omega_I$ ) case. A) Spin system with  $S=1/2$  and  $I=1/2$  with isotropic hyperfine interaction. B) With a spin  $S=1/2$  and  $I=1$  this is typical for an energy diagram of a deuteron in a weak coupling case as for example deuterons in an H bond to a phenoxy oxygen. The quadrupole coupling and electron Zeeman interaction are not to scale for illustration purposes.

## 2.2 High-Field Spectroscopy for Small Hyperfine Couplings

### 2.2.1 Detection of Hyperfine Interaction

The HF interactions were introduced in §2.1.3 are as closely related to the electronic structure of the individual radical. The local structure information is connected to the HF interactions of individual nuclei surrounding an electron spin. The typical interaction range is given with 0-10 Å, for high  $\gamma$  nuclei (2-14). Due to the transient nature of the radicals studied here the measurements are performed in frozen solution. This connected to the  $g$  anisotropy, which helps to retrieve the direction of the dipolar part of the coupling. This can always be used if the spectral width due to  $g$  anisotropy is larger than the excitation

bandwidth of the spectrum. For organic radicals this is only fulfilled by operating at high-fields.

### 2.2.2 Nuclei Accessible in Hyperfine Spectroscopy

A typical system investigated within this thesis should be introduced from the magnetic interaction point of view, as shown in Figure 2-6. The 3-amino tyrosine has many internal couplings as presented in Figure 2-6 A, without isotope labeling  $^{13}\text{C}$  is seldom detected. For nitrogen  $^{14}\text{N}$  couplings are observed. In a non-isotopically labeled buffer the  $^1\text{H}$  nuclei will be observed, by buffer exchange to  $\text{D}_2\text{O}$  external deuterons can be distinguished from  $^1\text{H}$  as  $^2\text{H}$  nuclei (cf. Figure 2-6 B). However, the amino protons will also be exchanged. Thus, even in a deuterated protein these contributions cannot be separated.

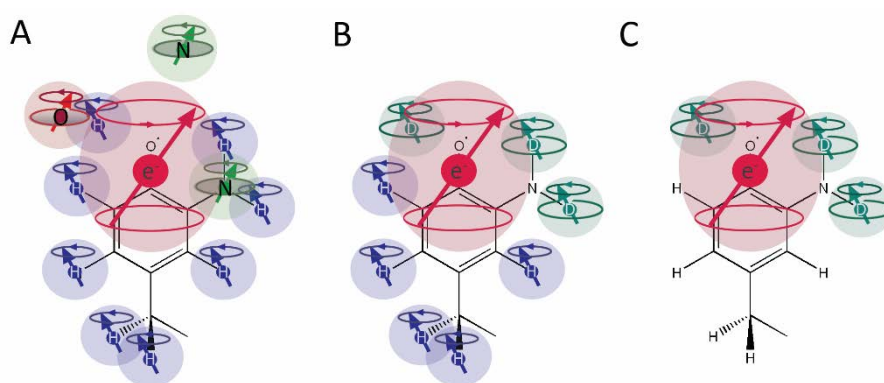


Figure 2-6: Nuclear spins coupled to a  $\text{NH}_2\text{Y}\cdot$ . The electron spin ( $e^-$ , red) is here the 3-amino tyrosine radical. A) Several magnetic nuclei isotopes are in the interaction sphere for the tyrosine analog, displayed are  $^1\text{H}$ ,  $^{17}\text{O}$ ,  $^{14}\text{N}$ . B) Buffer exchange can introduce  $^2\text{H}$  at exchangeable sites. C) By separating the different nuclei due to different sizes of nuclear Zeeman couplings, one can select  $^2\text{H}$  HF couplings.

In the introduction, it was shown how resolution can be improved according to the electron Zeeman term for electron spin part. The same applies for the nuclear Zeeman contribution. Taking additionally common hyperfine interactions into account, the separation between low frequencies as X-band and high frequencies like W-band are depicted in Figure 2-7. Thus, several magnetic coupling nuclei can be specifically detected, i.e., exchangeable protons by their  $^2\text{H}$  resonance (Figure 2-6 C).

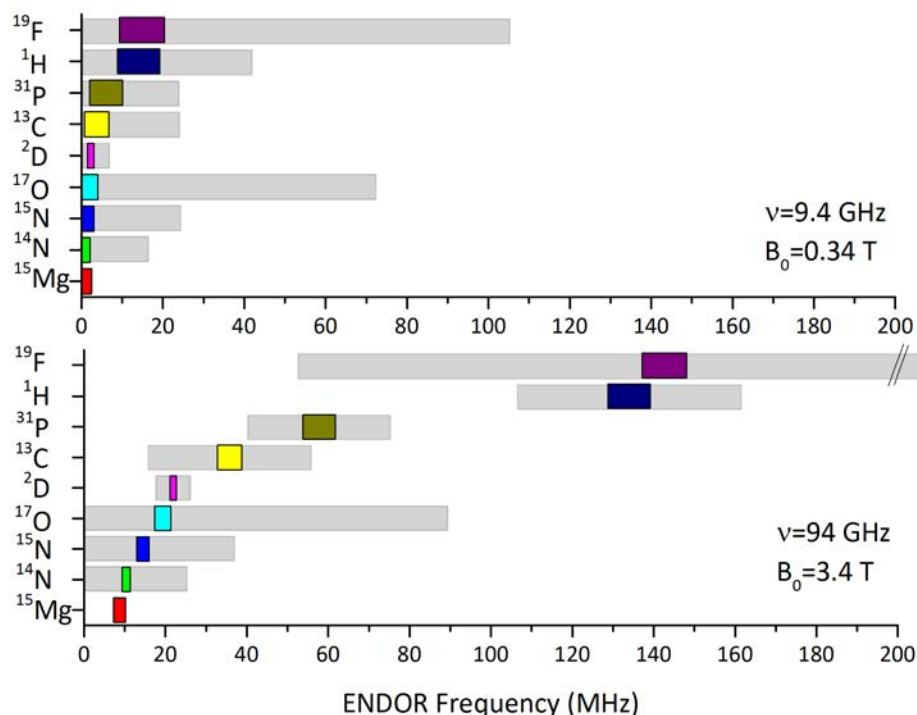


Figure 2-7: Gain in ENDOR resolution for organic radicals ( $S=1/2$ ) with increasing Zeeman field  $B_0$  and microwave frequency  $\nu$  (MW). Spectral line widths of typical nuclei in tyrosine spin probes (neutral organic radicals) are shown. In color intermolecular interaction ranges and in gray intramolecular coupling sizes are estimated from DFT calculations and ref. 135, 153. The spectral overlap at X-band ENDOR is evident, but the HF coupling becomes separated at W-band (94 GHz/3.4 T) for nuclei coupled over a non-covalent bond to the electron spin.

The typical interaction strength marked in Figure 2-6 demonstrates that external interactions are weaker than internal ones. Therefore external couplings as  $^2\text{H}$  will generally not be resolved in the splitting patterns of an EPR line shape. Here specialized techniques are employed. Especially at high frequency for small HFC Mims ENDOR has been used to study H bonds around organic radicals.<sup>55, 152, 153, 155</sup>

### 2.2.3 Mims-ENDOR Spectroscopy

Electron-nuclear double resonance (ENDOR) in general is a double resonance technique resolving small couplings due to the selective pumping of nuclear transitions ( $\Delta m_I = 1$  &  $\Delta m_S = 0$ ) or NMR transitions. The name NMR transition might be misleading. Typically, transitions detected in an ENDOR spectroscopy experiment have sensitivities higher than those of conventional nuclear magnetic resonance (NMR) detection<sup>180</sup> and higher selectivity because of detection through the electron spin. The higher Boltzmann



polarization of the electron spin is advantageous here. On the contrary due to this interaction broad lines are observed.

ENDOR was first introduced to the scientific community by Feher,<sup>181</sup> shortly after two techniques were developed and named after their inventor Davis<sup>182</sup> and Mims ENDOR<sup>183</sup>. Already in the 1970s it could be shown that Davis ENDOR suffers from broad blind spots near the Larmor frequency of each nuclear spin.<sup>184</sup> Thus Mims ENDOR was used throughout this thesis for small couplings up to  $a_{\text{iso}} \approx 2$  MHz. The Mims pulse sequence consists of a stimulated echo sequence on the electron transitions and an inversion pulse swept over nuclear frequencies. The stimulating echo sequence has three microwave pulses generating an echo after third pulse and the delay  $\tau$ , as shown in Figure 2-8.<sup>183</sup>

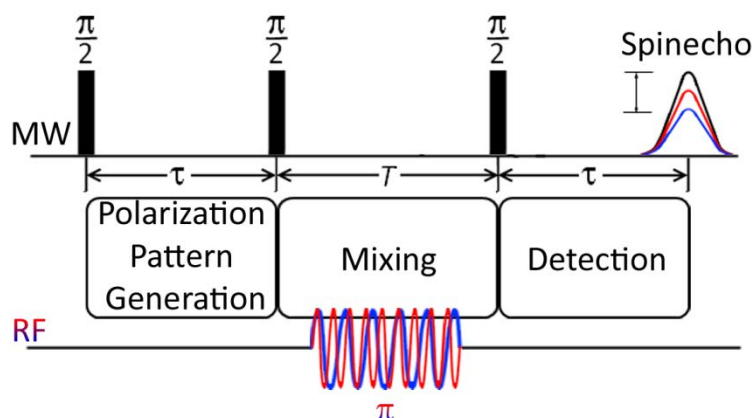


Figure 2-8: Mims ENDOR sequence for the detection of small HF couplings. The microwave frequency of the pulses stays constant detecting a stimulated echo. By varying the radio frequency of a  $\pi_{\text{RF}}$  pulse different NMR transitions (black, red and blue) are probed. If a nuclear resonance is met, the echo amplitude will be reduced (red and blue echo).<sup>183</sup>

Ideally the detection with the last  $\pi/2$  only reads out the  $M_z$  magnetization. Therefore the mixing is acting on the  $M_z$  magnetization. For small couplings microwave irradiation is in most cases not selective enough. Furthermore the echo width increases beyond the detection limit with an increase in pulse length or selectivity. In the classical picture for a non-selective mw pulse Mims ENDOR is described as phase offset dependent on the nuclear frequency ( $\Delta \approx A_{\text{HF}}$ ), as illustrated in Figure 2-9B. The part unaffected by nuclei offset will interfere destructively with the magnetization pattern with the additional phase shift, which then decreases the echo size. Overall an increase of sensitivity for small offset  $\Delta$  is achieved. Therefore, the Mims ENDOR is superior if a selective excitation of the

nuclei spins is prohibited due to the small coupling sizes by Davis ENDOR. Davis ENDOR has a different magnetization pattern as indicated by the original line shape in Figure 2-9A.

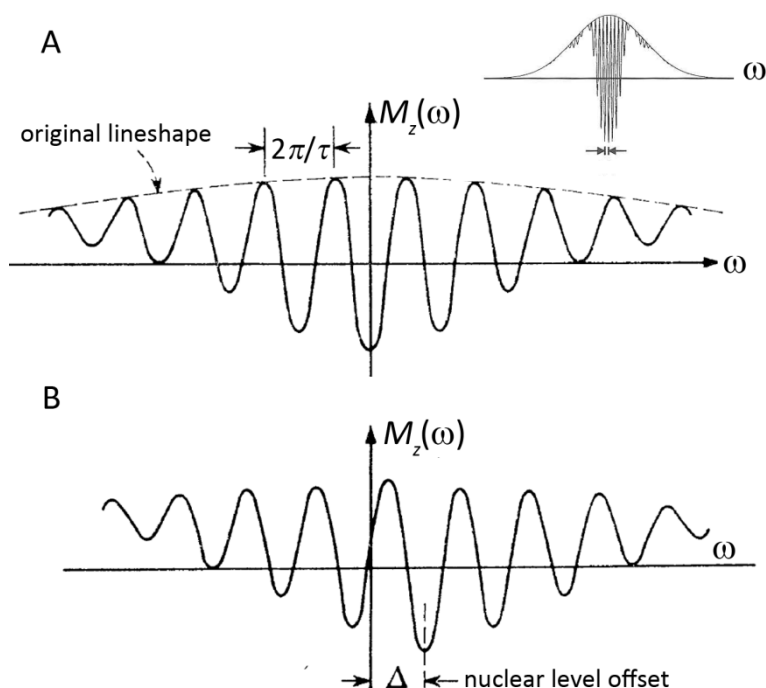


Figure 2-9: Illustrative picture of the pattern created in the preparation sequence ( $\pi/2-\tau-\pi/2$ ). The inset shows the pulse sequence acting on a broad line. Enlarged (A) shows an artificial pattern imposed on the line. B) Displacement by a resonant nuclei with an interaction energy of  $\hbar\Delta$ . Adapted from references 172 & 183.

The population  $P$  and its population difference  $P_i$  between the energy levels  $i$  ( $=1, 2, 3$  &  $4$ ), assigned in Figure 2-5A (p.38), is given by Eq. (2-27).<sup>183</sup>

$$P_{(1+2)-(3+4)}(\omega) = P_{(1+2)-(3+4),0}(\omega) \cdot \left( 1 - \frac{3}{2} \cos\left(\frac{\omega}{2\pi\tau}\right) \right) - \frac{1}{2} P_{(1-3)} \cos\left(\frac{\omega+\Delta}{2\pi\tau}\right) - \frac{1}{2} P_{(2-4)} \cos\left(\frac{\omega-\Delta}{2\pi\tau}\right) \quad (2-27)$$

A drawback of Mims ENDOR lies in the constructive interference of the patterns generated. In the spectrum this leads to regions where the echo cannot be diminished, Mims holes are generated. These Mims holes depend on the following hole function (Figure 2-10A)<sup>172, 183</sup>

$$I_{MimsEndor} \propto 1 - \cos(2\pi A_{HF}) \quad (2-28)$$

To avoid holes within the spectrum an upper limit can be set for each investigated coupling with the largest hyperfine coupling  $A_{\max}$  Eq. (2-29) can be used. Measurements to average out blind spot effects are often prohibited by the long measurement time for low concentrated biological samples ( $\ll 50 \mu\text{M}$ ).<sup>172</sup>

$$A_{\max} = 1/(2\tau) \quad (2-29)$$

The efficiency of Mims ENDOR  $F_{\text{Mims ENDOR}}$  (2-30) increases tremendously for small couplings with the interpulse delay  $\tau$ .<sup>180</sup> One could think about increasing the Mims holes to a frequency in the order of the Nyquist frequency, but this is prohibited by fast  $T_2$  relaxation in the xy magnetization plane (Figure 2-10A).

$$F_{\text{Mims ENDOR}} = \frac{1}{4}(1 - \cos(A_{\text{HF}}\tau)) \quad (2-30)$$

Practically the distortions are often too severe in powder spectra. Therefore, the largest  $\tau$  in agreement with Eq. (2-29) is chosen. The center line for  $A_{\text{HF}}$  approaching zero is only theoretically completely suppressed. For protons it is often the most intense line due a large number of distant protons.<sup>185</sup> The matrix line is observed due to the finite bandwidth of the RF pulse.<sup>185</sup>

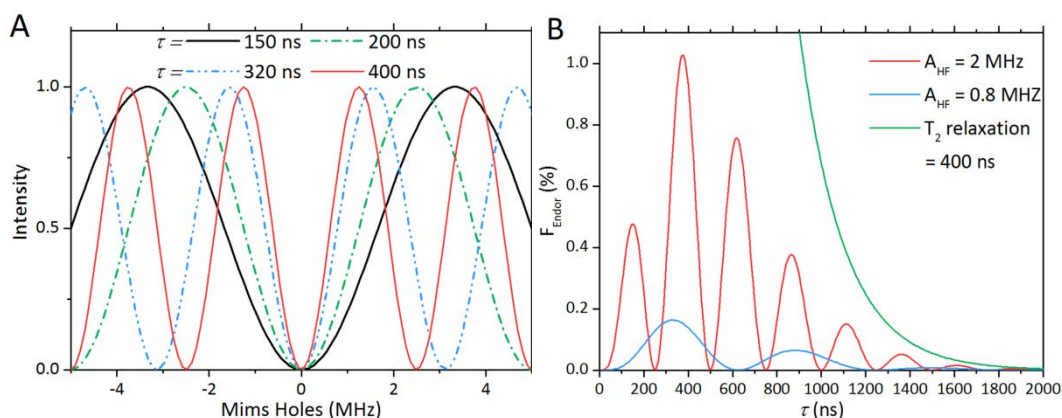


Figure 2-10: Mims hole functions in dependence of the interpulse delay  $\tau$  (A). B) ENDOR efficiency according to multiplication of Eq. (2-29) with the hole function and the  $T_2$  relaxation function (green) for two different small HF couplings 2 MHz (red) and 0.8 MHz (green).

## 2.2.4 Comparison to Other Hyperfine Detection Methods

HF detecting techniques characterize couplings too complex or too small to be resolved in conventional EPR spectra. There are several other techniques that allow for the detection of HF couplings. One of them is called ESEEM, which is most efficient at low fields and will

not be further discussed here.<sup>172</sup> Another technique, called Davies ENDOR, has already been partially introduced. An emerging technique is called electron double resonance (ELDOR) detected NMR<sup>186</sup>, here instead of another RF pulse a highly selective microwave pulse is used to drive transitions. Because both techniques are polarization transfer techniques these two can readily be compared. The efficiency of both techniques can be described by their polarization transfer capabilities as shown in Figure 2-11. Here the character of each technique becomes evident; the excitation bandwidth in a typical RF pulse is much narrower than available in any MW ELDOR pulse. Thus, Davies can be much more selective in terms of orientation selection and omitting line broadening of HF patterns, but ELDOR detected NMR is able to excite more spins and has therefore advantages in the sensitivity. A 30-times higher sensitivity has been reported on organic, ubiquitously used nitroxide labels.<sup>187</sup> Even more could be achieved by newly developed detection schemes.<sup>188</sup> A drawback is that the lines can be broader compared to a standard ENDOR setup.

The relaxation behavior is also different. The high turning angle ELDOR pulse acts directly on the initial  $M_z$  magnetization. Especially for small couplings, Davies ENDOR requires long preparation pulses turning the magnetization into the  $xy$ -plane; here faster  $T_2$  relaxations can diminish the signal for fast relaxing paramagnetic centers. ELDOR detected EPR was meanwhile successfully applied to several high spin systems, so it seems to be robust in terms of  $T_1$  relaxation.<sup>189, 190</sup> Here especially low  $\gamma$  nuclei such as oxygen  $^{17}\text{O}$  have been detected.<sup>189-191</sup> One example even shows a narrow central line of a second shell water molecule. Although a forbidden transition is used, it seems it can detect even small HF couplings.<sup>191</sup> Notably, this has not been investigated thoroughly up to now.<sup>135</sup>

A big disadvantage of ELDOR detected NMR is the large blind spot around the detecting microwave frequency, which is influenced by the ELDOR pulse length.<sup>187</sup> Here the detectable magnetization is reduced to 0. However, this blind spot does not depend on the coupling size as in ENDOR techniques therefore these techniques can be complimentary.<sup>184, 186</sup> Selective Mims ENDOR employs an analogous polarization scheme as Davies ENDOR in Figure 2-11A.<sup>183</sup>

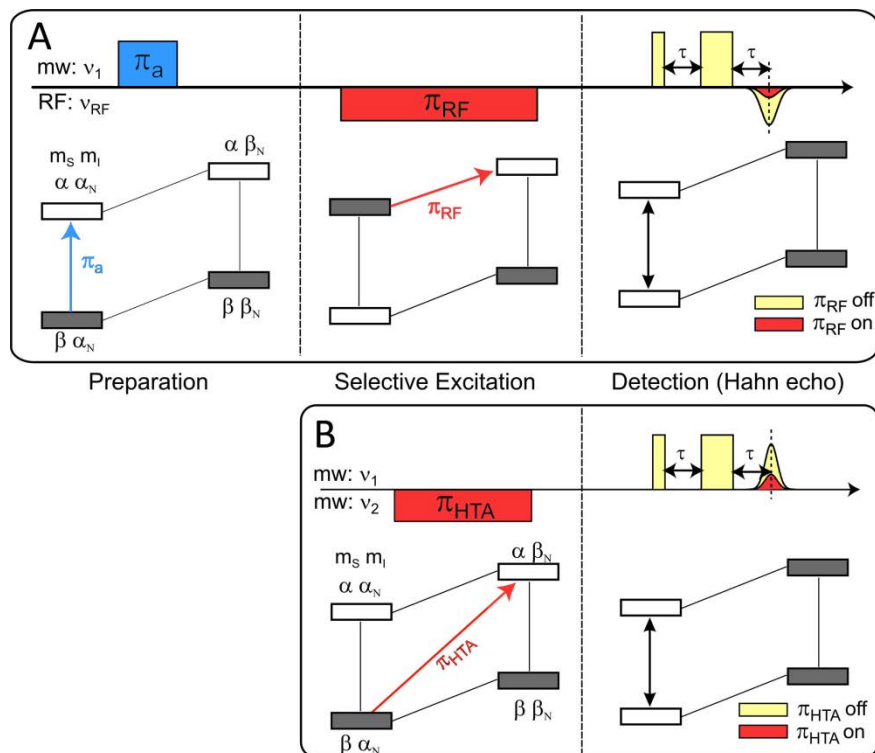


Figure 2-11: Comparison of Davies ENDOR (A) and pulsed ELDOR-detected NMR (B). Below the pulse sequences the concomitant spin population development is shown in a phenomenological description of an  $S=1/2$  and  $I=1/2$  system. Polarizations transfer in the Davies-type pulse ENDOR experiment involves allowed electron nuclear spin transitions. The preparation pulse  $\pi_a$  is normally a selective soft pulse and the radio frequency pulse  $\pi_{RF}$  is strong and short. Polarization transfer occurs in the ELDOR detected NMR experiment with a high turning angle pulse  $\pi_{HTA}$  including allowed and forbidden transitions of the hyperfine coupled electron and nuclear spins. Adapted from ref. 135.

## 2.2.5 Hyperfine Tensors and Origin

Based on the energy level diagram (Figure 2-5, p. 38) and the hyperfine coupling mechanism (§2.1.3) the appearance of these interactions should be illustrated. Typical hyperfine spectroscopy pake patterns found in tyrosine systems should be introduced. Quadrupole splittings and rhombicity of the HF tensor are neglected for simplicity.

The simplest case is a distant coupling, which is only governed by the dipolar interaction. The full pake pattern is seen in Figure 2-12A. A good example of this would be distant protons as found in yeast RNR or even nearby protons non-interacting with the  $p_z$  orbital.<sup>152, 153</sup>

The second case occurs if the orbital directly interacts with a spin bearing nucleus. Good examples are protons on electron negative nuclei like the amino protons in the 3-amino tyrosine. Here the tensor shape is strongly governed by the opposite signs between  $a_{\text{iso}}$  and  $T_{\parallel}$ , as illustrated in Figure 2-12 C.<sup>110, 134</sup>

The H bond axial to the ring plane as described by Argirević *et al.* is an intermediate case as illustrated in Figure 2-12B.<sup>110</sup> In this case the  $p_z$  orbital interferes directly with the  $s$  orbital of the nuclei. Negative spin density at the nuclei is produced slight (bonding) overlap of the wave functions of the nuclei (cf. HF interaction §2.1.3).<sup>110</sup> The  $p_z$  orbital has no spherical symmetry. Therefore the interaction  $a_{\text{iso}}$  is a function of distance and angle.

The last case is a nearly isotropic coupling with an  $a_{\text{iso}} > 0$ . This case can be observed for  $\beta$ -methylene couplings (Figure 2-12D).

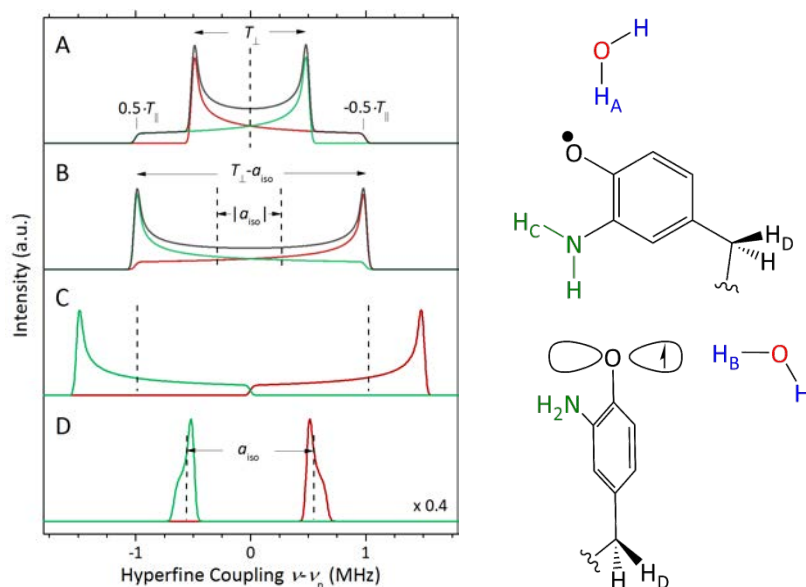


Figure 2-12: Hyperfine powder patterns for different ratios of  $a_{\text{iso}}$  to  $T$ . A)  $a_{\text{iso}}=0$ ; B)  $a_{\text{iso}}=-1/4 \cdot T_{\parallel}$ ; C)  $a_{\text{iso}}=-1/3 \cdot T_{\parallel}$ ; D)  $a_{\text{iso}}=5 \cdot T_{\parallel}$ . On the left side examples are shown where these types of couplings had been found. The proton couplings  $H_X$  corresponds to case  $X=A, C, B$  or  $D$ .

## 2.3 Density Functional Theory: Limitations and Advantages

The idea behind the determination of HFC and  $g$  values as presented in the previous sections is one part of the information and the understanding of structural restraints, the visualization of the geometry is another. DFT has been found to be a valuable tool for correlating spectral parameters with structure and compare different spectroscopic methods. To understand the advantages of this comparison and its limitations the following section will introduce some basics of DFT theory. EPR and NMR parameters can be treated in DFT by taking the effective Hamiltonians on the bases of the “occupied orbitals only” ground state. The focus will lie on certain DFT methods used in this thesis. The interested reader is referred to a didactically written perspective of the origin of DFT and the development of their density functional approximations.<sup>192</sup>

The core idea was formed by Hohenberg, Kohn and Sham in 1964-65.<sup>193, 194</sup> The nuclear potential  $v_{\text{ext}}(r_i)$  defines the Hamiltonian  $\hat{\mathcal{H}}$  (2-31) at the wave function  $\Psi_0$  and the wave function defines the electron density  $\rho$ . This has been shown to be reversible,<sup>193</sup> thus from the electron density everything of the ground state system will be known for the given coordinates [Eq. (2-32)].

$$\hat{\mathcal{H}} = -\frac{1}{2} \sum_i \nabla_i^2 + \sum_i v_{\text{ext}}(r_i) + \frac{1}{2} \sum_{j \neq i} \sum_i \frac{1}{|r_j - r_i|} \quad (2-31)$$

For simplicity atomic units are used here, where  $\hbar$ ,  $m_e$ ,  $e$ , and  $4\pi\epsilon_0$  are set to be 1.

$$\begin{aligned} v_{\text{ext}} &\rightarrow \Psi_0 \rightarrow \rho \\ \rho &\xrightarrow{F(\rho)} v_{\text{ext}} \rightarrow \Psi_0 \end{aligned} \quad (2-32)$$

The function  $F(\rho)$  connecting the spin density to  $v_{\text{ext}}(r_i)$  is unknown. However, it could be shown by the variation principle that only the correct spin density will lead to the energy minimum. Thus, searching for the correct spin density is a minimization problem.<sup>193</sup> Non-representative variational densities will collapse, thus it was necessary to separate the known total kinetic energy  $T_0(\rho)$  and classical Coulomb  $V_{\text{ee}}(\rho)$  self-exchange from the unknown smaller exchange correlation  $E_{\text{EX}}(\rho)$ . Although the exchange correlation is a small contribution to the total energy, it is the essence for covalent bonds and attractive non-electrostatic interactions. Otherwise, the theory to this point is complete. Electrons in atoms, molecules, and solids can be viewed as independent particles moving in effective potential  $v_{\text{KS}}$ .<sup>192</sup>

### 2.3.1 Explaining Tendency within the Functionals

The theory laid out how everything depends on exchange correlation  $E_{XC}$ , but how is it calculated? Here density functional approximations have been formulated.

In the main, three ways to calculate the Kohn Sham exchange term  $E_{XC}$  have been developed:

- i. The local density approximation (LDA) has been applied. It assumes that the exchange-correlation energy has the local volume  $\rho(r)$  of the spin density. This is a bold assumption for molecules originating from the idea of an ideal (uniform) electron gas (similar as found in metals). Based on the adiabatic (constant density) approximation the coupling strength can be integrated over the individual couplings. Localized pairs of non-exchanging spin densities can be separated as correlation only cases. These are called exchange “holes.” Generally this approximation leads to overbinding, thus shorter internuclear distances.
- ii. Generalized gradient approximations (GGA) should reduce this overbinding effect. Here not only the local density is considered, but also the gradient at the local position. Subtracting from the local density exchange  $E_x^{LDA}$  this gradient to a certain order is the basic idea, albeit fitting the ratio and exponent of the local gradient to the uniform electron gas or benchmark sets; the functional is still LDA with a correction. A weak overbinding tendency was thus retained due to the localization of delocalized exchange “holes.”
- iii. The so-called hybrid functionals mix Hartree Fock exchange correlation with LDA and GGA exchange correlations in order to fit atomic absorption data. For the first time, delocalized “holes” are taken into account due to the Hartree Fock exchange. The exact Hartree Fock exchange is underbinding due to the unconsidered electron correlation.

Known pitfalls of these GGA and hybrid functionals are the following: an overestimation of molecular radicals, poor treatment of charge transfer processes and the inability to account for dispersion interactions (methods are introduced in the next section).

These interatomic effects cannot be treated by the density functionals made to describe a tightly packed uniform electron gas. For an unpaired electron the localized approximations fail to localize this highly delocalized exchange minimum or “hole.” This over stabilizes the radical state. The delocalization increases also for lighter atoms.



Local DFT approximations had been shown therefore to have a barrier too low for hydrogen-atom transfers, especially in  $\text{H}_2 + \text{H} \rightarrow \text{H} + \text{H}_2$ .<sup>195,196</sup> Visually the problem can be shown for the dissociation curve of  $\text{H}_2^+$  in Figure 2-13.<sup>192</sup>

DFT functionals with  $N^4$  scaling will have a certain underestimation of barrier heights. PBE0 as functional is within this set the best choice by a comparison shown by Becke with a mean error of -3.6 kcal/mol.<sup>192</sup> It is notable that this has been chosen by C. Riplinger from Neese group to calculate the PCET between radical intermediates in  $\alpha$ -RNR Ia.<sup>110</sup>

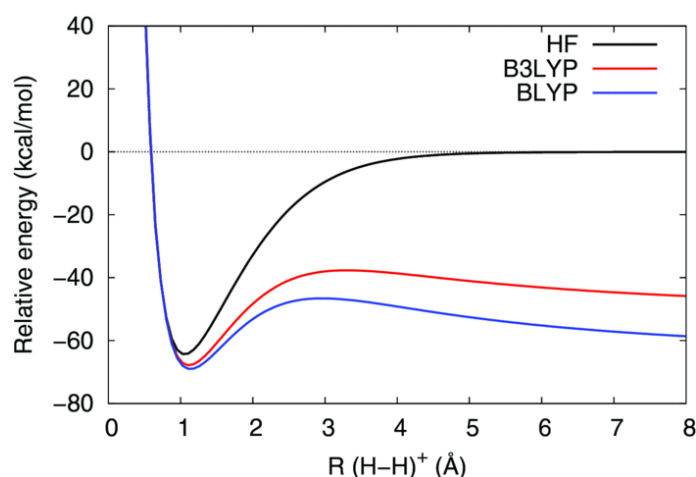


Figure 2-13: Dissociation curve of  $\text{H}_2^+$ . A typical local approximation error falls increasingly below the exact curve. Here BLYP and B3LYP display an artificial maximum and an erroneous asymptote almost as low as the bond minimum. Cited from ref. 192.

### 2.3.2 Dispersion Correction

Dispersion interaction is especially important for intramolecular interactions. In this thesis, several complexes will contain dispersive interactions. For instance, the interaction between two tyrosines in close proximity is governed by electrostatics and London dispersion interactions.<sup>197,198</sup> After the development of local DFT approximations, non-local effects should also be treated. Therefore dispersion correction was applied to functionals and basis sets. This can become quite complex. A straightforward implementation is the addition of the empirical London forces scaling with  $r^{-6}$  and  $r^{-8}$ .<sup>199</sup> The empirical potential has influence in the local field, for instance, below 3 Å for an argon gas interaction as shown in Figure 2-14.<sup>200</sup> The method is reported to be robust and has not shown any basis set or functional dependent errors.<sup>201</sup>

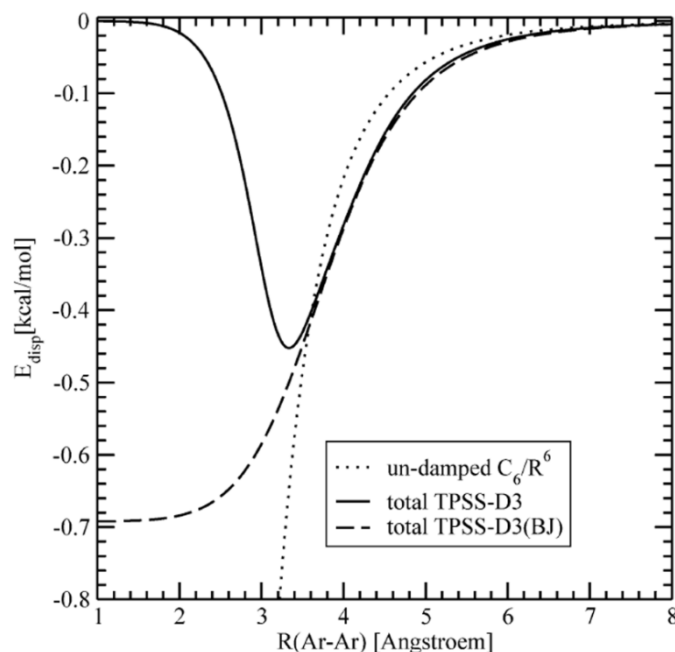


Figure 2-14: Dispersion correction for two argon atoms. The dispersion correction (--) takes sixth- and eighth-order terms into account, in contrast an un-damped  $C_6R^{-6}$  term ( $\cdots$ ) and zero (—) Becke and Johnson damping is shown. Obtained from ref. 200.

The absence of considered dispersion interaction has been shown to have an impact on geometry optimization of two phenols. In this study the stacked orientation of the phenol rings could only be obtained with wave function theory or by dispersion corrected DFT. The energetics of the barrier heights for proton transfers were not significantly improved upon dispersion correction.<sup>113</sup> For these barrier calculations the PBE0 functional has shown better capability in obtaining values comparable to the QM gold standards.<sup>192,202</sup>

In this thesis we use the robust correction method<sup>203</sup> shown in Figure 2-14 in combination with the well-known and often tested B3LYP functional. Also we used effective triple zeta diffuse basis sets (see 2.3.3, p. 51) operating near the basis set limit. Recently, this combination has been tested for its performance and offered the best performance to cost result.<sup>204</sup>

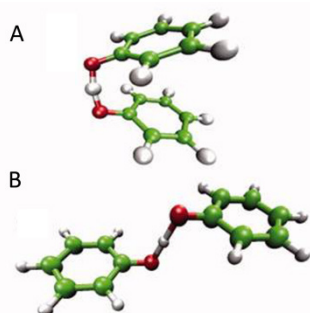


Figure 2-15: Two geometry-optimized phenoxy/phenol structures. The stacked conformation (A) could only be found in dispersion corrected B3LYP-DFT, whereas all possible structures could be obtained by CASSCF. Picture modified from ref. 113.

### 2.3.3 Basis Sets

In current DFT applications, Gaussian type orbitals are nearly always employed. These approximated orbitals are faster to compute than more realistic Slater type orbitals. Compared with each other, they have different exponential behaviors with  $e^{-\zeta r}$  and  $e^{-ar^2}$  for Slater type orbitals and Gaussian type orbitals respectively. Additionally, Gaussian type orbitals (GTO) have typical for Gaussian functions a broad area around  $r=0$ , whereas Slater type orbitals (STO) are cusp, as seen in Figure 2-16.<sup>205</sup>

The fit of three Gaussian type orbitals to one Slater type orbital for a single atomic orbital is the minimal basis set, as would be applicable to H and He. For an oxygen there would be five basis functions 1s, 2s and 2p<sub>x,y,z</sub>. The difference in the  $r \rightarrow 0$  dependence effect especially EPR parameter as HF couplings. An effect caused by the HF couplings dependency on the core shell. However, an early recognized beneficial compensation of errors is reported to overcome this effect in DFT geometries.<sup>167</sup>

In the triple zeta case, three basis sets are used for each atomic orbital. The first approach was to segment these additional contracted orbitals into valance shell and core shell, as in well-known 6-311G basis sets. Meanwhile they are coefficient optimized for loose and tight discrepancy of valance and core shell orbitals, respectively. This is also called correlation consistent. These basis sets offer the same quality, but a better calculation performance.

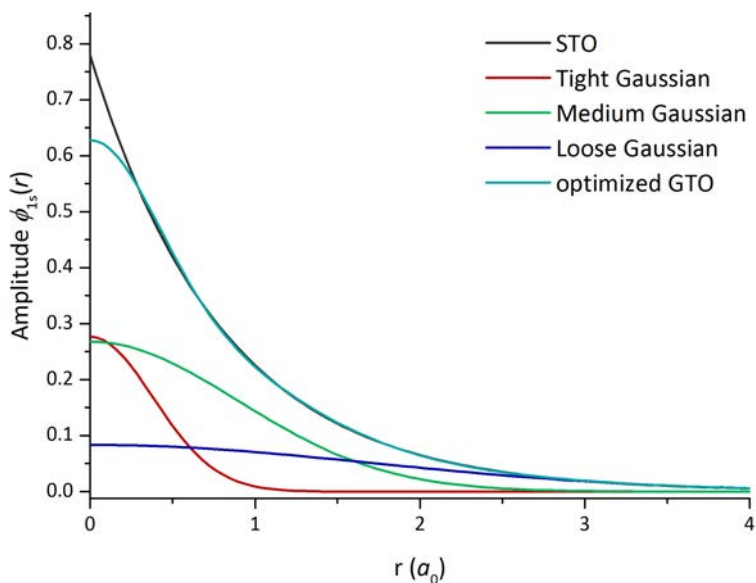


Figure 2-16: Comparison between Slater type  $\phi_{1s}^{STO}(r)$  orbital (STO) and Gaussian type orbitals contracted to fit the STO. Three Gaussian functions red, green and blue up are combined (cyan) to fit one STO (black). The fit does not increase by the addition of more GTOs, this basis set is called STO-3G. The def2-TZVPP used here also employs polarization functions (PP) and diffuse basis sets (def2). Polarization is included by a method, in which higher orbital functions (i.e., f and g) are also considered for in the electron density. For instance, an H atom includes an additional p orbital contribution to take a polarization into account. This basis set is close to the basis set limit in DFT calculations.<sup>206-208</sup> Diffuse basis sets consider effects, which have long reaching interactions, as typically occurring in anions for instance. These effects cannot be considered with these with  $e^{-ar^2}$  decaying basis sets. Therefore diffuse basis sets are very broad over the whole radial distance.<sup>206, 208</sup>

### 2.3.4 Effective Hamiltonian and Perturbation Theory for DFT

The effective Hamiltonian as the spin Hamiltonian (§2.1, p. 28) can be incorporated into DFT. Based on the Breit-Pauli approximations<sup>209</sup> the spin-orbit coupling contribution is treated as a second order perturbation in a one-component relativistic treatment.<sup>210-212</sup>

In the one-component treatment, all-electron contributions have a single origin (gauge origin), and no other relativistic effects beyond the spin-orbit coupling are treated, as current dependence in the exchange functional or admixture of the exact exchange. The sum over all occupied orbital and virtual orbital states of the spin-orbit coupling contribution on

the wave function is formed. The mean field approximation used for the sum over states contribution to the  $\mathbf{g}$  tensor is similar to the high-field approximation used in analytical treatments of EPR interactions (cf. §2.1.6, p.37).

Further relativistic effects are small and have been neglected in the default ORCA<sup>214</sup> (§ 3.6, p.73) EPR property calculation. Due to this one-component treatment the  $\mathbf{g}$  tensor is not gauche invariant. Methods were reported to compensate this gauche dependence.<sup>167</sup> Methods such as the gauche invariant atomic orbitals correction<sup>213</sup> have not been implemented up to now in ORCA.<sup>214</sup> However, scalar relativistic effects were introduced via certain basis sets (ZORA<sup>215</sup>) recently.<sup>156</sup> Especially for the small spin-orbit couplings treated here, these errors are often well encompassed by the uncertainty of the structure determination.<sup>167</sup> For the determination of  $g$  values the combination of UB3LYP and EPRII has proven to be effective and has been applied on various  $\pi$  radicals.<sup>110,216,217</sup>

The solutions for the HF couplings in DFT connect the wave function of the before mentioned spin Hamiltonian to the obtained spin densities (§2.1, p. 28). The HF calculation at least on the same geometry is only minor affected on the DFT functional set used.<sup>167</sup> Due to the mismatch in core potential with Gaussian functions often very flexible core basis sets are used (see last section). Here flexible double  $\zeta$  functionals for first and second row elements as EPR-II are often advantageous.<sup>167,218-220</sup> For certain nuclei IGLO III offers a flexible core in combination with a triple  $\zeta$  basis set.<sup>167,218-220</sup> The combination of UB3LYP and TZVPP has been shown to be efficient for precise  $\mathbf{g}$  tensor calculations.<sup>221</sup>

## 2.4 Proton Coupled Electron Transfer

To understand the different regions and dynamics of proton coupled electron transfer first a pure electron transfer will be considered. In principle one can show that if the rate limiting step is a long distance electron transfer the PCET kinetic is determined by  $k_{ET} = k_{ET}^1 + K_{PT}k_{PT}^1$ . The index denotes proton transfer PT and electron transfer ET, respectively. The forward reaction kinetic constant is  $k^1$  and the equilibrium constant is  $K$ . Here the electron transfer term can dominate, thus an electron transfer could be the rate limiting step in a PCET.<sup>97</sup> In the  $\beta$  subunit such a long-range electron transfer could be envisioned based on the current models ( $>16 \text{ \AA}$ ).<sup>22</sup>

### 2.4.1 Electron Transfer

The electron transfer is generally described by the Marcus theory<sup>222</sup> as a transfer in the limits of the Born Oppenheimer (BO) approximation. At the transition state the Landau Zener semi-classical integration of the dynamical problem can be taken into account.<sup>223, 224</sup> A time-dependent solution of the Hamiltonian is then analytical possible with a time-dependent perturbation as a linear function of time. A coupling between the diabatic states is fixed and the energy difference is also linearly time dependent. Two main contributions are most frequently discussed the reorganization energy  $\lambda$  and the free Gibbs energy  $\Delta G$  of the reaction.<sup>222</sup> The general form is<sup>222</sup>:

$$k_{ET} = \nu_n \kappa_{el} \exp \left[ -\frac{(\Delta G_R^\circ + \lambda)^2}{4\lambda k_B T} \right] \quad (2-33)$$

Where  $\nu_n$  is an effective nuclear frequency for the motion along the reaction coordinate that allows the transition state to be reached and  $\kappa_{el}$  is the electronic transmission coefficient, given by:

$$\kappa_{el} = \frac{1 - \exp\left(\frac{-\nu_{el}}{2\nu_n}\right)}{1 - \frac{1}{2} \exp\left(\frac{-\nu_{el}}{2\nu_n}\right)} \quad (2-34)$$

with:

$$\nu_{el} = \frac{V_{IF}^2}{\hbar} \sqrt{\frac{\pi}{\lambda k_B T}} \quad (2-35)$$

For the non-adiabatic limit the prefactor of the exponential term reduces to  $\nu_{el}$ , whereas for the adiabatic case  $\nu_n$  is the prefactor (Figure 2-17b). A special case is the Marcus-inverted region, where a decrease of  $\Delta G_R^\circ$  the rate  $k_{ET}$  slows down. This is caused because the dependence of  $k_{ET}$  on  $\Delta G_R^\circ$  is an inverse parabolic function with an optimum for  $\lambda = -\Delta G_R^\circ$ . In Figure 2-17 the relevant parameters are shown by an ET between the initial state I and the final state F. The crossing of potential surfaces is assumed here for small  $V_{IF}$  ( $\ll k_B T$ ) in the non-adiabatic regime. The case of an adiabatic regime is shown in Figure 2-17b.<sup>96</sup>

This equation has been substantiated tremendously in the meantime. And some general aspects are known about electron transfers in biology. In oxidoreductases most electron transfers take place between metal centers, shuttling one or two electrons. The most often found distance limit of pure electron transfer is 14 Å.<sup>99</sup> Due to the short distances even endogenous steps of up to 450 mV can be tolerated.<sup>99</sup> This was shown under the conditions of an ideal Marcus ET ( $\lambda = -\Delta G_R^\circ$ ).<sup>99</sup>

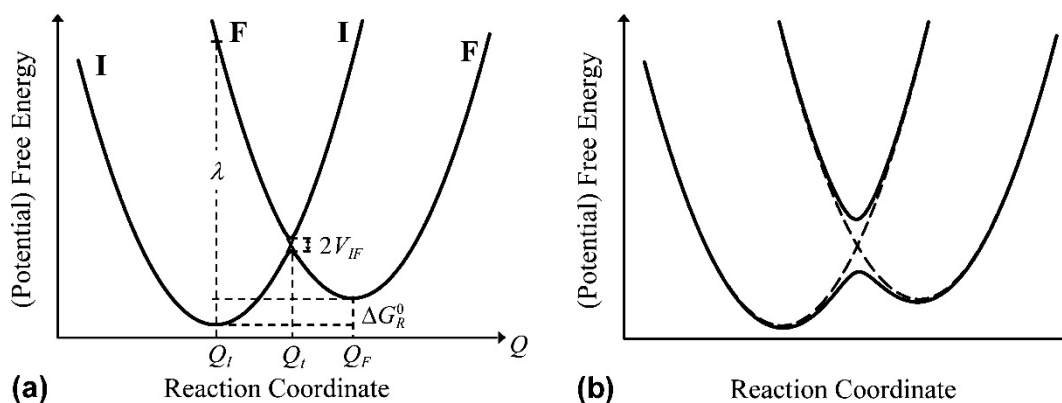


Figure 2-17: Cross section of the free energy surface along a nuclear reaction coordinate  $Q$  for ET. B) Motion on the effective potential surface is assumed to be a simple function of the potential energy (frictionless motion). The initial (I) and the final (F) electronic states are represented by diabatic (localized) parabolas. The equilibrium state of nuclear coordinates is denoted by  $Q_I$  and  $Q_F$ , for initial and final state, respectively. At the lowest energy crossing of the nuclear coordinate the transition state  $Q_t$  is marked. The minimum splitting between the adiabatic states approximately equals  $2V_{IF}$ . The free reaction energy  $\Delta G_R^\circ$  and the reorganization energy  $\lambda$  are marked. The values of  $V_{IF}$  and  $\lambda$  are a function of coupling of the two electronic states. B) Adiabatic level crossing is shown for the case of  $V_{IF} \gg k_B T$ . Here the system evolution proceeds on adiabatic ground states. The figure is from ref. 96.

## 2.4.1.1 Distance Dependence of ET and Development of ET Theory

An electron transfer is distance dependent. This has been studied by artificial photochemical electron transfer reactions.<sup>100</sup> In Figure 2-18 the result is presented. It could be shown that the distance dependence is influenced by the intervening medium. The dielectric packing between donor and effector for instance varies between proteins and water. A distance dependence was proposed on the modeled  $\beta$  parameter. A general Arrhenius type law has been applied with  $k \propto \exp(-\beta(Q_F - Q_I))$ .<sup>100, 225</sup> For proteins, the distance decay parameter  $\beta$  has been found to be between 1.1-1.4  $\text{\AA}^{-1}$ , depending on the secondary structure of the protein.<sup>100</sup>

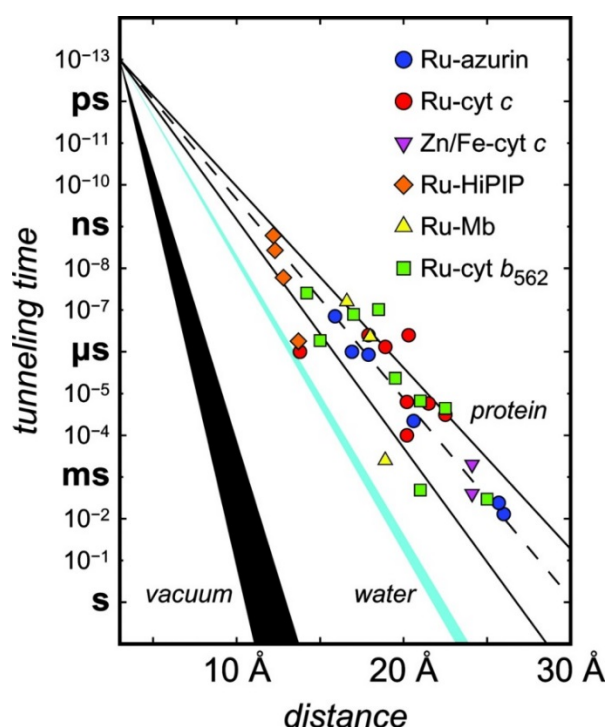


Figure 2-18: Distance dependence between acceptor and donor of an activationless electron tunneling  $\tau_e$ . Several intermediate media and oxidoreductases have been measured. A decay parameter  $\beta$  for proteins is in the range of 1.0  $\text{\AA}^{-1}$  to 1.4  $\text{\AA}^{-1}$ . The solid lines illustrate the tunneling-pathway predictions for coupling along  $\beta$ -strands ( $\beta = 1.0 \text{\AA}^{-1}$ ) and  $\alpha$ -helices ( $\beta = 1.3 \text{\AA}^{-1}$ ); the dashed line illustrates a 1.1- $\text{\AA}^{-1}$   $\beta$ . Distance decay for electron tunneling through glassy water is shown as a cyan wedge. Estimated distance dependence for tunneling through vacuum is shown as the black wedge. Data from ref. 100.

Further development in the theory is ongoing, and meanwhile it has been pointed out that even structured water<sup>226</sup> and small “gaps”<sup>227</sup> along the electron transfer can be tolerated



without a significant loss in catalytic rate. Another recent investigation, considers fast movements and local quantum molecular effects.<sup>228</sup> In this study it could be shown that the energy matching of the bridge to donor and acceptor can be improved by the molecular movement.<sup>228</sup> A transfer path can be sustained unperturbed for electron transfer, if the time of ET is faster than the rearrangement frequency.<sup>228</sup> Here several states are super positioned and can demonstrate a longer range flickering resonance transfer.<sup>229</sup>

## 2.4.2 Expansion to an Electron Coupled Proton Transfer

To consider the coupling of the electron transfer to a proton transfer the larger masses in these quantum transfer processes have to be considered, as done early by Marcus *et al.*<sup>230</sup> The two-dimensional ET coordinate becomes one cross section in the PCET energy landscape. The second proton transfer coordinate  $X$  is the third dimension as illustrated in Figure 2-19 A (p.59). Two coordinates can be seen in the square scheme introduced above (Figure 1-9, p.13). In this case, the proton transfer occurs along coordinate  $X_p$ , whereas the two possible electron transfer steps are along coordinate  $Q_e$ .

For the PCET in  $\alpha$  especially the Soudackov-Hammes-Schiffer (SHS) theory is of interest. SHS has been applied to discriminate between HAT and a CPET.<sup>109, 231</sup> These two similar cases are proposed for di-tyrosine peptides by theorists.<sup>106, 107, 232</sup> They especially discussed in the  $\alpha$  subunit the PCET step between  $Y_{731}$  and  $Y_{730}$ . Therefore, this section will focus on the SHS theory. However, many diverse theories will give rise to a statistically Arrhenius dependence either multiplied or summed with a dynamic prefactor.<sup>97</sup> Nevertheless, they differ in the actual realization as reviewed in recent reviews.<sup>95-97, 233</sup>

The SHS theory is based on a VB description of the four possible steps in the consecutive processes of ET/PT and PT/ET. It uses for the environment a multistate continuum model instead of atomistic models for considering solvent effects. The proton donor-acceptor motion has been incorporated. For this motion linear response theory in combination with Fermi's golden rule formulation were used here. In most of the modern models the vibronic coupling is taken into account by summation of the Boltzmann populations  $P_k$  of the initial state.  $S_{\mu\nu}$  is the overlap of the vibrational wave functions for the  $\mu$  and the  $\nu$  state. This is fully analog to the description of absorbance and fluorescence probabilities by the Frank Condon theory.<sup>234-236</sup> A rate constant for an equilibrated system at each  $X$  value can be obtained from these approximations (Eq. 2-36).<sup>237</sup>

$$k_{PCET} = \int_0^\infty dX \sum_\mu P_\mu(X) \sum_\nu \frac{|V_{IF}^{el} S_{\mu\nu}^p(X)|^2}{\hbar} \sqrt{\frac{\pi}{\lambda_{\mu\nu}(X) k_B T}} \times \exp\left[-\frac{(\Delta G_R^\circ(X) + \lambda_{\mu\nu}(X))^2}{4\lambda_{\mu\nu}(X) k_B T}\right] \quad (2-36)$$

In the high temperature and or low frequency regime, the Eq. (2-36) for the  $X$  mode it is further simplified. Taken an equilibrium position at  $\Delta X = 0$ , the simplest form can be derived as Eq. (2-37).<sup>238, 239</sup>

$$k_{PCET} = \sum_\mu P_\mu \sum_\nu \frac{|V_{IF}^{el} S_{\mu\nu}^p|^2}{\hbar} \sqrt{\frac{\pi}{\lambda_{\mu\nu} k_B T}} \times \exp\left(\frac{2\alpha_{\mu\nu}^2 k_B T}{M_p \omega_p}\right) \exp\left[-\frac{(\Delta G_R^\circ + \lambda_{\mu\nu})^2}{4\lambda_{\mu\nu} k_B T}\right] \quad (2-37)$$

Here the exponential decay is dependent indirectly on  $X$ .  $M_p$  and  $\omega_p$  are the  $X$ -mode effective mass and frequency, respectively.  $\alpha_{\mu\nu}$  is the decay parameter of the vibrational overlap.  $S_{\mu\nu}^p$  is here the vibronic overlap in the equilibrium state ( $\Delta X = 0$ ).

The model of Dogonadze, Kuznetsov and Levich has not only separated the electron from the proton movement (BO approximation), but also considered a second case where the proton movement is adiabatic to the solvent (frequency =  $\omega_0^S$ ). To illustrate possible relative effects the following magnitudes were given:  $\omega_0^S \approx 10^{11}$  Hz  $\ll \omega_n \approx 10^{14}$  Hz  $\ll \omega_e \approx 10^{15}$  Hz. Here  $\omega_n$  describes the frequency of the bound reactive proton (I and F state) and  $\omega_e$  the electron frequency bound to the proton acceptor in an ionic PT step.

Both hydrogen atom transfer (HAT) and concerted proton coupled electron transfer (CPET) are usually vibronically non-adiabatic due to the small proton wave function overlap that produces vibronic couplings  $\ll k_B T$ .<sup>109</sup> Many biological PCETs are electronically non-adiabatic. For CPET reactions within these non-adiabatic reactions, the Eq. (2-37) is valid.<sup>240</sup>

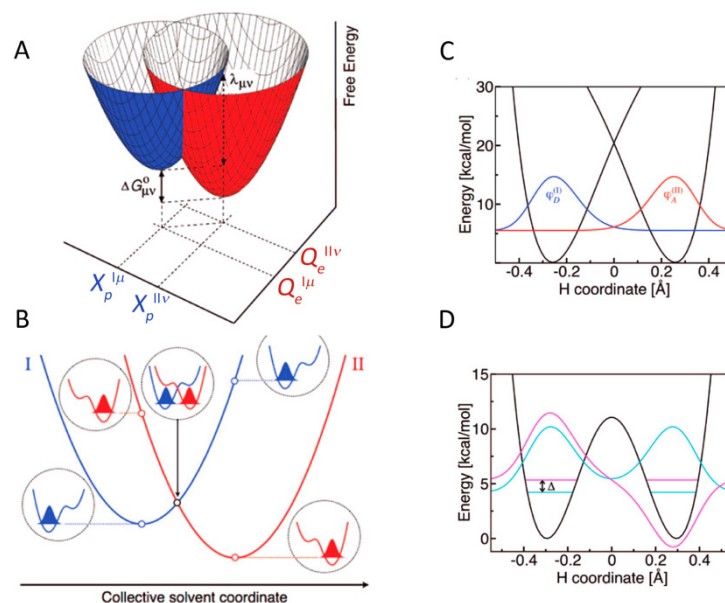


Figure 2-19: Extension from ET to a PCET A) The extension to a second coordinate  $X$  renders the ET to a two dimensional diabatic electron proton free energy surface connecting the vibronic states  $\mu$  and  $\nu$  as functions of two collective solvent coordinates. One coordinate is strictly related to ET ( $Q_e$ ) and the other associated with PT ( $X_p$ ). The equilibrium coordinates, the reaction free energy  $\Delta G_R^\circ$  and reorganization energy  $\lambda_{\mu\nu}$  are indicated similarly to Figure 2-17. Adapted from ref 241. B) Free energy along the reaction coordinate represented by the dashed line in the nuclear coordinate plane of panel A. Qualitative potential energy surfaces (PESs) and pertinent ground state proton vibrational functions are shown in correspondence to the reactant minimum, transition state and product minimum. ref. 242 C) Vibrational mode overlap in the diabatic PESs for the initial and final ET states and vibrational function: initial  $\psi_D^{(I)}$  (blue) and final state  $\psi_D^{(II)}$  (red). Small  $V_{IF}^{el}$  case is depicted. D) Large electronic coupling  $V_{IF}^{el}$  in an adiabatic ground PES. For an adiabatic system the vibronic coupling is half of the splitting between the energies of the symmetric (cyan) and antisymmetric (magenta) vibrational states of the proton. The excited vibrational state of the antisymmetric state is shifted up by 0.8 kcal/mol for a better visualization. Adapted from ref. 109.

#### 2.4.2.1 CPET versus HAT

The comparison between HAT and CPET is difficult. Already the definitions are essential, whereas the HAT and the CPET is known to account for a single site and a multisite acceptor, respectively. This definition is fragile. Quantum effects hamper the knowledge of an exact position at a given time, thus superposition of different acceptors has to be treated.<sup>242, 243</sup> Thus, especially in the transition between a tyrosine radical stacked to a tyrosine, the electron acceptor orbital is not exactly defined.<sup>106, 107</sup>

A more vigorous definition follows from the nature of the transferred particle. For an HAT an electron neutral particle is transferred, leading to minimal reorganization energies. Thus, the electron is moving stringent to the adiabatic Born Oppenheimer approximation concomitant with the proton. In the CPET case a non-adiabatic transfer is present. By the comparison of a benzyl/toluene and a phenyl/phenoxy system it was revealed that the first case is an HAT and the later a CPET.<sup>244</sup> A strong difference between the proton transfer  $\tau_p$  and the electron transfer speed  $\tau_e$  could be shown in the two cases. The ratio between  $\tau_p$  and  $\tau_e$  is the adiabaticity degree parameter  $p$ . Thus  $p \ll 1$  are PCET reactions and  $p \gg 1$  are HAT reactions. The transfer in the phenoxy/phenol couple occurred over a  $\pi$ -complex (proton donor-acceptor distance: 2.4 Å) with electrons 80 times faster than the proton movement.

In the benzyl/phenol case a  $\sigma$  complex (proton donor-acceptor distance: 2.72 Å) was formed here the proton movement was calculated to be 3.5 times faster than the electron, thus the electron can respond instantaneously to the proton motion. Further analysis revealed that the electronic coupling  $V_{IF}^{el}$  is significantly different with 700  $\text{cm}^{-1}$  to 14300  $\text{cm}^{-1}$  (CASSCF calculations) between cases Figure 2-20 A and B, respectively. Figure 2-20 demonstrates the effect and clearly illustrates the differences between both cases. In general, the adiabaticity of a PCET reaction can be taken as a good indicator to discriminate PCET and HAT.<sup>109</sup>

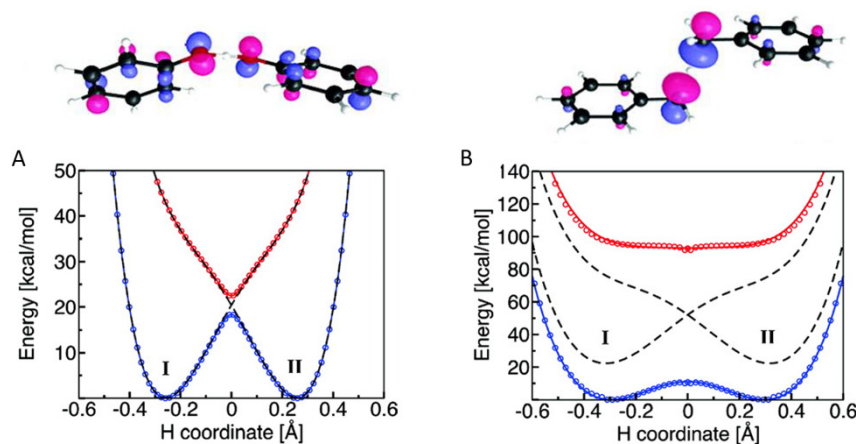


Figure 2-20: Adiabatic potential along the transferring hydrogen coordinate. Two cases the phenoxy/phenol (A) and the benzyl/toluene (B) system are shown. The ground state is depicted in blue dots and the excited state in red dots. The black dashed lines represent the initial I and the final state II. The mixing of these states with the electronic coupling  $V_{IF}^{el}$  leads to the adiabatic ground and excited states as shown by the calculation (red and blue dots). In case A, the adiabatic and diadiabatic states are virtually identical due to the small electronic coupling. Picture modified from ref. 109.

#### 2.4.2.2 CPET between a di-Tyrosine Model

The interaction between two backbone connected Y groups has been also studied in the biological context for  $Y_{730}$  and  $Y_{731}$  in  $\alpha$  by Kalia and Hummer.<sup>106</sup> They could show that in the “ $\pi$ -stacked” arrangement in contrast to the linear geometry of Figure 2-20A, the ground state potential decreases and the electronic coupling increases. Nevertheless, they came to the conclusion that a PCET takes place between this geometry. Water participation is possible but the energy barrier increases for water molecule mediated PCET from 8.5 to 14.1 kcal/mol. Notably, their model revealed that by exchanging the Y with a  $\text{NO}_2\text{Y}$  (cf. Figure 1-6, p.10) with a higher redox potential, this bias favors water mediated PCET. In this thesis, we will also apply bias on the natural di-tyrosine, by the introduction of a 3-amino tyrosine. The change from vacuum to water in a conductor like screening model increased the barrier by up to  $\approx 4$  kcal/mol.

Over all, this also demonstrates the necessity for high level calculations. In general, it highlights that QM and MM calculations are important to understand the basics and common principles of PCET reactions.

### 2.4.3 Water Participation in ET and PCET

From initial studies of electron transfers in water it was estimated, that water is a slow ET media (cf. Figure 2-18). This in general has been shown to be an incomplete statement.<sup>226</sup> Several studies working with a structural water environment have shown that here the ET kinetic rates are comparable up to 2 intervening water molecules to protein media.<sup>245-248</sup> And for distances up to 12 Å, the kinetic effect of structured water was still detectable, compared to the rates of unstructured water shown in Figure 2-18 (p.56). It seems that electrostatic and van der Waals effects can reduce pathways, which interfere destructively with the donor acceptor electron transfer.<sup>226</sup> This triggered further investigations on how transfers are possible in fast changing mobile media. The delocalization of protons can be also advantageous for PCET transfers.<sup>249</sup> However, as shown by studies on flickering resonance (up to 15 Å), the limit is the kinetic rate.<sup>228</sup> As long as the kinetic rate is faster than the reorganization of ET pathways the transfer stays feasible. This does in part set an upper limit on distance and on the barrier height. The investigations for water participation in PCET have just started, by for instance pH dependent proof of principle investigations.<sup>250-252</sup>

## 3 MATERIALS AND METHODS

### 3.1 Materials

D<sub>2</sub>O (99.8% isotopically enriched) and <sup>25</sup>MgO (95.75% isotopically enriched) was purchased from Euriso-Top. Glycerol-D<sub>3</sub>, di-sodium ethylenediaminetetraacetic acid (EDTA), tris(hydroxymethyl)aminomethane (TRIS) was purchased from Cambridge Isotope Laboratories, Fluka, and J.T.Baker, respectively. 4-(2-Hydroxyethyl)-1-piperazineethanesulfonic acid (Hepes), adenosine-5'-triphosphate (ATP), cytidine-5'-diphosphate (CDP), Sephadex® G-25, 2-methylbutan, hydrochloric acid solution (molecular biology grade, 36.5-38%) and sodium hydroxide were purchased from Sigma-Aldrich. Amicon® Ultra concentration device (30 kDa filter) was bought from Merck KGaA, whereas Glycerol and Magnesiumsulfate was used from Roth. Polyacrylamid Gels (PAGE, 7.5%, Tris-HCl) were bought from Biorad.

The following buffers were used:

- i. A buffer consists of TRIS (50 mM), EDTA (1 mM) and glycerol (5% v/v) adjusted to pH 7.6
- ii. Assay buffer consists of HEPES, MgSO<sub>4</sub> (15 mM), EDTA (1 mM) adjusted to pH 8.0
- iii. Desalt buffer consists of TRIS (30 mM) and glycerol (5% v/v) adjusted to pH 7.6

The following EPR tubes were used:

- i. 263 GHz: Vitrocom CV2033S/Q (Ø 0.33 mm)
- ii. W band: Bruker E600-213/ST9O (Ø 0.9/0.5 mm) and Wilmad glass quartz tubes (Ø 0.9/0.5 mm); Bruker
- iii. QBand: Bruker quartz tubes ER221TUB-Q-10 (Ø 1.6/1.1 mm).

### 3.2 Sample Preparation

$\alpha$ -NH<sub>2</sub>Y<sub>730</sub>,  $\alpha$ -NH<sub>2</sub>Y<sub>731</sub> and  $\beta$ -NH<sub>2</sub>Y<sub>356</sub> were prepared and purified as previously described,<sup>44, 67</sup> beside the absence of DTT in the final Sephadex column.<sup>253</sup> These preparations were performed by T. Argirević from our group and for  $\beta$ -NH<sub>2</sub>Y<sub>356</sub> by E. Minnihan from the Stubbe lab at the MIT. For  $\alpha$ -NH<sub>2</sub>Y<sub>731</sub> the truncated form was removed by an additional anion exchange column (MonoQ, equilibrated in  $\alpha$ -buffer) against a NaCl gradient (2.5-400 mM) over 50 mL. This step was performed with the help of Florian Brodhun in the Feussner lab (Georg August University, Göttingen). All NH<sub>2</sub>Y mutated subunits were mixed in equimolar ratios with their corresponding wt (prereduced  $\alpha/\beta$ ) and spin concentrated to 100-200  $\mu$ M ( $\alpha_2\beta_2$ ) in D<sub>2</sub>O (>99 %) and H<sub>2</sub>O assay buffer.<sup>134</sup> The concentration was checked by UV-vis spectroscopy on tyrosine and tryptophan absorption bands  $\epsilon_{280\text{ nm}} \cong 320 \text{ mM}^{-1}\text{ cm}^{-1}$  ( $\alpha_2^{44} \cong 189 \text{ mM}^{-1}\text{ cm}^{-1}$  +  $\beta_2^{69} \cong 131 \text{ mM}^{-1}\text{ cm}^{-1}$ ). The samples were stored in 0.5 mL Eppendorf tubes per 10  $\mu$ L aliquots in liquid N<sub>2</sub>. The double mutant samples were directly obtained as a 1:1 complex by Wankyu Lee from the Stubbe lab at MIT.<sup>254</sup>

$\beta$ -2,3,5-F<sub>3</sub>Y<sub>122</sub>• mixed with  $\alpha$ -wt or  $\alpha$ -Y<sub>731</sub>F was prepared by Kanchana Ravichandran from the Stubbe lab at the MIT, as described previously.<sup>120</sup> The samples in D<sub>2</sub>O (>99 %) and H<sub>2</sub>O assay buffer were stored in 100  $\mu$ L aliquots at 80K. pBAD-*nrdB*<sub>122TAG</sub> and pBAD-*FnYRS-E3* were co-transformed into *E. coli* TOP10 chemically competent cells and grown at 37°C on LB-agar plates containing 100  $\mu$ g/mL ampicillin (Amp) and 35  $\mu$ g/mL chloramphenicol (Cm). A starter culture (2 mL) supplemented with the antibiotics was inoculated with a single colony and grown until saturation (37°C, 12 h). This starter culture was diluted 100-fold into fresh 2X YT media containing Amp and Cm. After 16 h, the cultures were diluted 100-fold into 4 x 2 L of 2X YT with antibiotics and 0.7 mM 2,3,5-F<sub>3</sub>Y (500 mM stock solution in water, NH<sub>4</sub>OH solubilized). At an OD<sub>600</sub> of 0.5, 100  $\mu$ M o-phenanthroline (100 mM stock solution in 0.1 M HCl) was added to chelate iron. 30 min



later, 0.05% (w/v) L-arabinose (10% w/v stock solution in water) was added to induce the F<sub>n</sub>YRS and NrdB. Growth was continued for an additional 5 h and the cells were harvested by centrifugation (3500 x g, 15 min).

Apo  $\beta_2$ -Y<sub>122</sub>(2,3,5-)F<sub>3</sub>Y was purified using anion-exchange chromatography as previously described.<sup>255</sup> Typical yields of 10-15 mg pure protein/g cell paste were obtained.

*Reconstitution of Apo  $\beta_2$ -Y<sub>122</sub>(2,3,5-)F<sub>3</sub>Y.* Apo  $\beta_2$ -Y<sub>122</sub>(2,3,5-)F<sub>3</sub>Y was deoxygenated and taken into an anaerobic chamber maintained at 4°C. 5 equiv. of Fe<sup>II</sup>(NH<sub>4</sub>)<sub>2</sub>(SO<sub>4</sub>)<sub>2</sub> was incubated with the protein for 15 min. The sample was brought out of the chamber sealed, and O<sub>2</sub> in the form of O<sub>2</sub>-saturated 50 mM hepes pH 7.6, 5% glycerol was added to reconstitute the cluster. 250  $\mu$ L of  $\beta_2$ -Y<sub>122</sub>(2,3,5-)F<sub>3</sub>Y was frozen in an EPR tube immediately after reconstitution to quantitate radical content. Typical yields of 0.6-1.0 2,3,5-F<sub>3</sub>Y<sub>122</sub><sup>•</sup>/ $\beta_2$  were obtained for the reconstituted protein.

<sup>25</sup>Mg<sup>2+</sup>-samples were prepared by first washing the protein in 5 concentration (to 20% v/v) dilution steps with desalt buffer and buffer exchanged the sample with a <sup>25</sup>MgCl<sub>2</sub> (15 mM) assay buffer with additional 5 steps. The <sup>25</sup>MgCl<sub>2</sub> was obtained quantitatively by dissolving <sup>25</sup>MgO (12.3 mg, 30 mM) in concentrated hydrochloric acid solution (98.4  $\mu$ L, 120 mM) in test tube overnight, similarly as described previously.<sup>256</sup> Milli-Q® water was added and the HCl was allowed to evaporate in a desiccator and afterwards the product was dried under high vacuum. ESI-MS of the product dissolved in Methanol showed mass shift of 1 m/z compared to MgCl<sub>2</sub> in natural abundance. 4% of <sup>24</sup>Mg(II) could be observed.

EPR samples were prepared by thawing each aliquot at 4°C and followed equilibration at 25°C for 10 min. The reaction was initiated by adding CDP and ATP in H<sub>2</sub>O/D<sub>2</sub>O assay buffer with final concentration 2 and 6 mM, into the reaction mixture (1  $\mu$ L 263 GHz, 2.5  $\mu$ L W band and 6  $\mu$ L Q band) with final complex concentrations of 90-100  $\mu$ M. Each reaction was allowed to proceed for 10-20 s and manually freeze quenched inside an EPR tube with liquid N<sub>2</sub>. For Q-band PELDOR samples glycerol-D<sub>3</sub> (20 % v/v) was added after 10-20 s, and then the reaction was frozen in ice cold 2-propanol ( $\approx$ 185 K). The quench times were varied based on the individual kinetic rates of the different samples as measured by UV-vis stopped flow<sup>44, 67, 254</sup> or Rapid Freeze Quench.<sup>28</sup> This should ensure a maximum radical yield.

### 3.3 X/Q-Band Spectroscopy

Q-Band spectra were obtained by a Bruker Elexsys E 580 spectrometer with a nominal output power of 3 W. The ESE traces and PELDOR traces were recorded in a Bruker (EN5107D2) cavity. The cooling of the cavity was achieved within a liquid Helium continuous flow cryostat (CF95550, Oxford Instruments). PELDOR<sup>257</sup> ( $\pi_{MW1}/2-\tau_1-\pi_{MW1}-[\tau_1+x]-\pi_{MW2}-[\tau_2-x]-\pi_{MW1}-\tau_1$ -echo) spectroscopy is a constant time 4 pulse experiment. PELDOR uses pulses at a pump (MW2) and detect microwave (MW1) frequency and was carried out by measuring the dipolar evolution over the time  $x$  in steps of 8 ns. Experimental details are given in the figure captions.

X-Band measurements were performed on a Bruker Elexsys E500 spectrometer, with a HighQ CW-resonator (4122SHQE, Bruker) in an ESR900 (Oxford Instruments) cryostat.

### 3.4 W-Band Spectroscopy

The EPR and ENDOR spectra were recorded on an Elexsys® E680 with 400 mW output power and typical  $\pi/2$  pulse length of 16 ns at 70 K. The cooling was performed under continuous Helium flow in Oxford Instruments cryostat. A pulsed ENDOR probehead (1021H, Bruker) was used as a resonator.

Mims-ENDOR<sup>183</sup> ( $\pi/2-\tau-\pi/2$ -RF- $\pi/2-\tau$ -echo) spectroscopy was carried out with a 40  $\mu$ s RF pulse amplified by a 250 W RF amplifier (250A250A, Amplifier Research). All obtained ENDOR spectra were normalized to compare with simulations.

### 3.5 263 GHz Spectroscopy and Calibration

The spectra were recorded on a prototypical Elexsys® E780 from Bruker Biospin. The 263 GHz spectrometer works with a quasi optical front end. The front end produces a Gaussian beam that is focused to a corrugated waveguide. The typical output power of the bridge was 15 mW. The corrugated waveguide is coupled to a single mode (TE<sub>011</sub>) cylindrical cavity (E9501610) with a typical quality factor ( $Q$ ) of 500-1000. The electron spin echo ( $\pi/2-\tau-\pi-\tau$ -echo, ESE) was recorded with a typical microwave field strength  $B_1$  of 10-17 MHz. The ESE spectra were recorded by 70 K, if not stated otherwise. The individual  $B_1$  is measured via the pulse length necessary for inversion of the magnetization ( $\pi_p$ ) by a nutation recorded by an inversion recovery experiment ( $\pi_{ip}-T-\pi/2-\tau-\pi-\tau$ -echo) scanning

over the pulse length of  $\pi_{tp}$ . A standard coal sample is used. The microwave field strength can be obtained by the turning angle  $\mathcal{G}$  of each pulse length  $t_p$  by Eq. (3-1).

$$\mathcal{G} = \sqrt{S(S+1) - m_s(m_s+1)} \frac{g\beta_e B_1}{\hbar} t_p \quad (3-1)$$

Freeze quench samples in 0.33 mm EPR tubes were inserted under liquid nitrogen into the resonator surrounded by liquid nitrogen and then transferred into the precooled (80 K) EPR cryostat (Oxford Instruments).

To assess the accuracy of the  $g$  values several error contributions have to be considered. As reported for other high frequency spectrometer<sup>258</sup> the frequency change over a measurement is not a significant source of error. The spectrometer has a sweep coil with 250 mT range and the main magnet operating until 12 T. If the main magnetic field is changed a systematic change of all  $g$  values has to be considered. Therefore, a reliable calibration of the field is necessary. Field calibration was originally performed based on a multiline Mn(II) standard sample, by Bruker. Normally, the Mn(II) (0.02% in MgO) has been used with a  $g$  value of 2.001015(5) and the HF coupling  $A = -243.9$  (1) MHz.<sup>259,260</sup> The Mn(II) in marble used by Bruker and Jeol has different values with  $g = 2.0011$  and  $A = -241.6$  MHz.<sup>261,262</sup> With this standard sample a single field point can be calibrated and the linearity of the sweep coil sweep is evaluated by the 6 lines of the <sup>55</sup>Mn hyperfine interaction within the Kramers doublet. The non-linearity originates mainly from the self-inductance of the sweep coil, and the mutual inductance of the sweep and main magnet coil.<sup>258</sup> To compensate this non-linear behavior of the ratio between gauss to amp, Bruker implemented a linearization protocol for magnetic field sweeps in CW-EPR spectra. In this protocol the typically small measurement range for organic radicals (20-50 mT) is always measured by a full sweep range of the sweep coil. Here the curve difference to a linear behavior can be approximated by a second order fit (cf. Figure 3-2). Hence, the sweep coil has to be driven through the full (250 mT) sweep range. This extends the measurement time by a factor of 5 to 13 depending on the sweep range. To be able to omit this large drawback, the impact on the spectral accuracy of this linearization option was evaluated. For this reason, the CW-EPR spectra of the manganese standard sample in increasing field direction were measured with and without the linearization procedure. After aligning the first line (Figure 3-1 inset left) the shift was measured on each line position. Thus, the scan over the six lines performed with the linearization procedure is about 4.4 G narrower than one without linearization. This gives an estimate of the systematic error introduced by removing

the linearization procedure and reducing the measurement time. The additional error for a typical field sweep of 30 mT is 0.36 mT based on a fit of the data (Figure 3-2). Compared to the typical field of 9350 mT, this error is  $3.9 \cdot 10^{-5}$  mT. Due to the  $g$  factor of approximately two (for organic radicals in this thesis), a systematic error of  $8 \cdot 10^{-5}$  is obtained. The overall systematic shift in the ampere to gauss ratio has to be re-adjusted from time to time, to align with the standard values with the setting. However, the standard sample used here could be only observed by CW-EPR with a sharp line width of  $\approx 0.12$  mT. Therefore, another sample was necessary in order to test the pulsed set up.

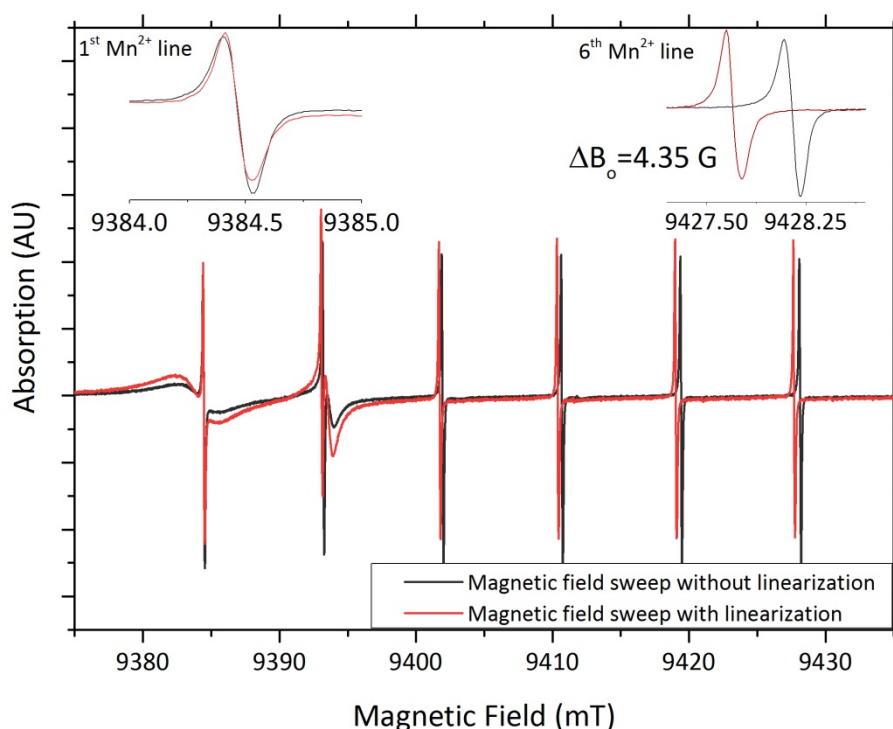


Figure 3-1: Comparison of CW 263-GHz EPR spectra of  $\text{Mn}^{2+}$  (in  $\text{CaO}$ , 0.02%) at room temperature with and without linearization. Exp. details: Field sweep range = 100 mT; modulation amplitude = 0.5 G; conversion time=100 ms; single scan.

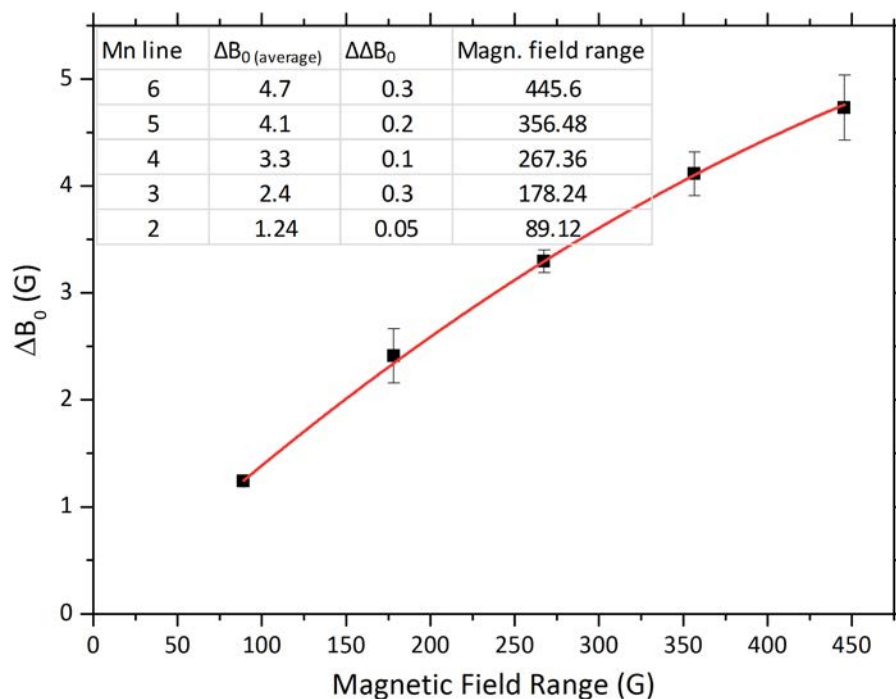


Figure 3-2: Linearization improvement compared in CW 263 GHz EPR measurements. The difference in magnetic field between the linearized and the non-linearized field sweep as  $\Delta B_0$  is plotted against the width of the  $Mn^{2+}$  resonance lines. The points can be fitted with a second order polynomial (red line) with:  $y=0.148(1)\cdot x - 9.2(4)\cdot 10^{-6}\cdot x^2$  and  $R^2=0.99994$ .

To test the field accuracy in the pulsed mode the  $\beta_2$ - $Y_{122}\bullet$  *E. coli* RNR sample was used, which is well characterized at high-field EPR. An advantage of taking the  $Y_{122}\bullet$  as a standard is that it can be used as an internal standard for the RNR samples studied. This internal standard is detectable at 10 K and is hidden at elevated temperatures (70 K).<sup>55, 148, 152</sup> The derivative has to be formed to assign the principle axis values of  $g_x$ ,  $g_y$  and  $g_z$  in the  $\mathbf{g}$  tensor broadened line. The spectrum of  $Y_{122}\bullet$  has been recorded at 10 K. The spectrum was then compared to high-field powder<sup>157</sup> and crystal data<sup>63</sup> of  $Y_{122}\bullet$ . Högbom *et al.* have used as a calibration standard a narrow single line Li:F  $g$ -standard (Li in LiF,  $g = 2.002293 \pm 0.000002$ <sup>263</sup>) measured at two different frequencies.<sup>63</sup> Gerfen *et al.* used multiline Mn(II) (0.02% in MgO)<sup>264</sup> with a  $g$  value of 2.001015(5) and the HF coupling  $A = -244.1(1)$  MHz.<sup>157, 259, 260</sup> The  $Y_{122}\bullet$  spectrum measured at our instrument was compared to a simulation based on these two literature values, as shown in Figure 3-3. The simulation parameters reported by Gerfen (gray) *et al.* show an agreement with the spectrum in terms of  $g$  values and deviate from those reported by Högbom *et al.* (green) at  $g_z$  and  $g_y$  by  $2\cdot 10^{-5}$  and  $6\cdot 10^{-5}$ , respectively. In both experiments an error of  $4\cdot 10^{-5}$  or  $5\cdot 10^{-5}$  was estimated.<sup>63, 84</sup>

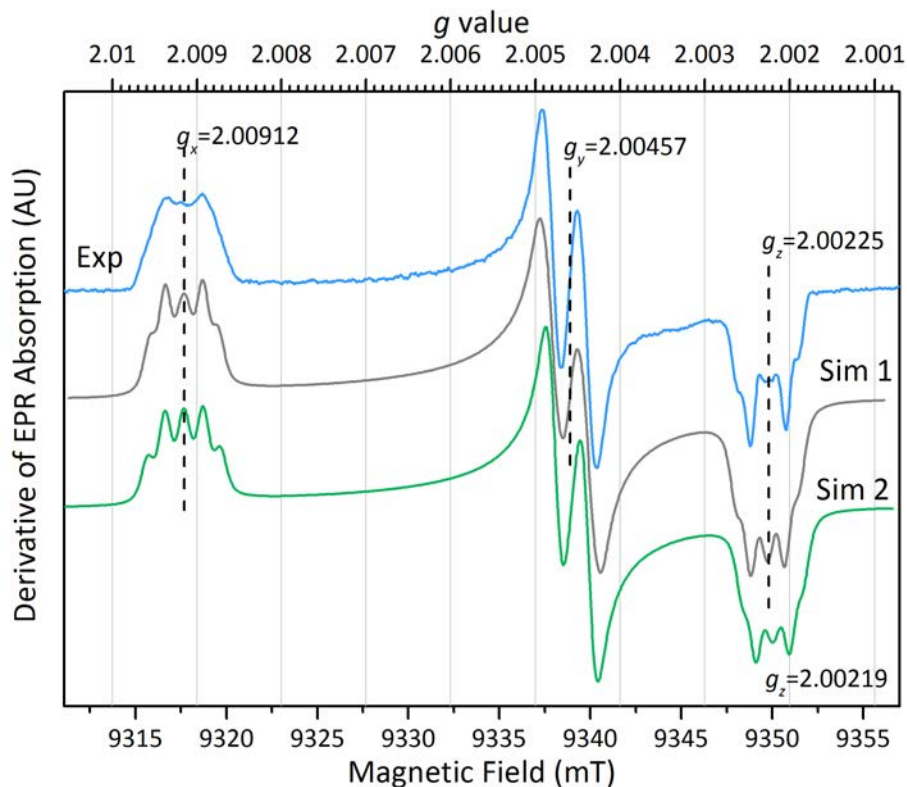


Figure 3-3: Pulsed-EPR spectrum of the  $\beta_2\text{-Y}_{122}\bullet$  as calibration standard. The experimental trace is shown in blue and the simulation gray and green with values from 157 and 63, respectively. Exp. details: ESE, 262.0109 GHz,  $T=10$  K,  $\pi(\pi/2)=52(90)$  ns,  $\tau=319$  ns, shots per point (SPP)=50, shot repetition time (SRT)=15 ms, scans = 43. The derivative was built by a Savitzky-Golay filter (second order, 3 points).

Another calibration with a  $\text{N@C}_{60}$  sample<sup>265</sup> (from A. Schneggs lab at the Helmholtz Zentrum, Berlin) was performed recently by I. Tkach in our group. He found a standard deviation within 8 resonance frequencies averaged over three line measurements to be in  $g$   $3.3 \cdot 10^{-6}$ . By reducing the sweep range from 60 mT by a factor of 10 a systematic shift of  $-1.5 \cdot 10^{-5}$  could be observed, based on 3 observing frequencies and 12 measured resonances. The change of other parameters by a factor of ten, like a tenfold increase in sweep time gave no significant shifts. All of these errors are far below the errors reported within this thesis and are therefore neglected in the future discussion. Based on the measurements, the systematic error with or without linearization procedure in CW and pulsed EPR spectroscopy can be estimated. The error estimated by the differences observed here is below  $5 \cdot 10^{-5}$  in  $g$  scale. For experiments where field linearization has not been used a

systematic error of  $9 \cdot 10^{-5}$  is estimated. However, due to low signal to noise ratios (S/N) and broad line widths, the g value uncertainty can vary in an individual spectrum.

## 3.6 Density Functional Theory Calculations

### 3.6.1 Set-up of the Models

DFT calculations have been performed with the ORCA 3.0.0 program package<sup>214</sup>. DFT calculations were originally performed by Christoph Riplinger (ORCA 2.9.0) from the Neese group and had been performed as previously reported.<sup>110</sup> The geometry-optimized large models are based on the crystal structure (wt- $\alpha$ , PDB ID 4R1R) and had shown by energy-optimized relaxed surface scans, along the reaction coordinate, energy barriers in agreement or lower than previously reported values with smaller models by DFT theorists.<sup>106,107,266</sup> To compare these models to experimental findings, Simone Kossmann from the Neese group incorporated the amino group at Y<sub>731</sub>• and re-optimized the geometry. The EPR parameters were calculated by Simone Kossmann. The adaptation into magnetic resonance convention and the interpretation of the output was done by me. Small model calculations have been performed to test different environment dependencies of the structurally ill-defined region.

### 3.6.2 Geometry Optimizations

#### 3.6.2.1 Large Models 1, 2 and 3

Initially, the coordinates of the large models **7** and **8** used in ref<sup>110</sup> augmented by the amino group in the 3 position of Y<sub>731</sub> and a water molecule between Y<sub>731</sub> and Y<sub>730</sub> for Model 3. These coordinates were first geometry optimized without further restraints. During the optimization the distance between C<sub>439</sub> and Y<sub>730</sub> increased constantly. It was supposed this results from the missing contact to the  $\beta$  subunit in the model, thus the coordinates were restrained for all C <sub>$\alpha$</sub>  and for all C <sub>$\beta$</sub> . For Y<sub>730</sub>, NH<sub>2</sub>Y<sub>731</sub> and C<sub>439</sub> only the C <sub>$\alpha$</sub>  were restrained. Additionally the Cartesian coordinates of the hydrogen atoms in the truncated GPD model replacing the bonds between C<sub>4</sub> and C<sub>5</sub> of the ribose as well as the bond between C<sub>1</sub> of the ribose and the base were kept fixed.

The model structures were geometry optimized using a generalized gradient density functional the unrestricted BP86<sup>267,268</sup> in combination with Ahlrich's diffuse TZVP basis set

of triple- $\zeta$  quality<sup>207, 269</sup>. Grimme's dispersion correction<sup>200, 270</sup> has been now added on top of the SCF calculation. The Resolution of the Identity (RI) approximation with the corresponding auxiliary basis sets (def2-TZVP(P)/JK<sup>150</sup>) has been employed throughout.

### 3.6.2.2 Small Models

In the small models the geometry optimization was performed on the B3LYP<sup>268, 271, 272</sup> hybrid density functional in combination with the TZVPP basis set and def2-TZVPP/JK auxiliary basis set. In the models adapted from the large models only the dihedral angle of the peptide bond of Y<sub>730</sub> and Y<sub>731</sub> was fixed and the Cartesian restraints for all surrounding C $\alpha$ 's were kept. In order to compensate the electrostatics from the environment here a solvation model (COSMO<sup>273</sup>) with polarity of ethanol ( $\epsilon=24$ ) was used. Otherwise Grimme's dispersion correction<sup>199-201</sup> and RIJCOSX<sup>274</sup> approximations has been employed. The energy has been converged to  $10^{-9}$  E<sub>h</sub>, if not stated otherwise.

### 3.6.3 EPR Calculations

The EPR calculations were carried out with the B3LYP<sup>268, 271, 272</sup> hybrid density functional in combination with the RIJCOSX<sup>274</sup> approximation. In the small models COSMO was retained for the single point calculations. Here Barone's EPR-II (IGLO-II for sulfur) basis set of double- $\zeta$  quality has been used in combination with the def2-TZVPP/JK auxiliary basis set for all atoms.<sup>219, 220, 275</sup> The  $g$  values were calculated<sup>210</sup> using the tyrosine (analog) C<sub>4</sub> as gauge origin. In single amino acid models the def2-TZVPP basis set was held consistent with the geometry optimization step.<sup>207</sup> The dihedral scans were performed with a geometry optimization for each restrained dihedral. The energy has been converged to  $10^{-9}$  E<sub>h</sub>.



## 4 3-AMINO TYROSINE RADICAL INTERMEDIATES

To compare Ys in terms of electronic and molecular structure in enzymatic reactions like the radical propagation of E.coli RNR small differences in electronic and molecular structure have to be resolved. The multi-frequency characterization of radicals is commonly used to disentangle magnetic field dependent (for instance  $g$  values) and independent parameters (for instance HFC's).<sup>276</sup> The spectral width of the EPR spectrum influenced by the  $\mathbf{g}$  tensor and the coupling strength of the nuclei in the surrounding are the factors governing the choice of a suitable frequency (cf. §2.2). Compared to Ys ( $g_x$ - $g_z$ : 4.3-6.9 ppt) our amino tyrosine have generally a smaller spectral width ( $g_x$ - $g_z$ : 3 ppt) and were until now characterized by 9 to 180 GHz spectroscopy.<sup>92</sup> Nevertheless, not all values were determined to a high precision (<0.2 ppt) and the question of possible underlying radicals remained open.

In order to extend the applicability of this radical probe and to answer open questions in the radical process of RNR, 263 GHz EPR spectroscopy was employed. The results will be first presented beginning with the last step of the forward radical process. Here previous EPR data had shown that  $\text{NH}_2\text{Y}_{730}\bullet$  hosts a well-defined H bond network (cf. §1.5.3, p.21).<sup>92, 110,</sup>

<sup>134</sup> A part of this chapter has already been published.<sup>254</sup>

## 4.1 Electrostatic Environment of 3-Amino Tyrosines in the $\alpha$ Subunit

### 4.1.1 263 GHz Spectra of $\text{NH}_2\text{Y}_{730}\bullet$

The higher  $g$  value resolution for  $\text{NH}_2\text{Y}_{730}\bullet$  should determine accurately resolved  $g$  values. Transient radicals were generated by adding to wild type  $\beta_2$  and  $\alpha_2\text{-NH}_2\text{Y}_{730}$  an excess of substrate (CDP) and the corresponding effector (ATP). The reaction proceeded 30 s, until the reaction was quenched in liquid  $\text{N}_2$ . To suppress line broadening from weak intermolecular  $^1\text{H}$ -couplings the protein samples were buffer exchanged with  $\text{D}_2\text{O}$  before the reaction. A  $^2\text{H}$  from a  $\text{D}_2\text{O}$  buffer has the advantage to provide a 6.5 ( $\nu\text{-}^1\text{H}/\nu\text{-}^2\text{H}$ ) times weaker hyperfine (HF) interaction, scaling linearly with its gyromagnetic value (cf. §2.1.3, p.33). The half-site reactivity of this homodimer corresponds to the optimal yield, as reported to be around 50% based on all observed radical. The remaining contribution is the stable  $\text{Y}_{122}\bullet$ . The relaxation times of  $\text{Y}_{122}\bullet$  are rather short because of the proximal diiron cofactor (4.6 Å,  $\text{Y-O:Fe}_1$ ).<sup>55</sup> Full suppression of the signal of  $\text{Y}_{122}\bullet$  is accomplished even by recording the spectra at 70 K with short interpulse delays (200 ns).<sup>55, 148, 152</sup> In this delay time the phase memory time ( $1/T_m$ ) influences the decay of the signal by three contributions: (i) spin-spin relaxation ( $1/T_2'$ ), (ii) lifetime broadening ( $1/(2T_1)$ ) and (iii) spin-lattice relaxation of spins in the vicinity ( $1/T_1^{(B)}$ ), i.e., iron spin states.<sup>172, p. 214</sup> This relaxation filter will be applied in all  $\geq 70$  K experiments throughout this thesis to separate pathway radical contributions (i. e.  $\alpha\text{-NH}_2\text{Y}_{730}\bullet$ ,  $\alpha\text{-NH}_2\text{Y}_{731}$  and  $\beta\text{-NH}_2\text{Y}_{356}$ ) from the  $\text{Y}_{122}\bullet$  signal (Figure 3-3). An absorptive electron spin echo (ESE) spectrum of pathway radicals is shown in Figure 4-1. The absorptive line (green) displays a rhombic  $g$  tensor. A better resolution of the different orientations of the molecules along the magnetic field ( $B_0 \parallel g_x, g_y, g_z$ ) is observed when the derivative (black) is formed.

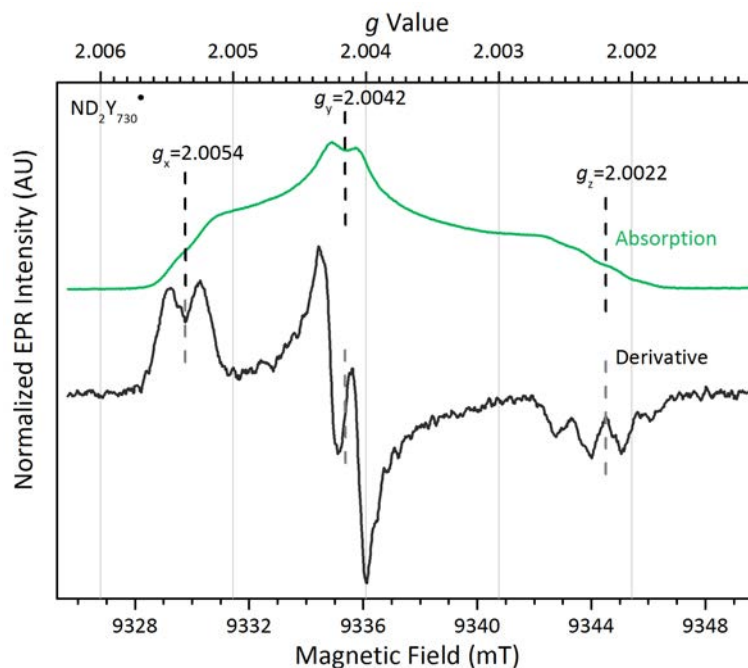


Figure 4-1: 263-GHz echo detected spectrum of  $Y_{730}NH_2^\bullet$ , quenched after 30s reaction time. Green shows the absorption spectrum and black the enlarged derivative (obtained by a 5 points second order Savitzky-Golay filter). Exp. details: ESE,  $\pi(\pi/2)=60(120)$  ns,  $\tau=300$  ns, shot repetition time (SRT)= 3 ms, shots per point (SPP)=50, 140 scans. Not linearized field sweep, difference to linearize in this case 0.00001 at  $g_y$  (cf. Figure 4-3, Methods §3.5, p.66).

The spectral features contributing to the rhombic spectrum are clearly depicted in the first derivative (blue, Figure 4-1). The spectrum displays the three canonical orientations  $g_x$ ,  $g_y$  and  $g_z \parallel B_0$ , marked as black dashed lines. The line shape around for  $B_0 \parallel g_x$  shows a broadened doublet peak, the  $g_y$  displays also a doublet and  $g_z$  a quartet (doublet of triplet, 1:2:2:1). The  $g$  values directly observed from this line shape are 2.0054 2.0042 and 2.0022. The difference to the multi-frequency EPR study reported before for  $g_x$  is subtle (0.2 ppt) but significant, compared to the error of 50 ppm (Methods §3.5). The major nearly isotropic splitting (29.8 MHz), consistent with the previous reports, is due to a  $\beta$ -methylene  $^1H$  HF coupling from hyperconjugated methyl protons (see Figure 4-2).<sup>110</sup> The quartet arises from the overlay of this doublet and the triplet of the anisotropic  $^{14}N$  hyperfine interaction. An additional observation is the tiny doublet splitting observed on top of the quartet. It is a contribution not resolved along other canonical orientations and is 9-10 MHz in size at  $g_z$  (Figure 4-3, inset). Generally HF tensors from protons bound to an aromatic ring have a slightly rhombic tensor shape, with ( $A_1 < A_2 \leq A_3$ ) the smallest value is along the bond direction and the largest along the  $\pi$  orbitals of the aromatic ring (see §2.2.5).<sup>277</sup> Due to spin



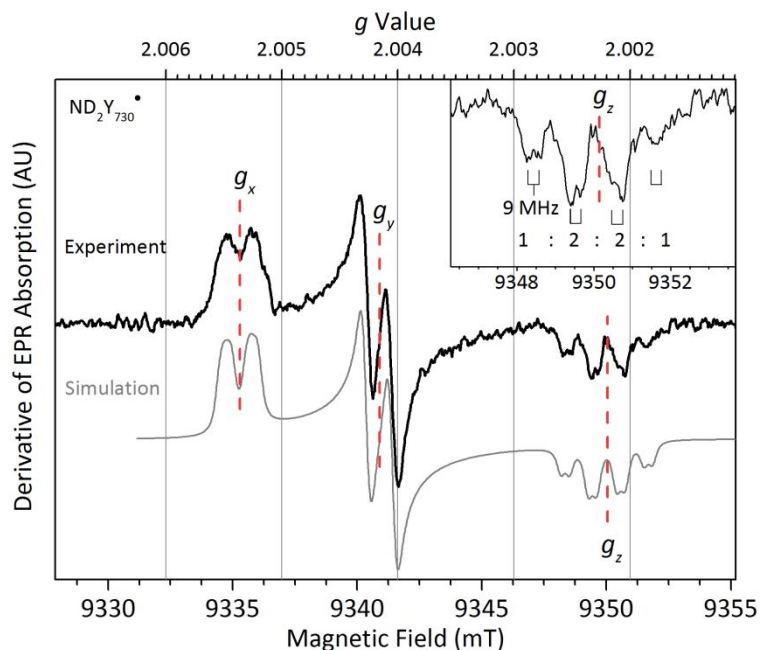


Figure 4-3: 263-GHz echo detected spectrum of  $\text{Y}_{730}\text{ND}_2\bullet$ , quenched after 38 s reaction time, and simulation. Black shows the derivative and gray line the simulation. The inset shows the coupling pattern at  $g_z$  enlarged. A quartet coupling pattern ( $\sim 30$  MHz) of 1:2:2:1 ratio and on top a doublet (9 MHz) are visible. The simulation was performed with the parameters of Table 4-1 and a line broadening of 1 G was used. Exp. details: ESE,  $\pi(\pi/2)=130(64)$  ns,  $\tau=277$  ns, SRT=6 ms, SPP=500, 8 scans. The derivative was obtained by a 5 points second order Savitzky-Golay filter.

#### 4.1.2 263 GHz Spectra of $\text{NH}_2\text{Y}_{731}\bullet$

The large resolution of the  $\mathbf{g}$  tensor for organic radicals offers also the possibility to search for conformers and different hydrogen bond environments.<sup>55, 110, 144, 278</sup> Particularly at  $\text{NH}_2\text{Y}_{731}\bullet$  two conformations were found in X-ray crystal diffraction structures (XRD, cf. Figure 1-12B<sup>67</sup>), and preliminary work of T. Argirević showed time-dependent changes in the EPR spectra.<sup>92</sup> However, measured PELDOR spectra only showed a narrow Gaussian distance distribution, which was found to be consistent with a defined conformation in a direct  $\pi$  stacking geometry.<sup>43, 67</sup> Initially, different time points were measured within the second to minutes time scale at W-band (Appendix Figure A - 2, p.193). The results were inconclusive, due to contributions supposed to arise from an insufficient separation of residual  $\text{Y}_{122}\bullet$ ,  $\text{Mn}^{2+}$  lines and glass signals.

At 263 GHz unprecedented resolution could be obtained in Figure 4-4. The spectrum of  $\text{NH}_2\text{Y}_{731}\bullet$  is displayed in blue. The reaction conditions were kept unchanged and the

reaction mixture was frozen at 18 s in liquid N<sub>2</sub>. The spectrum shows clearly separated maxima of  $g_x=2.00511(5)$ , the second zero-crossing at  $g_y= 2.00399(5)$  and the last local minimum at  $g_z=2.0022$ . The first minimum resembles a triplet from two overlapping HF contributions in a 2:1 ratio. This and the doublet at  $g_y$  as well as the quartet at  $g_z$  were expected from previous 94 GHz spectra.<sup>92</sup> The  $\beta$ -methylene HF coupling is here the isotropic contribution with ( $a_{iso}=22$  MHz). The anisotropic coupling with a larger value at  $g_x$  and  $g_z$  has a typical tensor form of a ring proton coupling, with small HF coupling contributions along  $g_y$ . It is tentatively assigned to a ring proton at C<sub>6</sub> position (see §4.4). Notably, the spectral feature marked with an asterisk (\*) at  $g_z$  was overlapping with the  $g_z$  line shape at W-band. At 263 GHz this contribution is resolved from the canonical orientation of  $B_0 \parallel g_z$  (Eq. (2-11), Theory §2.1.2). Due to the smaller C <sub>$\beta$</sub> -H with  $a_{iso}=22$  MHz smaller couplings can contribute to the line shape, which were not considered in the simulation. For instance a ring proton coupling becomes visible compared to NH<sub>2</sub>Y<sub>730</sub>• (Table 4-1). The structural consequences of the assignment will be discussed in more detail together with the DFT models (§4.4 p.98). The  $g$  values shifted by 0.1-0.2 ppt with respect to  $g$  values previously reported. Notably, also the  $g_y$  value shifted by 0.1 ppt, though this is within error of the 94 GHz data (0.1 ppt). All other values remained unchanged within the error of previous studies.<sup>92</sup>

The spectra in protonated and deuterated buffer gave comparable  $g$  values (Figure 4-5). It is worth noting that a difference in quench time of 1:52 min between both samples also does not affect the  $g$  values, which is in agreement with the 94 GHz data (see Appendix Figure A - 2, p.193). In order to simulate the spectral line shape in protonated NH<sub>2</sub>Y<sub>731</sub>• only the line broadening caused by the amino deuterons had to be taken into account. The simulation parameters for the <sup>1</sup>H amino protons were taken from orientation selective <sup>2</sup>H ENDOR spectra and scaled by their gyromagnetic ratio (cf. Table 4-6 p.104).<sup>92</sup>

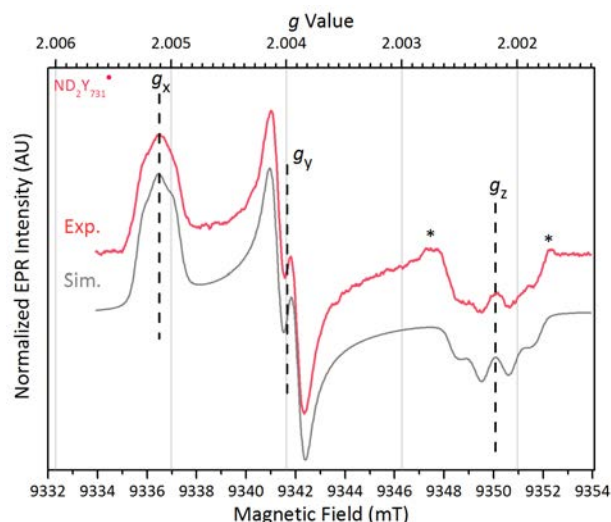


Figure 4-4: 263-GHz ESE spectrum  $\text{ND}_2\text{Y}_{731}\bullet$  recorded for a sample quenched after 18 s reaction time. The red line shows the experimental derivative of the absorption spectrum (obtained by 8 points second order Savitzky-Golay smooth) and the gray line the simulation. For simulation the parameters in Table 4-1 were used and an isotopic line broadening of 2.8 G. Exp. details: ESE,  $\pi/2=70$  ns,  $\tau=270$  ns, SRT= 6 ms, SPP=100, 74 scans.

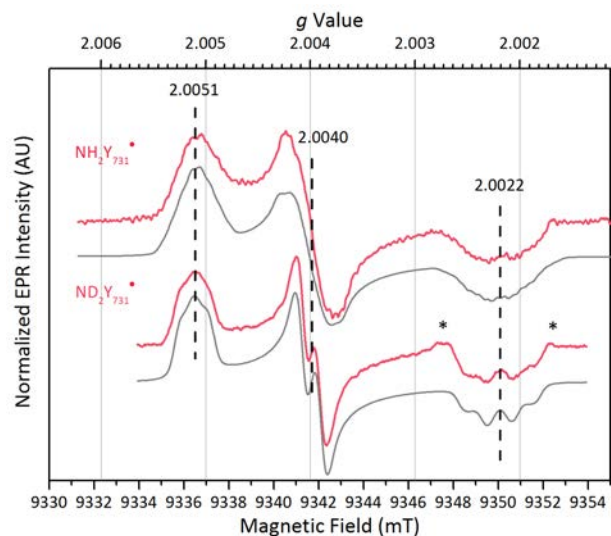


Figure 4-5: 263-GHz ESE spectrum obtained from  $\text{ND}_2\text{Y}_{731}\bullet$  and  $\text{NH}_2\text{Y}_{731}\bullet$  with a reaction time of 18 s and 2 min, respectively. The red line shows the derivative of the absorption spectrum (obtained by 7 points second order Savitzky-Golay smooth) and gray line the simulation. For simulation the parameters in Table 4-1 were used and an isotopic line broadening of 2.8 G. Exp. details: ESE,  $\pi/2(\pi)=48(94)$  ns,  $\tau=180$  ns, SRT= 2 ms, SPP=500, 200 scans. Parameter for  $\text{ND}_2\text{Y}_{731}\bullet$  see Figure 4-4.

Table 4-1: Parameters of the simulation for 263-GHz and 94-GHz EPR spectra for  $\text{NH}_2\text{Y}_{731}\bullet$  and  $\text{NH}_2\text{Y}_{730}\bullet$ .<sup>a</sup>

$g$	$g_x$	$g_y$	$g_z$	$A$ [MHz]	$A_x$	$A_y$	$A_z$
$\text{NH}_2\text{Y}_{730}\bullet$	2.0054	2.0042	2.0022	$A(\text{C}_\beta\text{-H}_1)$	30.8	29	28.0
	2.0052**			$A(\text{C}_\beta\text{-H}_2)$	10	5	9
$\text{NH}_2\text{Y}_{731}\bullet$	2.0051	2.0040	2.0022	$A(\text{C}_\beta\text{-H}_1)$	23	22	22
				$A(\text{C}_6\text{-H})$	13	5	10

a) The  $^{14}\text{N}$  hyperfine tensor of the  $\text{NH}_2\text{Y}\bullet$  was not varied in the simulations and kept  $A_x = 2.4$  MHz,  $A_y = 1.6$ -5 MHz,  $A_z = 30.7$  MHz.<sup>134</sup> Uncertainty in  $g$  values is about 0.05 ppt.

### 4.1.3 Comparing Simulation Parameters from 263 GHz EPR and 94 GHz EPR Spectra

In order to find a unique parameter set the parameters from the 263 GHz simulation and the 94 GHz spectra have to fit to the same parameter set. Therefore, the spectra reported earlier by T. Argirević were simulated again with the new parameters (Table 4-1).<sup>92</sup> The spectra and the simulation are still in agreement with each other as shown in Figure 4-6. The spectrum in Figure 4-6 of  $\text{NH}_2\text{Y}_{730}\bullet$  shows an agreement of the simulation based on the modified  $g$  values from the 263 GHz measurements. For the transient radical formed at the  $\alpha$  interface,  $\text{NH}_2\text{Y}_{371}\bullet$ , two regions indicate differences to the simulation as marked with an asterisk (\*). The low field asterisk marks a deviation due to the sharp  $g_y$  feature (cf. Figure 3-3) of residual  $\text{Y}_{122}\bullet$  and the lower field asterisk shows the resonance frequency of glass peaks observed due to quartz defects in the sample tubes. The impurity of  $\text{Y}_{122}\bullet$  was estimated based on the  $g_x$  feature height to be around 5%.

The consistent set of  $g$  values for  $\text{NH}_2\text{Y}_{730}\bullet$  and  $\text{NH}_2\text{Y}_{731}\bullet$  at 94 and 263 GHz is particularly interesting in its  $g_x$  value. The observed  $g_x$  value shift of 1 ppt is substantial compared to the value of a free  $\text{NH}_2\text{Y}\bullet$ .<sup>110</sup> The narrow line broadening and the high reproducibility up to the minute time scale of the spectra is indicative of a well-defined microenvironment and electrostatic environment. The increase in line broadening from 1 G to 2.5 G at  $\text{ND}_2\text{Y}_{731}\bullet$  can arise from a distribution of  $g$  values due to flexibilities at this position. Since H bonds are expected as predominant effects on  $g_x$  values, a possible correlation of the relative intensity and strength of HF couplings was examined.<sup>144</sup>

---

\*\* Value obtained by Argirević (PhD Thesis, Georg-August University Göttingen, 2012) based on 94 GHz simulations.



Additionally, also 180 GHz data has been discussed by T. Argirević.<sup>92</sup> A new alignment of the data could show consistency (data not shown) with the obtained  $g$  values at 263 GHz. 180 GHz were recorded in protonated buffer. This prevents a highly accurate  $g$  value determination, which has been observed before in other HF EPR studies in protonated buffer.<sup>84,160</sup>

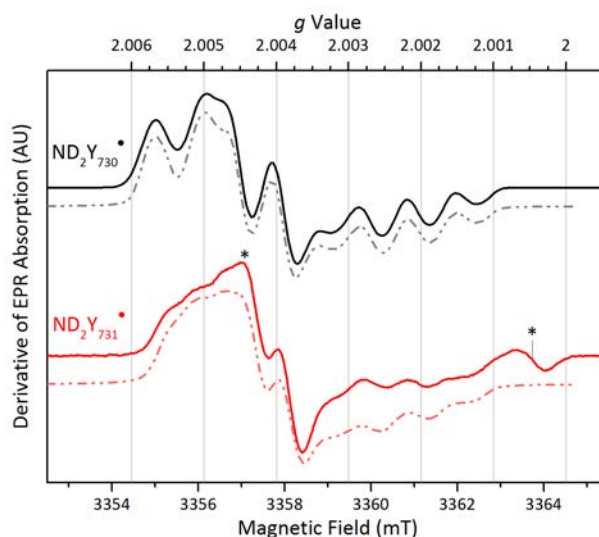


Figure 4-6: 94-GHz EPR spectra (-) and their simulations (---) of  $\text{ND}_2\text{Y}_s$  intermediates in  $\alpha$ . Simulation parameters are in Table 4-1. A line width of 1 G and 2.5 G was used for  $\text{NH}_2\text{Y}_{730}\bullet$  and  $\text{ND}_2\text{Y}_{731}\bullet$ , respectively. Exp. details ( $\text{NH}_2\text{Y}_{730}\bullet$  /  $\text{NH}_2\text{Y}_{731}\bullet$ ): ESE,  $T=70$  K,  $\pi/2 = 32/16$  ns,  $\tau = 260$  ns, SRT = 6/3 ms, SPP = 50, 700 / 50 scans.

## 4.2 ENDOR Spectroscopy of $\text{NH}_2\text{Y}_{731}\bullet$ Compared to $\text{NH}_2\text{Y}_{730}\bullet$ in the $\alpha$ Subunit

### 4.2.1 ENDOR on $\text{NH}_2\text{Y}_{731}\bullet$

After the EPR spectrum has identified  $\text{NH}_2\text{Y}_{731}\bullet$  as a single species within the available resolution, it is important to understand the H bond network present at this position. As just shown in the last part, the  $g_x$  value is 0.3 ppt lower as compared to  $\text{NH}_2\text{Y}_{730}$  indicating a higher polarity. In proteins, this polarity is nearly exclusively associated with H bonding.<sup>143,144</sup> Exchangeable protons are observed as deuteron (D) nuclei ( $^2\text{H}$ ) in Mims ENDOR spectra. To disentangle the contributions of different hyperfine couplings the spectrum was measured in a deuterated buffer. In  $\text{D}_2\text{O}$  the spectral contributions in  $^2\text{H}$  ENDOR are reduced to the large amino deuteron couplings (up to  $\pm 2.3$  MHz), the very weak couplings

from the central line (matrix line region up to  $\pm 0.3\text{MHz}$ ) and H bond range in between absolute values of 0.4-0.8 MHz (cf. §2.2.2 p.39). The  $\text{ND}_2\text{Y}_{731}\bullet$  ENDOR spectrum was recorded at  $B_0 \parallel g_y$  in Figure 4-7B, and has a similar shape as already observed for  $\text{ND}_2\text{Y}_{730}\bullet$ .<sup>110</sup> By comparing the  $^2\text{H}$  ENDOR spectra in Figure 4-7 it becomes evident that the sharp feature has a larger resonance position increasing from  $\pm 0.62\text{ MHz}$  for  $\text{NH}_2\text{Y}_{730}\bullet$  to  $\pm 0.78\text{ MHz}$  for  $\text{NH}_2\text{Y}_{731}\bullet$ . The splitting of the lines of this resonance position arises from an additional small coupling, i.e., the quadrupolar coupling, which is larger for  $\text{ND}_2\text{Y}_{731}\bullet$  than observed for  $\text{ND}_2\text{Y}_{730}\bullet$ . Previously, two weak H bonds ( $\approx 1.8\text{ \AA}$ ) to  $\text{ND}_2\text{Y}_{731}\bullet$  had been simulated to account for the line shape, as in the  $\text{ND}_2\text{Y}_{730}\bullet$  ENDOR case.<sup>92</sup> The necessity of both contributions for the sharp feature was spectroscopically not mandatory. Hence, another simulation approach was performed using a single stronger H bond with a larger quadrupole coupling instead of a second H bond. It is worth noting that the simulation is in agreement with the orientation selective data in Figure 4-8 and with the field dependent spectra simulated before (see Figure 4-4). The simulation parameters are collected in Table 4-6 (p. 104). The simulation has a reasonable fit, pointing out that  $\text{NH}_2\text{Y}_{731}\bullet$  has a larger HF coupling contribution with a scalar ( $a_{\text{iso}}$ ) contribution (see Figure 2-12 p. 46). This large  $a_{\text{iso}}$  (i.e.,  $2 \cdot a_{\text{iso}} = T_{\perp}$ ) originates from interaction with the  $p_z$  SOMO (Theory §2.1.3). However, this does not lead to an assignment. For the assignment more precise angle dependence and control studies will be performed in the following sections.

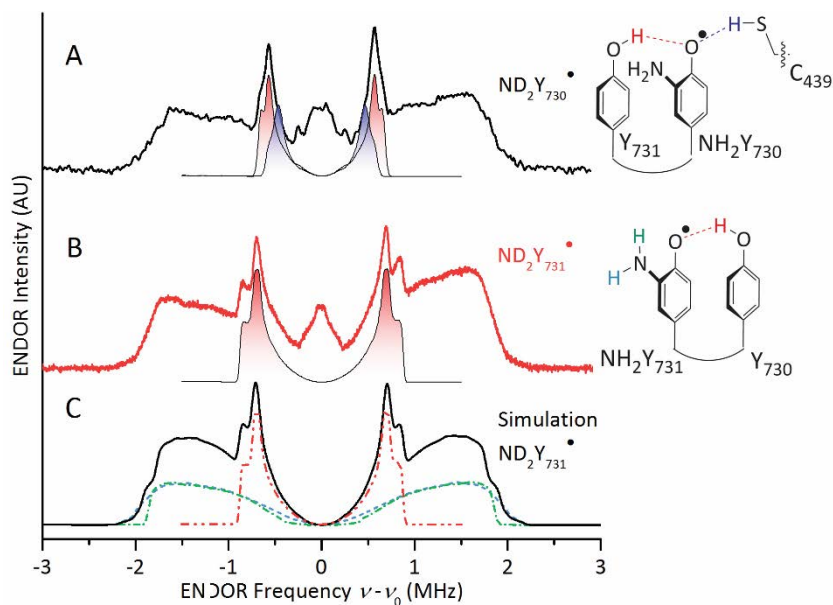


Figure 4-7: 94-GHz  $^2\text{H}$  Mims ENDOR spectra at  $B_0 \parallel g_y$  of trapped  $\text{NH}_2\text{Ys}\bullet$  intermediates in  $\alpha$ . A) Spectrum of  $\text{ND}_2\text{Y}_{730}\bullet$  at 10 K taken from Argirević *et al.*<sup>92,110</sup> The H bond pake patterns assigned to an H bond from  $\text{Y}_{730}$  (red gradient) and  $\text{C}_{439}$  (blue gradient) are highlighted below.<sup>254</sup> B)  $\text{ND}_2\text{Y}_{731}\bullet$  ENDOR spectrum obtained at 70 K. The red gradient highlights the H bond resonance contribution (assignment on the right side). Exp. details: Mims ENDOR,  $\pi/2 = 20$  ns,  $\tau = 200$  ns,  $\pi_{\text{RF}} = 40$   $\mu\text{s}$ , SRT = 10 ms, random RF acquisition<sup>279</sup> at 1 SPP, acquisition time = 24 h. Excitation in the EPR line was at  $B_0 \parallel g_y$ . ENDOR spectrum is centered at the Larmor frequency  $\nu_0$  of  $^2\text{H}$ , i.e., 21.9 MHz at a field of 3.3 T. C) Simulation of the  $\text{ND}_2\text{Y}_{731}\bullet$  ENDOR spectrum. Individual contributions are shown in dashed/dotted lines below for the individual assignments of  $\text{ND}^1$  (blue),  $\text{ND}^2$  (green) and  $\text{DO-Y}_{730}$  (red). The simulation is done based on the experimental parameters and parameters in Table 4-2 (p.86) with a line width of 55 kHz including a Mims hole function (Methods §3.4 p.66).<sup>172</sup>

#### 4.2.2 Direction of the H bond Observed at $\text{NH}_2\text{Y}_{731}\bullet$

Evidence for an H bond interaction along the  $p_z$  SOMO can be found by the orientation dependence of the  $^2\text{H}$  ENDOR resonances through the EPR line. Orientation selective measurements were performed at the canonical orientations of  $B_0 \parallel g_{x,y,z}$  as shown in Figure 4-8A. Powder patterns are observed at each orientation, because the ratio between excitation bandwidth (FWHM  $\approx 1.8$  mT) and spectral width of ( $\approx 8$  mT) is large. Still, each orientation shows clear differences in line shape. For  $\text{NH}_2\text{Y}_{730}\bullet$  an HF tensor for a perpendicular H bond in the form of  $|A_z| \geq |A_y| > |A_x|$  (using the definition  $|A_x| < |A_y| < |A_z|$ ) has been reported previously.<sup>110</sup> This nearly axial tensor shape is also observed here. If the magnetic field is aligned along  $g_x$  or  $g_y$ , the large roughly perpendicular  $A_{\perp}$  component at

$\approx \pm 0.7$  MHz is present. The parallel HF component  $A_{\parallel}$  is mainly along  $g_z$  with roughly  $\pm 0.6$  MHz. This already implies, that the isotropic HF has half the size but opposite sign with respect to the parallel component ( $-2|a_{\text{iso}}| \approx |T_{\perp}|$ ; cf. Figure 2-12, p.46). The spectra have different resonances of the H bond HF tensor in the upper and the middle spectrum of Figure 4-8A with  $\pm 0.7$  and  $\pm 0.8$  MHz, thus the HF tensor is slightly rhombic. It has been reported before that an H bond<sup>††</sup>, perpendicular to the tyrosine  $\pi$  plane has its smallest resonance along the H bond direction.<sup>110</sup> Thus the H bond lies roughly along the  $g_z$  molecular direction, consistent with the previous assignment based on the tensor shape. Simulations including the simulation of the EPR spectrum and excitation bandwidth were performed, as illustrated in Figure 4-8B. The simulation demonstrated that the HF tensor must nearly align with the  $\mathbf{g}$  tensor in order to reassemble three different resonances at  $B_0 \parallel g_x g_y g_z$ . Therefore, the angle between HF tensor and the  $\mathbf{g}$  tensor were not allowed to increase to more than  $\approx 20^\circ$ . Otherwise the contributions of the HF tensor were mixed at  $B_0 \parallel g_x g_y g_z$  and the resonances were identical at each observed orientation. A preliminary fit was obtained with H bond dihedral angle (cf. Figure 4-8C) of  $90^\circ$  from the phenol plane. This would be in agreement with the  $\text{C}_3\text{-C}_4\text{-O}_{\text{Y}731}\text{-O}_{\text{Y}730}$  dihedral of  $90^\circ$  found in the wt structure (2X0X).<sup>67</sup> The early simulations were therefore simulating the H bond contributions with collinear principal axes of the HF and  $\mathbf{g}$  tensor. The structural restraints, however, do not fit to such a  $90^\circ$  perpendicular angle nor could they explain the rhombicity of the HF tensor. The interplay between a possible  $\pi$  stacking interaction and the H bond with orbital overlap introduce structural restraints.  $\pi$  Stacking in a di-tyrosine peptide would have an optimized H bond dihedral angle  $50\text{-}60^\circ$ , as has been reported by Siegbahn et al. without considering a protein environment.<sup>107</sup> Here an H bond HF tensor with an angle  $\angle(A_x, g_y)$  equals  $70^\circ$  in Figure 4-8C reproduced the experimental spectrum. This is consistent with an H bond dihedral with the same  $70^\circ$  angle.

The small splitting on top of the resonances at  $\pm 0.6\text{-}0.8$  MHz is assigned to the quadrupole interaction. As a function of the electric field gradient the largest value (defined  $Q_z$ ) of the quadrupole interaction is along the H-X (X= O, N) bond of the H bond donor function. The splitting has its largest contribution (250 kHz) along  $B_0 \parallel g_z$  indicating a nearly collinear quadrupole and HF tensor (i.e.,  $A_z \parallel Q_z$ ). For this type of interaction the direct orbital overlap

---

<sup>††</sup> The H bond at  $\text{NH}_2\text{Y}_{731}\bullet$  has the assigned H bond donor  $\text{Y}_{730}\text{O-H}$ .

with the  $p_z$  orbital does not lead to strong quadrupole contributions. This is in agreement with other H bonds observed in previous work<sup>110</sup> and the DFT work shown in §4.4. An out-of-plane H bond has been mentioned before as a prerequisite of an effective HAT step in  $\pi$  radical as tyrosines.<sup>107</sup> Therefore and due to the proximity of  $Y_{731}$  and  $Y_{730}$  in most crystal structures<sup>22, 120</sup> this interaction is assigned to the proton of  $Y_{730}$ . The analog assignment in  $NH_2Y_{730}^\bullet$  has been made for the moderate perpendicular H bond previously (§1.5.3, p.21). Additional spectroscopic evidence should be obtained by double mutant ENDOR measurements in §4.3.5 p. 95. At first these mutants have to be characterized (§4.3).

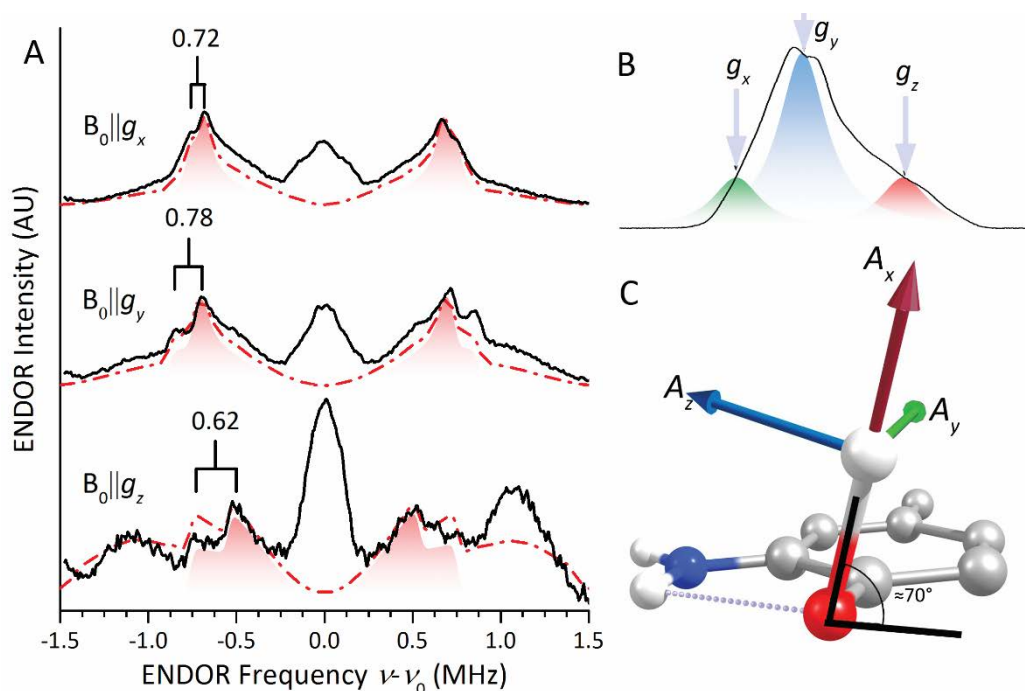


Figure 4-8: Orientation selective  $^2\text{H}$  Mims ENDOR spectrum of  $\text{ND}_2\text{Y}_{731}^\bullet$  in the  $\pm 1.5$  MHz region from T. Argirević<sup>92</sup>. A) Simulations of the spectra (red -) take into account  $\text{ND}_2$  and H bond HF coupling, discussed so far (see Table 4-2). Contributions from the H bond are shown separately as red peaks. Field positions and excitation bandwidth (green, blue and red) for the individual measurements are illustrated in B (cf. Figure 4-6). C) The orientation of the H bond tensor is illustrated in the molecular frame. A line broadening of 50 kHz was used in the simulation. Exp. details:  $T=10$  K,  $\pi/2=20$  ns,  $\tau=320$  ns,  $\pi_{\text{RF}}=40$   $\mu\text{s}$ , SRT = 150 ms, random RF acquisition<sup>279</sup>, acquisition time = 50 h/spectrum.

Table 4-2: Simulation parameters for the  $^2\text{H}$  ENDOR spectra of  $\text{ND}_2\text{Y}_{731}\bullet$ .

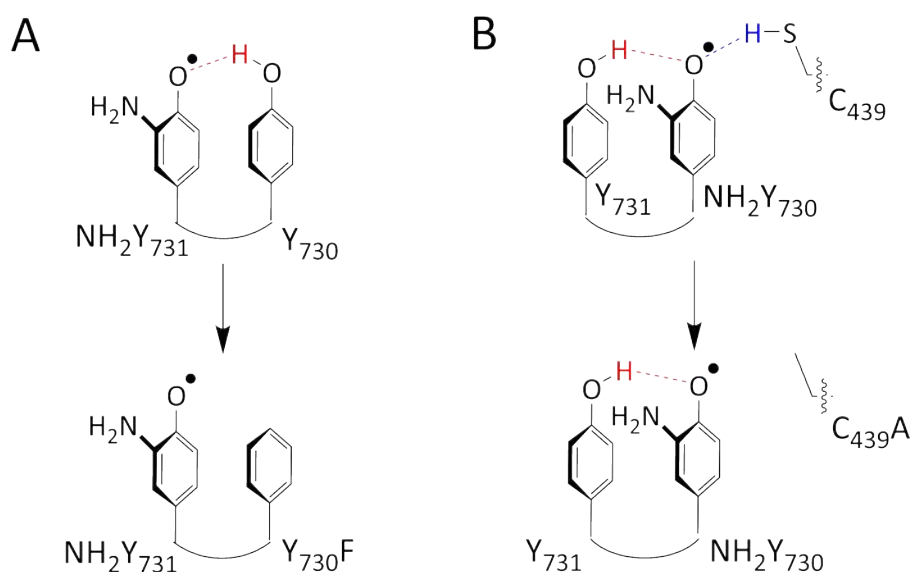
$\text{NH}_2\text{Y}_{731}\bullet$		$A_x$ [MHz]	$A_y$ [MHz]	$A_z$ [MHz]	$\alpha$ [ $^\circ$ ]	$\beta$ [ $^\circ$ ]	$\gamma$ [ $^\circ$ ]	$Q_x$ [MHz]	$Q_y$ [MHz]	$Q_z$ [MHz]
Simulation	$\text{Y}_{730}\text{-OD}$	1.3	-1.43	-1.63	-160 120	110 40	80 85	-0.03	-0.09	0.12
	$\text{ND}_2\text{D}(1)$	-0.6	-2.9	-3.8	-86 -92	98 93	90 -3	-0.04	-0.06	0.11
	$\text{ND}_2\text{D}(2)$	0.06	-3.1	-4.2	-96 -93	93 84	-31 -121	-0.06	-0.08	0.14

The central matrix line has not yet been discussed. Here weak coupled deuterium nuclei are present. In the 10 K spectrum in Figure 4-8 also the HF couplings of  $\text{Y}_{122}\bullet$  contributes to this matrix line.  $\text{Y}_{122}\bullet$  has been shown to be only weakly coupled ( $\pm 0.25$  MHz) to one proton.<sup>152</sup> To separate the effects a measurement was repeated at 70 K as shown in the Appendix Figure A - 4 (p.195). Compared to the previous work from T. Argirević<sup>92</sup>, still no HF coupling pattern was resolved, indicating at least one additional contribution in the line shape which is not present in the resolved central line at  $\text{ND}_2\text{Y}_{730}\bullet$ . However, one can mention that the largest resonance of the matrix line is present at  $B_0 \parallel g_x$  and  $g_y$  with  $\pm 0.2$  MHz and at  $B_0 \parallel g_z$  it is  $\pm 0.15$  MHz. At  $B_0 \parallel g_z$  another feature is visible at about  $\pm 0.1$  MHz. Under the assumption of a purely dipolar HF tensor this would be consistent with a dipolar tensor with diagonal elements of -0.1, -0.1 and 0.2 MHz.<sup>92</sup> However, contrary to the previous interpretation for a moderate perpendicular H bond, in a purely dipolar tensor the parallel tensor component  $T_{\parallel}$  is the largest value and along the H bond direction (cf. Figure 2-12).<sup>92</sup> Thus, an H bond in the  $g_x g_y$  plane would be indicated by the spectra observed. An analogous conclusion applies if the 0.1 MHz splitting resembles a quadrupolar splitting of the perpendicular HF tensor component. Then the H bond donor proton bond is within the ring plane  $\pm 40^\circ$  (H bond dihedral, cf. Figure 4-8C). With a point-dipole approximation (Eq. (2-17), Theory §2.1.3, p. 33) the two cases resemble a distance from the phenoxy oxygen nuclei of 2.9 Å or 2.5 Å, for an observed HF or quadrupole splitting, respectively. An oxygen spin density population of 0.21 was used in Eq. (2-17).<sup>110</sup>

### 4.3 Removal of one H Bond Partner by Double Mutants

#### 4.3.1 The Concept of the Double Mutant Study

In an effort to assign the H bonds donor to  $\alpha_2$ -NH<sub>2</sub>Y<sub>730</sub>• and  $\alpha_2$ -NH<sub>2</sub>Y<sub>731</sub>• double mutants  $\alpha_2$ -NH<sub>2</sub>Y<sub>730</sub>/C<sub>439</sub>A and  $\alpha_2$ -NH<sub>2</sub>Y<sub>731</sub>/Y<sub>730</sub>F were expressed. It has already been shown that the removal of one PCET pathway amino acid renders the protein inactive (§1.4.1.2 p. 7). The 3-amino tyrosines show still residual activity. Therefore it was additionally interesting how the modification of the direct environment would change the individual radical intermediate. We proposed a structured H bond network at NH<sub>2</sub>Y<sub>730</sub>•<sup>110</sup> (§1.5.3, p.21) and NH<sub>2</sub>Y<sub>731</sub>• (§4.2). Therefore the question arose if the absence of our assigned H bonds is detectable. Up to now our assignment was mainly based on proximities observed between the three amino acids Y<sub>731</sub>-Y<sub>730</sub>-C<sub>439</sub> in the inactive and reduced crystal structures. Here we hoped to see effects supporting our current assignment both kinetically and structurally. Scheme 1 explains the mutation strategy. The biochemical work and the SF-vis experiments were performed by Wanky Lee, from the Stubbe lab, at MIT. It is reported here to examine the effect of the local perturbation due to the double mutation.



Scheme 1: Mutation strategy involves removal of an individual H bond for NH<sub>2</sub>Y<sub>731</sub>• (A) and NH<sub>2</sub>Y<sub>730</sub>• (B). The amino acid subsequent in PCET pathway was exchanged by site directed mutagenesis into one without an H bond donor function as phenylalanine and alanine.

### 4.3.2 Kinetic Characterization of $\text{NH}_2\text{Y}_{731}/\text{Y}_{730}\text{F}$ and $\text{NH}_2\text{Y}_{730}/\text{C}_{439}\text{A}$

The radicals formed in the double mutants  $\text{NH}_2\text{Y}_{731}/\text{Y}_{730}\text{F}$  and  $\text{NH}_2\text{Y}_{730}/\text{C}_{439}\text{A}$  were characterized by SF-vis measurements observing the decay of  $\text{Y}_{122}\bullet$  at 410 nm and the formation of  $\text{NH}_2\text{Y}\bullet$  at 320 or 325 nm with wt- $\beta_2$ /CDP/ATP in assay buffer (Figure 4-9). The results are summarized in Table 4-3.

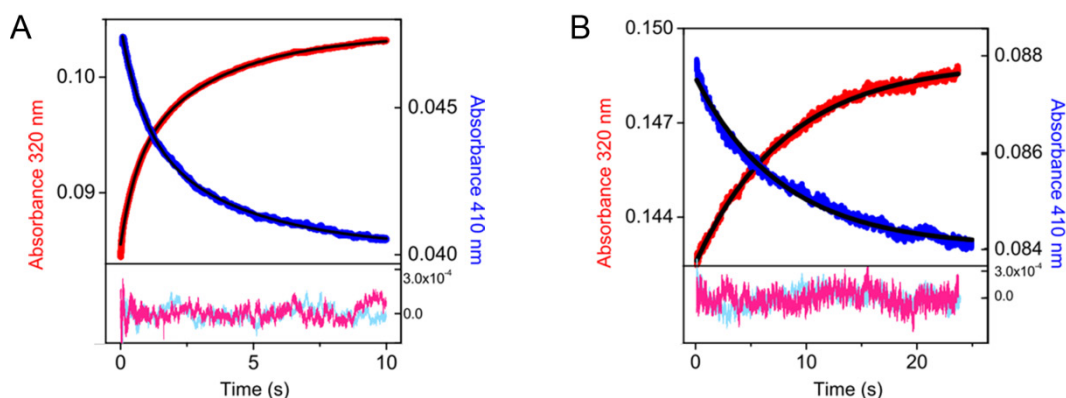


Figure 4-9: Kinetics of  $\text{NH}_2\text{Y}\bullet$  formation in  $\alpha_2\text{-NH}_2\text{Y}_{731}/\text{Y}_{730}\text{F};\beta_2\text{-wt}$  (A) or  $\alpha_2\text{-NH}_2\text{Y}_{730}/\text{C}_{439}\text{A};\beta_2\text{-wt}$  (B) with CDP and ATP by SF Vis spectroscopy. Double exponential fits in A or mono exponential fits in B to the data are shown in black. Residuals for the fit for  $\text{NH}_2\text{Y}\bullet$  formation is in magenta for  $\text{Y}\bullet$  disappearance is in cyan. The results represent the average of 6 to 8 spectra and fits were calculated with OriginPro software to minimize residuals (Table 4-3). This figure is cited from ref. 254.

The yield of  $\text{NH}_2\text{Y}_{731}\bullet/\text{Y}_{730}\text{F}$  with  $34\pm 3\%$  is identical within error to the yield of the corresponding single mutant ( $32\pm 3\%$ ). However, the rate constants are both slower, a factor of 6 is found for the fast rate constant and a factor of about 3 for the slow rate constant.

Table 4-3: Kinetics of  $\text{NH}_2\text{Y}\bullet$  formation for  $\alpha_2$  mutants.

Mutant <sup>a</sup>	$\text{NH}_2\text{Y}\bullet$ formation				
	$k_1$ ( $\text{s}^{-1}$ )	% $\text{A}_1$	$k_2$ ( $\text{s}^{-1}$ )	% $\text{A}_2$	% $\text{NH}_2\text{Y}\bullet$
$\alpha_2\text{-NH}_2\text{Y}_{731}\bullet$	$9.6 \pm 0.6$	$27 \pm 2$	$0.8 \pm 0.1$	$13 \pm 1$	$32 \pm 3$
$\alpha_2\text{-NH}_2\text{Y}_{730}\bullet$	$12 \pm 1$	$20 \pm 2$	$2.4 \pm 0.2$	$19 \pm 2$	$39 \pm 4$
$\alpha_2\text{-NH}_2\text{Y}_{731}/\text{Y}_{730}\text{F}$	$1.5 \pm 0.1$	$14 \pm 2$	$0.3 \pm 0.03$	$20 \pm 1$	$34 \pm 3$
$\alpha_2\text{-NH}_2\text{Y}_{730}/\text{C}_{439}\text{A}$	$0.13 \pm 0.01$	$14 \pm 1$	-	-	$14 \pm 2$

a) Rates were obtained from double exponential fits of 6-8 spectra of SF UV-vis spectra of the reaction with  $5\ \mu\text{M}$   $\alpha_2\text{-NH}_2\text{Y}_{731}$  and  $5\ \mu\text{M}$  wt- $\beta_2$  with CDP/ATP ( $1\ \text{mM}/3\ \text{mM}$ ) in assay buffer. The rate constants for  $\text{NH}_2\text{Y}_{730}$  and  $\text{NH}_2\text{Y}_{731}\text{-}\alpha_2$  have been reported previously.<sup>280</sup>

The  $\text{NH}_2\text{Y}_{730}\bullet/\text{C}_{439}\text{A}$  shows a reduction in overall yield by a factor of two and the rate constant of  $\text{NH}_2\text{Y}_{731}\bullet/\text{Y}_{730}\text{F}$  is 10-fold diminished. Here only one rate constant was sufficient



to fit the kinetic data. The effect of C<sub>439</sub>A mutation is quite large in terms of radical build up. This implies an effect on the PCET efficiency. Therefore another mutation was tested. Unfortunately  $\alpha_2$ -NH<sub>2</sub>Y<sub>730</sub>/C<sub>439</sub>S could not be successfully expressed.

### 4.3.3 Structural Comparison of NH<sub>2</sub>Y<sub>731</sub>•/Y<sub>730</sub>F and NH<sub>2</sub>Y<sub>730</sub>•/C<sub>439</sub>A with Their Single Mutants

In order to exclude larger structural rearrangements in the  $\alpha_2/\beta_2$  complex of either NH<sub>2</sub>Y<sub>731</sub>• or NH<sub>2</sub>Y<sub>730</sub>•, the diagonal distance to Y<sub>122</sub>• was measured for both double mutants.<sup>43</sup> After the PCET reaction 3-amino tyrosine radical and the stable Y<sub>122</sub>• are located in diagonally opposite monomers of  $\alpha$  and  $\beta$  (Figure 1-8, p. 12). Distances between radicals pairs can be measured at X (9 GHz) and Q-band (34 GHz) by pulsed electron double resonance (PELDOR/DEER) spectroscopy.<sup>257</sup> The reaction of the  $\alpha_2\beta_2$  complex (final concentration: 130  $\mu$ M) was performed with the same substrate and effector mixture, additional glycerol was added at 20 s and 25 s, for NH<sub>2</sub>Y<sub>731</sub>/Y<sub>730</sub>F and NH<sub>2</sub>Y<sub>730</sub>/C<sub>439</sub>A, respectively. Glycerol is not only a versatile cryoprotectant, but it prolongs  $T_2$  relaxation as well as deuterium exchange.<sup>281</sup> For PELDOR spectroscopy long  $T_2$  relaxation times in the order of several  $\mu$ s are required. The reaction was quenched at 40 s (NH<sub>2</sub>Y<sub>731</sub>/Y<sub>730</sub>F) or 1 min (NH<sub>2</sub>Y<sub>730</sub>/C<sub>439</sub>A) in ice-cold 2-methylbutan (~113 K) to insure a good heat conductivity for the larger Qband tubes.

#### 4.3.3.1 Diagonal Distance from NH<sub>2</sub>Y<sub>731</sub>•/Y<sub>730</sub>F to Y<sub>122</sub>•

The diagonal distance can be measured directly, if the whole spectrum is excited by the pump and detect pulses as common at X band. However, concentration sensitivity increases with the MW frequency, thus the measurement at Q band (34 GHz) is more sensitive.<sup>282-284</sup> Isabel Bejenke from our group demonstrated that complete distance distributions at Q band require orientation averaging. With the power of 2W five field points on the NH<sub>2</sub>Y<sub>730</sub>•-Y<sub>122</sub>• radical pair would be necessary.<sup>285</sup> However, the distance did not change at different field points. Thus if the distance is observed and it does not represent a double frequency (the parallel part of a pake pattern, see Figure 2-12), the distance is robust.

In Figure 4-10 the ESE-field sweep spectrum at 34 GHz shows NH<sub>2</sub>Y<sub>731</sub>• with a yield of 28%. Three pump and detect frequencies were set up covering the spectral width of the NH<sub>2</sub>Y<sub>731</sub>•. A dipolar oscillation was obtained from each detection position after

procession and analysis of the data (Figure 4-10B). By adding the normalized spectra a dipolar oscillation comparable to earlier X band studies was obtained.

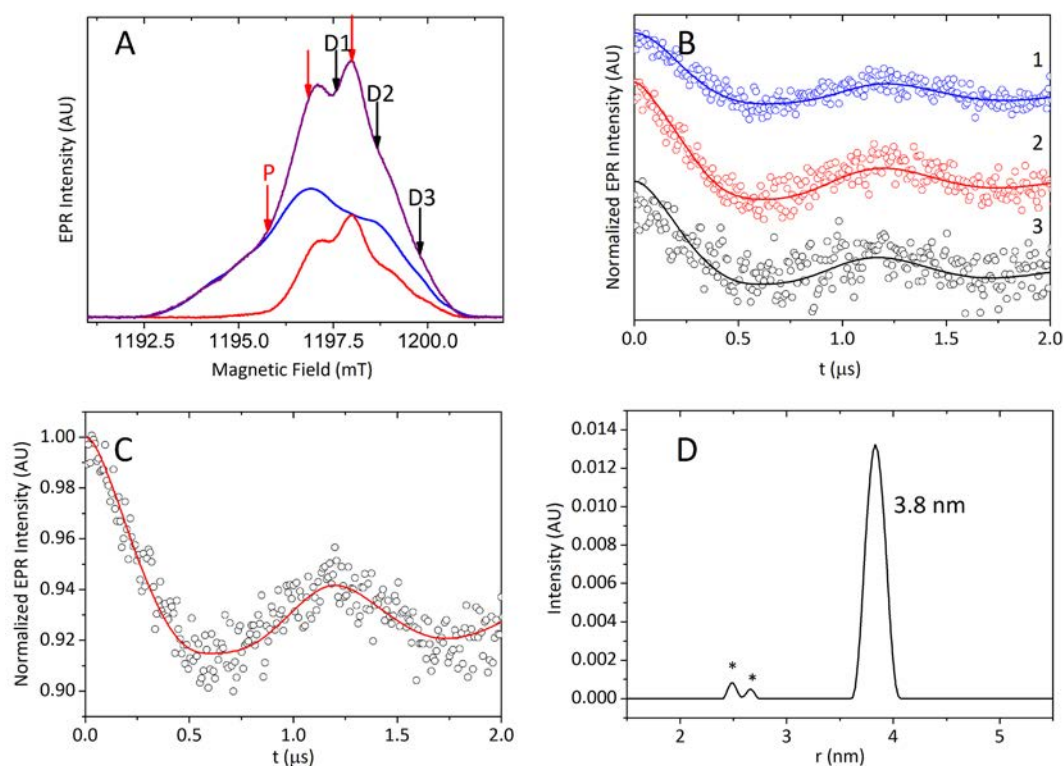


Figure 4-10: 34-GHz distance measurements between NH<sub>2</sub>Y<sub>731</sub>• and Y<sub>122</sub>• in the α<sub>2</sub>-NH<sub>2</sub>Y<sub>731</sub>/Y<sub>730</sub>F double mutant at 5 K. (A) The ESE spectrum of unreacted Y<sub>122</sub>• (blue) has been subtracted from the observed spectrum (purple), yielding the NH<sub>2</sub>Y• (28%) spectrum (red). Pump (P, π= 46 ns) and detect (D, π= 56 ns) pulses were separated by 55 MHz and are indicated by arrows and shifted stepwise (ΔB = 11 G) over the EPR line. (B) The three consecutive (1,2,3) four-pulse DEER traces were normalized and background corrected. (C) Average trace as sum of the three normalized traces. The red line describes a fit using DeerAnalysis<sup>286</sup> and Tikhonov regularization<sup>287</sup> procedure. (D) Distance distribution obtained from the analysis in (C). The measured distance distribution shows 3.84±0.15 nm as main distance.<sup>254</sup>

Fitting of the time domain trace including a Tikhonov regularization<sup>††287</sup> procedure a distance distribution was obtained as shown in Figure 4-10D (DeerAnalysis 2013)<sup>286</sup>. The distance distribution of  $3.84 \pm 0.15$  nm is identical to the distance distribution observed previously for the single mutant with  $3.81 \pm 0.12$  nm.

#### 4.3.3.2 Diagonal Distance from $\text{NH}_2\text{Y}_{730}\bullet/\text{C}_{439}\text{A}$ to $\text{Y}_{122}\bullet$

In another set of experiments the  $\text{NH}_2\text{Y}_{730}\bullet/\text{C}_{439}\text{A}$  distance to  $\text{Y}_{122}\bullet$  was tested by the same procedure, as shown in Figure 4-10. The measurement was carried out by I. Bejenke in our group.<sup>285</sup>  $\text{NH}_2\text{Y}_{730}\bullet$  yielded 17%, compared to  $\text{Y}_{122}\bullet$  (Figure 4-11A) in agreement with the low yield observed in SF-vis measurements (§4.3.2).

Processing procedure of the three measured field points was performed with DeerAnalysis.<sup>286</sup> A distance distribution from an incomplete powder average results (Figure 4-11D). Two components with 3.9 nm and 3.3 nm are prominent, which arise from  $\text{NH}_2\text{Y}_{730}\bullet\text{-Y}_{122}\bullet$  and  $\text{Y}_{122}\bullet\text{-Y}_{122}\bullet$  distances, respectively. The ratio is not as expected from the last dataset (Figure 4-10D). Here the 3.9 nm distant is the minor contribution. Reasons could be the lower yield, unfavorable orientation selection and the first detection (D1, Figure 4-11A) outside the spectral width of  $\text{NH}_2\text{Y}_{730}\bullet$  the contribution of the longer distance (3.9 nm). However, compared to the single mutant study the 3.9 nm distance probability (cf. Figure 4-10D) decreases from  $\text{NH}_2\text{Y}_{731}\bullet$  to  $\text{NH}_2\text{Y}_{730}\bullet$  as well.<sup>43</sup> In order to support the long distance, the effect of suppressing the long distance is shown in B2 and C in green. The RMSD in C (B2) is changing from 0.0025(0.0016) to 0.0036(0.0023) for the blue and green fit, respectively.

The distance measurements performed here provide evidence against global structural distortion introduced into the active enzyme for the observed  $\text{NH}_2\text{Y}_{730}\bullet$  intermediate by blocking the radical transfer. However, without a resolved dipolar oscillation (Figure 4-10B) with a frequency consistent to the long distance the assignment for  $\text{NH}_2\text{Y}_{730}\bullet/\text{C}_{439}\text{A}$  is questionable. Overall one can state that the longer distance observed in the single mutants was found as well in the double mutants.<sup>43, 254</sup>

---

<sup>††</sup> This includes weighting of the smoothing effect versus the RMSD.

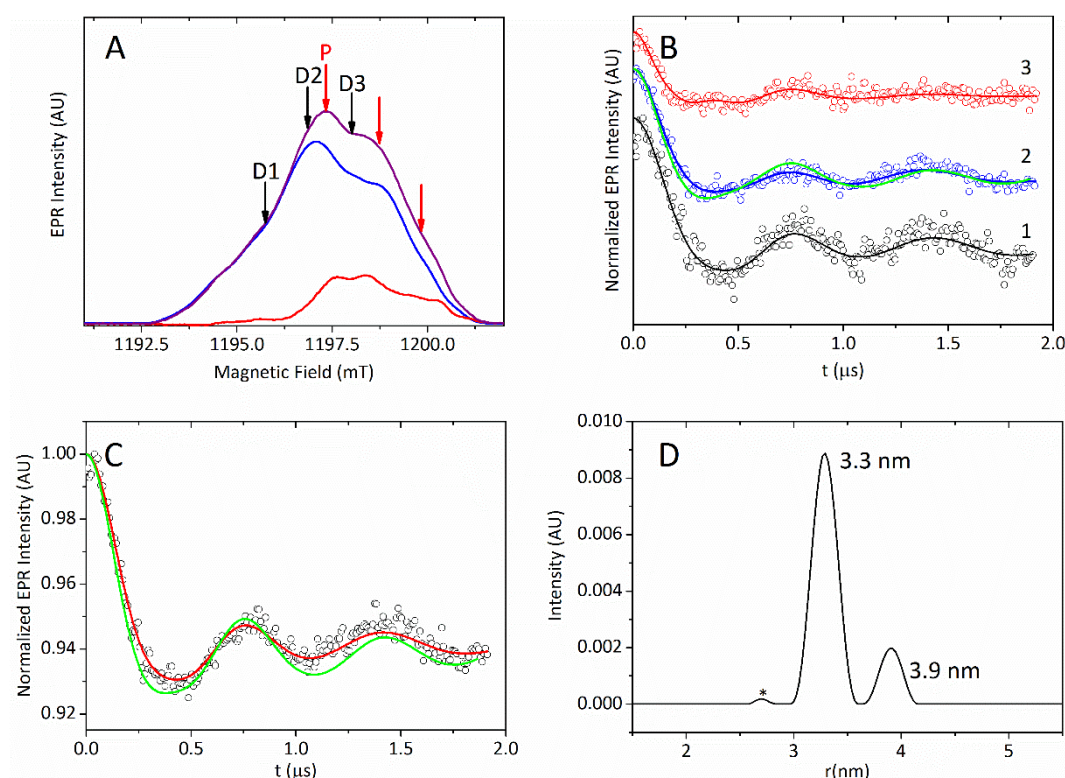


Figure 4-11: 34-GHz distance measurements between  $\text{NH}_2\text{Y}_{730}\bullet$  and  $\text{Y}_{122}\bullet$  in the  $\alpha_2$ - $\text{NH}_2\text{Y}_{730}/\text{C}_{439}\text{A}$  double mutant. (A) The composite EPR spectrum at 5 K (purple) followed by subtraction of the  $\text{Y}_{122}\bullet$  (blue) gives the  $\text{NH}_2\text{Y}\bullet$  spectrum (red) in 13% yield. (B) The DEER traces at 20 K were taken with detection pulses ( $\pi/2(\pi) = 20(40)$  ns) separated by 50 MHz from the pump pulse ( $\pi = 56$  ns). (B) Three consecutive traces (1, 2, 3) were measured at D1, D2 and D3 (see A), respectively, with 11 G spacing. (C) The averaged traces were summed and fit by DeerAnalysis<sup>286</sup> using Tikhonov regularization.<sup>287</sup> (D) In the distance distribution the distance of  $3.29 \pm 0.15$  nm and  $3.9 \pm 0.1$  nm is shown. B and C) In green the frequency suppressing distances larger than 3.45 nm is shown.

#### 4.3.4 Electrostatic Environment and Conformational State: Comparison of the Radicals Formed in Double Mutants and Single Mutants

The electronic structure reflected in the  $g$ -factor can be studied for  $\text{NH}_2\text{Y}_{731}\bullet/\text{Y}_{730}\text{F}$  and  $\text{NH}_2\text{Y}_{730}\bullet/\text{C}_{439}\text{A}$ . To compare the results with the single mutants and estimate also external effects like H bonding high-field EPR spectra were recorded and compared as shown in Figure 4-12. The spectra of the double mutants reveal the same coupling pattern for  $B_0$  along  $g_y$  and  $g_z$ . Along  $g_x$  all features are broader than observed in the single mutants. This is typical for a distribution of electrostatic environments around the oxygen of the phenyl ring. The

observed  $g$  shift is here 0.3-0.4 ppt.  $\text{NH}_2\text{Y}_{730}\bullet/\text{C}_{439}\text{A}$  shows a slightly smaller  $\beta$ -methylene coupling at  $g_y$  ( $\approx 24$  MHz) the couplings at  $g_z$  are identical with approximately 32 MHz to the value of the single mutant. The coupling obtained from the spectra for  $g_x$  is 38 MHz.

The  $\text{ND}_2\text{Y}_{731}\bullet$  double mutant (orange spectrum) compared to the single mutant (red spectrum) show an increase in dominant C- $\beta$  HF coupling ( $A_{\text{iso}} \approx 26$  MHz, Table 4-1 p.80). In order to disentangle the spectral contributions from  $g$  value and HF couplings further 263 GHz spectra were recorded as shown in Figure 4-13. Low signal intensity and yield (15%) of  $\text{NH}_2\text{Y}_{730}\bullet/\text{C}_{439}\text{A}$  at 70 K prevented an artifact free echo detected spectrum. Another signal is marked as an artifact with an asterisk (\*). The stimulated echo sequence was used to compensate the weak signal, thus a shorter  $T_m$  filtering has been used. Thus in part the signal could arise due to the  $\text{Y}_{122}\bullet$  signal. From 94 GHz spectra  $g_x$  was located in the center of the doublet splitting (38 MHz) at the low field side. The obtained parameters are summarized in Table 4-4.

The spectrum of  $\text{NH}_2\text{Y}_{731}\bullet/\text{Y}_{730}\text{F}$  (gray spectrum, Figure 4-13) displays a distinct triplet at the low field side of the 263 GHz spectrum. Compared to the single mutant (red spectrum), the dominant C- $\beta$  coupling increases ( $A_{\text{iso}} \approx 26$  MHz, Table 4-1 p.80). C- $\beta$  couplings are the only larger coupling contributions in these spectra, because the amino protons have been exchanged to deuterons. However, this HF coupling in combination with a weaker coupling to the second C- $\beta$  proton ( $A_{\text{iso}} < 26$  MHz) is not sufficient to generate the large triplet splitting (peak separation of  $\sim 1.1$  and  $1.4$  mT). Thus the splitting is assigned to a second component. Two different  $g_x$  values, but similar  $g_y$  and  $g_z$  values are typical for a second component with a different electrostatic environment. The individual parts of these two components are demonstrated via simulation of a larger (red) and smaller (blue)  $g_x$  value component. The weighted sum simulation (gray --) supports of the two component interpretation with a weight of 45% to 55% for red and blue, respectively (Table 4-4). These two contributions cannot be resolved at 94 GHz, where the spectral region around  $g_x$  shows only broadening (area marked in Figure 4-12). The results indicate that, as expected, removal of the H bond to  $\text{Y}_{730}$  perturbs the electrostatic environment at  $\text{NH}_2\text{Y}_{731}\bullet$  and destabilizes the radical. The broadening observed at 94 GHz originates from two distinct environments. Thus no Gaussian distribution of H bond interactions is present, a prerequisite for a further ENDOR investigation. The simulation demonstrated a good fit to the corresponding 94 GHz spectrum, as shown in the Figure 4-12.

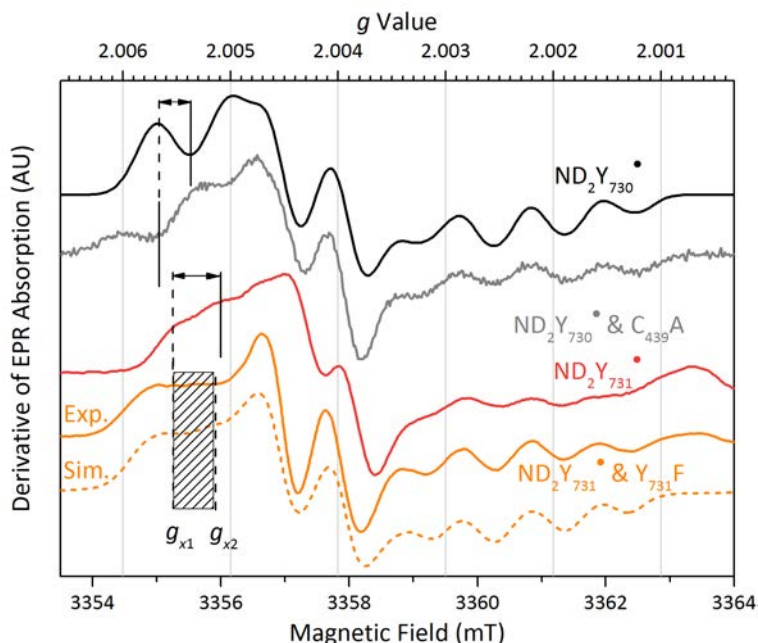


Figure 4-12: 94-GHz ESE spectra of  $\text{NH}_2\text{Y}_{730}\bullet/\text{C}_{439}\text{A}$  and  $\text{NH}_2\text{Y}_{731}\bullet/\text{Y}_{730}\text{F}$  compared to the corresponding single mutants. The spectra show  $\text{NH}_2\text{Y}_{730}\bullet/\text{C}_{439}\text{A}$  (gray) and  $\text{NH}_2\text{Y}_{731}\bullet/\text{Y}_{730}\text{F}$  (orange) together with  $\text{NH}_2\text{Y}_{730}\bullet$  (black) and  $\text{NH}_2\text{Y}_{731}\bullet$  (red) in  $\text{D}_2\text{O}$  exchanged buffer. The shift of  $g_x$  is marked in black. The simulation (orange,--) uses the parameters of Table 4-4. Exp. details: ESE,  $T=10\text{ K}$ ,  $\pi/2 = 18\text{ ns}$ ;  $\tau = 260\text{ ns}$ ;  $\text{SRT} = 6\text{ ms}$ ;  $\text{SPP} = 100$ ; scans = 15-110. To build the derivative spectra a 5 point, second order Savitzky-Golay filter was used.

Table 4-4: Parameters obtained from the double mutant  $\text{NH}_2\text{Y}_{730}\bullet/\text{C}_{439}\text{A}$  and  $\text{NH}_2\text{Y}_{731}\bullet/\text{Y}_{730}\text{F}$  EPR spectra and simulation parameters of Figure 4-12 & Figure 4-13.

	$g_x$	$g_y$	$g_z$	$g$ strain	$A$ [MHz]			
Experiment								
$\text{NH}_2\text{Y}_{730}\bullet/\text{C}_{439}\text{A}$	2.0056	2.00415	2.0022		$A(\text{C-}\beta\text{-H}_1)$	38	24	32
					$A(\text{H}_2)$	-	-	-
$\text{NH}_2\text{Y}_{731}\bullet/\text{Y}_{730}\text{F}$	2.0055	2.0042	2.0022	0.15 ppt	$A(\text{C-}\beta\text{-H}_1)$	29	28	21
					$A(\text{H}_2)$	6	4	6
$\text{NH}_2\text{Y}_{731}\bullet/\text{Y}_{730}\text{F}$	2.0052	2.0042	2.0022	0.15 ppt	$A(\text{C-}\beta\text{-H}_1)$	34	28	27
					$A(\text{H}_2)$	6	4	6

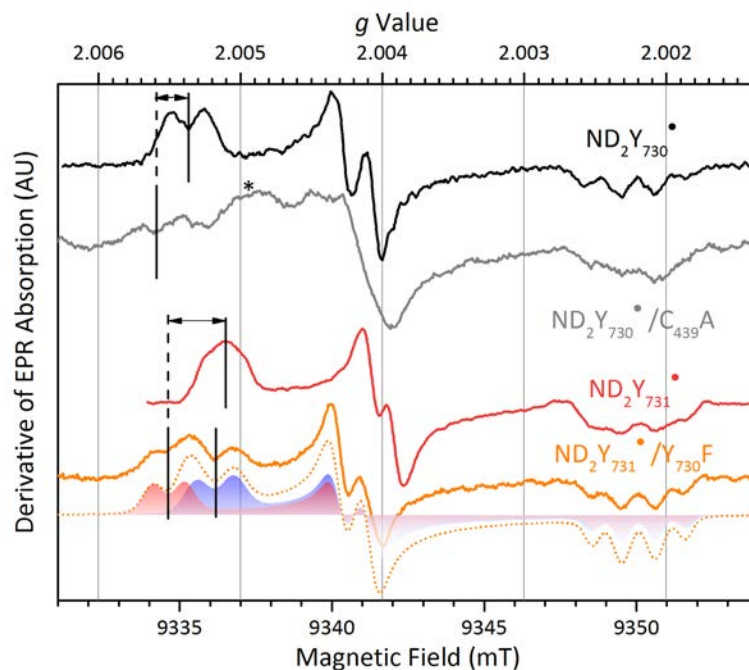


Figure 4-13: 263-GHz EPR spectra of  $\text{NH}_2\text{Y}_{730}\bullet/\text{C}_{439}\text{A}$  and  $\text{NH}_2\text{Y}_{731}\bullet/\text{Y}_{730}\text{F}$  compared to their corresponding single mutants. The spectra show  $\text{NH}_2\text{Y}_{730}\bullet/\text{C}_{439}\text{A}$  (gray) and  $\text{NH}_2\text{Y}_{731}\bullet/\text{Y}_{730}\text{F}$  (orange) together with  $\text{NH}_2\text{Y}_{730}\bullet$  (black) and  $\text{NH}_2\text{Y}_{731}\bullet$  (red) in  $\text{D}_2\text{O}$  exchanged buffer. The shift of  $g_x$  is marked in black. The simulation (orange dotted line, ...) takes two components into account (see Text, Table 4-4). Exp. details for double mutants (263 GHz): Stimulated echo (SE);  $T = 70\text{ K}$ ;  $\pi/2 = 110\text{ ns}$ ;  $\tau = 220\text{ ns}$ ;  $\text{SRT} = 6\text{ ms}$ ; number of averages = 7500 and 8750. To build the derivative spectra a 5 point, second order Savitzky-Golay filter ( $\text{NH}_2\text{Y}_{731}\bullet/\text{Y}_{730}\text{F}$ ) or a 10 G pseudo modulation ( $\text{ND}_2\text{Y}_{730}\bullet/\text{C}_{439}\text{A}$ ) was used. The asterisk (\*) denotes the presence of a background signal (see Text).

#### 4.3.5 Assignment of the H Bond Donors by ENDOR Spectra of the Double Mutants.

The high-field EPR spectra are partially consistent with a loss of a hydrogen bond. Thus it is interesting which  $^2\text{H}$  nuclei can be detected with  $^2\text{H}$  Mims ENDOR spectroscopy. Therefore, ENDOR spectra were recorded for the samples with the highest yield of 33% at 20 s and 14% at 30 s for  $\text{NH}_2\text{Y}_{731}\bullet/\text{Y}_{730}\text{F}$  and  $\text{NH}_2\text{Y}_{730}\bullet/\text{C}_{439}\text{A}$ , respectively. The  $^2\text{H}$  Mims ENDOR spectra at  $g_y$  are displayed in Figure 4-14, using deuterated assay buffer and a  $\tau$  value of 200 ns. They are directly compared with their single mutant counterparts described in §4.2.1.  $^2\text{H}$  ENDOR spectra of both double mutants showed an astonishingly decrease of sharp peaks at  $\pm 0.6\text{-}0.8\text{ MHz}$ . No sharp features are observed in  $\text{NH}_2\text{Y}_{731}\bullet/\text{Y}_{730}\text{F}$ , whereas a loss of  $\sim 70\%$  intensity compared to the single mutant is apparent in  $\text{NH}_2\text{Y}_{730}\bullet/\text{C}_{439}\text{A}$

mutant. Notably, this is in agreement with the assignment made before (§4.2 p.81) and previously (§1.5.3, p.21).<sup>110,254</sup>

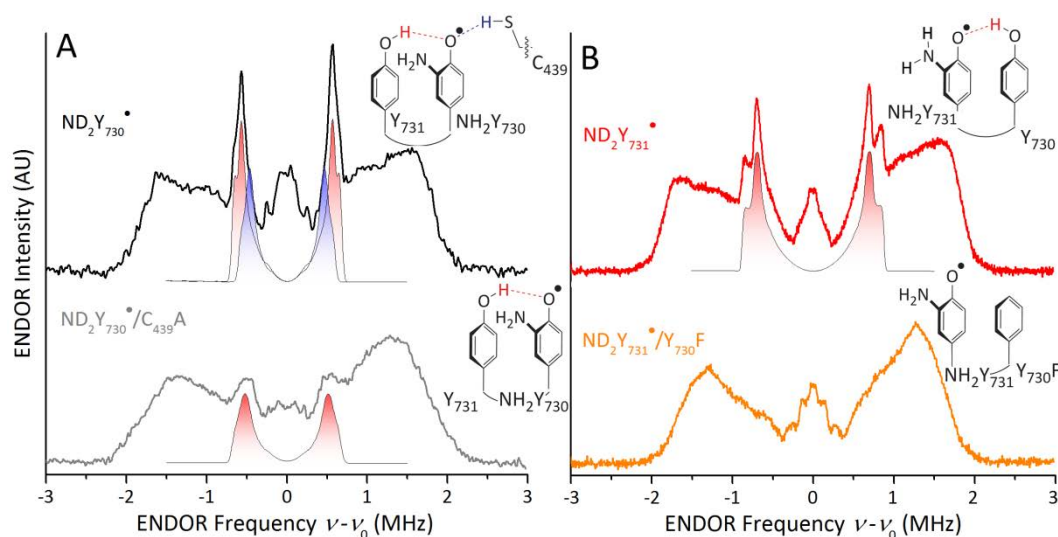


Figure 4-14:  $^2\text{H}$  Mims ENDOR spectrum of the double mutants  $\text{NH}_2\text{Y}_{730}\bullet/\text{C}_{439}\text{A}$  and  $\text{NH}_2\text{Y}_{731}\bullet/\text{Y}_{730}\text{F}$  (top) compared to its corresponding single mutant spectrum (bottom). A) The simulated tensor shape assigned to the H bond of the DO- $\text{Y}_{731}$  is shown in red. The resonance assigned to an H bond of D- $\text{C}_{439}$  has a blue gradient. B) No sharp feature was detected in the  $\text{NH}_2\text{Y}_{731}\bullet/\text{Y}_{730}\text{F}$ , in agreement with the loss of a perpendicular H bond. Exp. details:  $T = 70\text{ K}$ ,  $\pi/2 = 20\text{ ns}$ ,  $\tau = 200\text{ ns}$ ,  $\pi_{\text{RF}} = 40\ \mu\text{s}$ ,  $\text{SRT} = 5\text{ ms}$ , random RF acquisition<sup>279</sup> at 1 shot/point, acquisition time is 24 h (green) 50 h (gray).

Thus  $\text{NH}_2\text{Y}_{730}\bullet$  harbors two perpendicular H bonds and  $\text{NH}_2\text{Y}_{731}\bullet$  has one strong to moderate perpendicular H bond donor,  $\text{Y}_{730}$ . The broad range of the amino deuterons shows, furthermore, slight changes for  $\text{NH}_2\text{Y}_{730}\bullet$ , the double mutant has a 10% smaller HF coupling to the  $\text{ND}_2$  deuteron, whereas the other coupling stays in the same range as the single mutant. At  $\text{NH}_2\text{Y}_{731}\bullet$  both amino deuterons have a smaller coupling ( $\sim 20\%$ ). This could indicate a slightly changed distribution of spin density over the ring or a change in direct intermolecular interaction at the amino group. Nevertheless, both contributions can be simulated using a simply scaled tensor of the corresponding single mutant (data not shown).

Interestingly, the inner coupling range is also changing for  $\text{NH}_2\text{Y}_{731}\bullet$ , out of the unstructured matrix line a clear pattern emerges. It could be a small axial part of a powder pattern. Then a dipolar tensor with values of  $T_{\parallel} = -0.3\text{ MHz}$  and  $T_{\perp} = 0.6\text{ MHz}$  would be present. Otherwise a larger resonance contribution with 1.2 MHz is possibly overlaying with



the amino deuteron tensor resonances. This is in agreement with a low  $g_x$  value observed for 55% contribution of the  $\text{NH}_2\text{Y}_{731}\bullet/\text{Y}_{730}\text{F}$ . In contrast the inner coupling of  $\text{NH}_2\text{Y}_{730}\bullet$ , which shows a tensor in agreement with distal water, does not change. The  $\text{NH}_2\text{Y}_{731}\bullet$  double mutant located near the interface could compensate the loss of an H bond, which could explain good yield and the in part small  $g$  shift observed. Therefore it was interesting to observe from which direction this new contribution could arise from.

#### 4.3.5.1 Orientation Selective ENDOR from $\text{NH}_2\text{Y}_{731}\bullet/\text{Y}_{730}\text{F}$

A set of  $^2\text{H}$  ENDOR experiments along all canonical orientations of the  $\mathbf{g}$  tensor was performed. As we have seen before only three deuterium nuclei are present in this system two from the  $\text{ND}_2$  group and one from a here better resolved matrix line. The point of interest here was the inner coupling range and the orientation of a distant  $^2\text{H}$  coupling. For  $B_0$  oriented along  $g_z$  the features of the inner line get a single crystal like sharpness. The features get broader at  $B_0\parallel g_y$  and at  $B_0\parallel g_x$  the inner coupling has an overlap with resonances origin from the two amino deuterons. Section 5.3.4 (p.142) will show that in plane  $^2\text{H}$  HF couplings have quadrupole splitting in the order of  $\approx 0.15$  MHz. The splitting observed at  $g_z$  could be representative for an axial HF ( $T_{\perp} \approx 0.22$  MHz) including a quadrupole splitting of 150 kHz. Due to orientation selection no parallel HF tensor component for  $B_0\parallel g_z$  is visible for an H bond collinear ( $\pm 30^\circ$ ) to the  $g_x, g_y$  plane.<sup>55, 155</sup> A moderate H bond consistent to such a coupling (2.2 Å, Eq. (2-17)), would be sufficient to explain the difference in  $g$  value between the two environments. Without better resolved spectra (Figure 4-15), a simulation of these spectra would be speculative at this point.

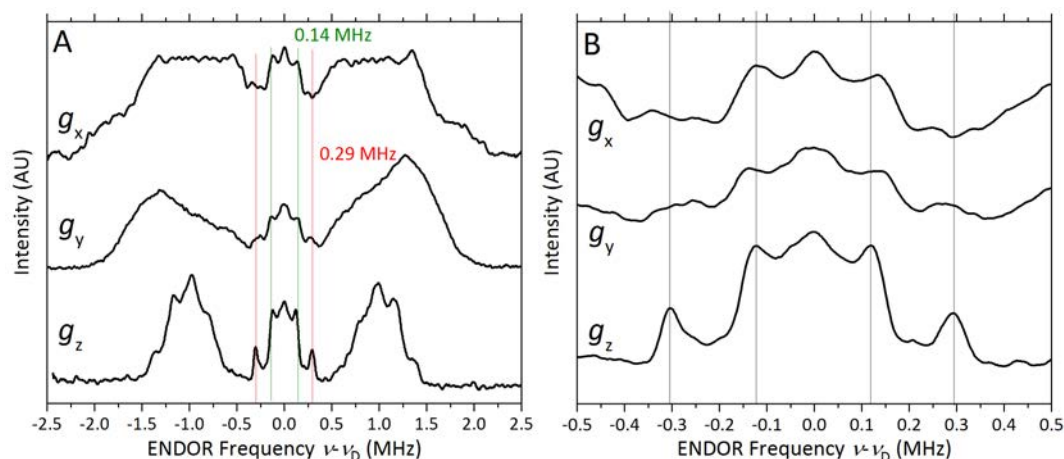


Figure 4-15: Orientation-selective  $^2\text{H}$  Mims ENDOR for  $\text{NH}_2\text{Y}_{731}\bullet/\text{Y}_{730}\text{F}$ . The traces were recorded at the magnetic field positions corresponding to the canonical values of the  $\mathbf{g}$  tensor ( $g_x$ ,  $g_y$ ,  $g_z$ ) at 70 K. The interaction of a  $^2\text{H}$  is marked with green ( $\pm 0.14$  MHz) and red lines ( $\pm 0.29$  MHz). Exp. details: Bottom:  $T = 10$  K,  $\pi/2 = 20$  ns,  $\pi_{\text{RF}} = 40$   $\mu\text{s}$ ,  $\tau = 200$  ns, SRT = 150 ms, random RF acquisition<sup>279</sup> at 1 shot/point, acquisition time = 1:07 h; top:  $T = 70$  K, SRT = 10 ms, acquisition time = 2:24 h. From top to bottom 20, 5 and 10 point adjacent averaging smoothing was used.

#### 4.4 Comparing Structural Models from DFT with EPR Parameters

At the beginning of this project, the overall idea was not only to measure EPR and ENDOR spectra but, ambitious as it sounds, to obtain a structural model of the radical state. Based on T. Argirević's EPR and Riplinger's DFT work (Introduction §1.5.3, p.21), a suitable model for  $\text{NH}_2\text{Y}_{731}\bullet$  in agreement with the EPR results of the previous sections should be found. This time the large models (>200 atoms), used for transition state calculations previously,<sup>110</sup> could be augmented by an  $\text{NH}_2$  group on  $\text{Y}_{731}$ .

The geometry optimization was performed by S. Kossmann in F. Neese's lab. An unrestricted gradient functional BP86 was employed with dispersion correction and a triple zeta  $\zeta$  functional operating in the basis set limit (Methods §3.6, p.71). Three models were studied with one, zero and two water molecules named Model 1, 2 and 3, respectively (Figure 4-16, p.100). The models were originally based on the inactive crystal structures<sup>67</sup> and took all known amino acids within 5 Å around the  $\text{NH}_2\text{Y}_{731}$  into account. In the optimized models the distance to the phenol H bond donor  $\text{Y}_{730}$  varies from 2.7 Å in Model 1 to 2.6 Å in Models 2 and 3 (Figure 2-16).

Nonetheless, all optimized models revealed a decreased  $O_{730}-O_{732}$  distance of 0.9 to 0.5 Å compared to the crystal structures (Figure 4-17). In the absence of a water molecule (Model 2)  $\alpha$ -R<sub>411</sub> approaches the  $NH_2Y_{731}^\bullet$ . The guanidinium group comes here within H bond distance  $R(N_{411}-O_{731}) \geq 2.9$  Å, where the closest encounter found in crystal structures is 3.6 Å (cf. Figure 2-16). The  $O_{wat2}-O_{731}$  distance, of a second water, considered in Model 3 is with 2.8 Å comparable to the distances ( $R_{o-o} \approx 2.6-3.6$  Å) observed in the vicinity of some X-ray structures of  $\alpha$ -wt and  $\alpha$ - $NH_2Y_{731/730}$  (see Figure 2-16). Despite the second H bond having a distance of  $R_{O-H} \approx 1.9$  Å, the stronger perpendicular H bond to  $Y_{730}$  remains.

Both interactions described by Model 2 and 3, find precedents in the literature. Common  $\pi$ -cationic interactions has been described for aromatic amino acids like tyrosine to amino acids like arginine.<sup>288, 289</sup> A arginine next to a tyrosine revealed a reduction in redox potential in small peptide model studies.<sup>290</sup> Strong H bond networks, including two water molecules, have also been proposed in PS II to have a strong effect on  $g$  values and an activation role for  $Y_z$ 's high activity.<sup>156, 291</sup>

In our models, the  $g$  values and the HF interaction were calculated using B3LYP and EPRII as functional and basis set (§2.3 p.47). The gauge origin of the  $\mathbf{g}$  tensor had to be laid into the radical (fixed at C4) to reduce gauge-dependent errors. The main two variables in the 3-amino tyrosines extracted from the high-field EPR spectra are the  $g$  values and the  $\beta$ -methylene couplings that are tabulated in Table 4-5. For the  $g$  values we see that within the uncertainty of the DFT of 0.5 ppt all values are consistent with the experimental  $g$  values. Within the models  $g_z$  is not varying significantly and  $g_y$  follows the trend of  $g_x$  between Model 1 and 2 to a smaller extent as expected by  $g$  value theory (Theory §2.1.2, p.31).

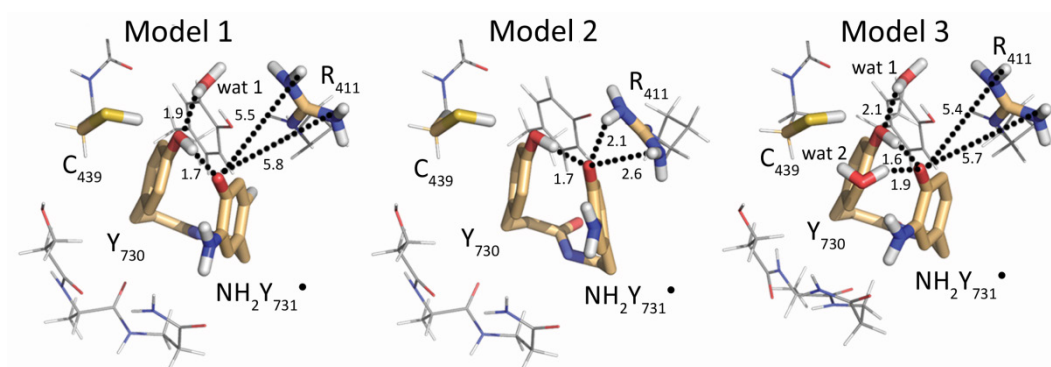


Figure 4-16: Central part of the DFT geometry optimized  $\text{NH}_2\text{Y}_{731}\bullet$  models. The models are based on the models used for the energy barrier calculation (Introduction §1.5.3, p.21) of the  $\text{Y}_{731}\text{-Y}_{731}\text{-C}_{439}$  triad. In gold the residues directly affecting the model are highlighted. Model 1 contains the water molecule wat1, Model 2 has no water molecule, and Model 3 considers an additional water (wat2) close to  $\text{NH}_2\text{Y}_{731}\bullet$ . The complete models are depicted in Figure A - 5 (p.196).

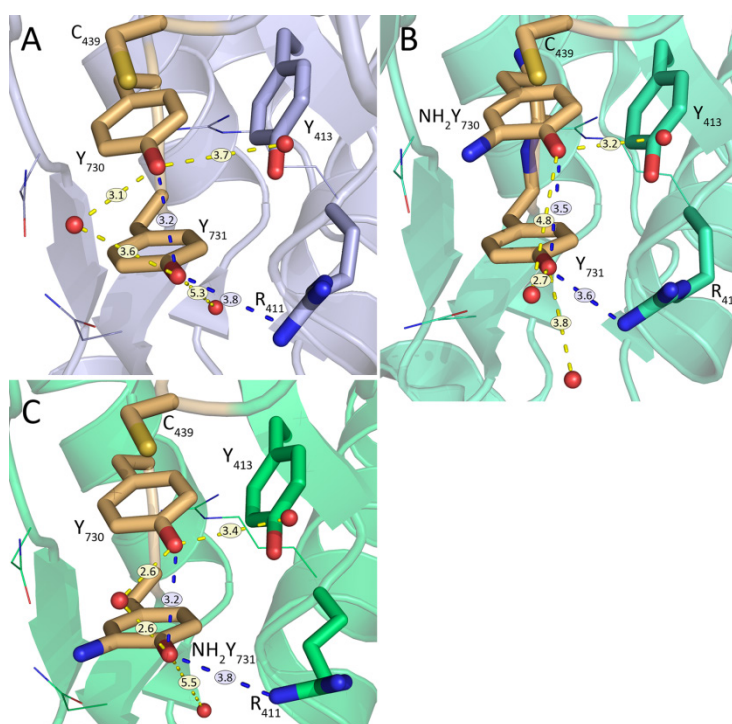


Figure 4-17: X-ray structures including water molecules in  $\alpha$  subunit.<sup>67</sup> 3 Crystal structures of: (A)  $\alpha$ -wild-type, PDB ID 2X0X, molecule C, 2.3 Å resolution; (B)  $\alpha$ - $\text{NH}_2\text{Y}_{730}$  PDB ID 2X04, molecule B, 2.7 Å resolution; (C)  $\alpha$ - $\text{NH}_2\text{Y}_{731}$  PDB ID 2X05, molecule C, 2.5 Å resolution. Only water oxygen atoms (red spheres), which are near to the phenolic oxygen ( $\leq 5.5$  Å) of the tyrosines, are displayed. The distances are given in Å.

Table 4-5: Summary of  $g$  values and C- $\beta$  HF couplings of  $\text{NH}_2\text{Y}\cdot$  at residues 730, 731, 356. The values were obtained from combined simulations of the 263 and 94 GHz spectra and compared with those obtained from DFT calculations. The  $^{14}\text{N}$  hyperfine tensor of the  $\text{NH}_2\text{Y}\cdot$  was not varied in the simulations and kept  $A_x=2.4$  MHz,  $A_y=1.6$ -5 MHz,  $A_z=30.7$  MHz.<sup>134</sup> Uncertainty in  $g$  values is about 0.05 ppt for the experiments and 0.5 ppt for DFT calculations. Uncertainty in HF couplings is up to 10% from spectral simulations and up to 20 % in DFT calculations.

	$g_x$	$g_y$	$g_z$	$A_{\text{iso}}(\text{C-}\beta)$ [MHz]
Experiment				
$\text{NH}_2\text{Y}_{730}\cdot$	2.0054 2.0052 <sup>‡</sup>	2.0042	2.0022	29
$\text{NH}_2\text{Y}_{731}\cdot$	2.0051	2.0040	2.0022	22
$\text{NH}_2\text{Y}_{356}\cdot$	2.0049	2.0041	2.0021	27
$\text{NH}_2\text{Y}_{730}\cdot/\text{C}_{439}\text{A}$	2.0056	2.00415	2.0022	31
$\text{NH}_2\text{Y}_{731}\cdot/\text{Y}_{730}\text{F}$	2.0055/52	2.0041	2.0022	26
DFT				
$\text{NH}_2\text{Y}_{731}\cdot$ Model 1, with wat1	2.0055	2.0042	2.0022	35
$\text{NH}_2\text{Y}_{731}\cdot$ Model 2, no water	2.0050	2.0040	2.0023	28
$\text{NH}_2\text{Y}_{731}\cdot$ Model 3, with wat1 and wat2	2.0051	2.0039	2.0021	22
free $\text{NH}_2\text{Y}\cdot$ <sup>Δ</sup>	2.0061	2.0045	2.0022	-

<sup>‡</sup> Value reported ref.<sup>134</sup> <sup>Δ</sup> value from 2-amino-4-methyl-phenol radical.<sup>110</sup>

To explain the dependence of the  $g_x$  values for the three models, one has to take a close look at the H bond interactions of the different models. It seems that weak (2.1 Å) to moderate (1.9 Å) H bonds make an effect of 0.4-0.5 ppt if they act together with a moderate H bond perpendicular oriented to the ring system. This is consistent with small model studies (Figure A - 6, p.197). It is worth mentioning that Model 2 and 3 lie closer to the observed experimental values. The  $\beta$ -methylene is best captured by Model 3. This model has a dihedral  $\theta_{\text{C}\beta}$  of -47.2°. As shown in Figure 4-18, this will decrease the second beta methylene coupling ( $H_{\beta 1}$ ) to nearly zero with  $a_{\text{iso}}(H_{\beta 1}) \approx 3$ -4 MHz (Model 1 & 3). Within these models  $a_{\text{iso}}(H_{\beta 1})$  cannot cause the HF interaction observed as a triplet at  $g_x$ . The next largest HF coupling is from the  $\text{C}_6$ -H with  $A_{x,y,z} = -9, -1, -13$  MHz (Model 3), therefore we assigned this coupling tentatively to  $A(\text{C}_6\text{-H})$ . This is a structural restrain, which could be considered in future studies, defined as in Figure 4-18. Since the  $\theta_{\text{C}\beta}$  angle is connected to the possible coupling sizes, for this angle only one dominant  $\beta$ -methylene  $^1\text{H}$  coupling is expected. It should be mentioned, that slight sterical changes from unconsidered interactions to the  $\beta$  subunit could introduce changes in the considered models.

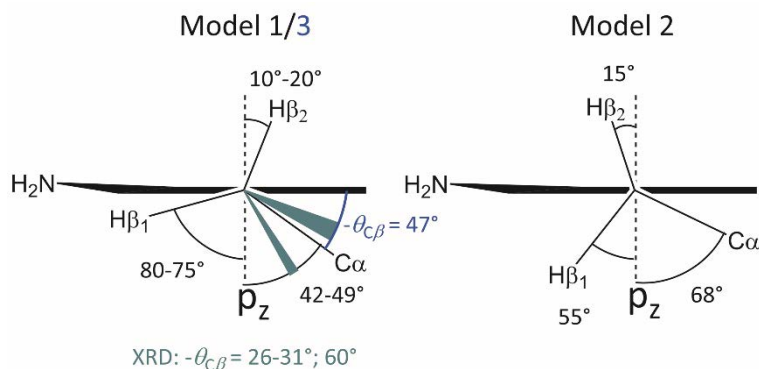


Figure 4-18: Ring dihedrals  $\theta_{C\beta}$  of the crystal structure (green) compared to models 1, 2 (black) and 3 (blue) considered for  $\text{NH}_2\text{Y}_{731}\cdot$  and  $\text{Y}_{731}\cdot$  (PDB ID: 2XOX, 2XOS and 2XO4).<sup>67</sup> The figure explains the observation, that both C- $\beta$  couplings become smaller, by an increase in  $\theta_{C\beta}$ .

In order to answer which DFT models are in agreement with the  $^2\text{H}$  ENDOR results Table 4-6 summarizes the acquired values. Direct comparison of Models 1 and 3 are in a good agreement to the experimental ENDOR work. However, all depicted models show the effect of a strong H bond toward  $\text{Y}_{730}$  nearly perpendicular to the ring plane. Uncertainty can be up to 20% for the DFT values and unique Euler angle sets are hardly found for orientation selective ENDOR, increasing the error to about 10%. Thus within the uncertainty only the coupling sizes of Model 2 disagree with the observed values. Especially, the  $\text{ND}_2$  tensor is in best agreement with Model 3, were the H bond, as depicted in Figure 4-19, is in best agreement with Model 1. Possibly an intermediate model could fit to both properties even better. The wat2 position could be modified as a more distant binding to the amino group ( $\geq 2 \text{ \AA}$ ) was obtained in an early optimized structure. Missing contacts have rendered the flexibility of a single water molecule on a more distant side too large to lead to an optimized geometry. Here structural information of any contact to the  $\beta$  subunit is of essence. The HF values of the wat2 deuterium with its calculated value of  $A_{\perp,\parallel} = -0.19, 0.37 \text{ MHz}$  could be unresolved from the discussed narrow matrix line of  $\text{NH}_2\text{Y}_{731}\cdot$  ( $\pm 0.2 \text{ MHz}$ ).

Addressing the Euler angles and the angular dependence of the H bond to  $\text{Y}_{730}$  the following Figure 4-19 should visualize the results. In order to compare on the same molecular bases, the HF tensor of the ENDOR simulation was rotated into the individual  $\mathbf{g}$  tensor system of the model. The angle differences show a stronger disagreement to Model 2 as discussed before based on the coupling size. Although Model 2 agrees well with the  $g$  values, the H bond direction does not. The other two models are within the uncertainty of  $30^\circ$  identical to the ENDOR simulation. All models are in a good agreement with the

H bond direction to Y<sub>730</sub>. Even if an additional water molecule is considered as in Model 3 the formed H bond interaction is weaker compared to the perpendicular H bond from Y<sub>730</sub>.

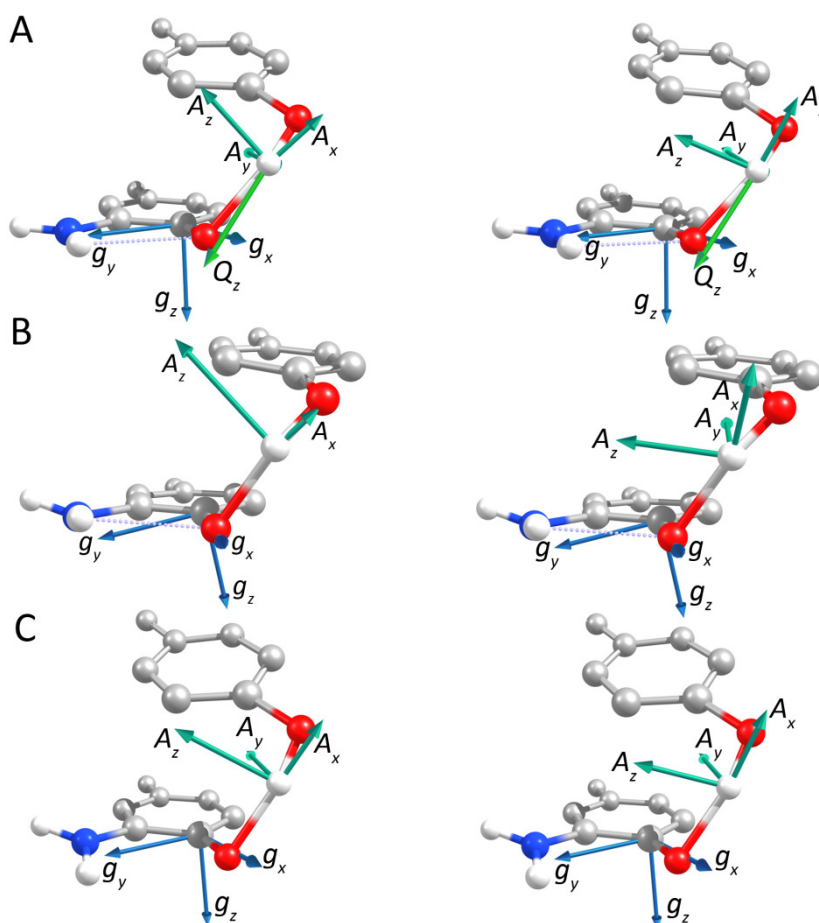


Figure 4-19: Comparison of DFT models (right) and H bond orientation from ENDOR simulation (left) parameters in their respective molecular frame. The  $\mathbf{g}$  tensor orientation (blue arrows) is defined in respect with the molecular frame and therefore for each model slightly different (up to  $10^\circ$ ). Row A, B and C are in the molecular frame of Model 1, Model 2 and Model 3, respectively. The hyperfine tensor and  $Q_z$  are displayed as mint green and green vectors. In all models  $Q_z$  has been found collinear to the O<sub>Y730</sub>-H bond and has been omitted for clarity.

## Comparing Structural Models from DFT with EPR Parameters

Table 4-6: Summary of EPR parameters for the H bond to NH<sub>2</sub>Y<sub>731</sub>•. Parameters were obtained from simulations of the orientation selective 94-GHz ENDOR spectra and comparison with the DFT models. Uncertainty in the parameters from the DFT and ENDOR simulations is estimated up to about 20%.

NH <sub>2</sub> Y <sub>731</sub> •		A <sub>x</sub> [MHz]	A <sub>y</sub> [MHz]	A <sub>z</sub> [MHz]	α [°]	β [°]	γ [°]	Q <sub>x</sub> [MHz]	Q <sub>y</sub> [MHz]	Q <sub>z</sub> [MHz]
Simulation	Y <sub>730</sub> -OD	1.3	-1.43	-1.63	-160 120	110 40	80 85	-0.03	-0.09	0.12
	ND <sub>2</sub> D(1)	-0.6	-2.9	-3.8	-86 -92	98 93	90 -3	-0.04	-0.06	0.11
	ND <sub>2</sub> D(2)	0.06	-3.1	-4.2	-96 -93	93 84	-31 -121	-0.06	-0.08	0.14
DFT: Model 1	Y <sub>730</sub> -OD	1.1	-1.4	-1.7	-164 119	137 39	79 85	-0.04	-0.06	0.10
	ND <sub>2</sub> D(1)	-0.4	-2.6	-2.8	-86 -92	98 93	90 -3	-0.05	-0.07	0.13
	ND <sub>2</sub> D(2)	0.04	-2.5	-3.7	-96 -93	93 84	-31 -121	-0.06	-0.08	0.14
DFT: Model 2	Y <sub>730</sub> -OD	0.75	-1.8	-2.2	-194 -104	147 121	58 -88	-0.04	-0.06	0.10
	ND <sub>2</sub> D(1)	0.25	-1.4	-1.5	-103 -111	137 80	95 12	-0.05	-0.07	0.13
	ND <sub>2</sub> D(2)	1.0	-1.0	-1.8	-113 -76	80 64	-17 -114	-0.06	-0.08	0.14
DFT: Model 3	Y <sub>730</sub> -OD	1.1	-1.7	-2.0	-163 106	122 25	81 84	-0.04	-0.06	0.09
	ND <sub>2</sub> D(1)	0.47	-2.6	-3.4	-98 -95	99 80	72 -15	-0.05	-0.06	0.11
	ND <sub>2</sub> D(2)	0.67	-2.63	-3.97	-100 -98	84 103	-45 43	-0.05	-0.06	0.11
	OD <sub>2</sub> (1)	-0.36	0.66	-0.73	87 24	109 64	-124 94	-0.06	-0.07	0.13

a) The signs of the couplings from the simulation are only relative to each other within one tensor. The Euler angles ( $\alpha$ ,  $\beta$ ,  $\gamma$ ) are defined from the A or Q to the g tensor based on the y convention (positive sign for a rotation is counter clockwise, second rotation is around the y axis). The A- and Q (quadrupole) tensor are chosen such that  $|A_x| < |A_y| < |A_z|$ . Within this definition, for both the amino deuterons and the H bond deuteron the A<sub>x</sub> direction results along the bond direction. Euler angles from DFT (in the ORCA output positive rotations are defined clockwise) were transformed into the magnetic resonance convention, for comparison.



## 4.5 Discussion of the PCET in the $\alpha$ Subunit with $\text{NH}_2\text{Ys}\bullet$

Prior work has demonstrated that unnatural amino acids can be used successfully to obtain information from the  $\alpha_2\beta_2$  active *E. coli* RNR Ia enzyme.<sup>69</sup> Not only the globular structure but also positioning of  $\text{NH}_2\text{Ys}\bullet$  within the PCET relative to  $\text{Y}_{122}\bullet$  has been accessible (see Figure 1-8, p.12).<sup>43</sup> Whereas kinetic studies delivered rates of several PCET steps, the incorporation of  $\text{NH}_2\text{Y}$  offered the opportunity to measure the radical state directly after a reversible oxidation step and reorganization of the protein thereafter.<sup>110, 134</sup>

Especially in  $\alpha$  RNR the site selective incorporation<sup>44</sup> of  $\text{Y}_{730/731}$  with  $\text{NH}_2\text{Ys}$  offered the possibility to study the H bond network and electrostatics of the formed transient radical.<sup>92, 110</sup> This information can be probed by two EPR accessible parameters: the  $g_x$  value affected by (partial) positive charges and the hyperfine interaction of protons forming H bonds in varying strength. The two  $\text{NH}_2\text{Ys}$  at  $\text{Y}_{730/731}$  showed a strong decrease in  $g_x$  of 0.7-1.0 ppt compared to the value of the free  $\text{NH}_2\text{Y}\bullet$  (Table 4-5, p.101).<sup>92</sup> This electropositive microenvironment was previously correlated to a DFT calculation ( $\approx 140$  atoms, model 4) including all assigned H bond contacts assigned in the  $^2\text{H}$  ENDOR simulations as reported in the introduction (Figure 1-14, p.23).<sup>110</sup> In analogy  $^2\text{H}$  ENDOR spectra of  $\text{NH}_2\text{Y}_{731}\bullet$  have been assigned preliminary to two perpendicular H bonds ( $\approx 1.8 \text{ \AA}$ ) within T. Argirević's dissertation.<sup>92</sup> A spectroscopical evidence, however, for the H bond donor groups assigned in these models has not been presented and a comparison to the transition state calculations ( $>200$  atoms, models 7 and 8) is compromised by the difference in model sizes.<sup>92, 110</sup> Additionally, highly accurate ( $<0.1$  ppt) and resolved EPR spectra were not presented allowing several interpretations, as the number of conformers observed at  $\text{NH}_2\text{Y}_{731}\bullet$ .<sup>92</sup>

In this chapter, high-field 263-GHz EPR has demonstrated a slight, but significant, increase (0.3 ppt) of electrostatic interaction from the well-structured  $\text{NH}_2\text{Y}_{730}\bullet$  to  $\text{NH}_2\text{Y}_{731}\bullet$  and has found  $\text{NH}_2\text{Y}_{731}\bullet$  to be a single species within the reaction time of seconds and minutes. This thesis revealed that the number, orientation and strength of exchangeable H bonds differ at these two residues. The ENDOR data are consistent with one strong and one moderate perpendicular H bond toward  $\text{NH}_2\text{Y}_{730}\bullet$ , but displays only one strong perpendicular H bond toward  $\text{NH}_2\text{Y}_{731}\bullet$  (Figure 4-14). The corresponding double mutant ENDOR spectra were consistent with a loss of an H bond. Additionally, they exhibited a decrease in radical build up rate. A connection between the change in H bond network and

the lower reaction rate might be drawn. This would emphasize that a loss of an H bond leads to a decrease in radical build up rate. A analog argumentation<sup>292</sup> explains the tendency in the PS II, were the stronger H bonded<sup>156, 291</sup> Y<sub>Z</sub>• reacts faster than Y<sub>D</sub>•<sup>153, 293</sup>.

Spectroscopic evidence for the assignment of the  $\pi$ -stacking between Y<sub>731</sub>-Y<sub>730</sub> has been obtained by several independent observations. I) The direction of the H bond and the alignment to the axis of the H bond donor describes one perpendicular H bond toward Y<sub>730</sub> from NH<sub>2</sub>Y<sub>731</sub>• and vice versa for Y<sub>731</sub> toward NH<sub>2</sub>Y<sub>730</sub>•. II) The H bond dihedral angle (cf. Figure 4-8, p.85) indicates an intervening water molecule as described by a model of Kalia and Hummer to be unlikely. In their structure an H bond, from the water, shows an angle of about 45° between  $g_z$  and  $g_x$ . In this case the largest quadrupole splitting would be observed along  $g_z$  and  $g_x$  equally, which is not the case. On the contrary, the ENDOR spectrum at  $B_0 \parallel g_x$  shows the smallest quadrupole splitting at this orientation (see Figure 4-8). However, both H bond angles are in agreement with an angle nearly perpendicular toward the aromatic plane (50°<sup>110</sup> to 70°, see §4.2.2, p.83) as modeled to be ideal for this  $\pi$ -stacked interaction.<sup>107</sup> III) The double mutant (NH<sub>2</sub>Y<sub>731</sub>•/Y<sub>730</sub>F) misses the typical perpendicular H bond pake pattern. Whereas the H bond network at NH<sub>2</sub>Y<sub>731</sub>• has a moderate to strong perpendicular H bond. This demonstrates the H bond loss is directly dependent on the phenoxy group at the 730 residue. IV) The DFT models revealed that no matter if zero, one or, two waters are considered in the large models (1-3) the strongest interaction is the H bond formed between the  $\pi$  stacked residues (see Figure 4-16). Thus the results support the current PCET model that Y<sub>731</sub>• is the proton acceptor in the next forward PCET step to Y<sub>730</sub> (Figure 1-10, p.14). Notably, this geometry is present in several, but not all  $\alpha_2$  structures. Other conformeric states have been observed in wt yeast<sup>68</sup> and human<sup>50</sup>, and in NH<sub>2</sub>Y RNR  $\alpha_2$  structures<sup>67</sup>, as shown in Figure 1-3 (p.5) and Figure 1-12B (p.18). Geometric restraints like the nearly perpendicular H bond (§4.2.2, p.83) and a ring dihedral (§4.4, p.98) have been formulated, and underline the necessary geometry for this adiabatic CPET step<sup>106, 110</sup>. The optimum efficiency of the transfer has been studied by theorists,<sup>106, 107, 113, 244</sup> pointing toward an adiabatic electron and proton transfer in a geometry consistent with our data.

So far we could show that Y<sub>731</sub> interacts to Y<sub>730</sub> by a strong to moderate perpendicular H bond and can have only a weak H bond interaction toward the interface. DFT studies were performed by C. Riplinger from the Neese group (Mülheim) to explain

the observed  $g$  shift in great detail and to include electronic, steric and energetic effects for orientations of the H bonds of  $Y_{730}$  and  $Y_{731}$  toward each other (§1.5.3.2, p.26).<sup>110</sup> In this thesis the optimized  $\text{NH}_2Y_{731}\bullet$  models 1 and 2 were obtained from the transition state wt models 1' and 2' (models 6 and 7 in ref. <sup>110</sup>), as illustrated in Figure 4-20 left. Therefore the  $\text{NH}_2Y_{731}\bullet$  and  $Y_{731}\bullet$  models have the same structural basis and can be compared.

In this thesis Model 1, 2, and 3 were related to the EPR and ENDOR spectra of  $\text{NH}_2Y_{731}\bullet$  and had one, zero and two waters in their models, respectively. Models 1 and 3 were within uncertainty in agreement with the  $^2\text{H}$  HF couplings from the amino group and the  $g$  values. Model 3, however, could not be considered for a comparison of  $\text{NH}_2Y_{731}\bullet$  to  $Y_{731}\bullet$ , because  $Y_{731}$  lacks the  $\text{NH}_2$ -group necessary to stabilize a water molecule (wat2) at a distant ( $r_{\text{O-H}} = 1.9 \text{ \AA}$ ) position (see Figure 4-16, p.100). Based on the assignment one can return to the recent study of the transition states (TS) and energies of Model 1' and 2' by Riplinger.<sup>110</sup> For position  $\text{NH}_2Y_{730}\bullet$  the ENDOR data showed an H bond consistent with wat 1 in Model 1'. Therefore, a model with wat 1 near  $Y_{730}$  is supported for  $Y_{731}\bullet$  and  $Y_{730}\bullet$  equally. The energetic pathway has been predicted and compared to Model 2' without wat 1 and with a cation- $\pi$  interaction of  $R_{411}$  and  $Y_{731}\bullet$ , as shown in Figure 4-20 left.

In the calculation performed on the wt enzyme the structural effect in terms of energy barriers are now displayed. The lowest energy barrier reported so far between two tyrosines is observed between  $Y_{731}\bullet$  and  $Y_{730}\bullet$  for Model 1'. Additionally, the barrier heights of other DFT models from the literature are displayed in Figure 4-20.<sup>107, 112</sup> Siegbahn et al. as well as Kalia and Hummer have modeled their DFT work solely with a di tyrosine peptide model between  $Y_{731}$  and  $Y_{730}$  with or without a water molecule in between. Although they pointed out either the importance of (non-equilibrium) electrostatics<sup>106, 113</sup> or considered H bonds<sup>107, 232</sup> they could not consider them. Both aspects have now been tested and compared to the EPR work biased by the absence of structural knowledge at the interface. Therefore Model 1' takes these important interactions into account. Bu et al. states that the protein environment stabilizes the radical intermediates (by up to  $\sim 3$  kcal/mol) and thus increases their observed barrier height. Comparing Model 1' and 2' it is evident that the close electro positive influence of  $R_{411}$  (with a  $g_s$  shift in  $\text{NH}_2Y\bullet$  of 0.5 ppt) in Model 2' can destabilize the  $Y_{731}\bullet$  compared to the TS and diminish the activation barrier.<sup>110</sup> The geometry with the water (wat1) close to  $Y_{730}$ , however, stabilizes the  $C_{439}\bullet$  and decreases the necessary energy for this endergonic forward PCET step.<sup>110</sup> Therefore it is difficult to

quantify the effect for all considered interactions, however, compared to Siegbahn et al. the barrier height decreases by 2 kcal/mol for the first step between Y<sub>731</sub> and Y<sub>730</sub> and is identical within error of 1.2 kcal/mol for the second step to C<sub>439</sub>.<sup>110, 232</sup> Notably, all DFT models used the same hybrid functional, the work of Kalia and Hummer even by the same dispersion corrected diffuse TZVPP basis set. Furthermore Siegbahn et al. mentioned that the effect of the total energy does not depend strongly on the basis set, thus the comparison is admissible. Generally, it is expected that B3LYP works well for PCET barrier heights, but underestimates them.<sup>113, 192, 294</sup> This is an important point before one compare these barriers to kinetic rates.

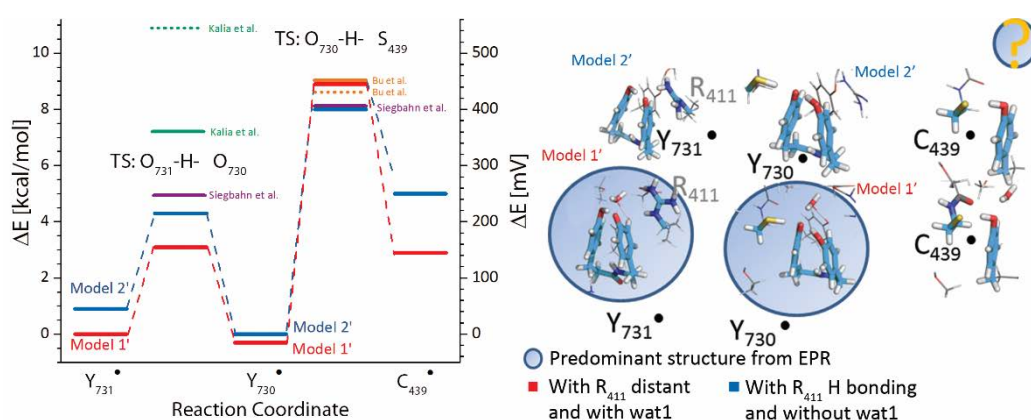


Figure 4-20: Energy diagram for the PCET in  $\alpha$ . Here the calculated energies from C. Riplinger are shown for the preferred Model 1' (red) and Model 2' (blue). Additional other DFT energy barriers are shown as HAT energies from Siegbahn et al. (violet),<sup>107</sup> the CPET energies of Kalia et al. (green)<sup>106</sup> and work from Bu et al. (orange)<sup>112</sup>. Barrier heights in solid lines are a direct PCET step, where points mark a water assisted transfer. The energies obtained from QM/MM structures of Bu et al. are 2-51 kcal/mol higher and were omitted here. Modified from ref. 110.

Kinetic rates were recently measured for the PCET step from a higher potential 2,3,5-F<sub>2</sub>-Y<sub>356</sub> to Y<sub>731</sub>-Y<sub>730</sub>-C<sub>439</sub>-nucleotide.<sup>86</sup> Activated by a photo trigger the 2,3,5-F<sub>3</sub>-Y<sub>356</sub>• decayed with a rate of 14000 s<sup>-1</sup>,<sup>86</sup> this is still slower than rates from B3LYP studies between Y<sub>731</sub>-Y<sub>730</sub>-C<sub>439</sub> with 10<sup>7</sup> per s.<sup>110</sup> The slower rate of 14000 s<sup>-1</sup> is in agreement with the proposed rate limiting step for this reaction to be the nucleotide reduction.<sup>86, 110</sup> Although this comparison does not enable us to judge the activation energy of single PCET steps, it tells us that no slow structural conversions can take place between our investigated triad of Y<sub>731</sub>-Y<sub>730</sub>-C<sub>439</sub>.

The interaction of Y<sub>731</sub> to C<sub>439</sub> was proposed to be direct in previous ENDOR studies. It was also observed in all resting state  $\alpha_2$  structures of wt, NH<sub>2</sub>Y<sub>730</sub>, and NH<sub>2</sub>Y<sub>731</sub>.<sup>22, 67</sup>

Bu *et al.* have strongly challenged this assignment. They claim that their two shell DFT (ONIUM) model based solely on the inactive  $\alpha_2$ -NH<sub>2</sub>Y<sub>730</sub> structure shows wat1 (H<sub>2</sub>O<sub>138</sub> in their notation) moving into a gap between Y<sub>730</sub> and C<sub>439</sub> during geometry optimization.<sup>112</sup> Notably, this has also been observed in some of our DFT models, if no restraints were used. It has been considered as an effect of the imperfect model based on the inactive crystal structure. In this chapter it could be demonstrated that the H bond resonance is missing in the NH<sub>2</sub>Y<sub>730</sub>•/C<sub>439</sub> ENDOR spectrum, in agreement with the energy models presented by Riplinger (Figure 4-20).<sup>110</sup> On the contrary, barrier height (Figure 4-20) and geometry of the intervening water of Bu *et al.* is similar for a water molecule (H<sub>2</sub>O<sub>138</sub>) or a cyteine S-H, as illustrated in Figure 4-21 (orange). Nevertheless, it can be stated that in the radical state of NH<sub>2</sub>Y<sub>730</sub>• the water they assigned to change its position (wat1/ H<sub>2</sub>O<sub>138</sub>) is still present in a distal position (cf. Figure 4-21, blue). Otherwise our methods cannot distinguish between a moderate H bond from and OH or an SH group. Agreement can be reached that assisting water molecules can stabilize the transition state as in the trend observed between Model 2' and Model 1' (cf. Figure 4-20). Nonetheless, a large energy barrier (60 kcal/mol) reported by them could not be reproduced even without wat1 in any other Y to Cys study including their own (Figure 4-20).<sup>112</sup> Though it could point out the strong distance dependence for a PT in a single PCET step.<sup>101, 112</sup>

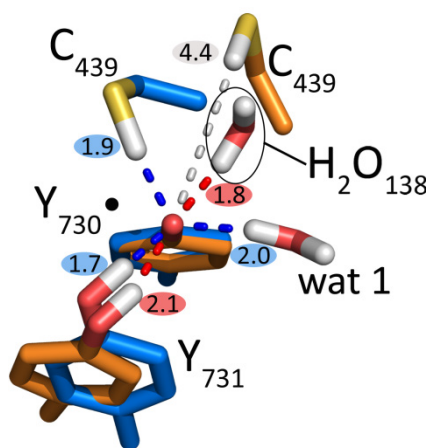


Figure 4-21: H bond environment of Y<sub>730</sub>• from DFT Model 1' (blue) and ONIUM model of Chen *et al.* (orange).<sup>110, 112</sup> The H bonds to Y<sub>730</sub>• are marked for Model 1' in red and for the ONIUM model in blue. The distance of the H bond is given next to the individual proton in Å. The distance between Y<sub>730</sub> phenoxyl oxygen and H-C<sub>439</sub> is marked in gray.

## 4.6 High-Field EPR Spectra of $\text{NH}_2\text{Y}_{356}\bullet$ in the $\beta$ Subunit

This part of the chapter will describe the results obtained using the 3-amino tyrosine mutation in the  $\beta$  subunit, more specifically at  $\text{Y}_{356}$  placed in the C terminal domain of the  $\beta$  protein. In  $\beta_2$  this part is highly flexible, nevertheless the last 32 amino acids were used to stabilize the  $\alpha_2$  complex in order to crystalize it (Figure 1-4 p. 7). Furthermore, it could be shown by NMR studies<sup>§§123</sup> or by the  $\text{NH}_2\text{Y}_{730}\bullet$  stabilized complex<sup>69</sup> that this part becomes ordered in the “active” complex. Focused on position 356, PELDOR studies based on a Dopa mutation have shown a narrow distance distribution ( $3.1\pm 0.1$  nm) at  $\text{Dopa}_{356}$  (Figure 1-6A p.10). Recently, also a narrow distance distribution of the  $\text{NH}_2\text{Y}_{356}\bullet\text{-Y}_{122}\bullet$  radical pair could be reported by PELDOR spectroscopy<sup>28</sup>(I. Bejenke, unpublished results). Based on these studies it became evident that a structuring around the flexible region takes place, but what does the local electronic structure look like?

In the following part the protein was prepared as published by E. Minnihan (Methods §3.2), the EPR samples, measurements and analysis were done in this thesis. The  $\text{NH}_2\text{Y}_{356}\text{-}\beta$  mutants have the intrinsic problem of the placement of an electronic sink near the “stable” tyrosine  $\text{Y}_{122}\bullet$ , thus only 0.5 radical/ $\beta_2$  compared to 1.2  $\text{Y}_{122}\bullet$  per wt- $\beta_2$ <sup>67</sup> could be generated by reconstitution methods.<sup>28</sup> A second batch in a 1:1 complex with an His6 tagged  $\alpha$  mutant was purified by W. Lee in the Stubbe lab at MIT.

### 4.6.1 EPR Spectra of $\text{NH}_2\text{Y}_{356}\bullet$ for Several Reaction Times

For the investigation of the electronic structure and the H bonding at  $\text{Y}_{356}\bullet$ , the time point for quenching the reaction had to be selected. These time points should be reproducible and should not contain further radical species. Although the SF-vis spectroscopy demonstrated a steady state at 1 s,<sup>67</sup> it is also interesting how the spectra develop during the radical decay with time points from s to minutes. As an example, conformational changes in this time scale could report on general local flexibilities of  $\text{NH}_2\text{Y}_{356}\bullet$ . Therefore EPR experiments were performed at 94 GHz for several time points from 6 s to 2 min, as shown in Figure 4-22. The spectra looked slightly different due to their contributions of glass peaks (high-field asterisk \*) and another contribution (low field asterisk \*) quite intense at 2 min and quite low in intensity for the 44 s. For both later time points the low field line at  $B_{0\parallel g_y}$  seem to be

---

<sup>§§</sup> This study has been performed with mouse RNR Ia.

broadened, therefore further studies were performed at earlier time points up to  $\approx 20$  s, where also the highest radical yield was obtained  $\approx 20\%$ .

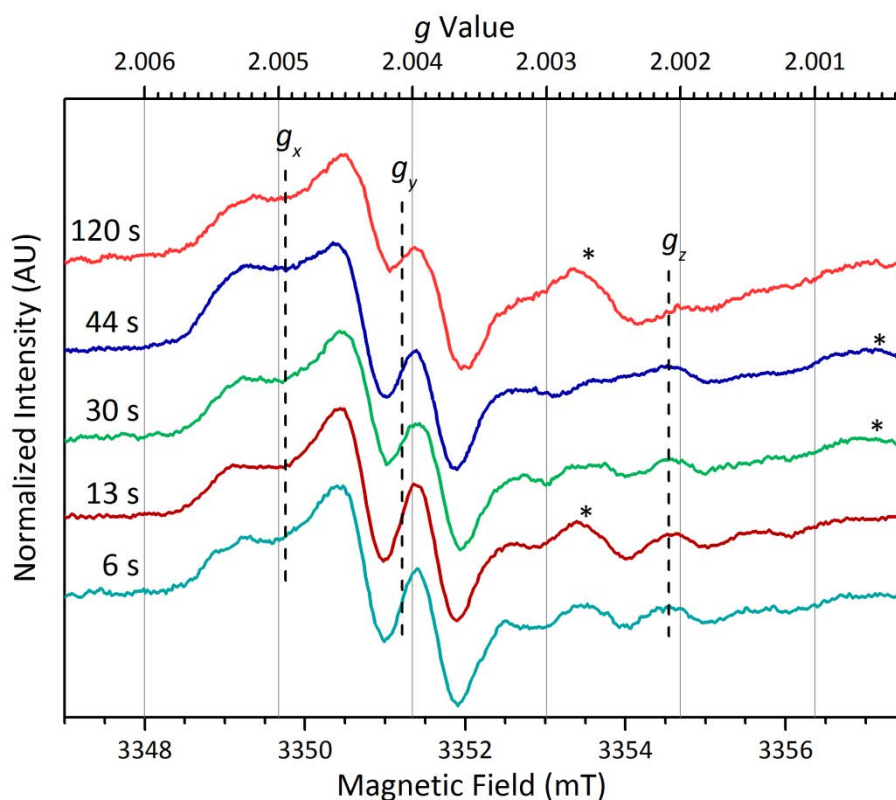


Figure 4-22: 94 GHz-Echo detected spectra of  $\text{NH}_2\text{Y}_{356}\bullet$  recorded at different freezing time points during the reaction. The spectra are sorted from 6s quench (bottom) to 2 min quench (top). The derivative was obtained from a 3 G pseudo modulation. Exp. details: 70 K;  $\pi(\pi/2)=32(16)$  ns; SRT=5 ms; Number of averages from (6-120 s): 1300, 6200, 450, 1500 and 3800.

#### 4.6.2 Polarity around $\text{NH}_2\text{Y}_{356}\bullet$ from 263 GHz and 94 GHz Spectra

In order to characterize the electrostatic environment and the electronic structure of  $\text{NH}_2\text{Y}_{356}\bullet$  spectra were measured and compared at various frequencies, E. Minnihan reported on 9 GHz<sup>67</sup> spectra and T. Argirević on 94 GHz spectra<sup>92</sup>. The 263 GHz spectra should be here compared to the  $g$  values already obtained HF parameters necessary for simulating the field dependent 94 GHz EPR spectra. 263 GHz spectroscopy was available to us since the beginning of 2012, but not all functions worked properly at the beginning. For example, the linearization procedure elongates the measurement time to an extent, for which at low radical yields no good S/N can be reached to measure in the accuracy of 50 ppm.

Thus, non-linearized field sweeps with an error of about 90 ppm had to be used. To show, however, that the spectra were consistent with or without linearization the first two spectra are included in Figure 4-23. It is clear that differences can be seen by eye. For instance the spectral width of the non-linearized field sweep is slightly larger. Nevertheless, the same  $g$  values are obtained within an error of 90 ppm (Methods §3.5). Another point is the signal contribution marked as artifact with an asterisk (\*), which is not present in the reactions quenched later. Hence, it was neglected as a signal arising from the background due to low radical yield of the sample ( $\approx 10\%$ ). Possibly a deterioration upon freeze and thawing cycles of the prepared enzyme could also explain this contribution.

The  $g$  values match already with the other investigated  $\text{NH}_2\text{Ys}\bullet$ . They are more clearly resolved in the derivative spectra of the linearized spectrum (Figure 4-24). A comparison with a simulation based on the previous results is shown in Figure 4-24. With a  $g_x$  of 2.0049 based on calibration with  $\text{Y}_{122}\bullet$  (Figure A - 7, p. 198), the radical has the highest polarity of all three  $\text{NH}_2\text{Ys}\bullet$ . The values are summarized in Table 4-7. The  $\beta$ -methylene HF coupling is within the range of 22 MHz and 29 MHz of the single mutants in  $\alpha$ . A consideration beyond the semi empirical McConnell<sup>295</sup> equation is discussed together with single amino acid DFT models in §4.6.4 (p.115). The trend in  $g_x$  values is consistent with the decreased spectral width of the  $\text{ND}_2\text{Y}_{356}\bullet$  spectra. As the  $g_x$  values is proportional to the spin density population of the oxygen nucleus, the atom in  $\text{Y}_{356}\bullet$  with the largest spin-orbit coupling, the result can be directly related to an increase of electrostatic environment around the oxygen (Theory §2.1.2). This leads to a trend of decreasing electrostatic interaction from  $\text{NH}_2\text{Y}_{356}$  over  $\text{NH}_2\text{Y}_{731}$  to  $\text{NH}_2\text{Y}_{730}$ , the in direction of forward PCET.



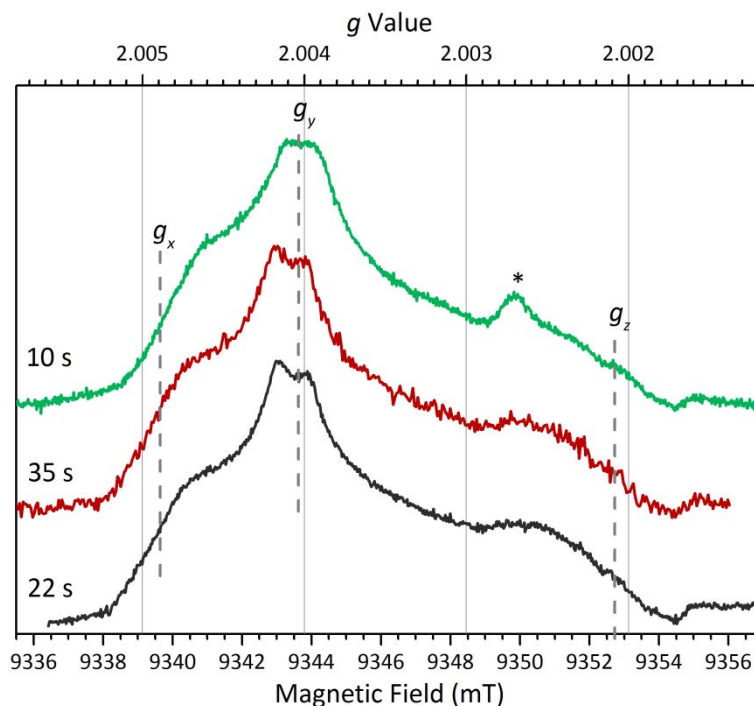


Figure 4-23: 263-GHz EPR spectra of  $\text{ND}_2\text{Y}_{356}\bullet$  measured at three reaction time points. Exp. details (from top to bottom): green: SE,  $\pi/2=90$  ns,  $\tau=260$  ns, SRT =2 ms, SPP=1000, 150 scans; red: ESE,  $\pi/2=100$ ,  $\tau=240$  ns, SRT=3 ms, SPP=100, 250 scans; black: ESE,  $\pi/2=100$ ,  $\tau=240$  ns, SRT=3 ms, SPP=100, 160 scans; black and red are not linearized.

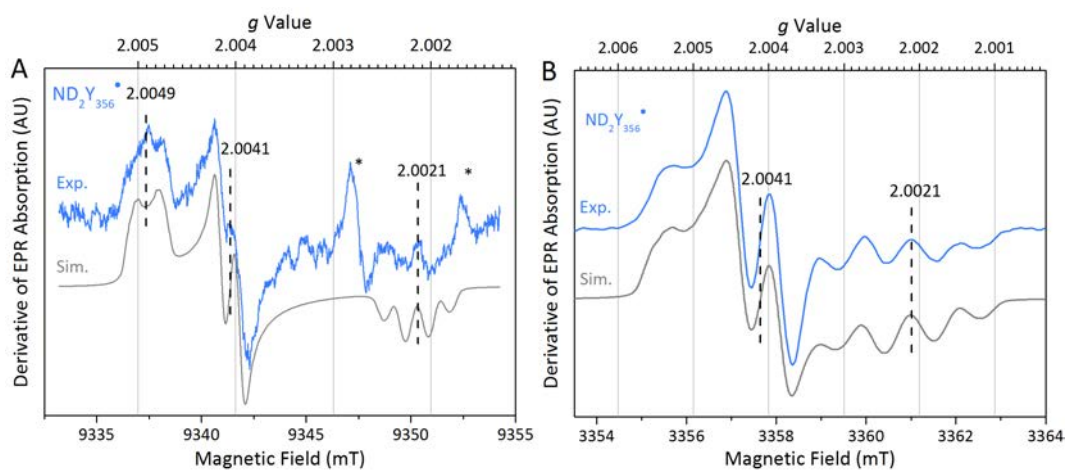


Figure 4-24: 94 and 263-GHz EPR spectra (blue) of  $\text{NH}_2\text{Y}_{356}\bullet$  and simulation (gray, Table 4-7). Exp. details: A) see Figure 4-23 (green); B) ESE at 94 GHz; T=70 K;  $\pi/2 = 32$  ns;  $\tau = 260$  ns; SRT = 5 ms; SPP = 50; scans = 750. The derivative is obtained by 10 and 3 points second order Savitzky-Golay filter for A and B, respectively.

Table 4-7: Summary of  $g$  values and HF couplings observed in the EPR spectrum of  $\text{NH}_2\text{Y}_{356}\bullet$ . The  $^{14}\text{N}$  hyperfine tensor of the  $\text{NH}_2\text{Y}\bullet$  was not varied in the simulations and kept  $A_x=2.4$  MHz,  $A_y=5$  MHz,  $A_z=30.7$  MHz.<sup>134</sup> Uncertainty in  $g$  values and HF couplings is about 0.05 ppt and 10%, respectively.

	$g_x$	$g_y$	$g_z$	$A_{\text{iso}}(\text{C}-\beta)$
$\text{NH}_2\text{Y}_{356}\bullet$	2.0049	2.0041	2.0021	27

#### 4.6.3 H bond interactions at $\text{NH}_2\text{Y}_{356}\bullet$

The observation of a polar environment around  $\text{NH}_2\text{Y}_{356}\bullet$  has enhanced the interest in the identification of its origin. Up to now, H bonds orthogonal to the ring plane were observed by ENDOR spectroscopy at  $\text{NH}_2\text{Y}_{731}\bullet$  and  $\text{NH}_2\text{Y}_{730}\bullet$ . These H bond interactions have always sharp features at  $B_0 \parallel g_y$  (cf. Figure 4-7). In  $\text{ND}_2\text{Y}_{356}\bullet$  the spectra at 94 GHz at  $B_0 \parallel g_y$  (Figure 4-25) did not show this sharp feature in a range of  $\pm 0.6$  to  $\pm 0.8$  MHz. It was quite astonishing to also see in the Q-band spectra (Appendix Figure A - 8, p.199) only contributions from the internal couplings of the amino deuterons and a matrix line with small contributions up to 0.48 MHz. A simulation considering only the matrix line and the amino deuterons is shown below the experimental result. The parameters are based on previous simulations of  $\text{ND}_2\text{Y}_{731}\bullet$  and its double mutant (§4.2.1). The difficulty in this case was that the structure and even local structural motifs are unknown. Thus, large DFT models as in the previous case could not be constructed. To evaluate the structural surrounding small models can be notwithstanding helpful. Up to now it can be stated that no strong exchangeable external H bond to  $\text{NH}_2\text{Y}_{356}\bullet$  is present, but a high electropositive environment around the oxygen is present.

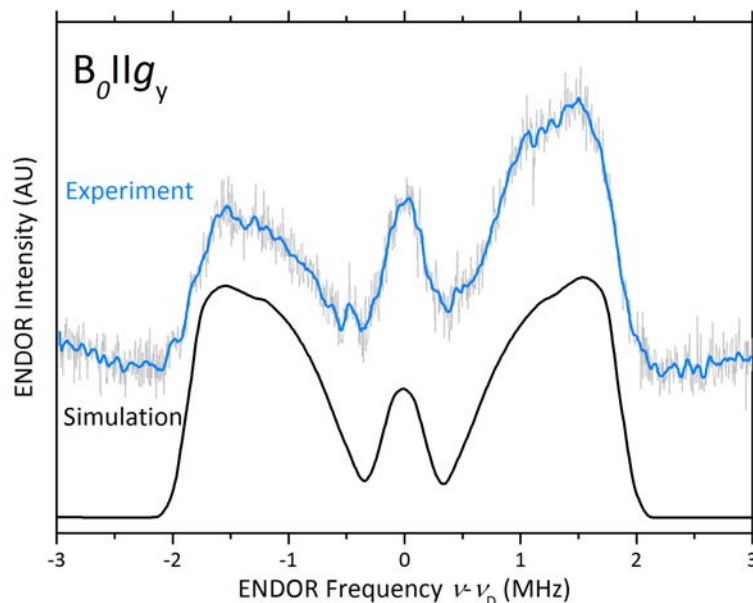


Figure 4-25:  $^2\text{H}$  ENDOR spectrum of  $\text{NH}_2\text{Y}_{356}\bullet$  quenched at 10 s compared with simulation. The experimental spectrum (gray) taken at 70K and  $B_0 \parallel g_y$  was smoothed (blue, adjacent averaging, 10 points). The simulation is shown below the parameters are reported in Table 4-8. Exp. details: Mims  $^2\text{H}$  ENDOR,  $\pi/2=20$  ns,  $\tau=200$  ns, 1 SPP random acquisition, SRT=7 ms, acquisition time = 48 h.

Table 4-8: Summary of EPR parameters for the exchangeable protons at  $\text{NH}_2\text{Y}_{356}\bullet$ . Parameters were obtained by 94-GHz  $^2\text{H}$  ENDOR spectra. Uncertainty in the parameters is up to 20%. The central line has not been assigned to a coupling, but to a matrix line. The size is given in the first line.

$\text{NH}_2\text{Y}_{356}\bullet$	$A_x$ [MHz]	$A_y$ [MHz]	$A_z$ [MHz]	$\alpha$ [°]	$\beta$ [°]	$\gamma$ [°]	$Q_x$ [MHz]	$Q_y$ [MHz]	$Q_z$ [MHz]
Simulation: Matrix line	-0.21	0.21	0.42	-	90	-	-0.06	-0.06	0.12
ND <sub>2</sub>	-0.6	-2.5	-3.5	-86	98	90	-0.04	-0.06	0.11
D(1)				-92	93	-3			
ND <sub>2</sub>	0.06	-3.1	-4.0	-96	93	-31			
D(2)				-93	84	-121	-0.06	-0.08	0.14

#### 4.6.4 Modeling $\text{NH}_2\text{Y}_s\bullet$ by DFT Calculations Considering One Amino-Acid

Quite unexpected results for  $\text{NH}_2\text{Y}_{356}\bullet$  were found, a high polarity on the one hand and on the other hand no strong resolved H bond interaction as in the other two  $\text{NH}_2\text{Y}$  single mutants. Any large DFT models at this residue have no structural foundation, thus DFT

calculations with single amino-acid models were performed on individual observable effects. First the effect of the conformer on the  $g$  value was investigated. In the second step the effect of the orientation dependence of a single H bond to  $\text{NH}_2\text{Y}\cdot$  was evaluated on  $g$  values and  $^2\text{H}$  HF couplings of the H bonding nucleus. Finally the polarity effect should be modeled by two approaches. For all three DFT studies there are examples in the literature.<sup>144, 154, 175</sup> Within these studies tyrosines or semiquinones have been investigated. The outcome cannot be directly transferred to the  $g$  values in 3-amino tyrosines. A linear scaling by  $g_x$  values or phenoxy oxygen spin density population cannot be assumed.

The error of treating the effects of conformer and H bonding separately is small as will be shown by the calculations. Generally, it should be noted that the uncertainties of DFT calculations are higher than the size of the effects studied here with 0.5 ppt for  $g$  values and up to 20% for HF couplings. Therefore the consistency within the models and the trend of the values can only be discussed here. The reason why we still describe these effects will also be highlighted by the experimental results of Chapter 5.

#### 4.6.4.1 The Conformer State of a $\text{NH}_2\text{Y}\cdot$

A relaxed surface scan over the ring dihedral  $\theta_{\text{C}\beta}$  has been performed as a DFT calculation. The B3LYP<sup>268, 271, 272</sup> hybrid functional and (def2-)TZVPP<sup>207</sup> have been used to obtain a geometry optimized dihedral within  $10^{-9}$   $E_h$  (Methods §3.6.2.2). The EPR parameter were calculated on the same basis including a continuum polarization model (COSMO<sup>296</sup>) adjusted to the polarizability of ethanol to account for a polar environment. The diheadral is defined by the angle between  $\text{C}_\beta\text{-C}_\alpha$  and  $\text{C}_1\text{-C}_6$  axis, as illustrated in Figure 4-26A. The used tyrosine model is illustrated in Figure 4-26B with typical Löwdin spin density population<sup>297</sup> of  $\rho_{\text{O}}$  24% and  $\rho_{\text{C}1}$  about 14%, here  $\theta_{\text{C}\beta}=60^\circ$  is shown. As an additional control of the relaxed surface scan the absolute energies report about a global minimum at  $\theta_{\text{C}\beta}=90^\circ$  (Figure 4-26C), the local maximum arises due to a sterical interaction of the backbone amine with a ring proton. This local maximum is not reported in a larger calculation on a dipeptide radical,<sup>129</sup> so could be a model error of the peptide bond removal.

The  $g_x$  value is minimal, when the  $\text{C}_\alpha$  is in eclipsed conformation to the  $p_z$  orbital (Figure 4-26D) due to the hyperconjugative interaction. The effect on the  $g$  value was found to be minor and in a range of 0.15 ppt. This change in  $g$  value is not significant, therefore only the trend within this model can be considered here. In Figure 4-26E&F a  $\sin^2(\theta_{\text{H}\beta})$  dependence of the HF coupling to the dihedral angle becomes evident. The  $\beta$ -methylene

HF coupling is increased if one of the protons is parallel to the  $\pi$  system, i.e.,  $H_{\beta 1}$  overlaps with  $p_z$  of  $C_1$  (Figure 4-26A). This hyperconjugation leads to an increase in spin density population in the nucleus parallel to the aromatic  $\pi$  system, therefore a nearly isotropic and positive HF interaction results. The calculation of the conformeric state reproduces the form of the McConnell equation.<sup>295</sup> The  $\beta$ -methylene proton behaves similar as the Karplus equation in NMR<sup>298</sup> on the overlap of the spin interactions. The lowest HF interaction for both beta methylene couplings is observed at for  $C_{\beta}$  axial and the highest for  $C_{\beta}$  parallel to the ring plane, with 2.0061 and 2.0059 respectively.

Although the  $g$  value is in the typical range of a free  $NH_2Y$ , the HF couplings for  $H_{\beta}$  display the full range of observed  $C_{\beta}$  HF couplings. The maximal coupling of 34 MHz found in  $\alpha-NH_2Y_{730}\bullet/C_{439}A$  as well as the smallest coupling of 22 MHz of  $\alpha-NH_2Y_{731}\bullet$  (cf. Table 4-7) lie on the curve. The  $H_{\beta}$  HF coupling has been reported in tyrosines to be inversely proportional to the oxygen spin density population.<sup>277</sup> The effect is quite small in  $NH_2Y$ 's, due to the second electronegative group in ortho position to the oxyl function. Still the phenoxy spin density population varies within the models in this section from 24% to 19% (p.124). In this case, the 27 MHz of  $NH_2Y_{356}\bullet$  from  $a_{iso}$  for  $H_{\beta}$  (Table 4-7) would correspond to a dihedral angle  $\theta_{C\beta}$  from 10-20° or 50-60°, as directly obtained from Figure 4-26E. Only in the latter case ( $55\pm 5^\circ$ ) the second  $\beta$ -methylene coupling is smaller than 10 MHz and thereby unresolved, thus  $\theta_{C\beta}$  is approximately 55°. An uncertainty of 15° can be estimated.

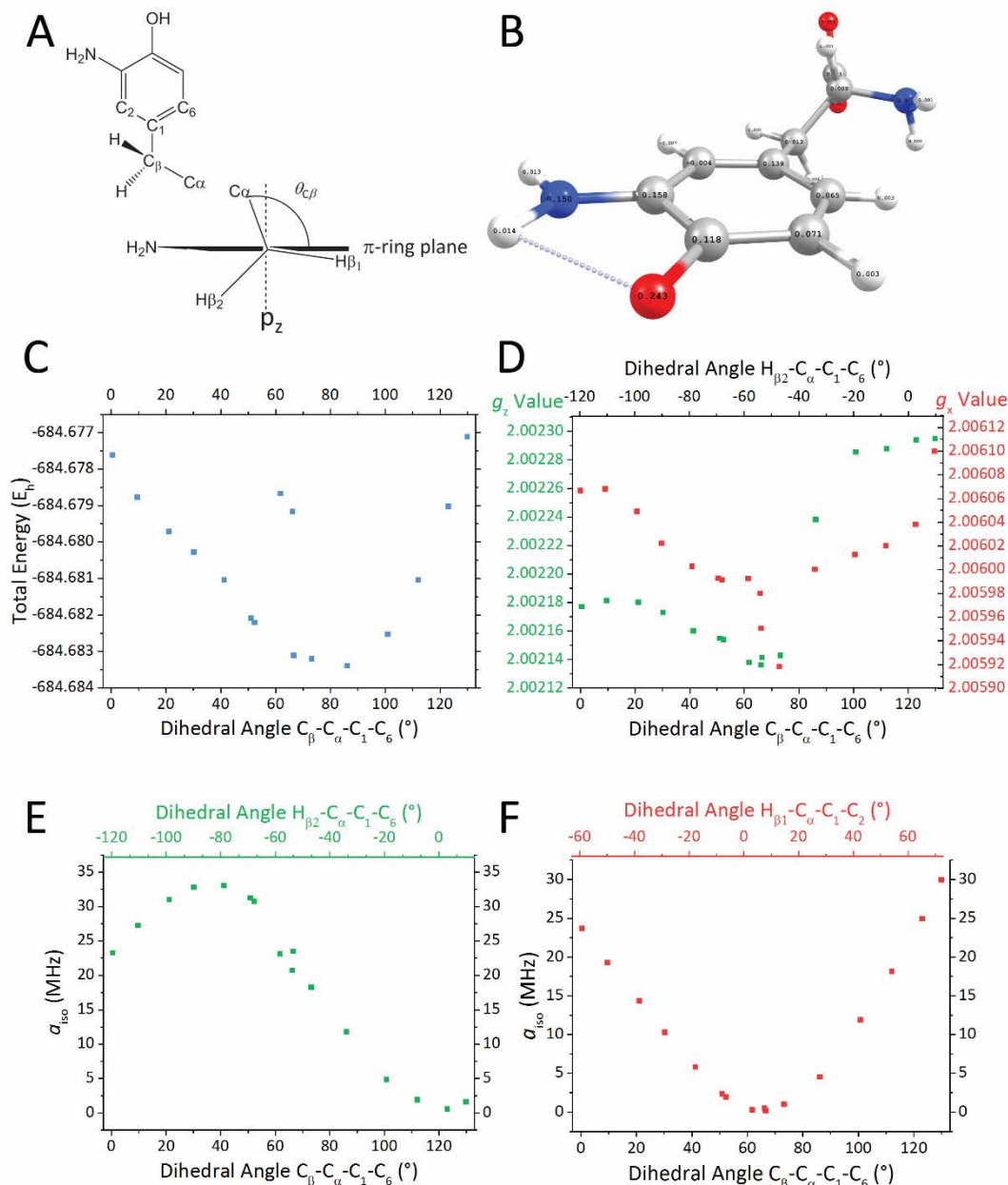


Figure 4-26: Dihedral scan over the ring dihedral. A) The ring dihedral  $\theta_{C\beta}$  is defined as  $\text{C}_\beta\text{-C}_\alpha\text{-C}_1\text{-C}_6$  on a model of a neutral 3-amino tyrosine $^\bullet$  (B). The energy in Hartree (C), the  $g_{z,x}$  value (D) and  $a_{\text{iso}}(\text{C-}^1\text{H}_{\beta 1,2})$  (E and F) are plotted against the on the ring dihedral. E and F show the dependence of  $a_{\text{iso}}(^1\text{H})$  for the individual  $\text{H}_{\beta 2/1}$  and its individual dihedral  $\theta_{\text{H}_{\beta 2/1}}$  on top of the graph for  $\text{H}_{\beta 2/1}$  (green/red).

#### 4.6.4.2 Water Dihedral Scan

The same procedure of a dihedral relaxed surface scan was applied to calculate the dihedral of one H bond from a water molecule ( $\theta_{\text{H}_2\text{O}}$ , Figure 4-27A) to  $\text{NH}_2\text{Y}^\bullet$  (§4.6.4.1). Because no

further restraints were applied, the lowest lying conformer was found in all geometry optimization models for the individual  $\theta_{\text{H}_2\text{O}}$ . Also the H bonding geometry changes slightly in course of the calculation Figure 4-27B. The  $\text{O}_{\text{NH}_2\text{Y}}\text{-H}_{\text{H}_2\text{O}}$  distance obtained correlates nicely to the  $g_x$  value of the EPR parameter calculation (Figure 4-27C).

The energy variation  $10^{-3} E_{\text{H}}$  between the models is approximately an order of magnitude smaller than in the conformeric scan (Figure 4-27C). However a clear minimum is found for the water within the plane (up to  $\pm 30^\circ$ ) with the phenoxy ring. This is in contrast to the  $\theta_{\text{H}_2\text{O}}$  of single mutant  $\text{NH}_2\text{Ys}\bullet$  discussed so far. Here in both cases a perpendicular H bond has been found. An in-plane H bond is in agreement with other tyrosine radical H bonds as found in yeast RNR  $\text{Y}_{122}\bullet$  correspondent<sup>152</sup> or in the  $\text{Y}_{\text{D}}$  of photosystem II.<sup>153</sup> The H bond angles of tyrosine radicals in  $\alpha$  are the exception in the literature, to the best of my knowledge.

The HF tensor of the H bond was therefore a core interest. Although the values obtained from the calculation had a rhombicity increasing up to  $\theta_{\text{H}_2\text{O}}=40^\circ$ , and only then an absolute axial symmetric tensor forms. For the sake of argument, only the averaged axial component  $T_{\perp}$  of the individual tensors are plotted in Figure 4-27E. Both the orthogonal and the parallel HF interaction increase with dihedral angle  $\theta_{\text{H}_2\text{O}}$ . This is in absolute contrast to the decrease in distance and increase of  $g_x$  value, in C. The orthogonal component of the HF values  $T_{\perp}$  increase faster than the parallel  $T_{\parallel}$  values. The increase is consistent with an increasing isotropic HF interaction  $a_{\text{iso}}$ , which acts on each individual HF component. It changes  $A_x$ ,  $A_y$  and  $A_z$  in the principle axis system simultaneously. The isotropic HF  $a_{\text{iso}}$  interaction is a direct indication for orbital interaction, because it is only governed by spin density in the 1s orbital of the  $^1\text{H}$  nucleus (Theory §2.1.3, Eq. (2-13)). The increase of interaction, albeit the longer H bond distance, is a consequence of the non-spherical symmetry of the  $p_z$  orbital. This is nothing astonishing *per se*,<sup>185</sup> but explains why a tensor can appear a lot weaker by a change in H bond angle.<sup>299</sup> Mostly the orthogonal component of the tensor is observed in the HF spectra, like ENDOR. The broad parallel component can be difficult to observe in these overlaying spectra. The  $g$  value variation with H bond dihedral is about 0.2 ppt. As a comparison, this is the difference between  $\alpha\text{-NH}_2\text{Y}_{731}\bullet$  and  $\beta\text{-NH}_2\text{Y}_{356}\bullet$  assuming an in-plane H bond at  $\beta\text{-NH}_2\text{Y}_{356}\bullet$ . The  $\text{C}_1$  spin density population was only minor effected by the change of H bond dihedral with standard deviation of 1.4% of the  $\rho_{\text{C1}}$  value ( $\Delta\rho_{\text{C1Lowdin}}=0.2\%$ ).

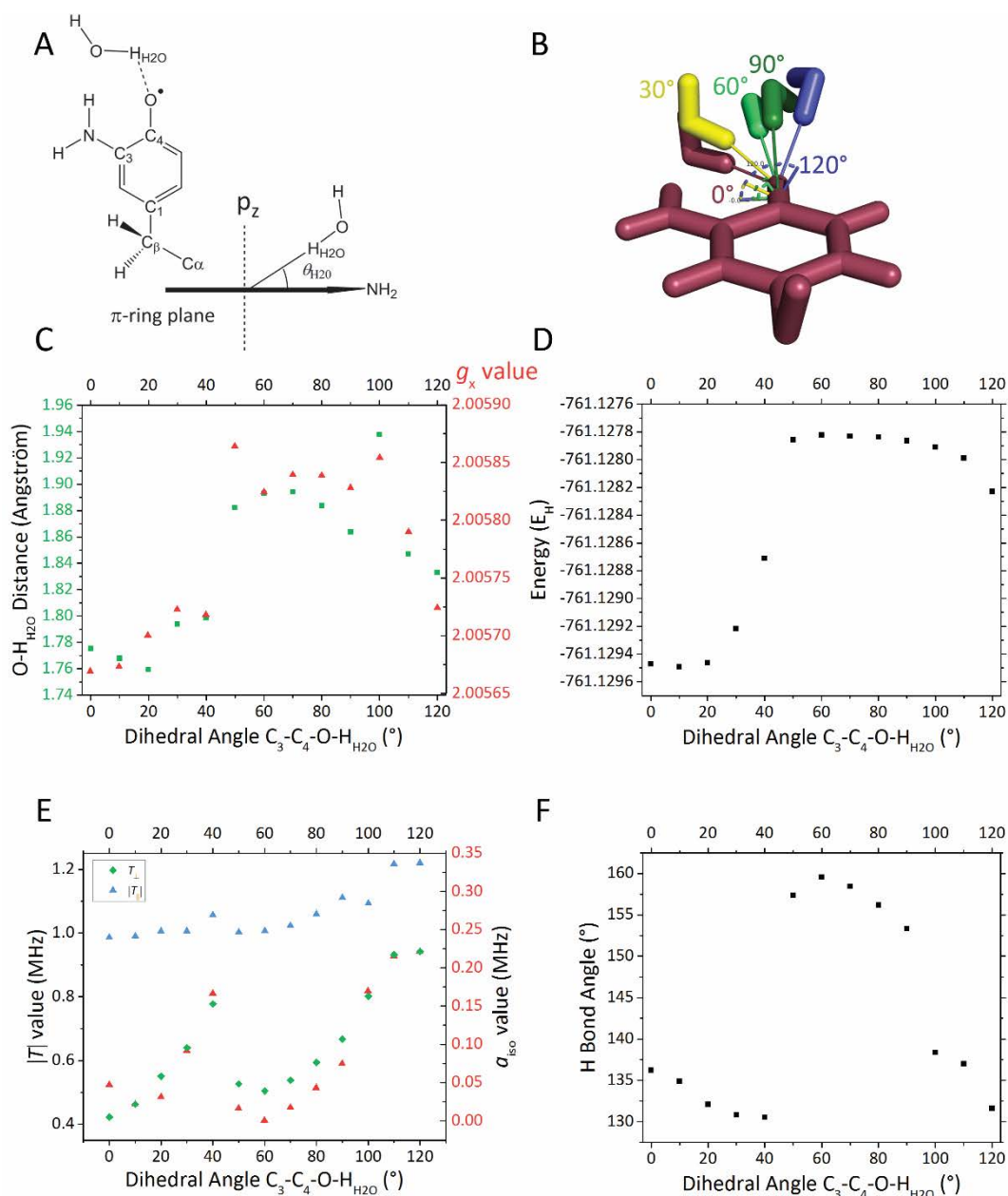


Figure 4-27: Dihedral scan over the H bond dihedral. A) The ring dihedral  $\theta_{\text{H}_2\text{O}}$  is defined as  $\text{C}_3\text{-C}_4\text{-O-H}_{\text{H}_2\text{O}}$  on a model of the neutral 3-amino tyrosine $^\bullet$  (B). C) The  $g_x$  value (red) correlates well with the H bond length (green). D) The energy in Hartree against the dihedral  $\theta_{\text{H}_2\text{O}}$ , is consistent with a global minimum at  $\theta_{\text{H}_2\text{O}}=0+30^\circ$ . E) The HF value (for  $^2\text{H}$ ) depending on the H bond dihedral is plotted. The anisotropic part is listed separately for its averaged axial ( $T_L$ , green) and absolute parallel ( $T_{||}$ , blue) value. Isotropic HF  $a_{\text{iso}}$  is shown in red. F) shows the H bond angle ( $\text{C}_4\text{-O-H}_{\text{H}_2\text{O}}$ ) as a control.



4.6.4.3 Water Network around  $\text{NH}_2\text{Y}_{356}^\bullet$ 

The last section opened up a new explanation for the  $^2\text{H}$  Mims ENDOR spectrum obtained with  $\text{NH}_2\text{Y}_{356}^\bullet$ . In plane water can have small axial HF tensor contributions of  $\approx 0.4$  MHz, but will still affect the  $g$  value by  $\approx 0.5$  ppt. Despite the high polarity used in the continuum model, this is still not the size of the effect of 1.1 ppt experimentally observed  $g_x$  shift (vs. free  $\text{NH}_2\text{Y}^\bullet$ , Table 4-5), compared to several reported DFT models of the isolated 3-amino tyrosine. The high uncertainty of DFT of about 0.5 ppt<sup>110</sup> will not deliver quantitative data, i.e., the number of H bonds present at the  $\text{NH}_2\text{Y}_{356}^\bullet$ . Therefore only the trend should be further investigated. Especially steric effects and polarity effects of a free  $\text{NH}_2\text{Y}^\bullet$  should be considered. The idea of modeling of  $\text{NH}_2\text{Y}_{356}^\bullet$  with water network emerged. Seveant et al. contributed to this idea by demonstrating a water network as a functional PCET system (Theory §2.4.3).<sup>250, 251</sup>

The models of the 3-amino tyrosine were built up successively with 1, 2 and 3 water molecules. After each additional water molecule the geometry was optimized and the EPR parameters were calculated by single point calculations. To observe the  $g$ -shift depending on weak H bonds formed by each water molecule  $g$  values and HF couplings were obtained for each H bond. Furthermore, one can observe how water molecules locate toward phenoxy oxygens, because the energy barriers are small enough to be overcome by the geometry optimization cycles. One water molecule is positioned after geometry optimization within the ring plane (Figure 4-28A) the minimum found in Figure 4-27C. After the addition of a second water in hydrogen bond distance of the phenoxy oxygen in the ring plane, the geometry optimization end up in model Figure 4-28B. Here one water is perpendicular ( $75^\circ$ ) to the ring plane H bonded to the phenoxy oxygen (wat1), the other one is H bonded to the amino proton and is located in the aromatic plane (Figure 4-28B wat2). If wat2 is removed from model B a water geometry comparable to Model A is regained, after geometry optimization. The addition of a third water molecule produced too much flexibility for its small energetic influence to converge in a DFT calculation. Albeit changes in the integration grid and removal of COSMO<sup>296</sup> polarities. Therefore, a relaxed surface scan for the third water was performed also without COSMO. It ranged from  $0^\circ$  to  $60^\circ$  H bond dihedral  $\theta_{\text{wat3}}$  with a step size of  $10^\circ$ . Figure 4-28C shows the converged geometry, a water molecule at  $40^\circ$  H bond dihedral  $\theta_{\text{wat3}}$ .

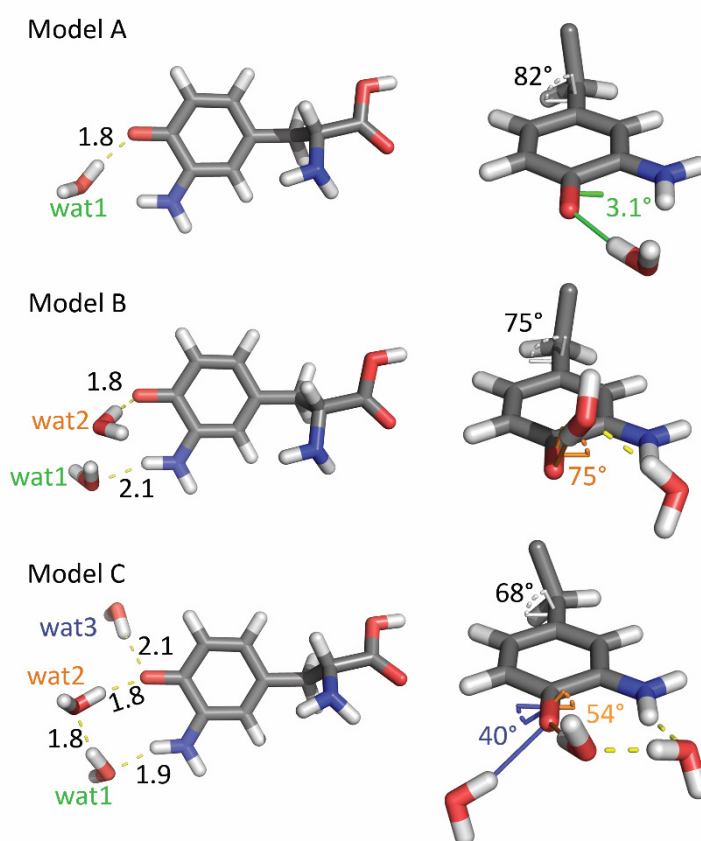


Figure 4-28: DFT models of different H bonding situations at a  $\text{NH}_2\text{Y}\cdot$ . The  $g_x$  value is compared for a model with one (A, 2.0057), (B, 2.0058) with two and with three (C, 2.0056) water molecules, named wat1 to wat3. The spin densities  $\rho$  varied through the models from  $\rho_{\text{O}}=23\%$  over 21% to 21% and for  $\rho_{\text{C1}}$  from 14% over 13% to 12% (after Löwdin<sup>297</sup>). The H bond length between the oxygen of the  $\text{NH}_2\text{Y}\cdot$  and the wat1 increases from B to C slightly with 1.79 over 1.81 to 1.83 Å. The distances in the figure are given in Å. The dihedrals are given on the left side. Calculation details: B3LYP, def2-TZVPP, COSMO(ethanol), energy converged to  $10^{-6}$  Eh.

From the  $g$  values point of view a clear trend of the H bond distance on the  $g$  value was found, as reported by C. Riplinger (Introduction, Figure 1-14C, p.23). Two H bonds almost axial to the ring plane have also been shown from his studies to suppress the  $g$  values by 0.5 ppt.<sup>110</sup> As shown on the small model calculations performed previously (Figure 1-14C, p.23), one axial H bond does not shift the  $g$  value strongly, only with a second H bond to the oxygen directed perpendicular toward the ring one could reduce the  $g_x$  by 0.9 ppt (Appendix: Figure A - 6, p.197). Model C shows the same tendency. However, the basis set used here gives slightly larger  $g$  values, because it is not as flexible as EPR II in the core region (cf. §2.3.3 p.51). Recalculating model C in order to compare it with the large models

with the smaller EPRII basis set reduces the  $g$  values to  $g_x=2.0022$ ,  $g_y=2.0043$  and  $g_z=2.0054$ . These values are within 0.5 ppt uncertainty of the DFT calculations consistent to the experimental ones (Table 4-7, p.114). Considering the large distances ( $\geq 1.8$  Å) of the two H bond partners, especially wat2, the  $g_x$  value is low enough to explain the  $g$  values observed at  $\text{NH}_2\text{Y}_{356}^\bullet$ . A protein environment can influence the H bond length for water for instance by polarization and local environment effects.<sup>300, 301</sup> Notably, the obtained ring dihedral  $\theta_{C\beta}=68^\circ$  of model C is within the prediction based on the conformeric DFT calculation with  $\theta_{C\beta}=55\pm 15^\circ$  (§4.6.4.1) in agreement to the experimental HF coupling (§4.1.2, p.77).

Additionally, one needs to discuss the HF tensors and sizes. Both H bond interactions to the oxygen from wat2 and wat3 in Model C are close to the ring plane and do not overlap with the  $p_z$  orbital of the oxygen. The  $a_{\text{iso}}$  values are with -40 and -70 kHz (for  $^2\text{H}$ ) are in the lower range of Figure 4-27E. Although all water containing models would result in a decrease of  $g_x$  value similar to the experiment, they do also show an HF tensor in a size, which would be larger than the observed matrix line. The values are collected in Table 4-9.

Table 4-9: EPR parameters from DFT of  $\text{NH}_2\text{Y}^\bullet$  in water Model C. The HF couplings are within 20% uncertainty and the  $g$  values have an uncertainty of 0.5 ppt. Both HF and  $g$  values are identical within uncertainty for two basis sets used here.

Proton HF	$A_x$ [MHz]	$A_y$ [MHz]	$A_z$ [MHz]
wat1- $^1\text{H}$	-2.7	-3.0	5.0
wat2- $^1\text{H}$	-4.0	-4.2	6.8
wat3- $^1\text{H}$	-2.7	-3.0	5.0
$\text{H}_{\beta 1}$ - $^1\text{H}$	2.2	-0.9	-1.1
$\text{H}_{\beta 1}$ - $^1\text{H}$	23	18	19
Deuteron HF	$A_x$ [MHz]	$A_y$ [MHz]	$A_z$ [MHz]
wat1- $^2\text{H}$	-0.42	-0.46	0.77
wat2- $^2\text{H}$	-0.41	-0.47	0.77
wat3- $^2\text{H}$	-0.62	-0.64	1.04
Basis set	$g_x$	$g_y$	$g_z$
TZVPP	2.0056	2.0042	2.0022
EPRII	2.0054	2.0043	2.0022

A perpendicular H bond orientation to  $\text{NH}_2\text{Y}_{356}^\bullet$  could be strongly disfavored based on the comparison between  $^2\text{H}$  ENDOR spectra of  $\text{NH}_2\text{Ys}^\bullet$  in  $\alpha$ . A proton bound within the ring

plane, however, with couplings ( $^2\text{H}$ ) of -0.5, -0.5 and 1 MHz could be unresolved in the  $\text{NH}_2\text{Y}_{356}\bullet$   $^2\text{H}$  ENDOR spectra. This coupling can be consistent to the experimentally observed matrix line  $\pm 0.4$  MHz, if the uncertainty of the calculated values and the broadening by quadrupole interaction are considered. The amino deuteron couplings, however, prevent an unambiguous assignment.

#### 4.6.4.4 Positive Charges in the Surrounding of $\text{NH}_2\text{Y}_{356}\bullet$

A second hypothesis for the structure between  $\beta\text{-W}_{48}$  and  $\beta\text{-Y}_{356}$  was postulated by Bollinger et al. in 2006. They proposed  $\text{Mg}^{2+}$  interaction along the PCET. They observed in a  $\text{Y}_{122}\text{F}$  mutant upon cofactor assembly a tryptophan radical  $\text{W}^+\bullet$ . The lifetime and the kinetic formation of a  $\text{Y}\bullet$  in  $\beta_2$  was dependent on the presence of  $\text{Mg}^{2+}$  and  $\beta\text{-Y}_{356}$ . It was proposed that  $\text{Mg}^{2+}$  in RNR is not only essential for nucleotide reduction,<sup>302</sup> but also for mediating the PCET between  $\text{W}_{48}$  and  $\text{Y}_{356}$ .<sup>74, 303</sup>

On the other hand earth alkaline metals in their +II oxidation state have been used in the literature to model polarity effects in DFT calculations. These models were used especially if direct treatment of explicit water was not enough to sufficiently reduce the  $g_x$  value to the experimental values.<sup>175, 304, 305</sup> It has been as well an alternative to “correction factors”<sup>216</sup> for treating H bonding effects in EPR/DFT calculations. Magnesium(II) is usually coordinated by six ligands, therefore a small DFT model taking these interactions into account was set up. It includes an essential glutamate residue either  $\beta\text{-E}_{52}$  or  $\beta\text{-E}_{350}$ , modeled by acetic acid required for charge balance. The geometry optimized model is shown in Figure 4-29. The  $g$  values reproduced a highly polar environment with 2.0051, 2.0040 and 2.0022 which is in excellent agreement with the experimentally observed spectra (Table 4-7). Although there is no evidence for such an  $\text{Mg}^{2+}$  coordination, it demonstrates the effect of positive charges in reducing the  $g$  values significantly. The oxygen spin density population is, after the Löwdin analysis with  $\rho_{\text{O}}=19\%$ , 2% lower than in the water network models.

In a more general picture positive charges are present in proteins also within individual amino acids.<sup>306</sup> Especially at the interface salt bridges and interactions with aromatic systems might govern protein-protein interaction.<sup>307</sup> Positively charged amino acids are not present in the 32 C-terminal amino acid tail. The difference in their isoelectric point has helped for instance in the separation of truncated and full length  $\beta$  peptides.<sup>308</sup> However, positively charged arginine's are observed in the  $\beta$  subunit and in the  $\alpha$  subunit as essential for activity

and could have an effect in subunit interaction.<sup>309</sup> The  $\beta$  32 amino acid tail harbors two glutamates which on the other hand introduce a negative charge. By forming salt bridges these positive charges could be neutralized to enhance a folding of this  $\beta$  C terminal tail. Therefore, positive charges residues should also be considered to lie within the interaction sphere of  $Y_{356}^\bullet$ .

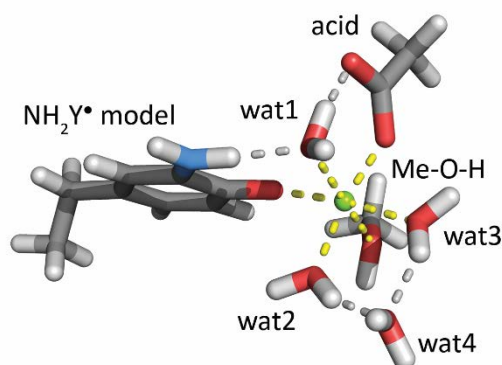


Figure 4-29: DFT model demonstrating the effect of positive charges ( $Mg^{2+}$ ) in the surrounding of the phenoxyl nucleus. In this model an  $Mg^{2+}$ -Ion (green) was placed and a coordination sphere (yellow dotted line) was modeled. An acid, an alcoholic function and 4 waters are included. Calculation details: B3LYP, def2-TZVPP, COSMO (ethanol), Energy converged to  $10^{-6}$  Eh.

#### 4.7 Discussion of the $\beta$ - $NH_2Y_{356}^\bullet$ Radical Intermediate

The essential radical intermediate formed at position 356 is of key interest in understanding how the RNR transfers an electron selectively through the  $\alpha/\beta$  subunit interface. There are no detailed structural information on  $Y_{356}$ . The diagonal distance between  $Y_{122}^\bullet$  and  $NH_2Y_{356}^\bullet$  could be determined in the active enzyme (Figure 1-8, p.12). The comparison between the  $pK_a$  values of Y intermediates using  $NO_2Y$  mutations has demonstrated that residue 356 is more polar than the Ys in  $\alpha$  (§1.4.5, p.16).<sup>41</sup> Investigations on  $NH_2Y^\bullet$ s show a similar electropositive environment at position  $Y_{731}$ ,  $Y_{730}$  and,  $Y_{356}$ , (Table 4-5, p.101).<sup>92</sup> So far no conclusions in agreement to the redox potential difference ( $\approx 60$  mV, Figure 1-11, p.17) between  $Y_{731}$ ,  $Y_{730}$  and,  $Y_{356}$  could be drawn. Furthermore, there is no information about the H bond network, which is crucial to understand the forward PCET mechanism.

$^2H$  ENDOR spectra on  $NH_2Y_{356}^\bullet$  did not resolve any exchangeable H bond in contrast to the Y intermediates in the  $\alpha$  subunit. The  $g_x$  value from 263 GHz EPR, as indicator for an electrostatic environment was correlated to number of intermolecular

H bonds. An apparent contradiction between zero perpendicular H bonds and a **g** tensor indicating high polarity has been discussed. On the one hand, an H bond network within the aromatic plane, could have unresolved HF interactions. The parallel component of the HF interaction  $T_{\parallel}$  is reported to be difficult to detect in Ys• due to their broad, low intense line shape.<sup>299</sup> On the other hand positive charges could be modeled to account for the **g** tensor and the HF tensor contributions.

Despite these problems, it could be demonstrated that a perpendicular strong or moderate H bond is absent at NH<sub>2</sub>Y<sub>356</sub>•. Thus it seems to be unlikely that the NH<sub>2</sub>Y<sub>356</sub>• can engage in a similar “ $\pi$ -stacking” geometry as Y<sub>731</sub> and Y<sub>730</sub>. Additionally, NH<sub>2</sub>Y<sub>731</sub>• has not shown any strong or moderate H bond toward the direction of residue 356. From a mechanistic point of view a perpendicular H bond has been pointed out to be a prerequisite for a “HAT geometry”, as illustrated in Figure 2-15A (p. 51),<sup>113</sup> allowing an adiabatic proton transfer. This point indicates that a collinear CPET step from Y<sub>356</sub> to Y<sub>731</sub> is unlikely. On the other hand drawbacks of the NH<sub>2</sub>Y mutation became obvious in the investigation of NH<sub>2</sub>Y<sub>356</sub>•. The introduced amine function can act as an H bond donor and thereby influences the H bond network. Especially for an in-plane H bond as found at residue 356 NH<sub>2</sub>Ys could be non-innocent reporters for H bonding networks (cf. Figure 4-28, p.122).

The NH<sub>2</sub>-group also changes the EPR property of Ys investigated. The broad ENDOR absorption of amino proton <sup>2</sup>H resonances is spectroscopically a resolution problem, which can lead to unresolvable H bond interactions. In the case of  $\beta$ -NH<sub>2</sub>Y<sub>356</sub>• it is aggravated by the intrinsically low S/N due to low Y<sub>122</sub>•/ $\alpha_2\beta_2$  ratios (0.5, see Methods) in  $\beta$  mutants.

The introduced H bond donor function (NH<sub>2</sub>) has been relatively unproblematic in the well-structured surrounding of  $\alpha$ -NH<sub>2</sub>Y<sub>730</sub>• as could be revealed by no additional H bond found compared to Y<sub>730</sub>• large model.<sup>67, 110</sup> In the  $\alpha$ -NH<sub>2</sub>Y<sub>731</sub>• for the first time water H bonded to the amino group (Model 3, p.98) was considered and reproduced the experimental results better.<sup>254</sup> In contrast, at  $\beta$ -NH<sub>2</sub>Y<sub>356</sub>• no structural information is at hand to separate the NH<sub>2</sub> effect from the Y<sub>356</sub>• H bond network. Thus, further experimental studies are necessary on a natural Y•. Therefore, we decided to simplify our system and searched for an alternative probe, which is described in the next chapter.

# 5 2,3,5-F<sub>3</sub>Y<sub>122</sub>• TO GENERATE Y• INTERMEDIATES IN THE PCET

## 5.1 Introduction of a New Rate Limiting Step to Generate Y<sub>356</sub>•

The idea of investigating naturally occurring radicals in the RT of RNR is tremendously appealing. While amino tyrosines offered the opportunity to compare all three transient tyrosin based radical intermediates, trapped tyrosines on the pathway have complimentary advantages. Recently, Yokoyama et al. published a new way of by-passing the natural conformational gating in ribonucleotide reductase.<sup>84, 118</sup> Here not the potential of the radical intermediate was lowered; instead they increased the potential of the Y<sub>122</sub> to prevent a completion of the reverse PCET. The formed intermediate radical is to a large extent (90%) Y<sub>356</sub>•. In this study, they have used  $\beta_2$ -NO<sub>2</sub>Y<sub>122</sub> with a large excess potential of 200 mV (cf. Figure 5-1A). This NO<sub>2</sub>Y<sub>122</sub>• not only has a short lifetime in  $\beta_2$ , but also can populate non-pathway side reactions. Additionally, it has to be coupled to cofactor assembly to reduce  $\beta_2$ -NO<sub>2</sub>Y in the first place. Thus the individual PCETs to Y<sub>122</sub> and from Y<sub>122</sub>• to Y<sub>356</sub>• cannot be studied separately.<sup>84</sup>

Nevertheless, the idea to trap a tyrosyl radical in its natural protein environment is appealing. 2,3,5-F<sub>3</sub>Y has shown to overcome the conformational gating despite the absence of a large over potential as in NO<sub>2</sub>Y.<sup>119, 127</sup> 2,3,5-F<sub>3</sub>Y is approximately 30 mV harder to

oxidize than Y to its neutral radical state.<sup>119</sup> In Chapter 4, it was demonstrated that an H bond interaction between  $\alpha_2$ - $Y_{731}$  and  $\alpha_2$ - $Y_{356}$  is unlikely. If an H bond interaction occurs this interaction would be only consistent with a weak H bond ( $a_{iso}\approx 0$ ). Therefore, it seemed to be possible to investigate with this 2,3,5- $F_3Y_{122}\bullet$  the forward (Figure 5-1C) as well as the reverse PCET (Figure 5-1B). For the former case, the pathway is blocked by a phenylalanine at  $\alpha$ - $Y_{731}$  after PCET initiation by 2,3,5- $F_3Y_{122}\bullet$ . In the latter case, wild type  $\alpha$  is used with  $\beta$ -2,3,5- $F_3Y_{122}$ . Here it has been postulated that a reverse PCET takes place based on the identical rate constant ( $20\text{ s}^{-1}$ ) of  $Y_{356}\bullet$  and CDP formation.<sup>\*\*\*</sup> This argument is analog to the one used for  $\beta_2$ - $NO_2Y_{122}\bullet$ .<sup>84</sup> As foundation to future work this thesis will investigate  $\beta$ -2,3,5- $F_3Y_{122}:\alpha$ -wt &  $\alpha$ - $Y_{731}F$  trapped on the second time scale. This time scale is comparable to the 3-amino tyrosine reaction times (Chapter 4). Initial studies of  $\beta$ -2,3,5- $F_3Y_{122}:\alpha$ -wt have shown identical 9 GHz spectra of 20 s freeze quench or RFQ samples.<sup>28</sup> However, the relative ratios between  $Y_{356}\bullet$  and 2,3,5- $F_3Y_{122}\bullet$  change from 50% to 30% for  $Y_{356}\bullet$ .<sup>28</sup>

The focus of this thesis is the identification of intermolecular interactions by HF ENDOR. For this purpose, a natural tyrosine is beneficial, because the absence of  $ND_2$  couplings in the  $^2H$  Mims ENDOR spectra in deuterated buffer offers a better resolution for small radical concentrations. The spin density population on the phenoxy nucleus is higher in  $Ys\bullet$  than  $NH_2Ys\bullet$ . Therefore one should expect an increase in dipolar HF couplings to the phenoxy oxygen [see Eq. (2-16)]. This larger HF coupling can increase the Mims ENDOR efficiency (cf. Figure 2-10B p.43). Up to now the forward radical transfer was discussed using  $NH_2Ys\bullet$ . Hence, the focus of this chapter will be the forward transfer.

---

<sup>\*\*\*</sup> Kanchana Ravichandran and J.A. Stubbe, MIT, unpublished results.



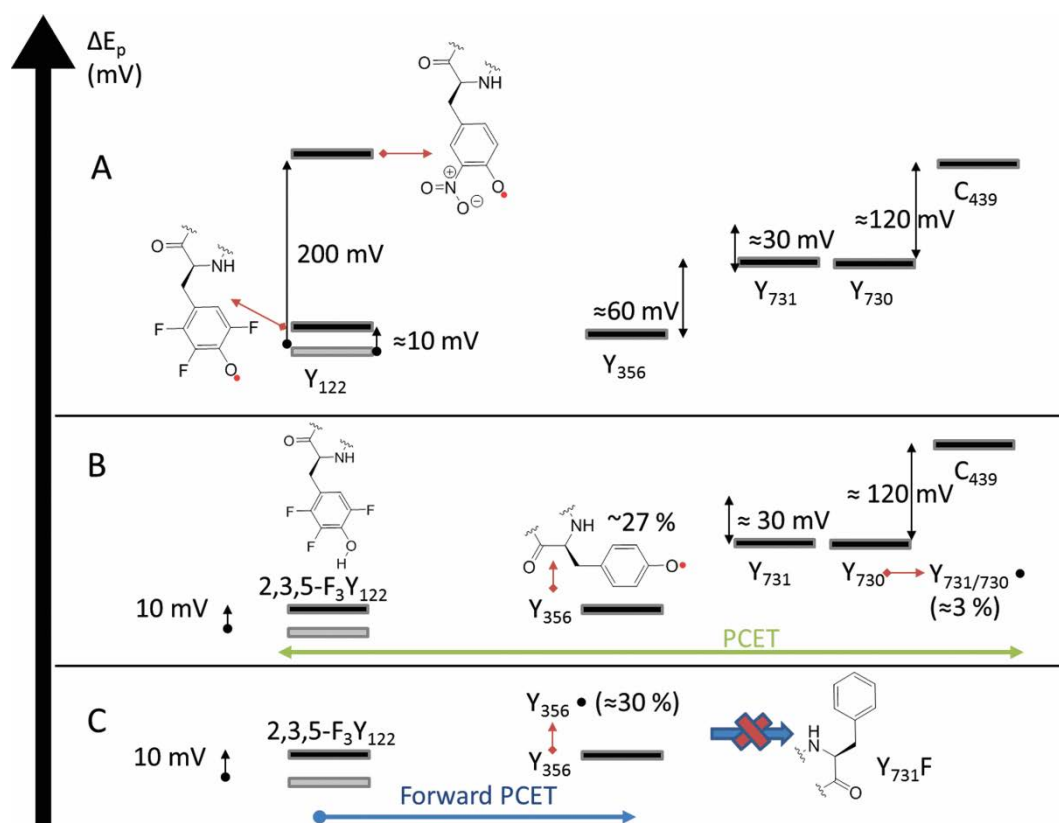


Figure 5-1: Reduction redox potentials are shown along the PCET in mV relative to the oxidation of  $Y_{122} \rightarrow Y_{122}^{\bullet} + e + H^+$ . The potential height is based on the work of recent publications.<sup>41,110</sup> A) To trap  $\beta$ - $Y_{356}^{\bullet}$  in a wild type environment the redox potentials of two mutations  $\beta$ - $2,3,5-F_3Y_{122}$  and  $\beta$ - $NO_2Y_{122}$  are shown. B) By using  $\beta$ - $2,3,5-F_3Y_{122}$  with  $\alpha$ -wt a radical assigned to  $\beta$ - $Y_{356}^{\bullet}$  could be trapped in the ns timescale.<sup>28</sup> Yields of 27%  $\beta$ - $Y_{356}^{\bullet}$  together with 3% of  $\alpha$ - $Y_{731}^{\bullet}$  and  $\alpha$ - $Y_{730}^{\bullet}$  are expected.<sup>84</sup> The PCET is free to proceed to nucleotide turnover and back, thus in the second time scale an equilibrium radical distribution will be observed. C) To observe a radical species of the forward PCET, most likely  $Y_{356}^{\bullet}$ , a PCET blockade at  $Y_{731}$  is introduced with  $Y_{731F}$ .

Prior investigations of the radical intermediates a high-field EPR characterization of  $\beta$ - $2,3,5-F_3Y_{122}$  was conducted. This was necessary due to several reasons. First, this species had already been demonstrated to have changed relaxation behavior in CW EPR spectra as observed by saturation experiments compared to  $\beta$ - $Y_{122}^{\bullet}$ .<sup>28</sup> We have observed in pulse EPR spectra that the relaxation filter as introduced for  $Y_{122}^{\bullet}$  does not work as efficiently with  $2,3,5-F_3Y_{122}^{\bullet}$ . Thus, possible contributions to the spectra have to be identified. Most importantly, one needs to check, if the newly incorporated mutation induce disturbances in the structure as compared to  $\beta$ - $Y_{122}$ .

The work of Seyedsayamdost et al. showed that 2,3,5-F<sub>3</sub>Ys are deprotonated in solution while Ys are protonated.<sup>119</sup> So it is necessary to understand more of the electronic structure of this mutant, and possibly understand how the conformational gating is circumvented by this UAA.<sup>120</sup>

## 5.2 Multifrequency EPR Characterization of 2,3,5-F<sub>3</sub>Y<sub>122</sub>•

In order to characterize the electronic structure of a radical the HF couplings and the *g* values have to be determined. Large HF couplings in 2,3,5-F<sub>3</sub>Y<sub>122</sub>• are the β-methylene <sup>1</sup>H and the <sup>19</sup>F couplings.<sup>28, 120</sup> To compare the effect of the mutation on the environment, especially the β-methylene coupling can give indications which conformer is present. Large couplings can be observed in the 9 GHz spectrum, whereas the **g** tensor is observable at high-field/frequency measurements. A simulation with a shared parameter set delivers the best obtainable parameters. In Figure 5-2 the spectra of 3 frequencies are shown with the best simulation below. The 9 GHz spectrum consists of a triplet, quartet, and triplet pattern. This demonstrates that the large β-methylene coupling is roughly the same size as the 2-<sup>19</sup>F HF interaction (Table 5-1). From a doublet of doublets a distorted triplet arises, as observed on the low and high-field side of this spectrum. The last triplet in the center overlaps with the rest of the spectrum consistent with a doublet observed in the higher field spectra at B<sub>0</sub>||g<sub>x</sub> or g<sub>y</sub>. At 94 GHz, the strong orientation dependence of the <sup>19</sup>F HF tensors becomes evident, here B<sub>0</sub>||g<sub>x</sub> and g<sub>y</sub> show only a doublet contribution. The triplet, quartet, and triplet pattern are only observed at B<sub>0</sub>||g<sub>z</sub>. The triplet at the high-field side seems to be strongly distorted and only merely visible within the S/N. One explanation could be a not completely integrated echo signal, diminishing weak intensities at the edges of the spectrum from these large HF couplings. The low field side overlaps with the g<sub>y</sub> doublet, thus only at the edges weak peaks are resolved. The 263 GHz spectrum continues the trend and delivers stronger constraints for the g<sub>x</sub> and g<sub>y</sub> values. As an internal standard the strong contribution of Mn<sup>2+</sup> ions can be used. These sharp peaks are clearly visible in the spectrum and distort the high-field line shape. For the simulation the β-methylene coupling and the *g* values were taken from the HF spectra were the large HF couplings present at B<sub>0</sub>||g<sub>z</sub> whereas taken from the 9 GHz spectrum. This resulted in a reasonable agreement of the simulation to the experimental spectrum in a small number of iterations if a full matrix diagonalization for the electron spin was used (EasySpin; cf. §2.1.6, p.36).<sup>169</sup> This is necessary in this case due to the

large  $^{19}\text{F}$  HF couplings observed here. To improve the values of the  $\beta$ -methylene couplings a Davies ENDOR improved variant<sup>310</sup> was recorded by R. Rizzato of our group (unpublished data).

A conformeric change can be observed from the obtained  $a_{\text{iso}}$  of  $\text{C}_\beta\text{-H}$  with 45 MHz. A semi-empirical formula [McConnell Eq. (5-1)] connects this  $a_{\text{iso}}$  value with the rotation angle around  $\text{C}_\beta\text{-C}_1$  axis, the ring dihedral  $\theta_{\text{pz}\beta}$ .<sup>178, 295</sup> In this equation the spin density population at  $\text{C}_1$  ( $\rho_{\text{C}_1}$ ) is a linear proportional to  $a_{\text{iso}}(\text{C}_\beta\text{-H})$  and  $B_1$  is an empirical constant. Wt-Y122• has an  $a_{\text{iso}}$  value of 55 MHz, which is significantly larger.<sup>157</sup> The spin density population is not *a priori* known for the new UAA; it can be derived either experimentally by stepwise isotopic labeling or theoretically by a DFT calculation. The DFT can give an estimate of the typical  $\text{C}_1$  spin density population  $\rho_{\text{C}_1}$  to determine the  $\text{C}_\beta\text{-H}$  hyperfine couplings [see Eq. (5-1)].<sup>178, 295</sup> The  $\text{C}_1$  spin density population  $\rho_{\text{C}_1}$  is experimentally obtained for  $\text{Y}_{122}\bullet$  with 38%.<sup>311</sup> DFT structures of  $\text{Y}\bullet$  under similar conditions obtain with 37% similar Mulliken<sup>312, 313</sup> spin density populations. The spin density populations calculated for a 2,3,5- $\text{F}_3\text{Y}_{122}\bullet$  (Figure 5-3A) are with 34% roughly 10% smaller and would lead to an  $a_{\text{iso}}(\text{C}_\beta\text{-H}) = 49$  MHz for the same conformer. This indicates a slight but significant conformeric change of the 2,3,5- $\text{F}_3\text{Y}_{122}\bullet$ . Using the McConnell Eq. (5-1) the angle  $\theta_{\text{pz}\beta}$  between the projection of  $\text{p}_z(\text{C}_1)$  and  $\text{C}_\beta\text{-H}_\beta$  is estimated to be  $16\text{-}25^\circ$ .<sup>176, 178, 314, 315</sup> For  $\text{Y}_{122}\bullet$  a  $\theta_{\text{pz}\beta}$  was obtained by single crystal EPR data to be  $12\text{-}16^\circ$ ,<sup>63</sup> thus the value is  $0\text{-}9^\circ$  larger. The  $\text{sp}^3$  geometry at  $\text{C}_\beta$  has angle of  $117.8^\circ \pm 0.6^\circ$ ,<sup>277</sup> thus a  $\theta_{\text{C}\beta}$  value between  $44\text{-}53^\circ$  is obtained (Figure 5-3B). X-ray diffraction has shown a dihedral  $\theta_{\text{C}\beta}$  of  $46.2^\circ$ , as seen in Figure 5-3C.<sup>63</sup> This gives a tendency of the occurred change in ring dihedral.

$$\begin{aligned}
 a_{\text{iso}}(\text{C}_\beta - \text{H}) &\approx B_1 \cdot \rho_{\text{C}_1} \cdot \cos^2(\theta_{\text{pz}\beta}) ; B_1 = 147 - 162 \text{ MHz} \\
 \Leftrightarrow \theta_{\text{pz}/\text{H}\beta} &\approx \left( \arccos \left[ a_{\text{iso}}(\text{C}_\beta - \text{H}) \cdot (B_1 \cdot \rho_{\text{C}_1})^{-1} \right] \right)^{1/2}
 \end{aligned}
 \tag{5-1}$$

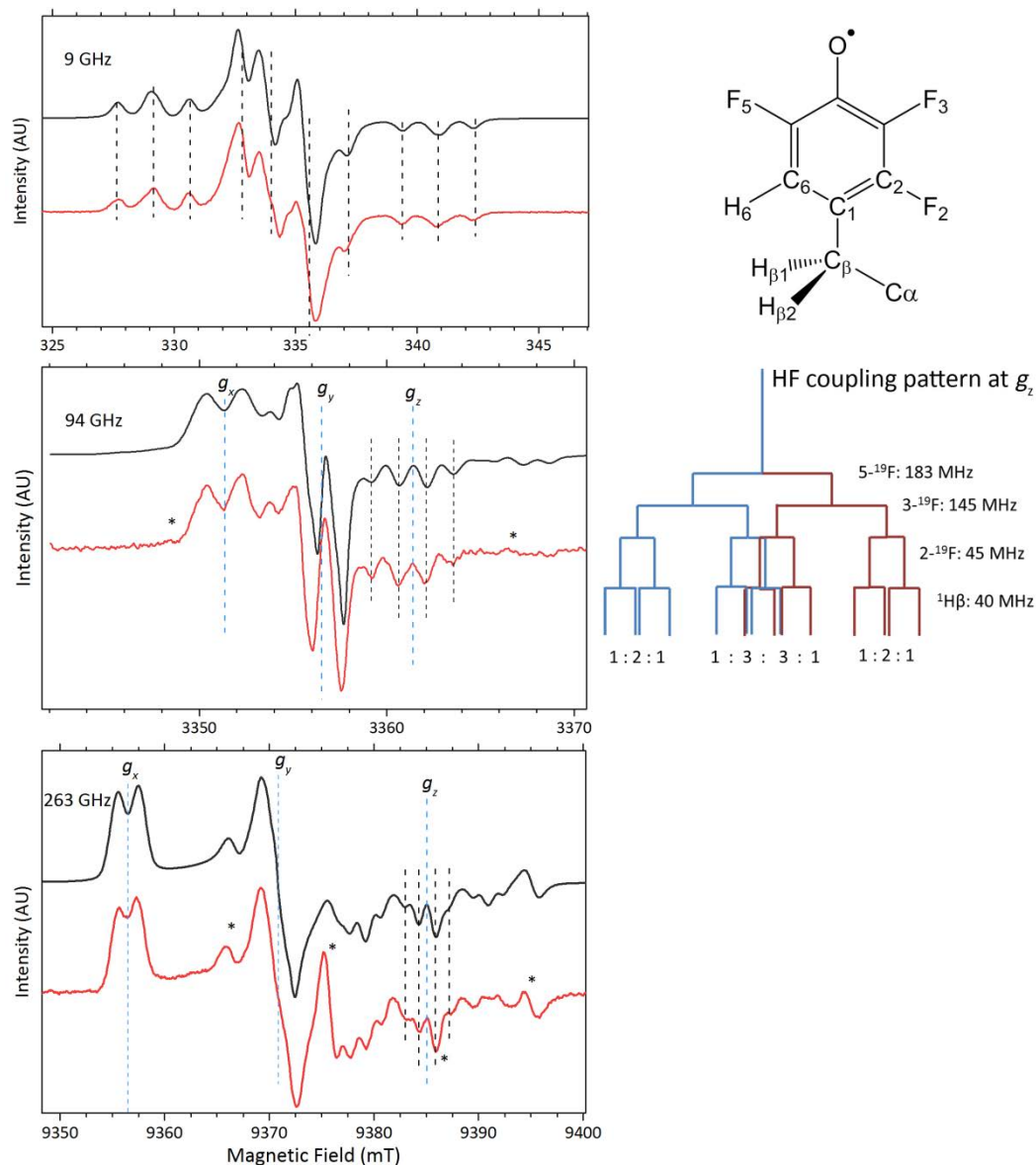


Figure 5-2: EPR spectra of 2,3,5-F<sub>3</sub>Y<sub>122</sub>• at different observing frequencies (9, 94 and 263 GHz). The experimental trace (red) and the simulation (black) are compared based on the same simulation parameters (Table 5-1). The black dashed lines show the HF coupling pattern. The canonical  $g$  values are marked as blue dashed lines in the 94 and 263 GHz ESE spectra. Right: The 2,3,5-F<sub>3</sub>Y• and the HF coupling pattern for  $B_0 \parallel g_z$  is shown. Exp. details: 9 GHz: CW-EPR spectra of 2,3,5-F<sub>3</sub>-Y<sub>122</sub>• in H<sub>2</sub>O at 80 K, MA=1 G, conversion time=80 ms, power attenuation = 17 dB, scans=16; 94 GHz: ESE spectrum of 2,3,5-F<sub>3</sub>-Y<sub>122</sub>• in D<sub>2</sub>O (50 μM) at 10 K,  $\pi/2(\pi)=30(60)$  ns,  $\tau=240$  ns, SRT=200 ms, number of averages = 16; 263 GHz: ESE spectrum of 2,3,5-F<sub>3</sub>-Y<sub>122</sub>• in D<sub>2</sub>O (50 μM) at 10 K,  $\pi/2(\pi)=60(120)$  ns,  $\tau=290$  ns, SRT=20 ms, number of averages = 1950. The 263 GHz spectra show a 3% Mn<sup>2+</sup> contribution ( $g_{\text{eff}}=2.00110$ ) with an HF coupling of  $A_{\text{Mn}} \sim 94$  G marked with an asterisk (\*). The derivative of the pulse spectra was built using a 10 points second order Savitzky-Golay filter.

The  $g$  values obtained by simulation are a source of information about the local electrostatics. In this case, the environment around  $Y_{122}$  is reported to be apolar and influenced by van der Waals interactions.<sup>46</sup> To separate the effect from the UAA 2,3,5-F<sub>3</sub>Y and the local polarity of the environment around 2,3,5-F<sub>3</sub>Y<sub>122</sub>• a DFT calculation delivered  $g$  values. The environment around  $Y_{122}$  has a lower polarity as other radicals discussed up to now. A continuum polarization<sup>296</sup> of chloroform ( $\epsilon=4$ ) was used in agreement with previous DFT calculations.<sup>294</sup> The  $\mathbf{g}$  tensor shown in Figure 5-3 and its values are summarized in Table 5-1. The  $\mathbf{g}$  tensor is identical within error to the simulation. The  $\beta$ -methylene in the final model was chosen similar to the McConnell estimate  $\theta_{C\beta}=55^\circ$ . In this case an  $a_{iso}$  of 47 MHz is within uncertainty identical to the experimentally obtained  $\beta$ -methylene HF coupling ( $a_{iso} = 45$  MHz). However, other HF couplings, like 3-F and 2-F, are generally too large and too less dipolar. In order to discriminate the error between neglected contributions of the protein and DFT more sophisticated calculations would be necessary. This is not within the scope of this thesis. Here one could clearly show that a difference in conformeric change and the already adjusted polarity around  $Y_{122}$  is in reasonable agreement with the experiment.

Table 5-1: Summary of obtained  $g$  values, C- $\beta$  HF couplings, and <sup>19</sup>F HF couplings. The results from the simulation are compared to results reported earlier from 9 GHz EPR spectra and with a small DFT Calculation (Figure 5-3).

	Multi-frequency simulation			Simulation of: Dr. William Myers (Britt Lab)			DFT model		
	$g_x$	$g_y$	$g_z$	$g_x$	$g_y$	$g_z$	$g_x$	$g_y$	$g_z$
	2.00832	2.00519	2.00220	NA	NA	NA	2.0083	2.0055	2.0022
	$A_x$ [MHz]	$A_y$ [MHz]	$A_z$ [MHz]	$A_x$ [MHz]	$A_y$ [MHz]	$A_z$ [MHz]	$A_x$ [MHz]	$A_y$ [MHz]	$A_z$ [MHz]
2-F	-3	15	-45	15	3	53	-2	10	-53
3-F	-3	-40	145	18	3	-152	-32	-44	168
5-F	-3	-25	183	-15	-3	183	-35	-48	181
H <sub><math>\beta</math>1</sub>	56	39	40	36	43	50	45	46	51
H <sub><math>\beta</math>2</sub>							-0.3	-0.8	5
6-H	7.8	7.5	2				4	6	11
[ $^\circ$ ]	$\alpha$	$\beta$	$\gamma$						
2-F	-60(120)	0	0						
3-F	42	0	0						
5-F	-138	0	0						

2,3,5-F<sub>3</sub>Y<sub>122</sub>• has a similar environment as Y<sub>122</sub>• including a small change in ring dihedral (<10°). This could be obtained from the multi-frequency EPR work supported by a small DFT model. The small structural changes might shed light on how 2,3,5-F<sub>3</sub>Y<sub>122</sub> is able to omit the conformational gating. On the one hand, this UAA has a lower pK<sub>a</sub> with 6.4 compared to 9.9 and could be deprotonated. On the other hand the protein has shown no deprotonation of NO<sub>2</sub>Y<sub>122</sub> mutant at this position, even if the pH of the protein buffer was altered up to 2.5 units above Acyl-NO<sub>2</sub>Ys solution pK<sub>a</sub>.<sup>118</sup> A conformeric change could be another plausible explanation. Thus, the reason for an omitted conformational gating is still open to further studies, which should consider the small change in backbone dihedral. Ideally the diagonal distances of the two β<sub>2</sub>-Y<sub>122</sub>• should be compared with two β<sub>2</sub>-2,3,5-F<sub>3</sub>Y<sub>122</sub>• in the resting β<sub>2</sub> and in the “active” β<sub>2</sub>:α<sub>2</sub> complex. The former is an experiment that can be directly done; for the latter one, a rigorous filter of the individual contributions has to be developed.

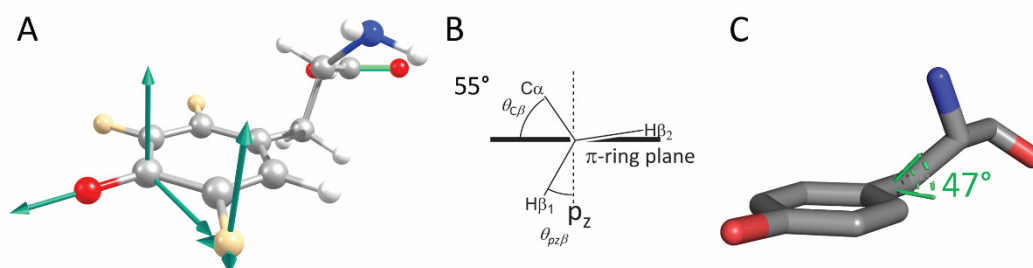


Figure 5-3: DFT model of 2,3,5-F<sub>3</sub>Y<sub>122</sub>•. A) The principal axes of the **g** and one exemplified prolate <sup>19</sup>F HF tensor are illustrated by green arrows on C<sub>4</sub> and F<sub>5</sub>, respectively. In this model the oxygen has 35% and the C<sub>1</sub> 34% spin density population (Mullikan). DFT Calculation details: UB3LYP, def2-TZVPP; COSMO(ethanol); converged to 10<sup>-9</sup> Eh. B) Dihedral angles  $\theta_{C\beta}$  and  $\theta_{pz\beta}$  discussed here are depicted along C<sub>β</sub>-C<sub>1</sub>. C) Y<sub>122</sub> and its dihedral angle  $\theta_{C\beta}$  from the crystal structure is shown.<sup>63</sup>

## 5.3 Characterization by Forward PCET $Y\bullet$ Formed with 2,3,5- $F_3Y_{122}\bullet$

### 5.3.1 Electrostatic Environment

This section starts with the forward PCET transfer, because many results indicated that the intermediate  $NH_2Y_{356}\bullet$  accumulates during forward PCET.<sup>67, 83, 91</sup> The relative reaction potential to the  $Y\bullet$  intermediates in  $\alpha$  was identified for a  $Y_{356}\bullet$  previously.<sup>84</sup> Derived by the analogy to  $NO_2Y_{122}\bullet$ :  $\alpha_2$ - $Y_{731}F$  and 2,3,5- $F_3Y_{122}\bullet$ : $\alpha_2$ -wt is was expected to find  $Y_{356}\bullet$  here.<sup>28, 84</sup>

The reaction was performed as described previously for the  $NH_2Y$ 's, *i.e.*, it was quenched in liquid nitrogen at two time points 10 and  $\approx 20$  s.

The spectra of the obtained pathway radical are shown in Figure 5-4. Both spectra show a typical tyrosine line shape with a pseudo quintet (doublet of triplets) at  $B_{0||g_x}$ , a doublet at  $g_y$ , and large doublet with a doublet from doublets at  $g_z$ . These features arise from the isotropic  $\beta$ -methylene HF coupling and an anisotropic 3/5- $^1H$  HF coupling. Where the 3/5- $^1H$  coupling is unresolved at  $B_{0||g_y}$ , it is only half the size of the  $\beta$ -methylene HF coupling collinear to  $g_x$ . The factor between the isotropic coupling and the 3/5- $^1H$  coupling is about 2.5 at  $B_{0||g_z}$ . Taking this into account the spectra could be simulated as shown in Figure 5-4 (gray). The simulation parameters are identical within error to the ones observed for a putatively forward  $Y_{356}\bullet$  at 140 GHz, as shown in Table 5-2.<sup>84</sup> It should be noted that the error in HF couplings in this thesis is smaller than reported previously.<sup>84</sup> A  $\beta$ -methylene  $a_{iso}$  of 47 MHz was obtained here. Typical spin densities  $\rho_{C1}$  of tyrosines in polar environments are reported for  $Y_D\bullet$ <sup>316, 317</sup>,  $Y_Z\bullet$ <sup>318</sup>, and  $Y\bullet$ <sup>319, 320</sup> in water values with 0.37<sup>316-318</sup>-0.34<sup>319, 320</sup>. Using Eq. (5-1) a  $\beta$ -methylene angle  $\theta_{pz\beta}$  of 14-28° ( $\theta_{C\beta}=42$ -56°) is obtained. A geometry illustrated in Figure 5-3B by  $\theta_{pz\beta} = 25^\circ$ . To summarize, we can report to have trapped a radical species with a very similar  $g$  and HF tensor as observed previously within  $\approx 15$  s with the  $\beta$ - $NO_2Y_{122}$  mutant.<sup>84</sup> A different value of  $a_{iso}(\beta\text{-}^1H)$  could arise from the simulation of the broad lines observed by Yokoyama *et al.*<sup>84</sup> The reaction in this thesis uses 2,3,5- $F_3Y_{122}\bullet$ , which is uncoupled from the oxidation of the  $Y_{122}$  mutant. The radical yield of 10 and 23 s was between 35 and 40%.

The later time point seems to have an additional contribution to the line shape compared to the radical quenched at 10 s. This will be discussed later after introducing the radical formed with wild type  $\alpha$  (§5.4).

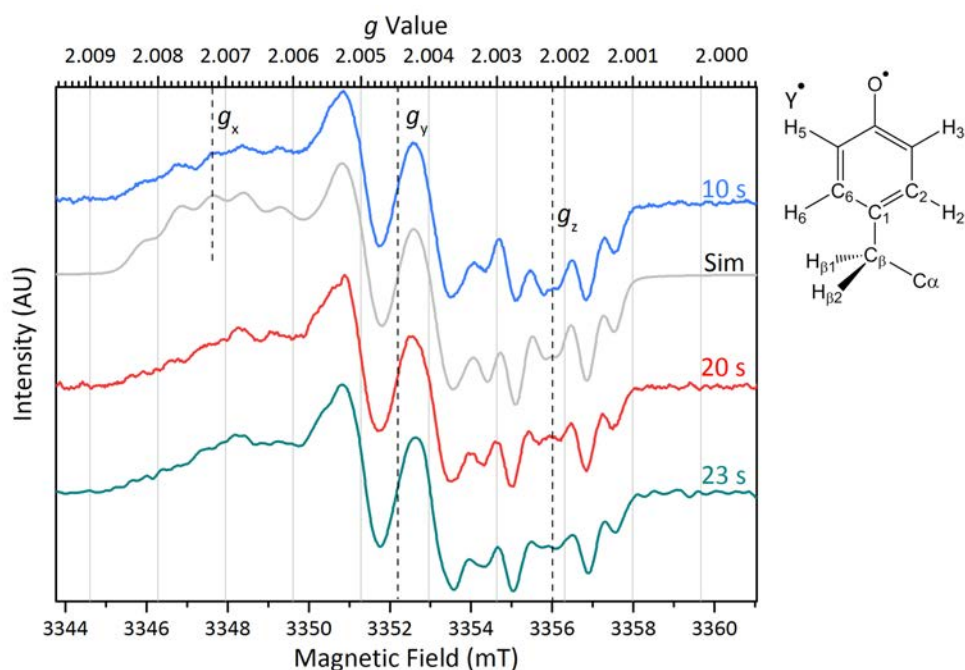


Figure 5-4: 94-GHz EPR spectrum of PCET radical formed with  $\beta_2$ -2,3,5- $F_3Y_{122}:\alpha_2$ - $Y_{731}F$  in deuterated buffer. Three reaction time points 10 (blue), 20 (red) and 23 s (green) are compared to the simulation (gray, Table 5-2). The inset on the right side shows a  $Y\cdot$ . Exp. details: 100 K ESE;  $\pi(\pi/2)=28/32/48(14/18/24)$  ns;  $\tau=267/227/272$  ns; SRT = 5 ms; 6000/600/600; blue & green: 3 G pseudo modulation, red was gained by a 15p second order Savitzky-Golay filter, green trace was additionally smoothed by 10 points.

In order to obtain high restraints for the simulation parameters the parameter set was concomitantly simulated with a Q-band spectrum (Figure 5-5). The Q-band spectrum shows an overlap of the spectral components; for instance part of the pseudo quintet is now observed at  $B_0 \parallel g_y$ . This helps to weight effects from the  $g$  values and the coupling size. The simulation aligns well with the spectrum, only at the high-field side (1199.8-1200.7 mT) the spectrum is distorted by the quartz peak from the EPR sample tube. Here the simulation shows discrepancy to the experimental EPR line-shape.



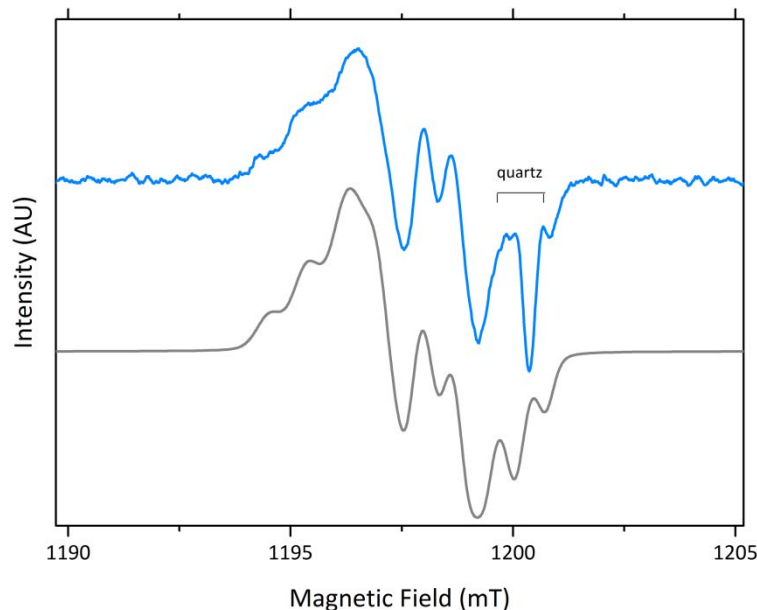


Figure 5-5: 34-GHz EPR spectrum of the PCET radical formed with  $\beta_2$ -2,3,5-F<sub>3</sub>Y<sub>122</sub>: $\alpha_2$ -Y<sub>731</sub>F in deuterated buffer. The derivative (blue) is compared to the simulation (cf. Table 5-2). Exp. details: Reaction time 18 s, then 20% glycerol-d<sub>3</sub>, quenched at 41 s in ice cold isopentane; ESE at 80 K, SRT = 1 ms,  $\pi$  = 40 ns,  $\tau$  = 210 ns, number of averages = 600, Savitzky-Golay (8 points, second order) filtered.

Table 5-2: Pathway radical observed with  $\beta_2$ -2,3,5-F<sub>3</sub>Y<sub>122</sub>: $\alpha_2$ -Y<sub>731</sub>F simulation parameters and comparison to Yokoyama et al.<sup>84</sup> The error is estimated with 10% for the HF couplings (>15 MHz) and is given in parenthesis for the last displayed digit for the *g* values.

$\beta_2$ -2,3,5-F <sub>3</sub> Y <sub>122</sub> : $\alpha_2$ -Y <sub>731</sub> F [this thesis]					A <sub>x</sub>	A <sub>y</sub>	A <sub>z</sub>
					[MHz]	[MHz]	[MHz]
	<i>g</i> <sub>x</sub>	<i>g</i> <sub>y</sub>	<i>g</i> <sub>z</sub>	$\beta$ - <sup>1</sup> H	45	48	49
<i>g</i> values	2.0072(1)	2.00446(5)	2.0022	3/5- <sup>1</sup> H <sup>a</sup>	-5/-3	-21/-17	-29/-23
$\beta_2$ -NO <sub>2</sub> Y <sub>122</sub> : $\alpha_2$ -Y <sub>731</sub> F <sup>84</sup>							
	<i>g</i> <sub>x</sub>	<i>g</i> <sub>y</sub>	<i>g</i> <sub>z</sub>	$\beta$ - <sup>1</sup> H	54	52	54
<i>g</i> values	2.0072(5)	2.0044(1)	2.0022(4)	3,5- <sup>1</sup> H <sup>a</sup>	4	18	26

a) The Euler angles are  $\alpha, \beta, \gamma = 90, 90, \pm 20$ , for the definition  $|A_x| < |A_y| < |A_z|$ .

For tyrosine radicals, it has been reported that the *g* shift is in most cases influenced from H bond interactions as already discussed in the previous chapter. A DFT study of *p*-methylpenoxy radical on its dependence of a single H bonding distance has led to an empirical formula, based on a least square fit of the obtained data.<sup>143</sup> This formula (S-2) is displayed below and should govern our expectations.

Here the  $g_x$  value is directly dependent on the H bond distance  $r$  in Å. Thus the expected value would be with 1.72 Å, which is rather short. However, this formula assumes a single H bond as the sole origin of electrostatic effects.

$$g_x = 2.0094 - \frac{0.0033}{(r_{O-H} - 0.5)^2} \quad (5-2)$$

Up to now, the EPR spectra recorded in deuterated buffer were discussed, because they facilitate the  $g$  value determination by sharpening the EPR spectrum. Based on the expectations one would expect similar results for the reaction performed in  $H_2O$  buffer but modified by a coupling of exchangeable protons. As discussed earlier, the gyromagnetic ratio is 6.5 higher thus the coupling size increases directly proportional [cf. Eq. (2-14) p.34]. The spectra were recorded under the same reaction conditions only in an  $H_2O$  buffer. For further tests 15 mM  $MgSO_4$  required for nucleotide reduction was exchanged stoichiometrically by  $^{25}MgCl_2$ . The results in Figure 5-6 show only minor changes in the line shape. Couplings up to the size of  $\sim 0.3$  mT are normally not resolved, but still contribute to line broadening as observed here.

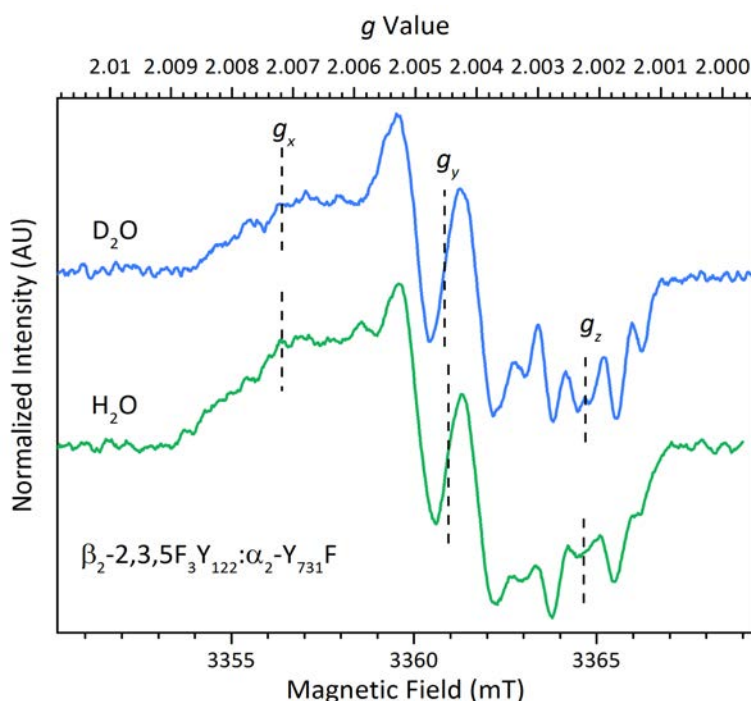


Figure 5-6 Comparison between radical formed from  $\beta_2-2,3,5-F_3Y_{122}:\alpha_2-Y_{731}F$  in  $H_2O$  (blue) and  $D_2O$  (green). Exp. details:  $H_2O$  ESE spectrum at 80 K; quenched at 15 s,  $\pi(\pi/2)=56(28)$  ns,  $\tau=240$  ns, SRT= 6 ms, number of averages = 6300. For parameters to the  $D_2O$  spectrum, see Figure 5-4 with 10 s reaction time.

### 5.3.2 Assignment of the Pathway Radical by the Diagonal Distance to 2,3,5-F<sub>3</sub>Y<sub>122</sub>•

One way to characterize this pathway radical is to measure its location along the PCET. This has been done for several radical intermediates along the pathway. Thus, we can easily compare these results, as illustrated in Figure 1-8 (p.12).

The differences of the two simulations parameters between this pathway radical and previous reported Y<sub>356</sub>• require additional confirmation of the assignment to residue β-356.<sup>84</sup> Thus, Q-band distance measurements (DEER/PELDOR) were performed to obtain experimental evidence for the assignment of the observed radical species to β-Y<sub>356</sub>•. In order to maximize the S/N Q-band was used instead of X-band PELDOR spectroscopy.<sup>282-284</sup> To compensate the effect of an incomplete spectral excitation, three experiments at 3 different field points (1-3) for pump (P) and detect (D) were performed (Figure 5-7A). At all field points a pronounced oscillation frequency was observed (Figure 5-7B). The averaged dipolar oscillations can be Fourier transformed; a pake pattern results with a perpendicular frequency, resulting in a distance of 3.06±0.03 nm (Figure 5-7C, Inset).

The averaged time traces can also be fitted (Eq. (2-18), Figure 5-7C) under a Tikhonov regularization<sup>287</sup> procedure a distance distribution as a probability function of distances is obtained (Figure 5-7D, DeerAnalysis).<sup>286</sup> Here a full pake pattern is assumed, but the value is still within the error of the pake pattern distance. The distance for this system was obtained with 3.04±0.06 nm (Figure 5-7C), identical within error to value obtained for Y<sub>122</sub>• to the Dopa356•<sup>43</sup> (3.05±0.06 nm) or NH<sub>2</sub>Y<sub>356</sub>• (3.02±0.16 nm)<sup>28, p.177</sup>. And also identical to the value reported by Yokojama *et al.* for NO<sub>2</sub>Y<sub>122</sub>• to Y<sub>356</sub>• (3.01±0.04 nm).<sup>84</sup>

In summary, the same forward radical distance is observed as reported in the millisecond time scale by Yokojama *et al.*<sup>84</sup> This distance has already been assigned to several UAA at the 356 position and can be assigned to β<sup>2</sup>-2,3,5-F<sub>3</sub>Y<sub>122</sub>•-- β<sup>1</sup>-Y<sub>356</sub>•.<sup>28, p.177, 43</sup> Noteworthy, also the β<sup>2</sup>-NO<sub>2</sub>Y<sub>122</sub>•-- β<sup>1</sup>-Y<sub>356</sub>• distance is stable up to the minute time scale.<sup>84</sup> Thus, despite the decay of roughly 10% of radical content in the second timescale the radical position is in respect to the diagonal distance to residue 122 stable.<sup>28</sup> Additionally, the PCET disruption at position 731 by phenylalanine does not change the distance compared to other reports of diagonal distances between the 122 and 356 position in β (cf. Figure 1-8, p.12). If Y<sub>731</sub> is H bonded to Y<sub>356</sub> a difference between α<sub>2</sub>-wt and α<sub>2</sub>-Y<sub>731</sub>F should be observable in the <sup>2</sup>H ENDOR spectra.

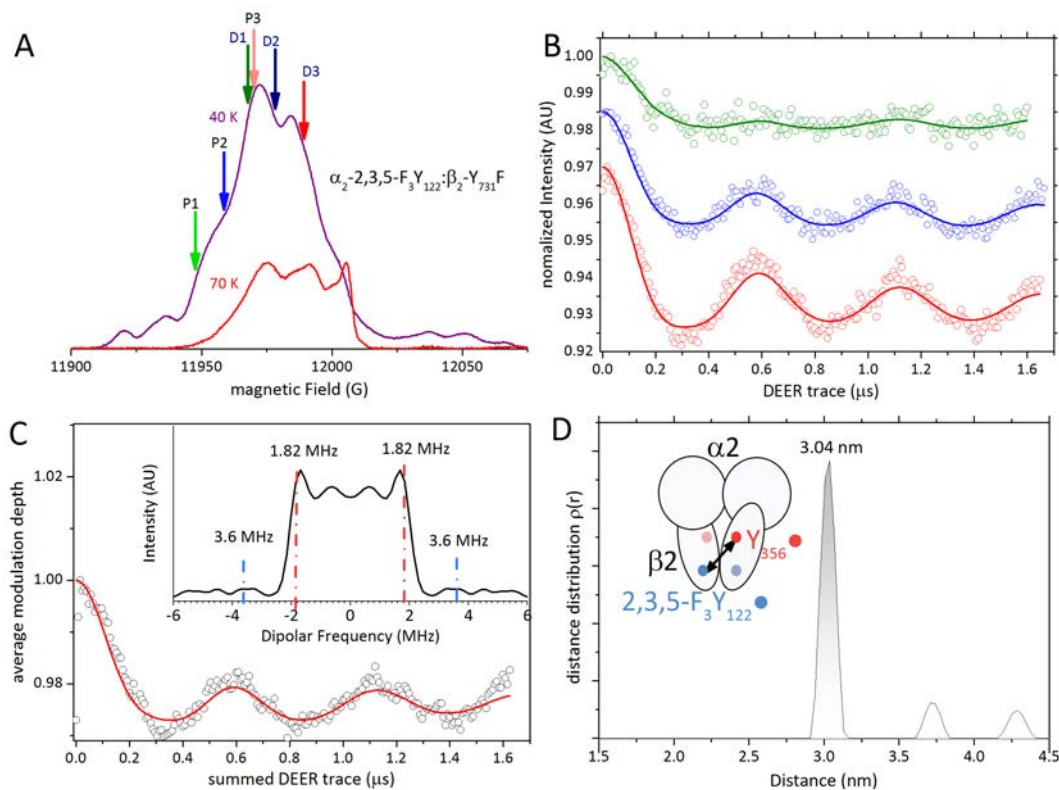


Figure 5-7: 34-GHz diagonal distance measurement with the pathway radical produced by  $\beta_2$ -2,3,5- $F_3Y_{122}$ :  $\alpha_2$ - $Y_{731}F$ . A) ESE spectrum at 40K (violet) and spectrum of pathway radical alone at 70 K (red) are shown together with the pump and detect positions in the DEER traces. Three consecutive measurements are spaced by 11 G. Pump (P1,P2 and P3;  $\pi= 56$  ns) and detect (D1, D2 and D3;  $\pi = 46$  ns) are separated by 54 MHz. The dipolar oscillations (green = 1, blue =2 and red =3) in B are illustrated. The dipolar oscillations are normalized and averaged to form C. From Fourier transformation a dipolar coupling pattern is obtained the perpendicular component (red, ---) of the powder pattern has a frequency of  $1.82\pm 0.05$  MHz (C, inset). This frequency results to an interspin distance of  $3.06\pm 0.03$  nm using Eq. (2-18). This trace was fitted to obtain a distance distribution D. The main observed distance is  $3.04\pm 0.06$  nm. The distances  $>3$  nm (frequencies  $< 0.8$  MHz) are in respect to the recorded dipolar oscillation not in the reliable distance range. Therefore they are regarded as unresolved in the pake pattern.

### 5.3.3 Mims ENDOR of Forward Radical Transfer to $Y_{356}\bullet$

The  $g_x$  value of  $\beta_2$ - $Y_{356}\bullet$ : $\alpha_2$ - $Y_{731}F$  is comparable with the  $g_x$  value of  $Y_D\bullet$  in the photosystem II, for which a value of 2.00756 has been reported.<sup>321</sup> It has been stated that  $Y_D\bullet$  has only one H bond,<sup>322</sup> also the wide doublet tyrosine of prostaglandin- $H_2$ -synthase harbor a single H bond ( $g_x=2.0075$ ).<sup>160</sup> Thus one stronger H bond or a contribution of a second  $^1H$  HF coupling would be expected in these  $Y_{356}\bullet$  ENDOR measurements. The ENDOR spectra in Chapter 4 show that the large couplings can be measured with an inter pulse delay  $\tau$  of

200 ns equivalent to 5 MHz modulation through the Mims whole conditions (Theory §2.2.3 p.40). Thus a range of strong couplings from  $\pm 0.5$  to  $\pm 2$  MHz is unsuppressed. The recorded spectra are shown in Figure 5-8. The spectra show a complete dipolar tensor ( $A_{\parallel} = -2 \cdot A_{\perp}$ ;  $\mathbf{A} \approx \mathbf{T}$ ) shape as typical for H bonds not interacting with nodal plane of the  $\pi$  system (see Figure 2-12 p.46). The values of the resolved turning points in the pake pattern of the HF interaction are  $\pm 0.6$  MHz and  $\pm 0.3$  MHz. It should be mentioned, that they are astonishingly similar to the values observed for yeast RNR with a 0.5 ppt larger  $g_x$  value.<sup>55</sup> In the comparison to the  $^2\text{H}$  MIMS ENDOR spectra of yeast RNR and  $\text{Y}\cdot$  with a comparable  $g_x$  values ( $2.0076 \pm 0.0001$ ) as yeast RNR, it becomes evident that their central region is occupied by a Mims hole (cf. Table 1-1, p.24).<sup>55, 155</sup> In contrast the central line in the region of  $\pm 0.2$  MHz has an intensity twice the size compared to the  $\pm 0.3$  MHz peaks. This could indicate another not completely resolved weaker H bond. The assignment of the direction of the here detected proton, could specify the direction of the H bond acceptor during forward PCET between  $\text{Y}_{122}$  and  $\text{Y}_{356}$ .

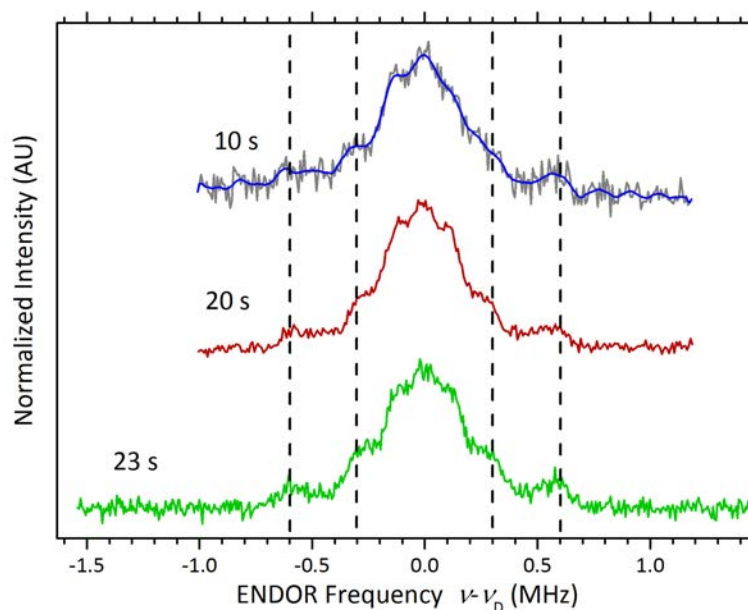


Figure 5-8:  $^2\text{H}$  ENDOR of  $\text{Y}_{356}\cdot$  with  $\alpha(\text{Y}_{731}\text{F})$ . Mims ENDOR spectrum was recorded for three samples with 10-23 s reaction time. All samples at  $B_{0\parallel}g_y$  show an HF coupling consistent with a weak to moderate H bond and a smaller unresolved central line contribution. Exp. details: T= 80-100 K  $\pi/2=20$  ns,  $\tau=200$  ns,  $\pi_{\text{RF}}=40$   $\mu\text{s}$ , one SPP random RF acquisition; gray: 100 K, SRT=10 ms; red: 100 K, SRT= 5 ms; green: 80 K, SRT= 10 ms; acquisition time = 42, 23 and 25 h for blue, red and green, respectively. The blue curve is 10 points adjacent averaged.

### 5.3.4 Direction of the H Bond

The <sup>2</sup>H Mims ENDOR spectra along each canonical orientation of the **g** tensor are shown in Figure 5-9. The interpulse delay  $\tau$  was adjusted to maximize the Mims ENDOR signal for the small coupling size (cf. Figure 2-10B p.43). Beside the central Mims hole, no other Mims holes are expected in the RF range investigated. The three orientations show three distinct spectra with an axial  $T_{\perp}$  tensor component with resonances of  $\pm 0.3$  MHz visible in all spectra, most sharply along  $B_0 \parallel g_z$ . In this spectrum, the parallel component  $T_{\parallel}$  is absent with resonances of  $\pm 0.6$  MHz. For  $B_0 \parallel g_x$  the parallel component is shallow but visible, the spectrum.  $B_0 \parallel g_y$  was shown before measured with a shorter  $\tau$  value (200 ns) suppressing this small coupling range a bit stronger than for  $B_0 \parallel g_x, g_z$ . In this  $B_0 \parallel g_y$  spectrum the parallel component is clearly visible and a complete powder pattern can be observed (see Figure 2-12 p.46). The spectra were first simulated with the starting parameters of yeast-RNR, due to the similarity in the size of the HF coupling. The simulation parameters, however, did not fit the obtained spectra. In yeast, an H bond approximately parallel to the C-O bond has been found, but the  $B_0 \parallel g_x$  orientation (Figure 5-9) has only a weak parallel component. In a purely dipolar tensor, as assumed here, the parallel component is along the dipolar axis, thus the O-H vector should be along  $g_y$ , possibly with a minor contribution along  $g_x$ . Therefore an angle dependent simulation approach was used. It considers each orientation of the HF tensor with respect to the **g** tensor within a resolution of 10° for one octant of the principle axis **g** tensor system (inset Figure 5-9). The quadrupole tensor is aligned along the H bond donor atom X-H bond (cf. Figure 4-19 p.103), thus it can be assumed to be parallel to the H bond direction and HF tensor for negligible protein structure restraints on the H bond donor. The best simulation has been selected and is shown in Figure 5-9. Simulations in which the parallel HF coupling component is approximately collinear to the  $g_x, g_z$  plane could be considered. Therefore the simulated <sup>2</sup>H HF tensor is from its orientation similar to the one reported in for Y<sub>D</sub>•, by Kessen *et al.*<sup>155</sup> (see Table 1-1, p.24).

To rationalize Euler angles between the **g** and HF tensor principle axis systems (see Table 5-3) one can relate them to the H bond dihedral angle  $\theta_{\text{H}_2\text{O}}$  discussed before (§4.6.4.2 p.118). Then the  $\gamma$  is the H bond angle ( $\text{H}_x\text{-O-C}_4$ ), because the  $\text{C}_4\text{-O}$  bond also defines the  $g_x$  axis in the PAS.  $\beta$  is the H bond dihedral angle + 90°, as shown in Figure 4-10. The angle  $\alpha$  has nearly no effect in the simulation and was set to 0°. The discrepancy of the simulation and the experimental data arises most probably from another smaller coupling in the range

of  $\pm 0.25$  MHz. This small coupling is not resolved from the matrix line and is therefore not assigned.

A single H bond geometry consistent with the obtained angles resembles a  $130 \pm 15^\circ$  H bond angle. In agreement to the H bond angle found with nearly no scalar ( $a_{\text{iso}}$ ) contribution in previous H bond dihedral scans (§4.6.4.2 p.118). The H bond dihedral can range from  $-35$ - $35^\circ$  without a strong deviation in the fit. To visualize the effects a small DFT model with a  $\theta_{\text{H}_2\text{O}}=30^\circ$  (Figure 5-10) has been calculated. Here the HF coupling values are overestimated by a factor of 1.5, but the angles are within the error of the experiment.

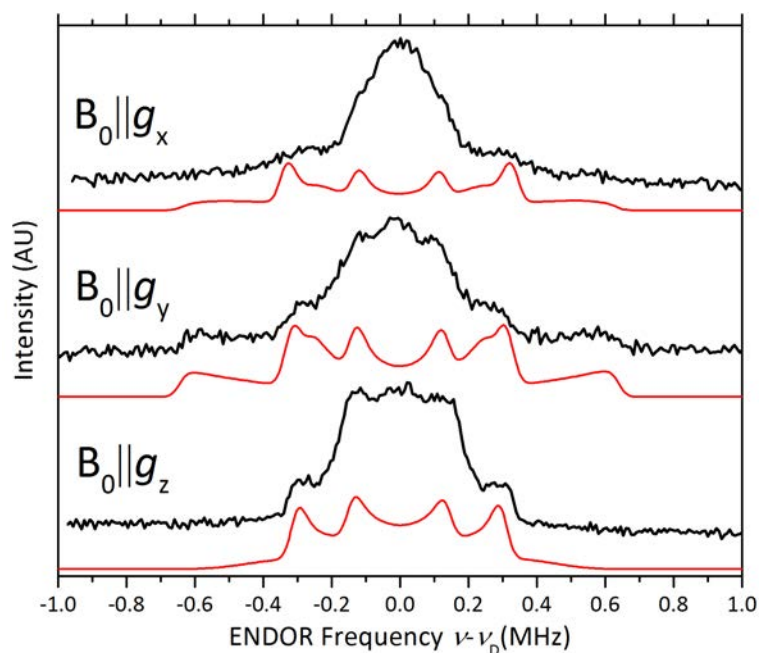


Figure 5-9: Orientation selective  $^2\text{H}$  ENDOR of  $\text{Y}_{356}\bullet$  with  $\alpha\text{-Y}_{731}\text{F}$ . The Mims ENDOR spectrum was recorded with  $B_0$  along  $g_x$ ,  $g_y$  and  $g_z$  (black). The simulation is shown beneath each trace in red. Exp. details:  $g_x$  and  $g_z$ :  $T=40$  K,  $\pi/2=36$  ns,  $\tau=400$  ns,  $\pi_{\text{RF}}=40$   $\mu\text{s}$ , one SPP random acquisition,  $\text{SRT}=10$  ms, acquisition time = 24 & 32 h;  $g_y$ : see Figure 5-8 (green). A line broadening of 45 kHz was used for the simulation. Further parameters are shown in Table 5-3.

Structurally, this has some implication compared to the work discussed in the  $\text{NH}_2\text{Y}'\text{s}$  (§4.2.2, p.83). This is the first spectroscopic evidence for an in-plane H bond at  $\text{Y}_{356}\bullet$ . It has an essentially zero  $a_{\text{iso}}$  contribution. This excludes spin polarization through the  $p_z$  oxygen orbital, because the H bond is in the  $p_z$  orbitals nodal plane (cf. Figure 5-10). In  $\text{Y}_{356}\bullet$  the stabilization of perpendicular H bond is absent, thus an energetically favored H bond is formed along the filled non-bonding  $\pi$  orbitals (see Figure 4-27D p.120).

Table 5-3: Simulation parameters of the unknown (X) H bond donor to  $Y_{356}\bullet$ . The Euler angle uncertainties are described in the text. The HF and quadrupole tensor has about 10% error. A DFT calculation with a water in the assumed  $\theta_{H_2O}=30^\circ$  is compared to the simulation. The DFT calculation has  $g$  values of (2.0077, 2.0045, 2.0022).<sup>a</sup>

$Y_{356}\bullet$		$A_x$ [MHz]	$A_y$ [MHz]	$A_z$ [MHz]	$\alpha$ [ $^\circ$ ]	$\beta$ [ $^\circ$ ]	$\gamma$ [ $^\circ$ ]	$Q_x$ [kHz]	$Q_y$ [kHz]	$Q_z$ [kHz]
Simulation	X-D $\approx 1.9 \text{ \AA}^b$	-0.44	-0.46	0.91	0 0	120 120	130 130	-54	-72	126
DFT $\theta_{H_2O}=30^\circ$	wat1-D 1.8 $\text{\AA}$	-0.77	-0.78	1.34	-10 15	104 113	138 140	-54	-74	128

a) Calculation details: B3LYP; basis set def2-tzvpv/EPRII. The polarizability of ethanol was used and dispersion correction. Both basis sets gave within 0.1 ppt or 5% identical HF and  $g$  values. b) Obtained with point-dipole approximation (§5.3.5).

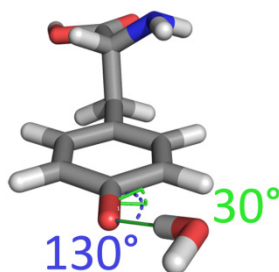


Figure 5-10: DFT model of a  $Y\bullet$  with one water molecule. A restrained geometry optimization was performed with H bond dihedral  $\theta_{H_2O}=30^\circ$ . An H bond angle ( $C_4-O-H_{wat1}$ ) of  $130^\circ$  was obtained.

### 5.3.5 $Y_{356}\bullet$ H bond Length

In the presence of a purely dipolar HF interaction a distance from the electron spin dipole to the nearest point charge can be approximated. Here oxygen is the nearest spin density bearing nucleus and has a  $\rho_O$  reported for  $Y_D\bullet^{316, 317, 323}$ ,  $Y\bullet^{319, 320}$  in water and  $Y_Z\bullet^{156, 318}$  to be between 0.28 and 0.25. One obtains a distance of 1.87-1.95  $\text{\AA}$  for the H bond by Eq. (2-17) (p.35). The nucleus is approximated as a point charge. Hence, the obtained distance is in tendency estimated as too large ( $\approx 5\%$ ).<sup>153, 295</sup> Nevertheless, this is a moderate to weak H bond. It could be shown before that the H bond distances increase with the number of H bonds (§4.6.4.3 p.121).<sup>110</sup> In the similar case of  $Y_D\bullet$  with an stronger H bond, but the same angle dependence, no matrix line or inner coupling was observed. Also the  $g$  value is



0.4 ppt higher than observed for  $\beta$ -Y<sub>356</sub>•:α-Y<sub>730</sub>F. The <sup>2</sup>H coupling connected to the central line is therefore a most likely more distant.

This has been qualitatively supported by a small DFT model. It considers two water molecules (wat 1&2) in the π-plane and a Y•. The wat2 is scanned for its distance from 2.4 to 2.2 Å. To insure a fast convergence the ring dihedral ( $\theta_{C\beta}=55^\circ$ ) and the dihedral to the first water ( $\theta_{\text{wat1}}=20^\circ$ ) was kept constant. The values are summarized in Table 5-4 below. To reproduce the  $g_x$  value exact a <sup>2</sup>H within a distance of 2.2 Å is necessary. However, all distances have  $g$  values within the uncertainty of the DFT. For wat2 with an H bond distance of 2.2 Å, an HF tensor of  $A_{xyyz} = -0.3, -0.4, 0.8$  MHz was found. A perpendicular component of 0.4 MHz could be still unresolved between the observed matrix line width and the larger HF coupling. Wat2 can occupy every orientation toward a Y•, except for orientations exceeding the matrix line width. For instance the line width at  $g_x \parallel B_0$  is smaller than 0.4 MHz, therefore  $A_z$  and  $Q_z$  parallel to  $g_x$  can be excluded. The HF tensors of wat1 are in agreement with the overestimation of the H bond HF couplings by DFT calculations. This has been observed previously.<sup>110, 254</sup>

Table 5-4: Small DFT model using a Y• and two waters scanning the distance of a distant of the second water (wat2).  $\rho_O$  was 0.34 after Muliken population analysis<sup>312, 313</sup>. The H bond dihedrals were kept constant with 20° (wat1) and 167° (wat2). The H<sub>wat</sub>-O-C<sub>4</sub> angle stayed constant with 117° (wat1) and 123° (wat2). The  $Q_z$  value was either 130 kHz for wat1 or 142 kHz for wat2.<sup>a</sup>

No.		O--H Distance [Å]	$A_x$ [MHz]	$A_y$ [MHz]	$A_z$ [MHz]	$Q_z$ [kHz]	$g_x$	$g_y$	$g_z$
1	H <sub>wat1</sub>	1.82	-0.63	-0.69	1.24	126			
	H <sub>wat2</sub>	2.20	-0.33	-0.38	0.78	142	2.0072	2.0046	2.0022
2	H <sub>wat1</sub>	1.82	-0.63	-0.70	1.24	126			
	H <sub>wat2</sub>	2.30	-0.30	-0.34	0.70	142	2.0073	2.0046	2.0022
3	H <sub>wat1</sub>	1.81	-0.64	-0.70	1.25	126			
	H <sub>wat2</sub>	2.40	-0.27	-0.31	0.64	146	2.0074	2.0046	2.0022

a) Calculation details: UB3LYP, def2-TZVPP, COSMO(Ethanol), RICOSX, Grimme dispersion corrected. The uncertainty of the coupling values is estimated with 20%.  $C_{\beta}$ -<sup>1</sup>H HF coupling stayed constant with  $a_{\text{iso}}=55$  MHz.

## 5.4 Equilibrium PCET Radical $Y_{356}^{\bullet}$ Formed during Reverse PCET

### 5.4.1 Multi-frequency Characterization

The pathway radical formed in the reaction of  $\beta_2$ -2,3,5-F<sub>3</sub>-Y<sub>122</sub> and  $\alpha_2$ -wt with substrate (CDP) and effector (ATP) has been quenched in the second timescale. EPR spectra of the putative forward radical transfer and that in PCET equilibrium can then be compared directly. The radical formed in PCET equilibrium can be observed without the disturbance of the mutation (Y<sub>731</sub>F) in  $\alpha$ , as in the previous section. Therefore the formed  $Y_{356}^{\bullet}$  is also relevant to the discussion of the forward radical transfer.<sup>28</sup> The 94 GHz EPR spectrum Figure 5-11A has the same pattern at  $B_0 \parallel g_x$  and  $g_z$ , only at  $B_0 \parallel g_y$  shows only a dominant  $\beta$ -methylene HF coupling. To constrain the HF couplings further a 34 GHz spectrum (Figure 5-11B) was recorded, then the two frequencies were simulated simultaneously. Simulating the spectra with one parameter set (Table 5-5) gave a reasonable fit of the experimental trace (Figure 5-11, gray). In addition to the simulation set for a  $Y_{356}^{\bullet}$ , a 10% additional contribution of  $Y_{731}^{\bullet}$  and  $Y_{730}^{\bullet}$  was taken into account. This contribution is only observable at the low field side of the 94 GHz and 9 GHz spectrum. Based on the knowledge from the 3-amino tyrosine the  $g_x$  value it was assumed to be larger than in the  $Y_{356}^{\bullet}$  case. A value of 2.0078 has been used, other values were not resolved therefore the suggested parameters of Yokojama *et al.* were used as parameters.<sup>84</sup> Also the parameters of  $Y_{356}^{\bullet}$  along the reverse PCET are identical within error to the published results (Table 5-5).<sup>84</sup> Thus only a single Q-band DEER trace was recorded, to verify the diagonal distance reported for radicals at  $Y_{356}$  (Appendix: Figure A - 9, p.200). This is an additional evidence for assigning the observed main pathway radical species to  $Y_{356}^{\bullet}$ .

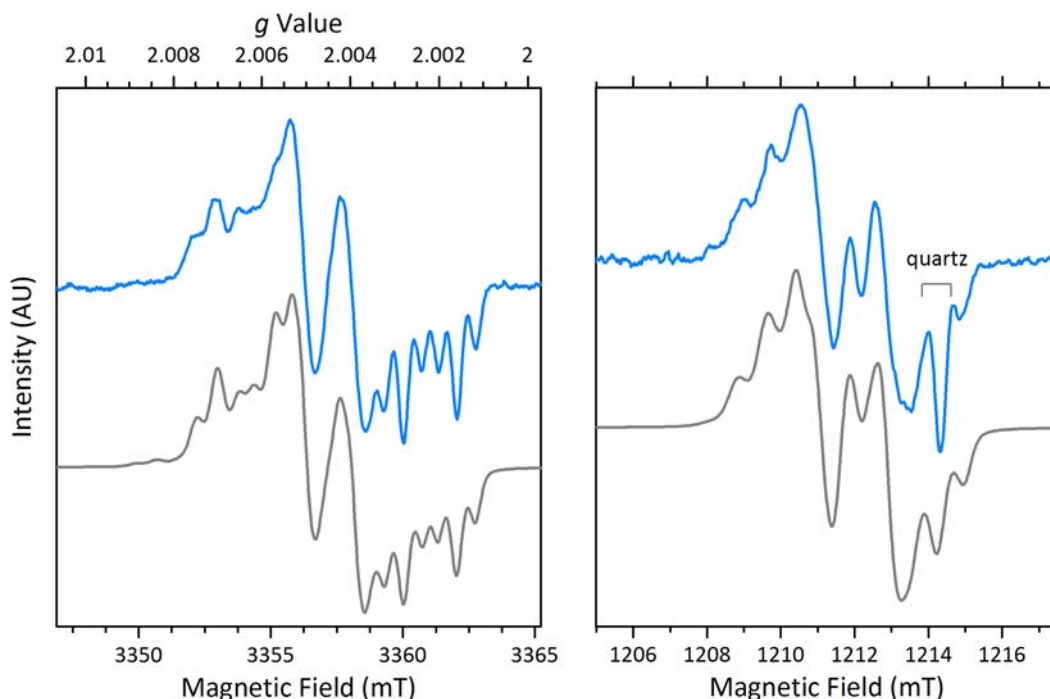


Figure 5-11: EPR spectra (blue) and simulation (gray) of the pathway radicals using  $\beta_2$ -2,3,5- $F_3Y_{122}:\alpha_2$ -wt at two frequencies. The 94 GHz and 34 GHz EPR spectra in  $D_2O$  buffer at 80 K are shown left and right, respectively. The simulation parameters are shown in Table 5-5. Exp. details: ESE, 94 GHz:  $\pi=40$  ns,  $\tau=270$  ns, SRT= 6 ms, the reaction was quenched at 11 s in liquid nitrogen; 34 GHz: ESE,  $\pi=40$  ns,  $\tau=220$  ns, SRT= 5 ms. The reaction was quenched in ice cold isopentane after 41 s, at 10 s 20% glycerol- $D_3$  was added. The derivative was obtained by 3 G pseudo modulation or by a Savitzky-Golay (5 points, second order) filter for 94 GHz and 34 GHz, respectively.

Table 5-5: Simulation parameters of the pathway radical observed with  $\beta_2$ -2,3,5 $F_3$ - $Y_{122}$  and wild type  $\alpha_2$  in comparison to  $Y_{356}\bullet$  formed with  $\beta_2$ - $NO_2$ - $Y_{122}:\alpha_2$ -wt. The errors for the g values were estimated and are given in parenthesis for the last shown digit. The error for the HF values  $>15$  MHz are 2 MHz, the errors for the smaller couplings are estimated to be approximately 3 MHz.

$\beta_2$ -2,3,5 $F_3$ - $Y_{122}:\alpha_2$ -wt [this thesis]					$A_x$ [MHz]	$A_y$ [MHz]	$A_z$ [MHz]
	$g_x$	$g_y$	$g_z$	$\beta$ - $^1H$	61	52	56
g values	2.0063(1)	2.0045(1)	2.0022(1)	$3/5$ - $^1H^a$	-5	-21	-24
					-3	-19	-24
$\beta_2$ - $NO_2$ - $Y_{122}:\alpha_2$ -wt <sup>84</sup>							
	$g_x$	$g_y$	$g_z$	$\beta$ - $^1H$	61	52	54
g values	2.0063(3)	2.0044(2)	2.0022(3)	$3,5$ - $^1H^a$	4	18	26

a) The Euler angles are  $\alpha, \beta, \gamma = 90, 90, \pm 20$ , for the definition  $|A_x| < |A_y| < |A_z|$ .

Interestingly, although  $Y_{356}\bullet$  is formed with  $\alpha$ -wt and  $\alpha$ - $Y_{731}F$  they have a significantly different  $g$  values and  $\beta$ -methylene HF couplings with  $a_{iso} = 47$  MHz to  $a_{iso} = 56$  MHz, they have the same diagonal distance to  $Y_{122}\bullet$ . Hence, either the spin density changes, the ring dihedral angle  $\theta_{C\beta}$ , or a combination thereof. Studying the semi-empirical McConnell Eq. (5-1) Svistunenko *et al.* demonstrated that the oxygen spin density population is inversely proportional to McConnell estimate of  $C_1$  spin density population.<sup>277</sup> An increase of 20 % in spin density population could explain the difference in  $\beta$ -methylene HF coupling. A value of  $\rho_{C1}$  between 0.41 and 0.45 would be obtained from  $\rho_{C1} = 0.34-0.38$ <sup>316-320</sup> used for the forward PCET  $Y_{356}\bullet$ . The larger value is comparable to the spin density population  $\rho_{C1} = 0.44-0.45$  observed in a recent  $Y_Z\bullet$  DFT study with  $g_x$  between 2.0055 and 2.0063.<sup>156</sup> A change in dihedral angle  $\theta_{C\beta}$  would correspond to 12-22° change for an oxygen spin density population in the range of 34%-38%.

The spectrum recorded for the reaction in  $H_2O$  buffer shows the same line shape as the spectrum in deuterated buffer (Figure S-12). The broadening due to D/H exchange is significantly stronger than in the forward PCET  $Y_{356}\bullet$ . This can partially be explained by the more intense shoulder at the high-field side of the spectra previously assigned to a contribution of  $Y_{731}\bullet$  and  $Y_{730}\bullet$ .

The  $A_\beta$  coupling is decreasing slightly as observed at  $g_z$ . And the  $g_x$  and  $g_y$  values seem to be slightly shifted between the two spectra below. Overall the concomitant change of time point and medium contribute to this spectrum. Here a rigorous investigation of different time points, preferentially by rapid freeze quench would bring more insight. Furthermore we will consider the single spectrum at 11 s. This 11 s sample is further used to record ENDOR spectra, which can be used to further investigate the different spectral line shapes observed here.

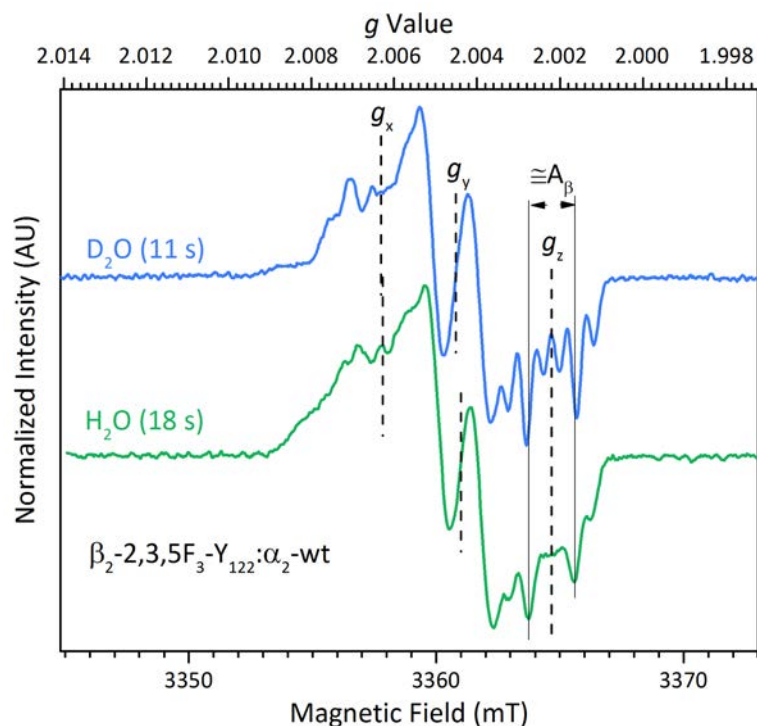


Figure 5-12: Comparison between an H<sub>2</sub>O and a D<sub>2</sub>O spectra of the Y<sub>356</sub>• formed β<sub>2</sub>-2,3,5F<sub>3</sub>-Y<sub>122</sub>: α<sub>2</sub>-wt. W-Band ESE spectrum of the reaction of 2,3,5-F<sub>3</sub>-Y<sub>122</sub>•(β) and wild type(α) with CDP/ATP. <sup>1</sup>H<sub>β</sub> HF coupling is marked at g<sub>z</sub> with A<sub>β</sub>. Exp. details: Blue: see Figure 5-11; Green: T= 80 K, π(π/2)=56(28) ns, τ= 614 ns, number of averages = 3150. The derivative was built with a Satitzky-Golay filter (20 points, second order).

#### 5.4.2 Mims ENDOR of Y<sub>356</sub>• Using Wild Type α

In order to understand the *g*-shift of 0.9 ppt (compared to Y<sub>356</sub>•:α<sub>2</sub>-Y<sub>730</sub>F) Mims ENDOR spectroscopy was performed for the radical transfer in equilibrium. A larger coupling is expected than observed for the radical in §5.3.3. Therefore the measurement shown in Figure 5-13 was recorded with a larger window for couplings of up to ±2 MHz. With the τ setting of 200 ns we create certain blind spots, thus a second τ value was measured with shifted blind spot criteria (3.3 MHz modulation, cf. Theory §2.2.3, p. 40). Nevertheless, identical spectra are obtained (5.13). The same coupling strength as before (§5.3.3) with ± 0.6 MHz for the parallel component is observed. Hence, the strength of the coupling apparently does not correlate with the *g* value shift. The number of H bonds, however, could correlate to the *g* value shift. In the amino tyrosine, the <sup>2</sup>H ENDOR intensities relative to each other for inter- and intra-molecular (NH<sub>2</sub>) nuclear couplings observed. For tyrosines in D<sub>2</sub>O buffer spectra only the anisotropic coupling and the matrix line can be observed. It can

be stated, however, that compared to the  $Y_{356}\bullet:\alpha_2$ - $Y_{730}F$  spectra with the blocked pathway the parallel component of the hyperfine is stronger and both turning points ( $\pm 0.6$  and  $0.3$  MHz) are slightly sharper. This could be an indication of a second anisotropic deuteron coupling.

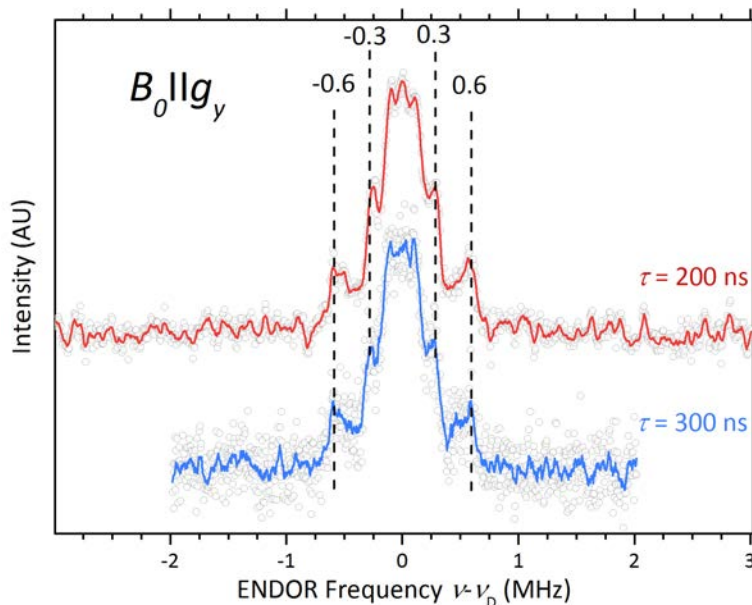


Figure 5-13:  $^2H$  ENDOR of  $Y_{356}\bullet$  with wild type  $\alpha$ . The pathway radical formed after 10 s was measured at 70 K with two different  $\tau$  values 200 ns (red) and 300 ns (blue) to ensure a broad coverage of possible resonances. The spectra show the  $B_0 || g_y$ , only a weak to moderate H bond and a matrix line. Exp. details: Mims ENDOR,  $T = 70$  K  $\pi/2 = 20$  ns,  $\tau = 200$ -300 ns, one SPP random acquisition, SRT = 11 ms, acquisition time = 24 and 48 h. The traces have been smoothed by 5 (red) and 6 (blue) points adjacent averaging.

The form of the tensor indicates that both H bonds should be within the plane of the tyrosine ( $\pm 30^\circ$ ,  $g_x g_y$  plane), otherwise a stronger non-dipolar contribution would be expected from the spectral analysis performed for the 3-amino tyrosines (Chapter 4). Orientation selective data can give spectroscopical evidence for an H bond along  $g_x$  or  $g_y$  as shown here (§5.3.4) or previously for instance in yeast RNR.<sup>55</sup>

#### 5.4.2.1 $^1H$ ELDOR Detected NMR of $Y_{356}\bullet$ Formed during Equilibrium PCET

The unprecedented low  $g_x$  value of 2.0063 has shown only distant H bonding protons ( $\approx 1.9$  Å) for the  $Y_{356}\bullet$  formed during PCET equilibrium. This seems contradictory at first. Although the effect can be rationalized a control was necessary to check if any larger couplings were not recorded due to line broadening or fast exchange conditions within the

S/N of the ENDOR measurement. Additionally, we only excited a part of the orientations at 94 GHz, thus couplings larger at other orientations could have been missed. At Q band, we were able to reach a nearly full pake pattern with one measurement, as shown by studies on amino tyrosines.<sup>92</sup>

Here, the experiment was performed at 80 K to suppress any contribution of  $\beta_2$ -2,3,5-F<sub>3</sub>-Y<sub>122</sub>• in the spectra. The spin-lattice relaxation ( $T_1$ ) at these temperatures is quite short compared to the long RF pulse. An HF detecting sequence, ELDOR detected NMR, has been often used in metallo proteins with intrinsically short relaxation times.<sup>186</sup> It has been reported to be less affected from short spin-lattice relaxation times ( $T_1$ ) as ENDOR (cf. Theory §2.2.4 p.43).<sup>135</sup> Indeed, first ENDOR spectra showed the need for long accumulation to gain sufficient S/N.<sup>92</sup>

The spectrum in Figure 5-14 was recorded with ELDOR detected NMR. It should be mentioned that the resolutions are not as high as in a comparable Davies <sup>1</sup>H ENDOR spectrum, but ELDOR detected NMR is more sensitive.<sup>188, 191</sup> Thus measurement times up to 72 h could be omitted.<sup>92</sup> Additionally, all internal tyrosine couplings contribute to this <sup>1</sup>H HF spectrum, making an assignment to individual couplings speculative. However, in comparison between the reactions performed in D<sub>2</sub>O and H<sub>2</sub>O the spectrum is a valuable control for the estimated couplings sizes (blue, Figure 5-14). Both spectra are completely identical to each other within S/N. Only around the central line the deuterated sample has a sharper central line (5.1 MHz vs. 7.8 MHz). The line width increase is consistent with the coupling observed in the Mims ENDOR spectra of 1.2 MHz (6.5 x 1.2 MHz = 7.8 MHz).

Thus, no stronger coupling was missed in the Mims ENDOR spectra, due to blind spots. The broad lines observed in the range of  $\pm(26-31)$  MHz are identified as beta methylene couplings, here the background subtraction led to a higher frequency uncertainty than in the central region of the spectrum. This is especially true at the edge of the experimental resonance conditions for the MW irradiation (DIP).

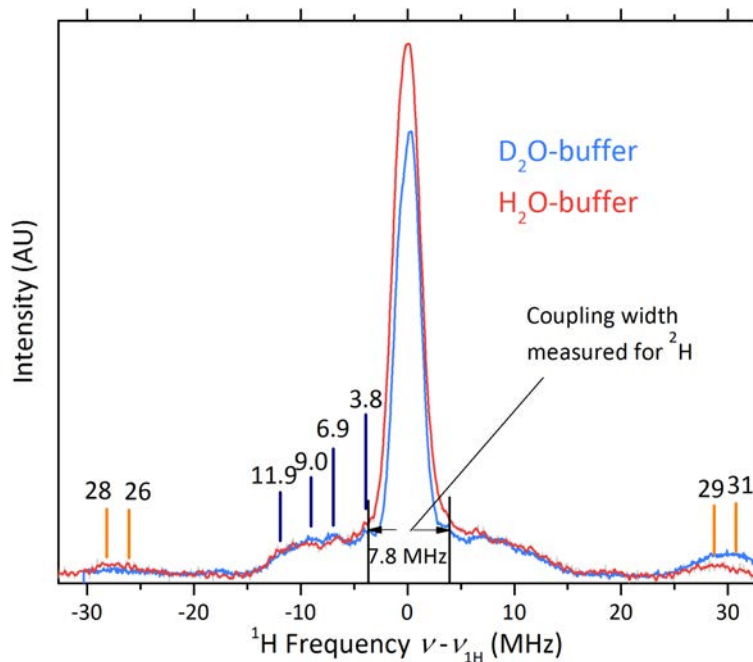


Figure 5-14: Comparison of  $Y_{356}\bullet$  with wild type  $\alpha$  in protonated and deuterated buffer. The EDNMR centered at the  $^1\text{H}$  Larmor frequency shows the resonances in  $\text{D}_2\text{O}$  (blue) and  $\text{H}_2\text{O}$  (red) spectrum. The same HF couplings are observed independently of the buffer, beside the  $\beta$ -methylene coupling (orange) and the broadened central line as discussed in the text. Exp. details:  $\pi(\pi/2)=200(100)$  ns;  $\tau = 500$  ns;  $\text{HTA}_{\text{ELDOR}}$  pulse = 2  $\mu\text{s}$ , SRT = 2 ms, acquisition time = 14 h (red) 11 h (blue). The recorded spectra were baseline corrected by a spline function.

#### 5.4.2.2 Correlating of the Number of H bonds to the $g$ Value

The  $g_x$  value is an indication for an electrostatic environment mainly around the phenoxy oxygen nucleus. H bonding is a major factor for electrostatic effects beside positive charges in the surrounding. Hence, one might correlate observed  $g_x$  value with the number of H bonds. Depending on the number and the distance several H bond networks have been reported, for instance two studies in a highly polar electrostatic environment come close to the  $g$  values observed for  $Y_{356}\bullet:\alpha_2\text{-wt}$  (Table 5-6). Two H bonds have been reported previously in Y crystals formed in hydrochloric acid solution.<sup>161</sup> And three H bonds have even been modeled for  $Y_Z\bullet$  in PSII (Introduction §1.5.2, p.20).<sup>156, 161</sup>

To reduce the number of parameters one can use the point dipole approximation from  $Y_{356}\bullet:\alpha_2\text{-Y}_{731}\text{F}$ . The distance derived in §5.3.5 (p. 144) can be applied, because even for lower  $g_x$  values the oxygen spin density population was found identical to the values used for the distance calculation with  $\rho_{\text{O}} = 0.25$ .<sup>156</sup> Hence, the H bond distance should be approximately  $1.87 \pm 0.10$  Å.



As Table 5-6 illustrates, examples in the literature of two H bonds include at least one strong H bond ( $\approx 1.6 \text{ \AA}$ ), but this is not in agreement with the derived distance for  $Y_{356}\bullet:\alpha_2\text{-wt}$  ( $1.87 \pm 0.10 \text{ \AA}$ ). Two DFT models were set up to calculate the value of the HF coupling to the external proton in a mean distance of 1.84 (model 4) and 1.7  $\text{\AA}$  (model 5). The former report an HF coupling of  $A_z=1.2 \text{ MHz}$  the latter  $A_z=1.4 \text{ MHz}$ . The shorter distance has a significantly larger value than experimentally observed (0.91 MHz). The value calculated for the longer distance with 1.84  $\text{\AA}$  is within uncertainty (30%) still in agreement to the  $^2\text{H}$  ENDOR simulation. Both models are within uncertainty to the obtained  $g$  values of  $Y_{356}\bullet$  formed with  $\alpha_2\text{-wt}$ . The  $g_x$  value of both models is 0.2 ppt (model 5) and 0.5 ppt (model 4) larger than experimentally observed. Notably, the H bond environment described in Model 4 is similar to Model C designed for discussing polarity effects around  $\text{NH}_2Y_{356}\bullet$  (§4.6.4.4, p.124).

Equilibrium PCET Radical  $Y_{356}\bullet$  Formed during Reverse PCET

 Table S-6: Comparison between experimental (white) and calculated (highlighted gray)  $g$  values and, number and distances of H bonds.<sup>a</sup>

$g_x$ value	$g_y$ value	$g_z$ value	No. of H bonds	$r_{O-H}^b$ [Å]	Structure description	$T_{\perp}^c$	Reference
2.0072(1)	2.00446(5)	2.0022	two	1.9(1) <sup>d</sup> ~2.2 Å <sup>e</sup>	$Y_{356}\bullet:Y_{731}F$	-0.45	EPR: This thesis
2.0063(1)	2.0045(1)	2.0022(1)	≥two	1.9(1) <sup>d</sup> -	$Y_{356}\bullet:wt$	-0.45	EPR: This thesis
2.00673	2.00453	2.00232	one	1.45 <sup>f</sup> 1.60 <sup>d</sup>	$Y_D\bullet$ (tensed) His-H	-0.80	EPR <sup>153</sup>
2.00774	2.00447	2.00232	one	1.75 <sup>f</sup> 1.84 <sup>d</sup>	$Y_D\bullet$ (relaxed)His-H	-0.53	EPR <sup>153</sup>
2.0066	2.0042	2.0024	two	1.60 <sup>g</sup> -	Modeled by: COOH function and a polarized HCl molecule	-	EPR on crystal <sup>161</sup>
2.0062	2.0042	2.0021	two	1.60 <sup>g</sup> -	Modeled by: COOH function and a polarized HCl molecule	-	EPR on crystal <sup>161</sup>
2.0063	2.0044	2.0023	two	1.59 1.78	Polarized His and water molecules	-	DFT calculation <sup>156</sup>
2.0055	2.0043	2.0023	three	1.59 1.78 1.76	Polarized His and 2 water molecules	-	DFT calculation <sup>156</sup>
2.0068(5)	2.0046(5)	2.0023(2)	two	1.85 <sup>h</sup> 1.83 <sup>h</sup>	Model 4 2 water molecules	-0.62	DFT calculation: This thesis <sup>i</sup>
2.0065(5)	2.0045(5)	2.0022(2)	two	1.70 <sup>j</sup> 1.70 <sup>j</sup>	Model 5: 2 water molecules	-0.78	DFT calculation: This thesis <sup>i</sup>

a) The error or uncertainty of the values is given for the last digit in parentheses. b) H bond distance between phenoxy oxygen and proton. c) Averaged value in MHz; d) Derived by the point dipole approximation the error of 10% of the HF coupling is not considered. e) Estimated by a relaxed scan over H bond distances in a DFT model. f) Derived by McConnell Eq.  $\rho_O=0.28$  g) from the reduced crystal structure. h) <sup>1</sup>H HF couplings are  $A_{x,y,z} = -3.9, -4.3, 7.8$  MHz and  $A_{x,y,z} = -3.3, -3.5, 7.4$  MHz. i) Calculation details: UB3LYP, def2-TZVPP, COSMO(Ethanol), RICOSX, D3BJ Grimme dispersion corrected. The H bond distances 1.7 Å were restrained. The uncertainty of the coupling values is estimated with 20% and the uncertainty of the  $g$  values is estimated with 0.5 ppt. j) <sup>1</sup>H HF couplings are  $A_{x,y,z} = -4.0, -4.0, 8.7$  MHz and  $A_{x,y,z} = -5.1, -5.1, 9.2$  MHz.

## 5.5 Discussion

### 5.5.1 Removing the Conformational Gating by 2,3,5-F<sub>3</sub>Y

Initial studies demonstrated that  $\beta_2$ -2,3,5-F<sub>3</sub>Y<sub>122</sub> is able to overcome conformational gating with potential difference of about 10 mV to Y<sub>122</sub>.<sup>28</sup> The potential difference is low enough that reverse PCET from  $\beta_2$ -Y<sub>356</sub>• to  $\beta_2$ -2,3,5-F<sub>3</sub>Y<sub>122</sub> could be observed for the first time.<sup>28</sup> At first, it has been discussed that 2,3,5-F<sub>3</sub>Y is deprotonated at the 122 position<sup>83</sup> due to its pK<sub>a</sub> of 6.4.<sup>119</sup> Then it was concluded that 2,3,5-F<sub>3</sub>Y is protonated based on the inability to observe  $\beta_2$ -NO<sub>2</sub>Y<sub>122</sub><sup>-</sup> within a pH dependent study (cf. §1.4.5, p.16).<sup>41, 120</sup> In this study, however, the reported solvent inaccessibility of Y<sub>122</sub> has not been considered.<sup>46, 324</sup> Thus it cannot be excluded that the protonation state of the buried 122 residue is unaffected by the buffer pH.

The EPR parameters of  $\beta_2$ -2,3,5-F<sub>3</sub>Y<sub>122</sub>• were compared to  $\beta_2$ -wt(Y<sub>122</sub>•). EPR spectra were recorded at three different frequencies (9, 94 and 263 GHz) to determine *g* values and the tyrosine ring dihedral angle  $\theta_{C\beta}$ . One set of simulation parameters has been found for all spectra. The 263 GHz EPR spectra reveal a *g<sub>x</sub>* value of 2.00832(±0.00005), which is slightly shifted from the value of 2.00912(±0.00005) found in wt Y<sub>122</sub>•. A small model DFT calculation could reproduce the *g* value considering a polarity of  $\epsilon=4$  described previously for Y<sub>122</sub>•.<sup>104, 107, 325</sup> Notably, no H bond interaction has been considered in the model. In a combination of the empirical McConnell equation and DFT calculation the ring dihedral was determined to be  $\theta_{C\beta}=55\pm 5^\circ$ . The reduced state in the crystal structure reports about  $\theta_{C\beta}=46^\circ$ , thus a  $\approx 10^\circ$  larger value is observed.<sup>63</sup> On the other hand, the oxidized Y<sub>122</sub>• displays a 1-5° smaller value than observed for reduced Y<sub>122</sub>.<sup>63</sup> How this structural change could influence the accessibility of residue 122 to the interface requires still a large DFT or QM/MM model of different conformational states taking the C<sub>α</sub>-C<sub>β</sub> bond into account.

### 5.5.2 Comparison between Y<sub>356</sub>• and NH<sub>2</sub>Y<sub>356</sub>• Forward PCET Radical Intermediates

Information on the radical transfer along the subunit interface is important to understand the PCET between the subunits and the activity control of RNR Ia. In *E. coli* RNR Ia several pieces of information have been gathered for the “stepping stone” of the PCET, residue 356. In the reduced state, pK<sub>a</sub> measurements indicated a solvent like environment for NO<sub>2</sub>Y<sub>356</sub>

independently from the formation of the  $\alpha_2\beta_2$  “resting state” complex.<sup>118</sup> The transient radical state reports about how the protein has reorganized directly after a single PCET step in the “active”  $\alpha_2\beta_2$  complex. In the “active”  $\alpha_2\beta_2$  complex the radical pair distance between residues  $\beta^1$ -356 and  $\beta^2$ -122 (PELDOR distance) of  $3.0 \pm 0.1$  nm is independent of mutation method and reaction time ranging from 8 ms up to a minute.<sup>28, 43, 84</sup> EPR high-field data has reported that two different polar environments can be obtained at  $Y_{356}^\bullet$ .<sup>84</sup> A combined examination of polarity and H bond network, however, has not been presented before.

As shown in the previous (§4.6 p.110) and in the current chapter, two different approaches have been pursued to characterize radical intermediates at residue  $\beta$ - $Y_{356}$ . In the first approach the radical was competitively trapped using an  $NH_2Y$  mutant at residue 356 with 3-10 % residual activity.<sup>67</sup> In the second approach a PCET blockade was used with an  $\alpha_2$ - $Y_{731}F$  mutant, which is inactive.<sup>47, 84</sup> Despite their differences, both radical intermediates formed at residue 356 inform us about H bonding and electrostatic environment. Also in the reaction of the  $\beta_2$ -2,3,5- $F_3Y_{122}:\alpha_2$ - $Y_{731}F$  RNR the PELDOR distance is reproduced (cf. §5.3.2, p.139).<sup>28</sup> Additionally,  $Y_{356}^\bullet$  and  $NH_2Y_{356}^\bullet$  have no perpendicular strong or moderate exchangeable H bonds. Perpendicular H bonds have been observed in the studies of the PCET transfer in the RNR  $\alpha$  subunit (Chapter 4).<sup>110, 254</sup> The in-plane H bond characterized in  $Y_{356}^\bullet$  might be hidden under the wide spectral feature of the amino deuterons for  $NH_2Y_{356}^\bullet$ . The hyperfine tensor is proportional to the nearby phenoxy oxygen spin density population ( $\rho_O$ ) due to the scaling of its dipolar part. Therefore an H bond observed in an  $Y_{356}^\bullet$  with ( $T_\perp = 0.45$  MHz) has a dipolar strength related to  $\rho_O$ . A value around 25-28% is reported for  $\rho_O$ .<sup>156, 316-320, 323</sup> In contrast, the spin density population for  $NH_2Y^\bullet$  is in the range of 17-21%<sup>110</sup> for the single mutant models (see §4.4). Thus a distance found for  $Y_{356}^\bullet$  of 1.87-1.95 Å would be estimated with an HF coupling of  $T_\perp \approx 0.29$ -0.38 MHz for  $NH_2Y_{356}^\bullet$  (see Eq. 2-17). The most prominent axial component  $T_\perp$  in the spectra would be with  $\pm 0.2$  MHz not resolved from the matrix line of  $NH_2Y_{356}^\bullet$ , which could explain the absence of clearly resolved H bond features in the  $^2H$  ENDOR spectrum of  $NH_2Y_{356}^\bullet$ .

Furthermore, high frequency EPR delivers  $g$  values for the forward radical transfer of  $NH_2Y_{356}^\bullet$  and  $\beta$ - $Y_{356}^\bullet:\alpha$ - $Y_{730}F$ . The  $NH_2Y_{356}^\bullet$  has a  $g_x$  value (2.0049) slightly lower than the strongly H bonded  $NH_2Y$ s in the  $\alpha$  subunit (Chapter 4). The  $\beta$ - $Y_{356}^\bullet$  with  $\alpha_2$ - $Y_{730}F$  has a  $g_x$  value of 2.0072. Thus  $Y_{356}^\bullet$  is by 1.9 ppt more effected by electropositive charges than  $Y_{122}^\bullet$  and even 0.4 ppt more than yeast or mouse RNR  $Y_{122}^\bullet$  equivalent with one H bond

(1.8 Å).<sup>55, 158</sup> The value is not as low as the metastable “tensed”  $Y_D^\bullet$  state with 2.0064 with an H bond of approximately 1.5 Å (see §1.5.2, p.20).<sup>153</sup> The electrostatic effect of  $NH_2Y_{356}^\bullet$  should correspond to a moderate to strong H bond ( $r_{O-H}$  1.6 Å and 1.8 Å) and at least one moderate H bond ( $r_{O-H}$  1.9 Å) found in  $NH_2Y_{730}$  and  $NH_2Y_{731}$  (see §4.4). This would imply for  $Y_{356}^\bullet$  another partially positive charge in  $<2$  Å surrounding of the oxygen nucleus. However, this could not be observed for  $Y_{356}^\bullet$  with  $\alpha_2$ - $Y_{730}F$ . Here the  $g$  value is consistent with a weak H bond (1.8 Å) and another distant proton ( $\geq 2.2$  Å, Table 5-4, p.145). A similar environment has been modeled for  $NH_2Y_{356}^\bullet$  (model C §4.6.4.3, p.121). For  $NH_2Y_{356}^\bullet$  the  $g$  value could not be reproduced by one moderate and one weak H bond, but was within uncertainty of 0.5 ppt consistent to the DFT model C (§4.6.4.3, p.121). The lack of additional structural information, however, allows various interpretations. Noteworthy,  $Y_{356}^\bullet$  formed during reverse PCET with  $\alpha_2$ -wt is more consistent to the  $g$  value observed at  $NH_2Y_{356}^\bullet$  and with three weak to moderate H bonds or two H bonds and a positive charge.

Additionally, two conformers were recently proposed for  $NH_2Y_{356}^\bullet$  by their different kinetic phases.<sup>326</sup> Further time-dependent measurements at high frequency EPR are necessary to decide if the  $NH_2Y$  changes the equilibrium between the two states observed with  $Y_{356}^\bullet$ . One can point out that the conformer observed for the forward PCET at  $NH_2Y_{356}^\bullet$  ( $\theta_{C\beta} = 55^\circ \pm 15^\circ$ ) and  $Y_{356}^\bullet$  ( $\theta_{C\beta} = 42-56^\circ$ ) is identical within uncertainty of the measurement and the small DFT models.

### 5.5.3 $Y_{356}^\bullet$ in Forward and Reverse PCET

This thesis covers the forward PCET transfer in RNR Ia, which requires an additional mutation to observe the forward  $Y_{356}^\bullet$  species. Therefore the preliminary results of  $Y_{356}^\bullet$ : $\alpha_2$ -wt, which is initially formed during reverse PCET<sup>28</sup>, should be discussed. It could be shown that the reverse  $Y_{356}^\bullet$  shares a common distance with the forward  $Y_{356}^\bullet$  species. This is in agreement with study focusing on the equilibrium radicals formed using  $\beta_2$ - $NO_2Y_{122}$ :  $\alpha_2$ -wt. Additionally, all  $Y_{356}^\bullet$  using 2,3,5- $F_3Y_{122}^\bullet$  properties observed here agree well with the properties found using the  $\beta_2$ - $NO_2Y_{122}^\bullet$ , such as polarity and ring dihedral. However, using 2,3,5- $F_3Y_{122}^\bullet$  one could separate the investigation of  $Y_{356}^\bullet$  from the cofactor assembly step, necessary to produce  $\beta_2$ - $NO_2Y_{122}^\bullet$ .

Hence,  $Y_{356}^\bullet$  residue could be observed during putatively reverse PCET<sup>28</sup> with a  $g_x$  value of  $2.0063 \pm 0.0001$  in an unusual polar environment. It has the same  $^2H$  HF coupling

size as observed for  $Y_{356}^\bullet$  during forward PCET. The electrostatic environment is within uncertainty of our models in agreement with at least two in-plane H bonds in the range of  $1.9 \pm 0.1 \text{ \AA}$ . For longer distances a third weak H bond might be considered as the second weak H bond in the forward  $Y_{356}^\bullet$ . This implies a structured H bond network, because unstructured  $Y^\bullet$  in aqueous solution need an acidic environment to produce similar low  $g_x$  values (Table S-6).<sup>161, 319</sup> Furthermore a rapid exchange would broaden the EPR line shape  $B_{0||g_x}$  and the  $^2\text{H}$  ENDOR spectra, in contrary the lines are sharper than observed with  $Y_{356}^\bullet:\alpha_2\text{-}Y_{731}\text{F}$ . However, other sources of structured polar environments as cations or charged groups are equally possible to explain the  $g_x$  shift. As has been pointed out for  $\text{NH}_2Y_{356}^\bullet$ , positive charges from cations as  $\text{Mg}^{2+}$  or gadolinium groups can in principle introduce a strong polarity around  $Y^\bullet$ . Binding of  $\text{Mg}^{2+}$ , has long been known to play an important, but still poorly defined role in  $\alpha/\alpha$ ,  $\alpha/\beta$  and  $\beta$  structure/chemistry.<sup>74</sup> Though a complex of  $Y_{356}^\bullet$  and  $\text{Mg}^{2+}$  additional to the two H bonds observed is unlikely considering the strong effect on the  $g$  value of a divalent cation.<sup>174, 175</sup> Orientation selective measurement can further limit the directions of the H bond(s) observed  $Y_{356}^\bullet:\alpha_2\text{-wt}$ , if an additional parallel tensor component ( $T_{||}$ ) can be observed either along  $B_{0||g_x}$  and  $B_{0||g_z}$  a second  $1.9 \pm 0.1 \text{ \AA}$  H bond would be present. A second H bond in this range would imply a similar geometry as observed for  $\text{NH}_2Y_{730}^\bullet$  with three H bonds 1.8, 1.8 and  $2.2 \text{ \AA}$ .<sup>110</sup>

The H bond network found at the  $Y_{356}^\bullet$  could be used to obtain the reversible redox potentials. Peptide models have been applied to measure reversible redox potentials of the radical intermediates without dimerization of the  $Y^\bullet$  in solution.<sup>62, 327, 121, 122</sup> The H bond network observed in this thesis at the RNR intermediates might aid the design of adequate peptide models, which are able to measure realistic redox potentials. Generally, it has been found that an additional H bond can reduce the redox potential by typically 60-120 mV.<sup>292</sup> An approximately 60 mV lower potential of  $Y_{356}^\bullet$  has been postulated based on kinetic data compared to the Y PCET intermediates  $Y_{731}^\bullet$  and  $Y_{730}^\bullet$  in the  $\alpha$  subunit (see Figure 1-11, p.17).<sup>28, 41, 84</sup>

Based solely on the Mims ENDOR spectra presented herein, it cannot be evaluated if the two  $Y_{356}^\bullet$  resemble two energetic minimum states or if the  $\alpha\text{-}Y_{731}\text{F}$  mutation influences the environment. It cannot be ruled out that an H bond bound to  $Y_{356}^\bullet$  is lost due to  $\alpha_2\text{-}Y_{731}\text{F}$  mutation, because a water molecule is also bound to  $\alpha_2\text{-}Y_{731}$ . However, in the last

chapter it could be shown that at least  $\text{NH}_2\text{Y}_{731}\bullet$  interacts only weakly with the subunit interface.

Additionally, a change in the isotropic  $\beta$ -methylene HF couplings from 47 to 56 MHz could be observed for forward to reverse  $\text{Y}_{356}\bullet$ , respectively. This might be an indication of two conformeric states of  $\text{Y}_{356}\bullet$ . A large change in  $\text{C}_\beta\text{-H}$  HF coupling is not a prerequisite for a conformational change. Here a significant change of 20% could be observed between forward and reverse PCET  $\text{Y}_{356}\bullet$ . If a conformational change occurs it could change the ET distance in the PCET by more than 6 Å, although the diagonal distance between  $\beta^1\text{-Y}_{356}\bullet$  and  $\alpha^2\text{-2,3,5-F}_3\text{Y}_{122}\bullet$  might be unaffected (Introduction §1.4.6, p.17). In this thesis, an unchanged diagonal distance has been found between forward and reverse PCET  $\text{Y}_{356}\bullet$ . The same was reported using  $\text{NO}_2\text{Y}_{122}\bullet$  to form forward and reverse  $\text{Y}_{356}\bullet$ .<sup>84</sup>

This could be further tested by rapid freeze quench EPR. In the EPR spectra a change in  $g_x$  value from the millisecond time to the second time scale could be investigated. With  $\text{Y}_{356}\bullet:\alpha_2\text{-wt}$  no difference were reported between RFQ and manual freeze quench at 9 GHz.<sup>28</sup> This could be an indication that the different H bond networks, observed with  $\text{Y}_{731}\text{F}$  and with wt  $\alpha$ , are indeed formed first during forward then during reverse PCET. A change in the H bond network might affect the PT distances.

### 5.5.4 Mechanistic Implications

Mechanistically the presence of a bidirectional PCET at  $\text{Y}_{356}$  has been suggested since the pH dependent measurements with various fluorinated  $\text{Y}_{356}$ .<sup>82, 119</sup> In combination with conserved glutamates (i.e.,  $\text{E}_{350}$ , see §1.4.1.2, p.7), a geometry similar to tyrosine analogs (1 or 2) of Hammerström et al.<sup>328</sup> was proposed, as shown in Figure 5-15.<sup>328, 329</sup> In these models, Hammerström et al. could show that the phenol reaction was pH independent in the presence of an intramolecular acid.<sup>328</sup> This has been observed during various  $\text{F}_n\text{Y}_{356}$  incorporations.<sup>82, 119</sup> However, there is not any spectroscopic evidence for a glutamate ( $\text{E}_{350}$ ) near residue 356. Additionally, no PT acceptor was found.

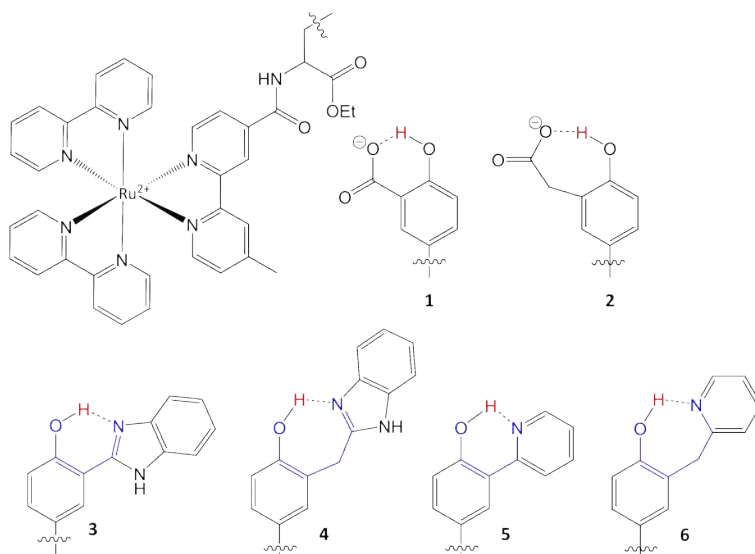


Figure 5-15: Biomimetic systems of H bonded tyrosine analogs linked to a photosensitizer. **1** and **2** are from ref. <sup>101, 330</sup> and 3-6 are studied in ref. <sup>101</sup>.

This thesis was able demonstrate a polar environment that stabilizes two different H bond environments of  $Y_{356}^{\bullet}$ . In both cases forward or reverse PCET only in-plane and moderate H bonds are observed. The H bonds found here might be from the proton acceptor function during forward PCET. Thus a proton acceptor function (X) would be within  $\approx 2.9 \pm 1 \text{ \AA}$  (distance  $O_{\text{phenoxy}}$  to X) within the ring plane. Small PCET model studies have shown similar geometries.<sup>101, 102</sup> Experimental studies point out that the kinetic rate in a bidirectional CPET by elongation of the ET distance from 12 to 21  $\text{\AA}$  is within error identical to the rate dependence of a pure electron transfer, for a short proton transport (PT) distance.<sup>331</sup> On the other hand, PT rates have been investigated for several donor acceptor distances within the ring plane (see 3-6, Figure 5-15), indicating that PT can be rate limiting.<sup>101, 252</sup> Due to the fast decay with PT distance, the H bond ( $\approx 1.9 \pm 1 \text{ \AA}$ ) found here could be a rate limiting with a donor acceptor distance  $d$  of  $2.9 \pm 0.1 \text{ \AA}$ , as illustrated by Figure 5-16.

However, the rate is strongly dependent on the distance and a change of  $\sim 0.2 \text{ \AA}$  changes the rate constant nearly 3 orders of magnitude. Currently, advanced EPR techniques combined with semi-empirical equations or HF parameter from DFT calculations employed here, are not precise enough to evaluate H bond distance changes of  $0.1 \text{ \AA}$ . Isotopical labeling with  $^2\text{H}$  could increase the resolution of  $^1\text{H}$  ENDOR spectroscopy in comparison to  $^2\text{H}$  ENDOR spectroscopy studied here.



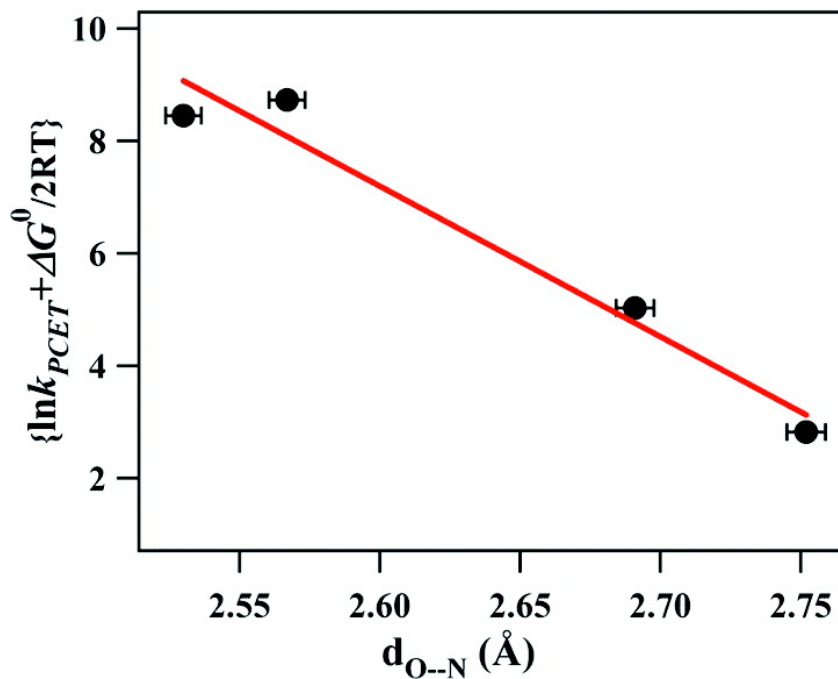


Figure 5-16: Dependence of the estimated PCET rate constant on the proton donor-acceptor distance  $d_{O-N}$  for a reaction without driving force ( $\Delta G^0=0$ ). The red line is a fit for  $\ln k_{PCET} = -\beta d_{O-N} + \text{constant}$ , with  $\beta \sim 27 \text{ \AA}^{-1}$ . Data plot from ref. <sup>101</sup>.

## 6 CONCLUSION

The intersubunit radical transfer from the diiron cofactor to the nucleotide reduction side in RNRs Ia has major unresolved issues. Although three Y• intermediates have been assigned, it is uncertain how these Ys transfer their protons to form Ys•. Structural information of the “active” state is still missing. In this thesis site specific incorporated 3-amino tyrosin forming NH<sub>2</sub>Ys• offered the unique opportunity to compare these three Y intermediates in high-field EPR investigations and resolve hydrogen (H) bonds networks and electrostatic environments at these radicals sites. At the Y intermediates  $\beta$ -356 another mutation strategy offered the possibility to characterize H bonds to Y<sub>356</sub>•.

### 6.1 NH<sub>2</sub>Y• Intermediates Investigated in the $\alpha$ Subunit

Pulsed-263-GHz EPR spectroscopy has been applied for the first time on NH<sub>2</sub>Ys• to unravel small changes in the electrostatic environment of NH<sub>2</sub>Y<sub>356</sub>•, NH<sub>2</sub>Y<sub>730</sub>• and NH<sub>2</sub>Y<sub>731</sub>•. The  $g_x$  value is most indicative for electrostatic changes, which arise due to positive and negative charges and H bond interactions. All three investigated intermediates showed low  $g_x$  values (> 0.6 ppt lower as the free NH<sub>2</sub>Y•) symptomatic for H bonded polar environments. NH<sub>2</sub>Y<sub>730</sub>• has been assigned before to harbor one moderate H bond (1.8 Å) and two weak H bonds ( $\geq 2.0$  Å),<sup>110</sup> in this thesis it had the highest  $g_x$  value of the three NH<sub>2</sub>Ys• intermediates. The  $g_x$  value from 263-GHz EPR spectra of NH<sub>2</sub>Y<sub>731</sub>• is with 0.3 ppt lower than found at NH<sub>2</sub>Y<sub>730</sub>• (see Table 4-7, p.114).

$^2\text{H}$  ENDOR spectroscopy revealed a strong H bond (1.6-1.7 Å) at  $\text{NH}_2\text{Y}_{731}\bullet$  (see Figure 4-7, p.83). A DFT calculation, consistent with the experimentally obtained  $g$  values, considered an additional weak in-plane H bond ( $\geq 1.9$  Å) from a nearby water molecule (Model 3 in Figure 4-16, p.100).

Thorough investigations lead from the initial hypothesis of  $\pi$  stacking between  $\text{Y}_{731}$  and  $\text{Y}_{730}$  to the first spectroscopic evidence for their interaction. First, two additional  $\text{NH}_2\text{Y}\bullet$  from double mutants were investigated, and thus underlying amino deuteron resonances could be separated from resonances of intermolecular H bonds. Two perpendicular H bonds at  $\text{NH}_2\text{Y}_{730}\bullet$  and one stronger H bond at  $\text{NH}_2\text{Y}_{731}\bullet$  were found consistent with the double mutants removing in each case one perpendicular H bond contribution. Second, to support the tensor shape indicating a contact interaction with the spin bearing  $p_z$  orbital, orientation selective ENDOR spectra at  $\text{NH}_2\text{Y}_{731}\bullet$  have been recorded. The simulation revealed an H bond and its H bond donor bond ( $\text{H-X}_{\text{Donor}}$ ) aligned  $\approx 70^\circ$  perpendicular to the ring plane (see Figure 4-7, p.83). Third, the interaction has been calculated by large DFT structures capturing the essential EPR parameters from 263-GHz EPR and 94-GHz ENDOR spectra. These calculations demonstrated a  $\pi$ -stacked geometry between  $\text{NH}_2\text{Y}_{731}\bullet$  and  $\text{Y}_{730}$  independent of the number of water molecules present in the models (1,2 & 3, Figure 4-16, p.100).

The combination of results from DFT models, EPR and orientation selective ENDOR spectra lead to the assignment of  $\text{H-O-Y}_{730}$  as H bond partner of  $\text{NH}_2\text{Y}_{731}\bullet$ . In the same DFT models without the  $\text{NH}_2$  group the  $\pi$  stacked conformation between  $\text{Y}_{730}$  and  $\text{Y}_{731}$  could be found in the oxidized and reduced state.<sup>110</sup> Together with the H bonds interaction at  $\text{NH}_2\text{Y}_{730}\bullet$  the mutual H bonding between position  $\text{Y}_{730}$  and  $\text{Y}_{731}$  could be demonstrated. This geometry is typical for an adiabatic proton transfer between  $\text{Y}_{731}$  and  $\text{Y}_{730}$ , formulated as HAT by Siegbahn *et al.* or as CPET by Kalia and Hummer.<sup>106, 107, 232</sup>

The DFT calculations of the large models could be closely correlated to the transition state calculations done prior to this thesis. A model including a distal water molecule (wat 1), H bonded to  $\text{Y}_{730}$ , is preferred based on the current data for the radical intermediate at 730 and 731 (Figure 1-14C, p.23). The structural bias of investigating a RNR Ia with  $\text{NH}_2\text{Ys}\bullet$  has been discussed.

RNR employs a highly selective PCET transfer. Seminal studies on the PCET showed that the removal of an OH group by mutation of a tyrosine to a phenylalanine is able

to shut down the whole pathway. H bond knock out double mutants (NH<sub>2</sub>Y<sub>731</sub>•/Y<sub>730</sub>F and NH<sub>2</sub>Y<sub>730</sub>•/C<sub>439</sub>A) highlighted this point again. They are intrinsically inactive due to the loss of an essential amino acid. However it was not expected that the radical build up rate would be directly affected, as the radical is generated - in PCET direction - before the mutation position. The double mutants form NH<sub>2</sub>Y• by a factor of 2 and 10 slower for NH<sub>2</sub>Y<sub>731</sub>•/Y<sub>730</sub>F and NH<sub>2</sub>Y<sub>730</sub>•/C<sub>439</sub>A, respectively (see Table 4-3, p.88). This showed once more how delicate this PCET pathway is in terms of activity. This is also in agreement with the recent slight over potential study of Olshansky et al., even here the radical decay of 2,3,5-F<sub>3</sub>Y<sub>356</sub>-β, was affected by a Y<sub>730</sub>F mutation in α, pointing out how important the PCET is for reducing the individually formed transient radical.<sup>86</sup>

Quite intriguing was the finding that the interaction from the α to the β subunit is not governed by a perpendicular moderate H bond as suggested previously.<sup>92</sup> However, a weak H bond ( $\geq 2$  Å) from the interface to NH<sub>2</sub>Y<sub>731</sub>• could not be excluded. Nevertheless, the data indicates that a close encounter as π stacking of Y<sub>356</sub> and Y<sub>731</sub> and a collinear PCET is unlikely.

## 6.2 NH<sub>2</sub>Y• and Y• Intermediates Investigated in the β Subunit

The investigation of radical intermediates in β was performed by the study of tyrosine intermediates at β<sub>2</sub>-Y<sub>356</sub>, in Chapter 4 with Y<sub>356</sub> mutated to NH<sub>2</sub>Y<sub>356</sub>.

263 GHz EPR spectroscopy revealed the highest polarity found in all NH<sub>2</sub>Ys• at NH<sub>2</sub>Y<sub>356</sub>• with a *g<sub>x</sub>* value of 2.0049 which is by 0.2-0.5 ppt significantly lower than in NH<sub>2</sub>Y<sub>730/731</sub>• (see Table 4-7, p.114). The ENDOR spectrum of NH<sub>2</sub>Y<sub>356</sub>•, however, was only in agreement with in-plane H bonds. In contrast to perpendicular H bonds, in-plane H bonds could be affected by the incorporated in-plane amino group. Here the innocent reporter role of the NH<sub>2</sub>Y• could not be anticipated anymore, therefore another mutation approach was necessary at residue 356. Here one could not find any evidence of a perpendicular or strong H bond at NH<sub>2</sub>Y•.

Y<sub>356</sub>• could be trapped using 2,3,5-F<sub>3</sub>Y<sub>122</sub>• with a ~10 mV higher reduction potential. Why 2,3,5-F<sub>3</sub>Y<sub>122</sub>• circumvents conformational gating and forms Y<sub>356</sub>• has not been understood.<sup>28</sup> A characterization of this mutant showed only a minor shift (9°) in ring dihedral compared to Y<sub>122</sub> (see Figure 5-3, p.134). If a difference in PT or indeed a general

deprotonated 2,3,5-F<sub>3</sub>Y<sub>122</sub><sup>-</sup> (pK<sub>a</sub> of N-acetyl-2,3,5-F<sub>3</sub>Y 6.3) triggers the unhindered PCET is still discussed.<sup>41</sup>

It has been discussed that a strong to moderate H bond is not expected between Y<sub>356</sub> and Y<sub>731</sub> based on NH<sub>2</sub>Y• studies. Therefore a PCET blockade as α<sub>2</sub>-Y<sub>731</sub>F should be a reasonable small perturbation to trap Y<sub>356</sub>• on the forward PCET. And indeed the yield was comparable to Y<sub>356</sub>• using α<sub>2</sub>-wt with about 30% for the manually quenched samples (s timescale).

The forward PCET Y<sub>356</sub>• was investigated by multi-frequency EPR at Q band and at 94 GHz. The spectra revealed a 0.4 ppt lower g<sub>x</sub> value of Y<sub>356</sub>• than observed for Y<sub>S</sub>• with one moderate H bond (1.8 Å), which is an indication for a higher electrostatic interaction. The <sup>2</sup>H Mims ENDOR spectra in combination with DFT calculations estimated an H bond distance of 1.9±0.1 Å to the phenoxy nucleus. The weak to moderate H bond was in-plane to the phenyl ring. Orientation selective ENDOR spectra could demonstrate an orientation perpendicular to the C-O bond axis similar to Y<sub>D</sub>• in PS II.<sup>155</sup> By comparison to other orientation selective measurements an additional smaller coupling was proposed.<sup>55</sup> In order to explain a small <sup>2</sup>H coupling pattern as well as the lower g<sub>x</sub> value (0.4 ppt compared to Y<sub>D</sub>•) a DFT Y• model was created. A moderate and a weak H bond with a distance of 1.8 and ≥2.2 Å could reproduce both EPR parameters.

The control study with β<sub>2</sub>-2,3,5-F<sub>3</sub>Y<sub>122</sub>•: α<sub>2</sub>-wt, reverse PCET Y<sub>356</sub>• showed a ring dihedral (θ<sub>Cβ</sub>=55±10°) and polarity similar to the forward NH<sub>2</sub>Y<sub>356</sub>• PCET case. The <sup>2</sup>H Mims ENDOR spectra, however, reported the same ENDOR pake pattern in size as Y<sub>356</sub>• formed during forward PCET. This apparent contradiction could be explained with a second moderate in-plane H bond (1.8 Å). Additionally, electrostatic influences have been discussed for NH<sub>2</sub>Y<sub>356</sub>• (during forward PCET) and Y<sub>356</sub>• (during reverse PCET). Higher resolution is necessary to further resolve the H bond environment during reverse PCET.

The absence of any strong or perpendicular H bond is an indication for a mechanistically different PCET in the β subunit in perspective to the observed π stacking in the α subunit.

## 6.3 Outlook

For the investigated tyrosyl radicals and their analogs, high frequency up to 263 GHz is necessary to measure resolved and accurate EPR spectra. In future studies the experimental

limit of resolvable nuclear distances can be expanded by the use of deuterated enzymes (Ys) in H<sub>2</sub>O buffer media to detect <sup>1</sup>H intermolecular ENDOR resonances. Theoretically, the broadening of the line and concomitant decrease in absorption is partially compensated by a higher detection efficiency for larger couplings (§2.2.3, p.40). Additionally, the splitting of the quadrupole coupling will be removed from the spectra, if intermolecular <sup>1</sup>H HF couplings are detected. It should be noted, that the quadrupole information on the electric field gradient will be lost. This information was valuable within this thesis. More recently developed high sensitive <sup>1</sup>H ENDOR schemes can be applied in isotope labeled samples.<sup>310,</sup>

332

Additional investigations on the reverse PCET have to be performed in shorter time scales within RFQ high-field EPR. A change in the *g* value over the reaction time might demonstrate the exchange between forward and reverse Y<sub>356</sub>• state. Additionally, the KIE should be measured between the PCET of 2,3,5-F<sub>3</sub>Y<sub>122</sub>• and Y<sub>356</sub>, because for the first time a putatively single PCET step can be investigated between Y intermediates in RNR.

Orientation selective PELDOR studies concomitantly with solid state NMR studies might investigate the structure of the “active” homodimeric complex using NH<sub>2</sub>Ys and an isotopically labeled β terminal tail.<sup>333-336</sup> The information from solid state NMR studies would be complementary, i.e., the reduced conformation of β<sub>2</sub>-Y<sub>356</sub> could be obtained if the reaction is trapped with NH<sub>2</sub>Y<sub>730</sub>•. New advances in cryo electron microscopy might also lead to structural insight with nearly atomic resolution (<3.0 Å).<sup>70,337,</sup>

338

Recently, several papers have used QM/MM calculations to investigate PCET reactions.<sup>339-341</sup> To observe if conformational changes occurring below the ms time scale QM/MM calculations of the subunit interface could contribute valuable insight in the ns timescale.

## 7 REFERENCES

1. Ehrenberg, A.; Reichard, P., Electron spin resonance of the iron-containing protein b2 from ribonucleotide reductase. *J. Biol. Chem.* **1972**, *247* (11), 3485-3488.
2. Stubbe, J.; van der Donk, W. A., Protein radicals in enzyme catalysis. *Chem. Rev. (Washington, DC, U. S.)* **1998**, *98* (2), 705-762.
3. Broderick, J. B.; Duffus, B. R.; Duschene, K. S.; Shepard, E. M., Radical s-adenosylmethionine enzymes. *Chem. Rev. (Washington, DC, U. S.)* **2014**, *114* (8), 4229-4317.
4. Stenkamp, R. E., Dioxygen and hemerythrin. *Chem. Rev. (Washington, DC, U. S.)* **1994**, *94* (3), 715-726.
5. Aye, Y.; Li, M.; Long, M. J. C.; Weiss, R. S., Ribonucleotide reductase and cancer: Biological mechanisms and targeted therapies. *Oncogene* **2015**, *34*, 2011–2021.
6. Torrents, E., Ribonucleotide reductases: Essential enzymes for bacterial life. *Front. Cell. Infect. Microbiol.* **2014**, *4* (52), 1-9.
7. Stubbe, J., Ribonucleotide reductases: The link between an RNA and a DNA world? *Curr. Opin. Struct. Biol.* **2000**, *10* (6), 731-736.
8. Reichard, P., From RNA to DNA, why so many ribonucleotide reductases? *Science* **1993**, *260* (5115), 1773-1777.
9. Thelander, L.; Reichard, P., Reduction of ribonucleotides. *Annu. Rev. Biochem.* **1979**, *48* (1), 133-158.
10. Reichard, P., Ribonucleotide reductases: The evolution of allosteric regulation. *Arch. Biochem. Biophys.* **2002**, *397* (2), 149-155.
11. Hofer, A.; Crona, M.; Logan, D. T.; Sjöberg, B.-M., DNA building blocks: Keeping control of manufacture. *Crit. Rev. Biochem. Mol. Biol.* **2012**, *47* (1), 50-63.

- 
12. Szekeres, T.; Fritzer-Szekeres, M.; Elford, H. L.; Jayaram, H. M., The enzyme ribonucleotide reductase: Target for antitumor and anti-HIV therapy. *Crit. Rev. Clin. Lab. Sci.* **1997**, *34* (6), 503-528.
  13. Nuno M. F. S. A. Cerqueira, S. A.; Fernandes, P. A.; Ramos, M. J., Ribonucleotide reductase: A critical enzyme for cancer chemotherapy and antiviral agents. *Recent. Pat. Anticancer Drug. Discov.* **2007**, *2* (1), 11-29.
  14. Shao, J.; Zhou, B.; Chu, B.; Yen, Y., Ribonucleotide reductase inhibitors and future drug design. *Curr. Cancer Drug Targets* **2006**, *6* (5), 409-431.
  15. Shao, J.; Liu, X.; Zhu, L.; Yen, Y., Targeting ribonucleotide reductase for cancer therapy. *Expert Opin. Ther. Targets* **2013**, *17* (12), 1423-1437.
  16. Mao, S. S.; Holler, T. P.; Yu, G. X.; Bollinger, J. M.; Booker, S.; Johnston, M. I.; Stubbe, J., A model for the role of multiple cysteine residues involved in ribonucleotide reduction - amazing and still confusing. *Biochemistry* **1992**, *31* (40), 9733-9743.
  17. Stubbe, J. A.; vanderDonk, W. A., Ribonucleotide reductases: Radical enzymes with suicidal tendencies. *Chem. Biol.* **1995**, *2* (12), 793-801.
  18. Licht, S.; Stubbe, J., Mechanistic investigations of ribonucleotide reductases. In *Comprehensive natural products chemistry*, Meth-Cohn, S. D. B. N., Ed. Pergamon: Oxford, 1999; pp 163-203.
  19. Licht, S.; Gerfen, G. J.; Stubbe, J., Thiyl radicals in ribonucleotide reductases. *Science* **1996**, *271* (5248), 477-481.
  20. Logan, D. T.; Andersson, J.; Sjöberg, B.-M.; Nordlund, P., A glycy radical site in the crystal structure of a class III ribonucleotide reductase. *Science* **1999**, *283* (5407), 1499-1504.
  21. Sintchak, M. D.; Arjara, G.; Kellogg, B. A.; Stubbe, J.; Drennan, C. L., The crystal structure of class II ribonucleotide reductase reveals how an allosterically regulated monomer mimics a dimer. *Nat. Struct. Mol. Biol.* **2002**, *9* (4), 293-300.
  22. Uhlin, U.; Eklund, H., Structure of ribonucleotide reductase protein R1. *Nature* **1994**, *370* (6490), 533-9.
  23. Eklund, H.; Fontecave, M., Glycyl radical enzymes: A conservative structural basis for radicals. *Structure* **1999**, *7* (11), R257-R262.
  24. Selmer, T.; Pierik, A. J.; Heider, J., New glycy radical enzymes catalysing key metabolic steps in anaerobic bacteria. *Biol. Chem.* **2005**, *386* (10), 981-988.
  25. Sun, X.; Harder, J.; Krook, M.; Jörnvall, H.; Sjöberg, B. M.; Reichard, P., A possible glycine radical in anaerobic ribonucleotide reductase from *Escherichia coli*: Nucleotide sequence of the cloned *nrdD* gene. *Proc. Natl. Acad. Sci. U. S. A.* **1993**, *90* (2), 577-581.
  26. Gambarelli, S.; Luttringer, F.; Padovani, D.; Mulliez, E.; Fontecave, M., Activation of the anaerobic ribonucleotide reductase by *s*-adenosylmethionine. *ChemBioChem* **2005**, *6* (11), 1960-1962.
  27. Jordan, A.; Reichard, P., Ribonucleotide reductases. *Annu. Rev. Biochem.* **1998**, *67* (1), 71-98.
  28. Minnihan, E. C. Mechanistic studies of proton-coupled electron transfer in aminotyrosine- and fluorotyrosine- substituted class Ia ribonucleotide reductase. PhD Thesis, Massachusetts Institute of Technology Cambridge US, 2012.



29. Lundin, D.; Torrents, E.; Poole, A. M.; Sjöberg, B. M., RNRdb, a curated database of the universal enzyme family ribonucleotide reductase, reveals a high level of misannotation in sequences deposited to genbank. *BMC Genomics* **2009**, *10* (589), 1471-2164.
30. Lundin, D.; Gribaldo, S.; Torrents, E.; Sjöberg, B.-M.; Poole, A., Ribonucleotide reduction - horizontal transfer of a required function spans all three domains. *BMC Evol. Biol.* **2010**, *10* (1), 383-401.
31. Dassama, L. M. K.; Krebs, C.; Bollinger, J. M.; Rosenzweig, A. C.; Boal, A. K., Structural basis for assembly of the MnIV/FeIII cofactor in the class Ic ribonucleotide reductase from chlamydia trachomatis. *Biochemistry* **2013**, *52* (37), 6424-6436.
32. Boal, A. K.; Cotruvo, J. A.; Stubbe, J.; Rosenzweig, A. C., Structural basis for activation of class Ib ribonucleotide reductase. *Science* **2010**, *329* (5998), 1526-1530.
33. Tomter, A. B.; Zoppellaro, G.; Andersen, N. H.; Hersleth, H.-P.; Hammerstad, M.; Røhr, Å. K.; Sandvik, G. K.; Strand, K. R.; Nilsson, G. E.; Bell Iii, C. B.; Barra, A.-L.; Blasco, E.; Le Pape, L.; Solomon, E. I.; Andersson, K. K., Ribonucleotide reductase class I with different radical generating clusters. *Coord. Chem. Rev.* **2013**, *257* (1), 3-26.
34. Stubbe, J.; Nocera, D. G.; Yee, C. S.; Chang, M. C. Y., Radical initiation in the class I ribonucleotide reductase: Long-range proton-coupled electron transfer? *Chem. Rev. (Washington, DC, U. S.)* **2003**, *103* (6), 2167-2202.
35. Lundin, D.; Berggren, G.; Logan, D.; Sjöberg, B.-M., The origin and evolution of ribonucleotide reduction. *Life* **2015**, *5* (1), 604-636.
36. Roshick, C.; Iliffe-Lee, E. R.; McClarty, G., Cloning and characterization of ribonucleotide reductase from chlamydia trachomatis. *J. Biol. Chem.* **2000**, *275* (48), 38111-38119.
37. Högbom, M.; Stenmark, P.; Voevodskaya, N.; McClarty, G.; Gräslund, A.; Nordlund, P., The radical site in chlamydial ribonucleotide reductase defines a new R2 subclass. *Science* **2004**, *305* (5681), 245-248.
38. Dassama, L. M. K.; Jiang, W.; Varano, P. T.; Pandelia, M.-E.; Conner, D. A.; Xie, J.; Bollinger, J. M.; Krebs, C., Radical-translocation intermediates and hurdling of pathway defects in "super-oxidized" (MnIV/FeIV) chlamydia trachomatis ribonucleotide reductase. *J. Am. Chem. Soc.* **2012**, *134* (50), 20498-20506.
39. Cox, N.; Ogata, H.; Stolle, P.; Reijerse, E.; Auling, G.; Lubitz, W., A tyrosyl-dimanganese coupled spin system is the native metalloradical cofactor of the R2F subunit of the ribonucleotide reductase of corynebacterium ammoniagenes. *J. Am. Chem. Soc.* **2010**, *132* (32), 11197-11213.
40. Cotruvo, J. A.; Stich, T. A.; Britt, R. D.; Stubbe, J., Mechanism of assembly of the dimanganese-tyrosyl radical cofactor of class Ib ribonucleotide reductase: Enzymatic generation of superoxide is required for tyrosine oxidation via a Mn(III)Mn(IV) intermediate. *J. Am. Chem. Soc.* **2013**, *135* (10), 4027-4039.
41. Minnihan, E. C.; Nocera, D. G.; Stubbe, J., Reversible, long-range radical transfer in E. coli class Ia ribonucleotide reductase. *Acc. Chem. Res.* **2013**, *46* (11), 2524-2535.
42. Parker, M. J.; Zhu, X.; Stubbe, J., Bacillus subtilis class Ib ribonucleotide reductase: High activity and dynamic subunit interactions. *Biochemistry* **2014**, *53* (4), 766-776.

- 
43. Seyedsayamdost, M. R.; Chan, C. T. Y.; Mugnaini, V.; Stubbe, J.; Bennati, M., PELDOR spectroscopy with DOPA- $\beta$ 2 and NH<sub>2</sub>Y- $\alpha$ 2s: Distance measurements between residues involved in the radical propagation pathway of E. coli ribonucleotide reductase. *J. Am. Chem. Soc.* **2007**, *129* (51), 15748-15749.
  44. Seyedsayamdost, M. R.; Xie, J.; Chan, C. T. Y.; Schultz, P. G.; Stubbe, J., Site-specific insertion of 3-aminotyrosine into subunit alpha 2 of E. coli ribonucleotide reductase: Direct evidence for involvement of Y-730 and Y-731 in radical propagation. *J. Am. Chem. Soc.* **2007**, *129* (48), 15060-15071.
  45. Climent, I.; Sjoeborg, B. M.; Huang, C. Y., Site-directed mutagenesis and deletion of the carboxyl terminus of Escherichia coli ribonucleotide reductase protein R2. Effects on catalytic activity and subunit interaction. *Biochemistry* **1992**, *31* (20), 4801-4807.
  46. Nordlund, P.; Sjoberg, B.-M.; Eklund, H., Three-dimensional structure of the free radical protein of ribonucleotide reductase. *Nature* **1990**, *345* (6276), 593-598.
  47. Ekberg, M.; Sahlin, M.; Eriksson, M.; Sjöberg, B.-M., Two conserved tyrosine residues in protein R1 participate in an intermolecular electron transfer in ribonucleotide reductase. *J. Biol. Chem.* **1996**, *271* (34), 20655-20659.
  48. Rova, U.; Goodtzova, K.; Ingemarson, R.; Behravan, G.; Graeslund, A.; Thelander, L., Evidence by site-directed mutagenesis supports long-range electron transfer in mouse ribonucleotide reductase. *Biochemistry* **1995**, *34* (13), 4267-4275.
  49. Rova, U.; Adrait, A.; Pötsch, S.; Gräslund, A.; Thelander, L., Evidence by mutagenesis that Tyr370 of the mouse ribonucleotide reductase R2 protein is the connecting link in the intersubunit radical transfer pathway. *J. Biol. Chem.* **1999**, *274* (34), 23746-23751.
  50. Fairman, J. W.; Wijerathna, S. R.; Ahmad, M. F.; Xu, H.; Nakano, R.; Jha, S.; Prendergast, J.; Welin, R. M.; Flodin, S.; Roos, A.; Nordlund, P.; Li, Z.; Walz, T.; Dealwis, C. G., Structural basis for allosteric regulation of human ribonucleotide reductase by nucleotide-induced oligomerization. *Nat. Struct. Mol. Biol.* **2011**, *18* (3), 316-322.
  51. Uppsten, M.; Färnegårdh, M.; Jordan, A.; Eliasson, R.; Eklund, H.; Uhlin, U., Structure of the large subunit of class Ib ribonucleotide reductase from salmonella typhimurium and its complexes with allosteric effectors. *J. Mol. Biol.* **2003**, *330* (1), 87-97.
  52. Kauppi, B.; Nielsen, B. B.; Ramaswamy, S.; Kjøller Larsen, I.; Thelander, M.; Thelander, L.; Eklund, H., The three-dimensional structure of mammalian ribonucleotide reductase protein R2 reveals a more-accessible iron-radical site than Escherichia coli R2. *J. Mol. Biol.* **1996**, *262* (5), 706-720.
  53. Smith, P.; Zhou, B.; Ho, N.; Yuan, Y.-C.; Su, L.; Tsai, S.-C.; Yen, Y., 2.6 Å X-ray crystal structure of human p53R2, a p53-inducible ribonucleotide reductase. *Biochemistry* **2009**, *48* (46), 11134-11141.
  54. Schmidt, P. P.; Andersson, K. K.; Barra, A.-L.; Thelander, L.; Gräslund, A., High field EPR studies of mouse ribonucleotide reductase indicate hydrogen bonding of the tyrosyl radical. *J. Biol. Chem.* **1996**, *271* (39), 23615-23618.
  55. Bar, G.; Bennati, M.; Nguyen, H. H. T.; Ge, J.; Stubbe, J.; Griffin, R. G., High-frequency (140-GHz) time domain EPR and ENDOR spectroscopy: The tyrosyl radical-diiron cofactor in ribonucleotide reductase from yeast. *J. Am. Chem. Soc.* **2001**, *123* (15), 3569-3576.

56. Climent, I.; Sjoeborg, B. M.; Huang, C. Y., Carboxyl-terminal peptides as probes for Escherichia coli ribonucleotide reductase subunit interaction: Kinetic analysis of inhibition studies. *Biochemistry* **1991**, *30* (21), 5164-5171.
57. Brown, N. C.; Reichard, P., Ribonucleoside diphosphate reductase: Formation of active and inactive complexes of proteins b1 and b2. *J. Mol. Biol.* **1969**, *46* (1), 25-38.
58. Ingemarson, R.; Thelander, L., A kinetic study on the influence of nucleoside triphosphate effectors on subunit interaction in mouse ribonucleotide reductase. *Biochemistry* **1996**, *35* (26), 8603-8609.
59. Hassan, A. Q.; Wang, Y. T.; Plate, L.; Stubbe, J., Methodology to probe subunit interactions in ribonucleotide reductases. *Biochemistry* **2008**, *47* (49), 13046-13055.
60. Martin Bollinger Jr, J.; Hangtong, W.; Ravi, N.; Hanh Huynh, B.; Edmondson, D.; Stubbe, J., Use of rapid kinetics methods to study the assembly of the diferric-tyrosyl radical cofactor of E. coli ribonucleotide reductase. In *Methods enzymol.*, Judith, P. K., Ed. Academic Press: 1995; Vol. Volume 258, pp 278-303.
61. Atkin, C. L.; Thelander, L.; Reichard, P.; Lang, G., Iron and free radical in ribonucleotide reductase: Exchange of iron and mößbauer spectroscopy of the protein b2 subunit of the Escherichia coli enzyme. *J. Biol. Chem.* **1973**, *248* (21), 7464-7472.
62. Hunter, E. P. L.; Desrosiers, M. F.; Simic, M. G., The effect of oxygen, antioxidants, and superoxide radical on tyrosine phenoxyl radical dimerization. *Free Radical Biol. Med.* **1989**, *6* (6), 581-585.
63. Hogbom, M.; Galander, M.; Andersson, M.; Kolberg, M.; Hofbauer, W.; Lassmann, G.; Nordlund, P.; Lenzian, F., Displacement of the tyrosyl radical cofactor in ribonucleotide reductase obtained by single-crystal high-field EPR and 1.4-Å X-ray data. *Proc. Natl. Acad. Sci. U. S. A.* **2003**, *100* (6), 3209-14.
64. Elledge, S. J.; Zhou, Z.; Allen, J. B.; Navas, T. A., DNA damage and cell cycle regulation of ribonucleotide reductase. *BioEssays* **1993**, *15* (5), 333-339.
65. Brignole, E. J.; Ando, N.; Zimanyi, C. M.; Drennan, C. L., The prototypic class Ia ribonucleotide reductase from Escherichia coli: Still surprising after all these years. *Biochem. Soc. Trans.* **2012**, *40*, 523-530.
66. Eriksson, M.; Uhlin, U.; Ramaswamy, S.; Ekberg, M.; Regnström, K.; Sjöberg, B.-M.; Eklund, H., Binding of allosteric effectors to ribonucleotide reductase protein R1: Reduction of active-site cysteines promotes substrate binding. *Structure* **1997**, *5* (8), 1077-1092.
67. Minnihan, E. C.; Seyedsayamdost, M. R.; Uhlin, U.; Stubbe, J., Kinetics of radical intermediate formation and deoxynucleotide production in 3-aminotyrosine-substituted Escherichia coli ribonucleotide reductases. *J. Am. Chem. Soc.* **2011**, *133* (24), 9430-9440.
68. Voegtli, W. C.; Ge, J.; Perlstein, D. L.; Stubbe, J.; Rosenzweig, A. C., Structure of the yeast ribonucleotide reductase Y2Y4 heterodimer. *Proc. Natl. Acad. Sci. USA* **2001**, *98* (18), 10073-10078.
69. Minnihan, E. C.; Ando, N.; Brignole, E. J.; Olshansky, L.; Chittuluru, J.; Asturias, F. J.; Drennan, C. L.; Nocera, D. G.; Stubbe, J., Generation of a stable, aminotyrosyl radical-induced  $\alpha 2\beta 2$  complex of Escherichia coli class Ia ribonucleotide reductase. *Proc. Natl. Acad. Sci. U. S. A.* **2013**, *110* (10), 3835-3840.

- 
70. Zimanyi, Christina M.; Ando, N.; Brignole, Edward J.; Asturias, Francisco J.; Stubbe, J.; Drennan, Catherine L., Tangled up in knots: Structures of inactivated forms of e. coli class Ia ribonucleotide reductase. *Structure* **2012**, *20* (8), 1374-1383.
71. Ando, N.; Brignole, E. J.; Zimanyi, C. M.; Funk, M. A.; Yokoyama, K.; Asturias, F. J.; Stubbe, J.; Drennan, C. L., Structural interconversions modulate activity of Escherichia coli ribonucleotide reductase. *Proc. Natl. Acad. Sci. USA* **2011**, *108* (52), 21046-21051.
72. Nordlund, P.; Aberg, A.; Uhlin, U.; Eklund, H., Crystallographic investigations of ribonucleotide reductase. *Biochem. Soc. Trans.* **1993**, *21* (3), 735-8.
73. Lendzian, F.; Sahlin, M.; MacMillan, F.; Bittl, R.; Fiege, R.; Pötsch, S.; Sjöberg, B.-M.; Gräslund, A.; Lubitz, W.; Lassmann, G., Electronic structure of neutral tryptophan radicals in ribonucleotide reductase studied by EPR and ENDOR spectroscopy. *J. Am. Chem. Soc.* **1996**, *118* (34), 8111-8120.
74. Saleh, L.; Bollinger, J. M., Cation mediation of radical transfer between Trp48 and Tyr356 during O<sub>2</sub> activation by protein R2 of Escherichia coli ribonucleotide reductase: Relevance to R1–R2 radical transfer in nucleotide reduction? *Biochemistry* **2006**, *45* (29), 8823-8830.
75. Bollinger, J. M.; Edmondson, D. E.; Huynh, B. H.; Filley, J.; Norton, J. R.; Stubbe, J., Mechanism of assembly of the tyrosyl radical dinuclear iron cluster cofactor of ribonucleotide reductase. *Science* **1991**, *253* (5017), 292-298.
76. Ge, J.; Yu, G.; Ator, M. A.; Stubbe, J., Pre-steady-state and steady-state kinetic analysis of E. coli class I ribonucleotide reductase. *Biochemistry* **2003**, *42* (34), 10071-10083.
77. Sjöberg, B. M.; Karlsson, M.; Jörnvall, H., Half-site reactivity of the tyrosyl radical of ribonucleotide reductase from Escherichia coli. *J. Biol. Chem.* **1987**, *262* (20), 9736-43.
78. Ferreira, K. N.; Iverson, T. M.; Maghlaoui, K.; Barber, J.; Iwata, S., Architecture of the photosynthetic oxygen-evolving center. *Science* **2004**, *303* (5665), 1831-1838.
79. Umena, Y.; Kawakami, K.; Shen, J.-R.; Kamiya, N., Crystal structure of oxygen-evolving photosystem II at a resolution of 1.9 Å. *Nature* **2011**, *473* (7345), 55-60.
80. Bennati, M.; Robblee, J. H.; Mugnaini, V.; Stubbe, J.; Freed, J. H.; Borbat, P., EPR distance measurements support a model for long-range radical initiation in e.coli ribonucleotide reductase. *J. Am. Chem. Soc.* **2005**, *127* (43), 15014-15015.
81. Chang, M. C. Y.; Yee, C. S.; Nocera, D. G.; Stubbe, J., Site-specific replacement of a conserved tyrosine in ribonucleotide reductase with an aniline amino acid: A mechanistic probe for a redox-active tyrosine. *J. Am. Chem. Soc.* **2004**, *126* (51), 16702-16703.
82. Yee, C. S.; Chang, M. C. Y.; Ge, J.; Nocera, D. G.; Stubbe, J., 2,3-difluorotyrosine at position 356 of ribonucleotide reductase R2: A probe of long-range proton-coupled electron transfer. *J. Am. Chem. Soc.* **2003**, *125* (35), 10506-10507.
83. Seyedsayamdost, M. R.; Yee, C. S.; Stubbe, J., Use of 2,3,5-F<sub>3</sub>Y-beta 2 and 3-NH<sub>2</sub>Y-alpha 2 to study proton-coupled electron transfer in Escherichia coli ribonucleotide reductase. *Biochemistry* **2011**, *50* (8), 1403-1411.
84. Yokoyama, K.; Smith, A. A.; Corzilius, B.; Griffin, R. G.; Stubbe, J., Equilibration of tyrosyl radicals (Y356\*, Y731\*, Y730\*) in the radical propagation pathway of the Escherichia coli class Ia ribonucleotide reductase. *J. Am. Chem. Soc.* **2011**, *133* (45), 18420-32.

85. Holder, P. G.; Pizano, A. A.; Anderson, B. L.; Stubbe, J.; Nocera, D. G., Deciphering radical transport in the large subunit of class I ribonucleotide reductase. *J. Am. Chem. Soc.* **2012**, *134* (2), 1172-1180.
86. Olshansky, L.; Pizano, A. A.; Wei, Y.; Stubbe, J.; Nocera, D. G., Kinetics of hydrogen atom abstraction from substrate by an active site thiyl radical in ribonucleotide reductase. *J. Am. Chem. Soc.* **2014**, *136* (46), 16210-16216.
87. Seyedsayamdost, M. R.; Stubbe, J., Site-specific replacement of Y-356 with 3,4-dihydroxyphenylalanine in the beta 2 subunit of E. coli ribonucleotide reductase. *J. Am. Chem. Soc.* **2006**, *128* (8), 2522-2523.
88. Wang, L.; Brock, A.; Herberich, B.; Schultz, P. G., Expanding the genetic code of Escherichia coli. *Science* **2001**, *292* (5516), 498-500.
89. Dawson, P.; Muir, T.; Clark-Lewis, I.; Kent, S., Synthesis of proteins by native chemical ligation. *Science* **1994**, *266* (5186), 776-779.
90. DeFelippis, M. R.; Murthy, C. P.; Broitman, F.; Weinraub, D.; Faraggi, M.; Klapper, M. H., Electrochemical properties of tyrosine phenoxy and tryptophan indolyl radicals in peptides and amino acid analogs. *J. Phys. Chem.* **1991**, *95* (8), 3416-3419.
91. Minnihan, E. C.; Seyedsayamdost, M. R.; Stubbe, J., Use of 3-aminotyrosine to examine the pathway dependence of radical propagation in Escherichia coli ribonucleotide reductase. *Biochemistry* **2009**, *48* (51), 12125-12132.
92. Argirević, T. High-field EPR and ENDOR spectroscopy for proton-coupled electron transfer investigations in E. coli ribonucleotide reductase. PhD Thesis, Georg-August University, Göttingen, 2012.
93. Bennati, M.; Weber, A.; Antonic, J.; Perlstein, D. L.; Robblee, J.; Stubbe, J. A., Pulsed ELDOR spectroscopy measures the distance between the two tyrosyl radicals in the R2 subunit of the E. coli ribonucleotide reductase. *J. Am. Chem. Soc.* **2003**, *125* (49), 14988-14989.
94. Reece, S. Y.; Nocera, D. G., Proton-coupled electron transfer in biology: Results from synergistic studies in natural and model systems. *Annu. Rev. Biochem.* **2009**, *78*, 673-99.
95. Weinberg, D. R.; Gagliardi, C. J.; Hull, J. F.; Murphy, C. F.; Kent, C. A.; Westlake, B. C.; Paul, A.; Ess, D. H.; McCafferty, D. G.; Meyer, T. J., Proton-coupled electron transfer. *Chem. Rev. (Washington, DC, U. S.)* **2012**, *112* (7), 4016-4093.
96. Migliore, A.; Polizzi, N. F.; Therien, M. J.; Beratan, D. N., Biochemistry and theory of proton-coupled electron transfer. *Chem. Rev. (Washington, DC, U. S.)* **2014**, *114* (7), 3381-3465.
97. Hammes-Schiffer, S.; Stuchebrukhov, A. A., Theory of coupled electron and proton transfer reactions. *Chem. Rev. (Washington, DC, U. S.)* **2010**, *110* (12), 6939-6960.
98. Stubbe, J.; Nocera, D. G.; Yee, C. S.; Chang, M. C. Y., Radical initiation in the class I ribonucleotide reductase: Long-range proton-coupled electron transfer? *Chem. Rev. (Washington, DC, U. S.)* **2003**, *103* (6), 2167-2201.
99. Page, C. C.; Moser, C. C.; Chen, X.; Dutton, P. L., Natural engineering principles of electron tunnelling in biological oxidation-reduction. *Nature* **1999**, *402* (6757), 47-52.
100. Gray, H. B.; Winkler, J. R., Long-range electron transfer. *Proc. Natl. Acad. Sci. U. S. A.* **2005**, *102* (10), 3534-3539.

- 
101. Zhang, M.-T.; Irebo, T.; Johansson, O.; Hammarström, L., Proton-coupled electron transfer from tyrosine: A strong rate dependence on intramolecular proton transfer distance. *J. Am. Chem. Soc.* **2011**, *133* (34), 13224-13227.
  102. Markle, T. F.; Rhile, I. J.; Mayer, J. M., Kinetic effects of increased proton transfer distance on proton-coupled oxidations of phenol-amines. *J. Am. Chem. Soc.* **2011**, *133* (43), 17341-17352.
  103. Markle, T. F.; Rhile, I. J.; DiPasquale, A. G.; Mayer, J. M., Probing concerted proton–electron transfer in phenol–imidazoles. *Proc. Natl. Acad. Sci. USA* **2008**, *105* (24), 8185-8190.
  104. Wörsdörfer, B.; Conner, D. A.; Yokoyama, K.; Livada, J.; Seyedsayamdost, M.; Jiang, W.; Silakov, A.; Stubbe, J.; Bollinger, J. M.; Krebs, C., Function of the diiron cluster of Escherichia coli class Ia ribonucleotide reductase in proton-coupled electron transfer. *J. Am. Chem. Soc.* **2013**, *135* (23), 8585-8593.
  105. Zlateva, T.; Quaroni, L.; Que, L.; Stankovich, M. T., Redox studies of subunit interactivity in aerobic ribonucleotide reductase from Escherichia coli. *J. Biol. Chem.* **2004**, *279* (18), 18742-18747.
  106. Kaila, V. R. I.; Hummer, G., Energetics of direct and water-mediated proton-coupled electron transfer. *J. Am. Chem. Soc.* **2011**, *133* (47), 19040-19043.
  107. Siegbahn, P. E. M.; Eriksson, L.; Himo, F.; Pavlov, M., Hydrogen atom transfer in ribonucleotide reductase (RNR). *J. Phys. Chem. B* **1998**, *102* (51), 10622-10629.
  108. McGaughey, G. B.; Gagné, M.; Rappé, A. K.,  $\pi$ -stacking interactions: Alive and well in proteins. *J. Biol. Chem.* **1998**, *273* (25), 15458-15463.
  109. Skone, J. H.; Soudackov, A. V.; Hammes-Schiffer, S., Calculation of vibronic couplings for phenoxy/phenol and benzyl/toluene self-exchange reactions: Implications for proton-coupled electron transfer mechanisms. *J. Am. Chem. Soc.* **2006**, *128* (51), 16655-16663.
  110. Argirević, T.; Riplinger, C.; Stubbe, J.; Neese, F.; Bennati, M., ENDOR spectroscopy and DFT calculations: Evidence for the hydrogen-bond network within  $\alpha 2$  in the PCET of E. coli ribonucleotide reductase. *J. Am. Chem. Soc.* **2012**, *134* (42), 17661-17670.
  111. Warren, J. J.; Mayer, J. M., Moving protons and electrons in biomimetic systems. *Biochemistry* **2015**, *54* (10), 1863-1878.
  112. Chen, X.; Ma, G.; Sun, W.; Dai, H.; Xiao, D.; Zhang, Y.; Qin, X.; Liu, Y.; Bu, Y., Water promoting electron hole transport between tyrosine and cysteine in proteins via a special mechanism: Double proton coupled electron transfer. *J. Am. Chem. Soc.* **2014**, *136* (12), 4515-4524.
  113. Inagaki, T.; Yamamoto, T.; Kato, S., Proton-coupled electron transfer of the phenoxy/phenol couple: Effect of Hartree-Fock exchange on transition structures. *J. Comput. Chem.* **2011**, *32* (14), 3081-3091.
  114. Pizano, A. A.; Lutterman, D. A.; Holder, P. G.; Teets, T. S.; Stubbe, J.; Nocera, D. G., Photo-ribonucleotide reductase beta 2 by selective cysteine labeling with a radical phototrigger. *Proc. Natl. Acad. Sci. U. S. A.* **2012**, *109* (1), 39-43.
  115. McMillen, D. F.; Golden, D. M., Hydrocarbon bond dissociation energies. *Annu. Rev. Phys. Chem.* **1982**, *33* (1), 493-532.

116. Benson, S. W., Thermochemistry and kinetics of sulfur-containing molecules and radicals. *Chem. Rev. (Washington, DC, U. S.)* **1978**, *78* (1), 23-35.
117. Yee, C. S.; Seyedsayamdost, M. R.; Chang, M. C. Y.; Nocera, D. G.; Stubbe, J., Generation of the R2 subunit of ribonucleotide reductase by intein chemistry: Insertion of 3-nitrotyrosine at residue 356 as a probe of the radical initiation process. *Biochemistry* **2003**, *42* (49), 14541-14552.
118. Yokoyama, K.; Uhlin, U.; Stubbe, J., Site-specific incorporation of 3-nitrotyrosine as a probe of pK(a) perturbation of redox-active tyrosines in ribonucleotide reductase. *J. Am. Chem. Soc.* **2010**, *132* (24), 8385-8397.
119. Seyedsayamdost, M. R.; Yee, C. S.; Reece, S. Y.; Nocera, D. G.; Stubbe, J., pH rate profiles of FnY356-R2s (n=2, 3, 4) in Escherichia coli ribonucleotide reductase: Evidence that Y-356 is a redox-active amino acid along the radical propagation pathway. *J. Am. Chem. Soc.* **2006**, *128* (5), 1562-1568.
120. Minnihan, E. C.; Young, D. D.; Schultz, P. G.; Stubbe, J., Incorporation of fluorotyrosines into ribonucleotide reductase using an evolved, polyspecific aminoacyl-tRNA synthetase. *J. Am. Chem. Soc.* **2011**, *133* (40), 15942-15945.
121. Ravichandran, K. R.; Liang, L.; Stubbe, J.; Tommos, C., Formal reduction potential of 3,5-difluorotyrosine in a structured protein: Insight into multistep radical transfer. *Biochemistry* **2013**, *52* (49), 8907-8915.
122. Glover, S. D.; Jorge, C.; Liang, L.; Valentine, K. G.; Hammarström, L.; Tommos, C., Photochemical tyrosine oxidation in the structurally well-defined  $\alpha 3\gamma$  protein: Proton-coupled electron transfer and a long-lived tyrosine radical. *J. Am. Chem. Soc.* **2014**, *136* (40), 14039-14051.
123. Lycksell, P. O.; Ingemarson, R.; Davis, R.; Graeslund, A.; Thelander, L., <sup>1</sup>H NMR studies of mouse ribonucleotide reductase: The R2 protein carboxyl-terminal tail, essential for subunit interaction, is highly flexible but becomes rigid in the presence of protein R1. *Biochemistry* **1994**, *33* (10), 2838-2842.
124. Baker, N. A.; Sept, D.; Joseph, S.; Holst, M. J.; McCammon, J. A., Electrostatics of nanosystems: Application to microtubules and the ribosome. *Proc. Natl. Acad. Sci. USA* **2001**, *98* (18), 10037-10041.
125. Winkler, J. R.; Gray, H. B., Long-range electron tunneling. *J. Am. Chem. Soc.* **2014**, *136* (8), 2930-2939.
126. Pievo, R.; Angerstein, B.; Fielding, A. J.; Koch, C.; Feussner, I.; Bennati, M., A rapid freeze-quench setup for multi-frequency EPR spectroscopy of enzymatic reactions. *ChemPhysChem* **2013**, *14* (18), 4094-4101.
127. Yokoyama, K.; Uhlin, U.; Stubbe, J., A hot oxidant, 3-NO<sub>2</sub>Y122 radical, unmasks conformational gating in ribonucleotide reductase. *J. Am. Chem. Soc.* **2010**, *132* (43), 15368-15379.
128. Offenbacher, A. R.; Watson, R. A.; Pagba, C. V.; Barry, B. A., Redox-dependent structural coupling between the  $\alpha 2$  and  $\beta 2$  subunits in E. coli ribonucleotide reductase. *J. Phys. Chem. B* **2014**, *118* (11), 2993-3004.
129. Range, K.; Ayala, I.; York, D.; Barry, B. A., Normal modes of redox-active tyrosine: Conformation dependence and comparison to experiment. *J. Phys. Chem. B* **2006**, *110* (22), 10970-10981.

- 
130. Offenbacher, A. R.; Burns, L. A.; Sherrill, C. D.; Barry, B. A., Redox-linked conformational control of proton-coupled electron transfer: Y122 in the ribonucleotide reductase  $\beta$ 2 subunit. *J. Phys. Chem. B* **2013**, *117* (28), 8457-8468.
131. Barry, B. A.; Chen, J.; Keough, J.; Jenson, D.; Offenbacher, A.; Pagba, C., Proton-coupled electron transfer and redox-active tyrosines: Structure and function of the tyrosyl radicals in ribonucleotide reductase and photosystem II. *J. Phys. Chem. Lett.* **2012**, *3* (4), 543-554.
132. Lendzian, F.; Galander, M.; Hogbom, M.; Nordlund, P.; Jung, C.; Schunemann, V.; Barra, A. L., Tyrosyl radicals in iron enzymes: Structural information from high-field EPR on frozen solutions and single crystals. *J. Inorg. Biochem.* **2003**, *96* (1), 64-64.
133. Barry, B. A., Reaction dynamics and proton coupled electron transfer: Studies of tyrosine-based charge transfer in natural and biomimetic systems. *BBA - Bioenergetics* **2015**, *1847* (1), 46-54.
134. Seyedsayamdost, M. R.; Argirević, T.; Minnihan, E. C.; Stubbe, J.; Bennati, M., Structural examination of the transient 3-aminotyrosyl radical on the PCET pathway of *E. coli* ribonucleotide reductase by multifrequency EPR spectroscopy. *J. Am. Chem. Soc.* **2009**, *131* (43), 15729-15738.
135. Möbius, K.; Lubitz, W.; Savitsky, A., High-field EPR on membrane proteins – crossing the gap to NMR. *Prog. Nucl. Magn. Reson. Spectrosc.* **2013**, *75*, 1-49.
136. Un, S.; Dorlet, P.; Rutherford, A. W., A high-field EPR tour of radicals in photosystems I and II. *Appl. Magn. Reson.* **2001**, *21* (3-4), 341-361.
137. Schünemann, V.; Lendzian, F.; Jung, C.; Contzen, J.; Barra, A.-L.; Sligar, S. G.; Trautwein, A. X., Tyrosine radical formation in the reaction of wild type and mutant cytochrome P450cam with peroxy acids: A multifrequency EPR study of intermediates on the millisecond time scale. *J. Biol. Chem.* **2004**, *279* (12), 10919-10930.
138. Fielding, A. J.; Brodhun, F.; Koch, C.; Pievo, R.; Denysenkov, V.; Feussner, I.; Bennati, M., Multifrequency electron paramagnetic resonance characterization of PpoA, a cyp450 fusion protein that catalyzes fatty acid dioxygenation. *J. Am. Chem. Soc.* **2011**, *133* (23), 9052-9062.
139. Lendzian, F., Structure and interactions of amino acid radicals in class I ribonucleotide reductase studied by ENDOR and high-field EPR spectroscopy. *Biochim. Biophys. Acta, Bioenerg.* **2005**, *1707* (1), 67-90.
140. Stoll, S., High-field EPR of bioorganic radicals. In *Electron paramagnetic resonance: Volume 22*, The Royal Society of Chemistry: 2011; Vol. 22, pp 109-122.
141. Stone, A. J., g Factors of aromatic free radicals. *Mol. Phys.* **1963**, *6* (5), 509-515.
142. Un, S.; Gerez, C.; Elleingand, E.; Fontecave, M., Sensitivity of tyrosyl radical g-values to changes in protein structure: A high-field EPR study of mutants of ribonucleotide reductase. *J. Am. Chem. Soc.* **2001**, *123* (13), 3048-3054.
143. Un, S.; Atta, M.; Fontecave, M.; Rutherford, A. W., g-values as a probe of the local protein environment: High-field EPR of tyrosyl radicals in ribonucleotide reductase and photosystem II. *J. Am. Chem. Soc.* **1995**, *117* (43), 10713-10719.
144. Un, S., The g-values and hyperfine coupling of amino acid radicals in proteins: Comparison of experimental measurements with ab initio calculations. *Magn. Reson. Chem.* **2005**, *43* (S1), S229-S236.



145. Himo, F.; Gräslund, A.; Eriksson, L. A., Density functional calculations on model tyrosyl radicals. *Biophys. J.* **1997**, *72* (4), 1556-1567.
146. Himo, F.; Eriksson, L. A.; Blomberg, M. R. A.; Siegbahn, P. E. M., Substituent effects on OH bond strength and hyperfine properties of phenol, as model for modified tyrosyl radicals in proteins. *Int. J. Quantum Chem.* **2000**, *76* (6), 714-723.
147. Stowell, M. H. B.; McPhillips, T. M.; Rees, D. C.; Soltis, S. M.; Abresch, E.; Feher, G., Light-induced structural changes in photosynthetic reaction center: Implications for mechanism of electron-proton transfer. *Science* **1997**, *276* (5313), 812-816.
148. Lawrence, C. C.; Bennati, M.; Obias, H. V.; Bar, G.; Griffin, R. G.; Stubbe, J., High-field EPR detection of a disulfide radical anion in the reduction of cytidine 5'-diphosphate by the E441Q R1 mutant of Escherichia coli ribonucleotide reductase. *Proc. Natl. Acad. Sci. U. S. A.* **1999**, *96* (16), 8979-8984.
149. Maly, T.; Zwicker, K.; Cernescu, A.; Brandt, U.; Prisner, T. F., New pulsed EPR methods and their application to characterize mitochondrial complex I. *BBA - Bioenergetics* **2009**, *1787* (6), 584-592.
150. Sahlin, M.; Petersson, L.; Graeslund, A.; Ehrenberg, A.; Sjoeborg, B. M.; Thelander, L., Magnetic interaction between the tyrosyl free radical and the antiferromagnetically coupled iron center in ribonucleotide reductase. *Biochemistry* **1987**, *26* (17), 5541-5548.
151. Hirsh, D. J.; Beck, W. F.; Lynch, J. B.; Que, L.; Brudvig, G. W., Using saturation-recovery EPR to measure exchange couplings in proteins: Application to ribonucleotide reductase. *J. Am. Chem. Soc.* **1992**, *114* (19), 7475-7481.
152. Bennati, M.; Farrar, C. T.; Bryant, J. A.; Inati, S. J.; Weis, V.; Gerfen, G. J.; Riggs-Gelasco, P.; Stubbe, J.; Griffin, R. G., Pulsed electron-nuclear double resonance (ENDOR) at 140 GHz. *J. Magn. Reson.* **1999**, *138* (2), 232-243.
153. Chatterjee, R.; Coates, C. S.; Milikisiyants, S.; Lee, C.-I.; Wagner, A.; Poluektov, O. G.; Lakshmi, K. V., High-frequency electron nuclear double-resonance spectroscopy studies of the mechanism of proton-coupled electron transfer at the tyrosine-D residue of photosystem II. *Biochemistry* **2013**, *52* (28), 4781-4790.
154. Brynda, M.; David Britt, R., Density functional theory calculations on the magnetic properties of the model tyrosine radical-histidine complex mimicking tyrosyl radical YD $\cdot$  in photosystem II. *Res. Chem. Intermed.* **2007**, *33* (8), 863-883.
155. Keßen, S.; Teutloff, C.; Kern, J.; Zouni, A.; Bittl, R., High-field 2H-Mims-ENDOR spectroscopy on PSII single crystals: Hydrogen bonding of YD. *ChemPhysChem* **2010**, *11* (6), 1275-1282.
156. Retegan, M.; Cox, N.; Lubitz, W.; Neese, F.; Pantazis, D. A., The first tyrosyl radical intermediate formed in the S2-S3 transition of photosystem II. *Phys. Chem. Chem. Phys.* **2014**, *16* (24), 11901-11910.
157. Gerfen, G. J.; Bellow, B. F.; Un, S.; Bollinger, J. M.; Stubbe, J.; Griffin, R. G.; Singel, D. J., High-frequency (139.5 GHz) EPR spectroscopy of the tyrosyl radical in Escherichia-coli ribonucleotide reductase. *J. Am. Chem. Soc.* **1993**, *115* (14), 6420-6421.
158. Schmidt, P. P.; Andersson, K. K.; Barra, A. L.; Thelander, L.; Graslund, A., High field EPR studies of mouse ribonucleotide reductase indicate hydrogen bonding of the tyrosyl radical. *J. Biol. Chem.* **1996**, *271* (39), 23615-23618.

- 
159. van Dam, P. J.; Willems, J.-P.; Schmidt, P. P.; Pötsch, S.; Barra, A.-L.; Hagen, W. R.; Hoffman, B. M.; Andersson, K. K.; Gräslund, A., High-frequency EPR and pulsed Q-band ENDOR studies on the origin of the hydrogen bond in tyrosyl radicals of ribonucleotide reductase R2 proteins from mouse and herpes simplex virus type 1. *J. Am. Chem. Soc.* **1998**, *120* (20), 5080-5085.
160. Dorlet, P.; Seibold, S. A.; Babcock, G. T.; Gerfen, G. J.; Smith, W. L.; Tsai, A. L.; Un, S., High-field EPR study of tyrosyl radicals in prostaglandin H-2 synthase-1. *Biochemistry* **2002**, *41* (19), 6107-6114.
161. Maniero, A. L.; Chis, V.; Zoleo, A.; Brustolon, M.; Mezzetti, A., Three different tyrosyl radicals identified in l-tyrosine HCl crystals upon  $\gamma$ -irradiation: Magnetic characterization and temporal evolution. *J. Phys. Chem. B* **2008**, *112* (12), 3812-3820.
162. Liu, C. C.; Schultz, P. G., Adding new chemistries to the genetic code. *Annu. Rev. Biochem.* **2010**, *79* (1), 413-444.
163. Xie, J.; Schultz, P. G., A chemical toolkit for proteins [mdash] an expanded genetic code. *Nat. Rev. Mol. Cell Biol.* **2006**, *7* (10), 775-782.
164. Schmidt, M. J.; Borbas, J.; Drescher, M.; Summerer, D., A genetically encoded spin label for electron paramagnetic resonance distance measurements. *J. Am. Chem. Soc.* **2014**, *136* (4), 1238-1241.
165. Liu, W.; Brock, A.; Chen, S.; Chen, S.; Schultz, P. G., Genetic incorporation of unnatural amino acids into proteins in mammalian cells. *Nat. Meth.* **2007**, *4* (3), 239-244.
166. Pless, S. A.; Ahern, C. A., Unnatural amino acids as probes of ligand-receptor interactions and their conformational consequences. *Annu. Rev. Pharmacol. Toxicol.* **2013**, *53* (1), 211-229.
167. Kaupp, M.; Bühl, M.; Malkin, V. G., Calculation of NMR and EPR parameters : Theory and applications. Wiley-VCH: Weinheim, 2004.
168. Stoll, S.; Schweiger, A., Easyspin, a comprehensive software package for spectral simulation and analysis in EPR. *J. Magn. Reson.* **2006**, *178* (1), 42-55.
169. Stoll, S.; Britt, R. D., General and efficient simulation of pulse EPR spectra. *Phys. Chem. Chem. Phys.* **2009**, *11* (31), 6614-25.
170. Slichter, C. P., Principles of magnetic resonance, with examples from solid state physics. Harper & Row: New York, 1963.
171. Carrington, A.; McLachlan, A. D., Introduction to magnetic resonance : With applications to chemistry and chemical physics. Harper & Row: New York, 1967.
172. Schweiger, A. J. G., *Principles of pulse electron paramagnetic resonance*. Oxford University Press: Oxford, UK; New York, 2001.
173. Atherton, N. M., *Principles of electron spin resonance*. Ellis Horwood : PTR Prentice Hall: New York, 1993.
174. Witwicki, M.; Jezierska, J., Protonated o-semiquinone radical as a mimetic of the humic acids native radicals: A DFT approach to the molecular structure and EPR properties. *Geochim. Cosmochim. Acta* **2012**, *86*, 384-391.
175. Witwicki, M.; Jezierska, J., Effects of solvents, ligand aromaticity, and coordination sphere on the g tensor of anionic o-semiquinone radicals complexed by mg<sup>2+</sup> ions: DFT studies. *J. Phys. Chem. B* **2011**, *115* (12), 3172-3184.

176. McConnell, H. M.; Chesnut, D. B., Theory of isotropic hyperfine interactions in  $\pi$ -electron radicals. *J. Chem. Phys.* **1958**, *28* (1), 107-117.
177. McConnell, H. M.; Robertson, R. E., Comments on "theory of isotropic hyperfine interactions in  $\pi$ -electron radicals". *J. Chem. Phys.* **1958**, *28* (5), 991-992.
178. McLachlan, A. D., Hyperconjugation in the electron resonance spectra of free radicals. *Mol. Phys.* **1958**, *1* (3), 233-240.
179. Schweiger, A.; Jeschke, G., *Principles of pulse electron paramagnetic resonance*. Oxford University Press: Oxford, UK; New York, 2001.
180. Gemperle, C.; Sorensen, O. W.; Schweiger, A.; Ernst, R. R., Optimized polarization transfer in pulse ENDOR experiments. *J. Magn. Reson.* **1990**, *87* (3), 502-515.
181. Feher, G., Observation of nuclear magnetic resonances via the electron spin resonance line. *Physical Review* **1956**, *103* (3), 834-835.
182. Davies, E. R., A new pulse endor technique. *Phys. Lett. A* **1974**, *47* (1), 1-2.
183. Mims, W. B., Pulsed ENDOR experiments. *Proc. Roy. Soc. A* **1965**, *283* (1395), 452-457.
184. Davies, E. R.; Reddy, T. R., An explanation of anomalously low intensity endor lines. *Phys. Lett. A* **1970**, *31* (7), 398-399.
185. Schlick, S.; Kevan, L.; Toriyama, K.; Iwasaki, M., The importance of nuclear spin diffusion as an angularly independent relaxation mechanism controlling the matrix ENDOR response of radicals in molecular crystals. *J. Chem. Phys.* **1981**, *74* (1), 282-287.
186. Schosseler, P.; Wacker, T.; Schweiger, A., Pulsed ELDOR detected NMR. *Chem. Phys. Lett.* **1994**, *224* (3-4), 319-324.
187. Nalepa, A.; Möbius, K.; Lubitz, W.; Savitsky, A., High-field ELDOR-detected NMR study of a nitroxide radical in disordered solids: Towards characterization of heterogeneity of microenvironments in spin-labeled systems. *J. Magn. Reson.* **2014**, *242*, 203-213.
188. Mentink-Vigier, F.; Collauto, A.; Feintuch, A.; Kaminker, I.; Tarle, V.; Goldfarb, D., Increasing sensitivity of pulse EPR experiments using echo train detection schemes. *J. Magn. Reson.* **2013**, *236*, 117-125.
189. Cox, N.; Retegan, M.; Neese, F.; Pantazis, D. A.; Boussac, A.; Lubitz, W., Electronic structure of the oxygen-evolving complex in photosystem II prior to O-O bond formation. *Science* **2014**, *345* (6198), 804-808.
190. Rapatskiy, L.; Cox, N.; Savitsky, A.; Ames, W. M.; Sander, J.; Nowaczyk, M. M.; Rögner, M.; Boussac, A.; Neese, F.; Messinger, J.; Lubitz, W., Detection of the water-binding sites of the oxygen-evolving complex of photosystem II using w-band 170 electron-electron double resonance-detected NMR spectroscopy. *J. Am. Chem. Soc.* **2012**, *134* (40), 16619-16634.
191. Cox, N.; Lubitz, W.; Savitsky, A., W-band ELDOR-detected NMR (EDNMR) spectroscopy as a versatile technique for the characterisation of transition metal-ligand interactions. *Mol. Phys.* **2013**, *111* (18-19), 2788-2808.
192. Becke, A. D., Perspective: Fifty years of density-functional theory in chemical physics. *J. Chem. Phys.* **2014**, *140* (18), 1-18.

- 
193. Hohenberg, P.; Kohn, W., Inhomogeneous electron gas. *Physical Review* **1964**, 136 (3B), B864-B871.
  194. Kohn, W.; Sham, L. J., Self-consistent equations including exchange and correlation effects. *Physical Review* **1965**, 140 (4A), A1133-A1138.
  195. Johnson, B. G.; Gonzales, C. A.; Gill, P. M. W.; Pople, J. A., A density functional study of the simplest hydrogen abstraction reaction. Effect of self-interaction correction. *Chem. Phys. Lett.* **1994**, 221 (1-2), 100-108.
  196. Lynch, B. J.; Zhao, Y.; Truhlar, D. G., Effectiveness of diffuse basis functions for calculating relative energies by density functional theory. *J. Phys. Chem. A* **2003**, 107 (9), 1384-1388.
  197. Kaplan, I. G., Intermolecular interactions: Physical picture, computational methods and model potentials. John Wiley & Sons: 2006.
  198. Stone, A., *The theory of intermolecular forces*. Oxford University Press: 2013.
  199. Grimme, S.; Antony, J.; Ehrlich, S.; Krieg, H., A consistent and accurate ab initio parametrization of density functional dispersion correction (DFT-D) for the 94 elements H-Pu. *The Journal of Chemical Physics* **2010**, 132 (15), 1-19.
  200. Grimme, S.; Ehrlich, S.; Goerigk, L., Effect of the damping function in dispersion corrected density functional theory. *J. Comput. Chem.* **2011**, 32 (7), 1456-1465.
  201. Ehrlich, S.; Moellmann, J.; Grimme, S., Dispersion-corrected density functional theory for aromatic interactions in complex systems. *Acc. Chem. Res.* **2013**, 46 (4), 916-926.
  202. Johnson, E.; Dilabio, G., Radicals as hydrogen bond donors and acceptors. *Interdiscip. Sci.* **2009**, 1 (2), 133-140.
  203. Risthaus, T.; Grimme, S., Benchmarking of london dispersion-accounting density functional theory methods on very large molecular complexes. *J. Chem. Theory Comput.* **2013**, 9 (3), 1580-1591.
  204. Calbo, J.; Ortí, E.; Sancho-García, J. C.; Aragón, J., Accurate treatment of large supramolecular complexes by double-hybrid density functionals coupled with nonlocal van der waals corrections. *J. Chem. Theory Comput.* **2015**, 11 (3), 932-939.
  205. McQuarrie, D. A.; Simon, J. D., *Physical chemistry : A molecular approach*. University Science Books: Sausalito, Calif., 1997.
  206. Cramer, C. J., *Essentials of computational chemistry : Theories and models*. Wiley: Chichester, West Sussex, England; Hoboken, NJ, 2004.
  207. Weigend, F.; Ahlrichs, R., Balanced basis sets of split valence, triple zeta valence and quadruple zeta valence quality for H to Rn: Design and assessment of accuracy. *Phys. Chem. Chem. Phys.* **2005**, 7 (18), 3297-3305.
  208. Weigend, F., Accurate coulomb-fitting basis sets for H to Rn. *Phys. Chem. Chem. Phys.* **2006**, 8 (9), 1057-1065.
  209. Breit, G., Dirac's equation and the spin-spin interactions of two electrons. *Physical Review* **1932**, 39 (4), 616-624.
  210. Neese, F., Prediction of electron paramagnetic resonance g values using coupled perturbed Hartree-Fock and kohn-sham theory. *J. Chem. Phys.* **2001**, 115 (24), 11080-11096.

211. Neese, F., Efficient and accurate approximations to the molecular spin-orbit coupling operator and their use in molecular g-tensor calculations. *J. Chem. Phys.* **2005**, *122* (3), 034107.
212. Neese, F., Spin-hamiltonian parameters from first principle calculations: Theory and application. In *Metals in biology : Applications of high resolution EPR to metalloenzymes*, Hanson, G. R.; Berliner, L. J., Eds. Springer: New York, 2012; p 175–229.
213. Schreckenbach, G.; Ziegler, T., Calculation of the g-tensor of electron paramagnetic resonance spectroscopy using gauge-including atomic orbitals and density functional theory. *J. Phys. Chem. A* **1997**, *101* (18), 3388-3399.
214. Neese, F., The ORCA program system. Wiley Interdisciplinary Reviews: Computational Molecular Science **2012**, *2* (1), 73-78.
215. van Lenthe, E.; Baerends, E. J.; Snijders, J. G., Relativistic total energy using regular approximations. *J. Chem. Phys.* **1994**, *101* (11), 9783-9792.
216. Kacprzak, S.; Kaupp, M., Electronic g-tensors of semiquinones in photosynthetic reaction centers. A density functional study. *J. Phys. Chem. B* **2004**, *108* (7), 2464-2469.
217. Flores, M.; Okamura, M. Y.; Niklas, J.; Pandelia, M.-E.; Lubitz, W., Pulse Q-band EPR and ENDOR spectroscopies of the photochemically generated monoprotonated benzosemiquinone radical in frozen alcoholic solution. *J. Phys. Chem. B* **2012**, *116* (30), 8890-8900.
218. Barone, V., Structure, epr parameters, and reactivity of organic free radicals from a density functional approach. *Theor. Chim. Acta* **1995**, *91* (3-4), 113-128.
219. Barone, V., Structure, magnetic properties and reactivities of open-shell species from density functional and self-consistent hybrid methods. 1995; Vol. 1, p 287-334.
220. Kutzelnigg, W.; Fleischer, U.; Schindler, M., The IGLO-method: Ab-initio calculation and interpretation of NMR chemical shifts and magnetic susceptibilities. In *Deuterium and shift calculation*, Springer Berlin Heidelberg: 1991; Vol. 23, pp 165-262.
221. Kossmann, S.; Kirchner, B.; Neese, F., Performance of modern density functional theory for the prediction of hyperfine structure: Meta-GGA and double hybrid functionals. *Mol. Phys.* **2007**, *105* (15-16), 2049-2071.
222. Marcus, R., Chemical and electrochemical electron-transfer theory. *Annu. Rev. Phys. Chem.* **1964**, *15* (1), 155-196.
223. Landau, L., Zur Theorie der Energieubertragung. II. *Phys. Z. Sowjetunion* **1932**, *2*, 46–51.
224. Zener, C., Dissociation of excited diatomic molecules by external perturbations. 1933; Vol. 140, p 660-668.
225. Oevering, H.; Paddon-Row, M. N.; Heppener, M.; Oliver, A. M.; Cotsaris, E.; Verhoeven, J. W.; Hush, N. S., Long-range photoinduced through-bond electron transfer and radiative recombination via rigid nonconjugated bridges: Distance and solvent dependence. *J. Am. Chem. Soc.* **1987**, *109* (11), 3258-3269.
226. Lin, J.; Balabin, I. A.; Beratan, D. N., The nature of aqueous tunneling pathways between electron-transfer proteins. *Science* **2005**, *310* (5752), 1311-1313.
227. Wenger, O. S., How donor–bridge–acceptor energetics influence electron tunneling dynamics and their distance dependences. *Acc. Chem. Res.* **2010**, *44* (1), 25-35.

- 
228. Zhang, Y.; Liu, C.; Balaeff, A.; Skourtis, S. S.; Beratan, D. N., Biological charge transfer via flickering resonance. *Proc. Natl. Acad. Sci. USA* **2014**, *111* (28), 10049-10054.
229. Beratan, D. N.; Liu, C.; Migliore, A.; Polizzi, N. F.; Skourtis, S. S.; Zhang, P.; Zhang, Y., Charge transfer in dynamical biosystems, or the treachery of (static) images. *Acc. Chem. Res.* **2014**, *48* (2), 474-481.
230. Marcus, R. A., Theoretical relations among rate constants, barriers, and broensted slopes of chemical reactions. *J. Phys. Chem.* **1968**, *72* (3), 891-899.
231. Mayer, J. M.; Hrovat, D. A.; Thomas, J. L.; Borden, W. T., Proton-coupled electron transfer versus hydrogen atom transfer in benzyl/toluene, methoxyl/methanol, and phenoxyl/phenol self-exchange reactions. *J. Am. Chem. Soc.* **2002**, *124*, 11142.
232. Siegbahn, P. E. M.; Blomberg, M. R. A., Quantum chemical studies of proton-coupled electron transfer in metalloenzymes. *Chem. Rev. (Washington, DC, U. S.)* **2010**, *110* (12), 7040-7061.
233. Layfield, J. P.; Hammes-Schiffer, S., Hydrogen tunneling in enzymes and biomimetic models. *Chem. Rev. (Washington, DC, U. S.)* **2013**, *114* (7), 3466-3494.
234. Franck, J.; Dymond, E. G., Elementary processes of photochemical reactions. *Transactions of the Faraday Society* **1926**, *21* (February), 536-542.
235. Condon, E. U., Nuclear motions associated with electron transitions in diatomic molecules. *Physical Review* **1928**, *32* (6), 858-872.
236. Condon, E., A theory of intensity distribution in band systems. *Physical Review* **1926**, *28* (6), 1182-1201.
237. Soudackov, A.; Hammes-Schiffer, S., Derivation of rate expressions for nonadiabatic proton-coupled electron transfer reactions in solution. *J. Chem. Phys.* **2000**, *113* (6), 2385-2396.
238. Hatcher, E.; Soudackov, A.; Hammes-Schiffer, S., Nonadiabatic proton-coupled electron transfer reactions: Impact of donor-acceptor vibrations, reorganization energies, and couplings on dynamics and rates. *J. Phys. Chem. B* **2005**, *109* (39), 18565-18574.
239. Soudackov, A.; Hatcher, E.; Hammes-Schiffer, S., Quantum and dynamical effects of proton donor-acceptor vibrational motion in nonadiabatic proton-coupled electron transfer reactions. *J. Chem. Phys.* **2005**, *122* (1), 014505.
240. Hammes-Schiffer, S., Proton-coupled electron transfer: Classification scheme and guide to theoretical methods. *Energy Environ. Sci.* **2012**, *5* (7), 7696-7703.
241. Hammes-Schiffer, S., Hydrogen tunneling and protein motion in enzyme reactions. *Acc. Chem. Res.* **2005**, *39* (2), 93-100.
242. Hammes-Schiffer, S.; Soudackov, A. V., Proton-coupled electron transfer in solution, proteins, and electrochemistry. *J. Phys. Chem. B* **2008**, *112* (45), 14108-14123.
243. Cukier, R. I., A theory that connects proton-coupled electron-transfer and hydrogen-atom transfer reactions. *J. Phys. Chem. B* **2002**, *106* (7), 1746-1757.
244. Mayer, J. M.; Hrovat, D. A.; Thomas, J. L.; Borden, W. T., Proton-coupled electron transfer versus hydrogen atom transfer in benzyl/toluene, methoxyl/methanol, and phenoxyl/phenol self-exchange reactions. *J. Am. Chem. Soc.* **2002**, *124* (37), 11142-11147.

245. Miller, N. E.; Wander, M. C.; Cave, R. J., A theoretical study of the electronic coupling element for electron transfer in water. *J. Phys. Chem. A* **1999**, *103* (8), 1084-1093.
246. Miyashita, O.; Okamura, M. Y.; Onuchic, J. N., Interprotein electron transfer from cytochrome c2 to photosynthetic reaction center: Tunneling across an aqueous interface. *Proc. Natl. Acad. Sci. U. S. A.* **2005**, *102* (10), 3558-3563.
247. Francisco, W. A.; Wille, G.; Smith, A. J.; Merkler, D. J.; Klinman, J. P., Investigation of the pathway for inter-copper electron transfer in peptidylglycine  $\alpha$ -amidating monooxygenase. *J. Am. Chem. Soc.* **2004**, *126* (41), 13168-13169.
248. van Amsterdam, I. M. C.; Ubbink, M.; Einsle, O.; Messerschmidt, A.; Merli, A.; Cavazzini, D.; Rossi, G. L.; Canters, G. W., Dramatic modulation of electron transfer in protein complexes by crosslinking. *Nat. Struct. Mol. Biol.* **2002**, *9* (1), 48-52.
249. Wang, L.; Fried, S. D.; Boxer, S. G.; Markland, T. E., Quantum delocalization of protons in the hydrogen-bond network of an enzyme active site. *Proc. Natl. Acad. Sci. USA* **2014**, *111* (52), 18454-18459.
250. Bonin, J.; Costentin, C.; Robert, M.; Routier, M.; Savéant, J.-M., Proton-coupled electron transfers: pH-dependent driving forces? Fundamentals and artifacts. *J. Am. Chem. Soc.* **2013**, *135* (38), 14359-14366.
251. Savéant, J.-M., Concerted proton-electron transfers: Fundamentals and recent developments. *Annu. Rev. Anal. Chem.* **2014**, *7* (1), 537-560.
252. Pizano, A. A.; Yang, J. L.; Nocera, D. G., Photochemical tyrosine oxidation with a hydrogen-bonded proton acceptor by bidirectional proton-coupled electron transfer. *Chemical Science* **2012**, *3* (8), 2457-2461.
253. Seyedsayamdost, M. R.; Stubbe, J., Chapter 3 replacement of Y730 and Y731 in the  $\alpha$ 2 subunit of Escherichia coli ribonucleotide reductase with 3-aminotyrosine using an evolved suppressor tRNA/tRNA-synthetase pair. In *Methods enzymol.*, Tom, W. M.; John, N. A., Eds. Academic Press: 2009; Vol. Volume 462, pp 45-76.
254. Nick, T. U.; Lee, W.; Koßmann, S.; Neese, F.; Stubbe, J.; Bennati, M., Hydrogen bond network between amino acid radical intermediates on the proton-coupled electron transfer pathway of E. coli  $\alpha$ 2 ribonucleotide reductase. *J. Am. Chem. Soc.* **2015**, *137* (1), 289-298.
255. Yokoyama, K.; Uhlin, U.; Stubbe, J., Site-specific incorporation of 3-nitrotyrosine as a probe of pKa perturbation of redox-active tyrosines in ribonucleotide reductase. *J. Am. Chem. Soc.* **2010**, *132* (24), 8385-97.
256. Crotty, D.; Silkstone, G.; Poddar, S.; Ranson, R.; Prina-Mello, A.; Wilson, M. T.; Coey, J. M. D., Reexamination of magnetic isotope and field effects on adenosine triphosphate production by creatine kinase. *Proc. Natl. Acad. Sci. USA* **2012**, *109* (5), 1437-1442.
257. Milov, A. D.; Maryasov, A. G.; Tsvetkov, Y. D., Pulsed electron double resonance (PELDOR) and its applications in free-radicals research. *Appl. Magn. Reson.* **1998**, *15* (1), 107-143.
258. Hoff, A. J., *Advanced EPR : Applications in biology and biochemistry*. Elsevier ; Distributors for the U.S. and Canada, Elsevier Science Pub. Co.: Amsterdam; New York; New York, NY, U.S.A., 1989.
259. Low, W., Paramagnetic resonance spectrum of manganese in cubic mgo and caf2. *Physical Review* **1957**, *105* (3), 793-800.

- 
260. Burghaus, O.; Rohrer, M.; Gotzinger, T.; Plato, M.; Mobius, K., A novel high-field/high-frequency EPR and ENDOR spectrometer operating at 3 mm wavelength. *Meas. Sci. Technol.* **1992**, *3* (8), 765.
261. Eaton, G. R.; Eaton, S. S.; Barr, D. P.; Weber, R. T., Quantitative EPR. **2010**.
262. Yordanov, N. D., Quantitative EPR spectrometry — “state of the art”. *Appl. Magn. Reson.* **1994**, *6* (1-2), 241-257.
263. Stesmans, A.; Van Gorp, G., Novel method for accurate g measurements in electron-spin resonance. *Rev. Sci. Instrum.* **1989**, *60* (9), 2949-2952.
264. Bellew, B. F. High frequency (139.5 GHz) electron paramagnetic resonance spectroscopy of biomolecules. PhD Thesis, Massachusetts Institute of Technology, 1996.
265. Mitchell, D. G.; Tseitlin, M.; Quine, R. W.; Meyer, V.; Newton, M. E.; Schnegg, A.; George, B.; Eaton, S. S.; Eaton, G. R., X-band rapid-scan EPR of samples with long electron spin relaxation times: A comparison of continuous wave, pulse and rapid-scan EPR. *Mol. Phys.* **2013**, *111* (18-19), 2664-2673.
266. Blomberg, M. R. A.; Siegbahn, P. E. M., Different types of biological proton transfer reactions studied by quantum chemical methods. *BBA - Bioenergetics* **2006**, *1757* (8), 969-980.
267. Perdew, J. P., Erratum: Density-functional approximation for the correlation energy of the inhomogeneous electron gas. *Phys. Rev. B* **1986**, *34* (10), 7406-7406.
268. Becke, A. D., Density-functional exchange-energy approximation with correct asymptotic behavior. *Phys. Rev. A* **1988**, *38* (6), 3098-3100.
269. Schäfer, A.; Huber, C.; Ahlrichs, R., Fully optimized contracted gaussian basis sets of triple zeta valence quality for atoms li to kr. *J. Chem. Phys.* **1994**, *100* (8), 5829-5835.
270. Grimme, S.; Antony, J.; Ehrlich, S.; Krieg, H., A consistent and accurate ab initio parametrization of density functional dispersion correction (DFT-D) for the 94 elements H-Pu. *J. Chem. Phys.* **2010**, *132* (15), 154104.
271. Lee, C.; Yang, W.; Parr, R. G., Development of the colle-salvetti correlation-energy formula into a functional of the electron density. *Phys. Rev. B* **1988**, *37* (2), 785-789.
272. Becke, A. D., Density-functional thermochemistry. III. The role of exact exchange. *J. Chem. Phys.* **1993**, *98* (7), 5648-5652.
273. Klamt, A.; Schüürmann, G., Cosmo: A new approach to dielectric screening in solvents with explicit expressions for the screening energy and its gradient. *Perkin Trans. 2* **1993**, (5), 799-805.
274. Neese, F.; Wennmohs, F.; Hansen, A.; Becker, U., Efficient, approximate and parallel Hartree–Fock and hybrid DFT calculations. A ‘chain-of-spheres’ algorithm for the Hartree–Fock exchange. *Chem. Phys.* **2009**, *356* (1–3), 98-109.
275. Weigend, F., A fully direct RI-HF algorithm: Implementation, optimised auxiliary basis sets, demonstration of accuracy and efficiency. *Phys. Chem. Chem. Phys.* **2002**, *4* (18), 4285-4291.
276. *Multifrequency electron paramagnetic resonance theory and applications*. Wiley-VCH ; John Wiley [distributor]: Weinheim; Chichester, 2011.



277. Svistunenko, D. A.; Jones, G. A., Tyrosyl radicals in proteins: A comparison of empirical and density functional calculated EPR parameters. *Phys. Chem. Chem. Phys.* **2009**, *11* (31), 6600-6613.
278. Gast, P.; Herbonnet, R. T. L.; Klare, J.; Nalepa, A.; Rickert, C.; Stellinga, D.; Urban, L.; Mobius, K.; Savitsky, A.; Steinhoff, H. J.; Groenen, E. J. J., Hydrogen bonding of nitroxide spin labels in membrane proteins. *Phys. Chem. Chem. Phys.* **2014**, *16* (30), 15910-15916.
279. Epel, B.; Arieli, D.; Baute, D.; Goldfarb, D., Improving W-band pulsed ENDOR sensitivity—random acquisition and pulsed special triple. *J. Magn. Reson.* **2003**, *164* (1), 78-83.
280. Seyedsayamdost, M. R.; Xie, J.; Chan, C. T. Y.; Schultz, P. G.; Stubbe, J., Site-specific insertion of 3-aminotyrosine into subunit alpha 2 of E. coli ribonucleotide reductase: Direct evidence for involvement of Y-730 and Y-731 in radical propagation. *J Am Chem Soc* **2007**, *129* (48), 15060-15071.
281. Dastvan, R.; Bode, B. E.; Karuppiah, M. P. R.; Marko, A.; Lyubenova, S.; Schwalbe, H.; Prisner, T. F., Optimization of transversal relaxation of nitroxides for pulsed electron–electron double resonance spectroscopy in phospholipid membranes. *J. Phys. Chem. B* **2010**, *114* (42), 13507-13516.
282. Polyhach, Y.; Bordignon, E.; Tschaggelar, R.; Gandra, S.; Godt, A.; Jeschke, G., High sensitivity and versatility of the DEER experiment on nitroxide radical pairs at Q-band frequencies. *Phys. Chem. Chem. Phys.* **2012**, *14* (30), 10762-10773.
283. Zou, P.; McHaourab, H. S., Increased sensitivity and extended range of distance measurements in spin-labeled membrane proteins: Q-band double electron-electron resonance and nanoscale bilayers. *Biophys. J.* **2010**, *98* (6), L18-L20.
284. Eaton, S. S.; Eaton, G. R., Frequency dependence of pulsed EPR experiments. *Concepts Magn. Reson. Part A* **2009**, *34A* (6), 315-321.
285. Bejenke, I. Orientation selection effects in DEER experiments on a rigid pair of amino acids at 34 GHz. Internship report, Georg-August University, Göttingen, 2014.
286. Jeschke, G.; Chechik, V.; Ionita, P.; Godt, A.; Zimmermann, H.; Banham, J.; Timmel, C. R.; Hilger, D.; Jung, H., DeerAnalysis2006—a comprehensive software package for analyzing pulsed ELDOR data. *Appl. Magn. Reson.* **2006**, *30* (3-4), 473-498.
287. Tikhonov, A. N., *Numerical methods for the solution of ill-posed problems*. Kluwer Academic Publishers: Dordrecht; Boston, 1995.
288. Gallivan, J. P.; Dougherty, D. A., Cation- $\pi$  interactions in structural biology. *Proc. Natl. Acad. Sci. USA* **1999**, *96* (17), 9459-9464.
289. Ma, J. C.; Dougherty, D. A., The cation- $\pi$  interaction. *Chem. Rev. (Washington, DC, U. S.)* **1997**, *97* (5), 1303-1324.
290. Sibert, R. S.; Josowicz, M.; Barry, B. A., Control of proton and electron transfer in de novo designed, biomimetic  $\beta$  hairpins. *ACS Chem. Biol.* **2010**, *5* (12), 1157-1168.
291. Saito, K.; Shen, J.-R.; Ishida, T.; Ishikita, H., Short hydrogen bond between redox-active tyrosine yz and D1-His190 in the photosystem II crystal structure. *Biochemistry* **2011**, *50* (45), 9836-9844.
292. Ishikita, H.; Saito, K., Proton transfer reactions and hydrogen-bond networks in protein environments. *J. Royal Soc. Interface* **2014**, *11* (91), 1-17.

- 
293. Saito, K.; Rutherford, A. W.; Ishikita, H., Mechanism of tyrosine D oxidation in photosystem II. *Proc. Natl. Acad. Sci. U. S. A.* **2013**, *110* (19), 7690-7695.
294. Siegbahn, P. E. M., Theoretical model studies of the iron dimer complex of mmo and RNR. *Inorg. Chem.* **1999**, *38* (12), 2880-2889.
295. McConnell, H. M.; Strathdee, J., Theory of anisotropic hyperfine interactions in  $\pi$ -electron radicals. *Mol. Phys.* **1959**, *2* (2), 129-138.
296. Klamt, A.; Schuurmann, G., Cosmo: A new approach to dielectric screening in solvents with explicit expressions for the screening energy and its gradient. *Journal of the Chemical Society, Perkin Transactions 2* **1993**, (5), 799-805.
297. Löwdin, P.-O., Quantum theory of many-particle systems. I. Physical interpretations by means of density matrices, natural spin-orbitals, and convergence problems in the method of configurational interaction. *Physical Review* **1955**, *97* (6), 1474.
298. Karplus, M., Contact electron-spin coupling of nuclear magnetic moments. *J. Chem. Phys.* **1959**, *30* (1), 11-15.
299. Un, S.; Tang, X. S.; Diner, B. A., 245 GHz high-field EPR study of tyrosine-D degrees and tyrosine-Z degrees in mutants of photosystem II. *Biochemistry* **1996**, *35* (3), 679-684.
300. Huš, M.; Urbic, T., Strength of hydrogen bonds of water depends on local environment. *J. Chem. Phys.* **2012**, *136* (14), 144305.
301. Hakala, M.; Nygård, K.; Manninen, S.; Huotari, S.; Buslaps, T.; Nilsson, A.; Pettersson, L. G. M.; Hämäläinen, K., Correlation of hydrogen bond lengths and angles in liquid water based on Compton scattering. *J. Chem. Phys.* **2006**, *125* (8), 084504.
302. Thelander, L., Physicochemical characterization of ribonucleoside diphosphate reductase from *Escherichia coli*. *J. Biol. Chem.* **1973**, *248* (13), 4591-4601.
303. Salamone, M.; Amorati, R.; Menichetti, S.; Viglianisi, C.; Bietti, M., Structural and medium effects on the reactions of the cumyloxyl radical with intramolecular hydrogen bonded phenols. The interplay between hydrogen-bonding and acid-base interactions on the hydrogen atom transfer reactivity and selectivity. *J. Org. Chem.* **2014**, *79* (13), 6196-6205.
304. Witwicki, M.; Jezierska, J.; Ozarowski, A., Solvent effect on EPR, molecular and electronic properties of semiquinone radical derived from 3,4-dihydroxybenzoic acid as model for humic acid transient radicals: High-field EPR and DFT studies. *Chem. Phys. Lett.* **2009**, *473* (1-3), 160-166.
305. Witwicki, M.; Jerzykiewicz, M.; Jaszewski, A. R.; Jezierska, J.; Ozarowski, A., Influence of Pb(II) ions on the EPR properties of the semiquinone radicals of humic acids and model compounds: High field EPR and relativistic DFT studies. *J. Phys. Chem. A* **2009**, *113* (51), 14115-14122.
306. Gitlin, I.; Carbeck, J. D.; Whitesides, G. M., Why are proteins charged? Networks of charge-charge interactions in proteins measured by charge ladders and capillary electrophoresis. *Angew. Chem. Int. Ed.* **2006**, *45* (19), 3022-3060.
307. Gallivan, J. P.; Dougherty, D. A., A computational study of cation- $\pi$  interactions vs salt bridges in aqueous media: Implications for protein engineering. *J. Am. Chem. Soc.* **2000**, *122* (5), 870-874.

308. Seyedsayamdost, M. R.; Stubbe, J., Forward and reverse electron transfer with the Y(356)DOPA-beta 2 heterodimer of e-coli ribonucleotide reductase. *J. Am. Chem. Soc.* **2007**, *129* (8), 2226-2227.
309. Narváez, A. J.; Voevodskaya, N.; Thelander, L.; Gräslund, A., The involvement of Arg265 of mouse ribonucleotide reductase R2 protein in proton transfer and catalysis. *J. Biol. Chem.* **2006**, *281* (36), 26022-26028.
310. Rizzato, R.; Bennati, M., Enhanced sensitivity of electron-nuclear double resonance (ENDOR) by cross polarisation and relaxation. *Phys. Chem. Chem. Phys.* **2014**, *16* (17), 7681-7685.
311. Hoganson, C. W.; Sahlin, M.; Sjöberg, B.-M.; Babcock, G. T., Electron magnetic resonance of the tyrosyl radical in ribonucleotide reductase from *Escherichia coli*. *J. Am. Chem. Soc.* **1996**, *118* (19), 4672-4679.
312. Mulliken, R., Electronic population analysis on lcao-mo molecular wave functions. II. Overlap populations, bond orders, and covalent bond energies. *J. Chem. Phys.* **1955**, *23* (10), 1841-1846.
313. Mulliken, R. S., Electronic population analysis on lcao-mo molecular wave functions. I. *J. Chem. Phys.* **1955**, *23* (10), 1833-1840.
314. Heller, C.; McConnell, H. M., Radiation damage in organic crystals. II. Electron spin resonance of (CO<sub>2</sub>H)CH<sub>2</sub>CH(CO<sub>2</sub>H) in β-succinic acid. *J. Chem. Phys.* **1960**, *32* (5), 1535-1539.
315. Fessenden, R. W.; Schuler, R. H., Electron spin resonance studies of transient alkyl radicals. *J. Chem. Phys.* **1963**, *39* (9), 2147-2195.
316. Rigby, S. E. J.; Nugent, J. H. A.; O'Malley, P. J., The dark stable tyrosine radical of photosystem 2 studied in three species using ENDOR and EPR spectroscopies. *Biochemistry* **1994**, *33* (7), 1734-1742.
317. Warncke, K.; McCracken, J.; Babcock, G. T., Structure of the YD tyrosine radical in photosystem II as revealed by 2H electron spin echo envelope modulation (eseem) spectroscopic analysis of hydrogen hyperfine interactions. *J. Am. Chem. Soc.* **1994**, *116* (16), 7332-7340.
318. Tommos, C.; Tang, X.-S.; Warncke, K.; Hoganson, C. W.; Styring, S.; McCracken, J.; Diner, B. A.; Babcock, G. T., Spin-density distribution, conformation, and hydrogen bonding of the redox-active tyrosine yz in photosystem II from multiple-electron magnetic-resonance spectroscopies: Implications for photosynthetic oxygen evolution. *J. Am. Chem. Soc.* **1995**, *117* (41), 10325-10335.
319. Sealy, R. C.; Harman, L.; West, P. R.; Mason, R. P., The electron spin resonance spectrum of the tyrosyl radical. *J. Am. Chem. Soc.* **1985**, *107* (12), 3401-3406.
320. Warncke, K.; McCracken, J., Analysis of static distributions in hydrogen hyperfine interactions in randomly oriented radicals in the solid state by using 2H electron spin echo envelope modulation spectroscopy: Conformational dispersion of β -2H coupling in the model tyrosyl radical. *J. Chem. Phys.* **1995**, *103* (16), 6829-6840.
321. Dorlet, P.; Rutherford, A. W.; Un, S., Orientation of the tyrosyl D, pheophytin anion, and semiquinone Q(a)(•-) radicals in photosystem II determined by high-field electron paramagnetic resonance. *Biochemistry* **2000**, *39* (26), 7826-7834.

- 
322. Kessen, S.; Teutloff, C.; Kern, J.; Zouni, A.; Bittl, R., High-field H-2-Mims-ENDOR spectroscopy on PSII single crystals: Hydrogen bonding of Y-D(center dot). *ChemPhysChem* **2010**, *11* (6), 1275-1282.
323. Alia; Hulsebosch, B.; van Gorkom, H. J.; Raap, J.; Lugtenburg, J.; Matysik, J.; de Groot, H. J. M.; Gast, P., Probing the electronic structure of tyrosine radical YD in photosystem II by EPR spectroscopy using site specific isotope labelling in spirodela oligorrhiza. *Chem. Phys.* **2003**, *294* (3), 459-469.
324. Sneeden, J. L.; Loeb, L. A., Mutations in the R2 subunit of ribonucleotide reductase that confer resistance to hydroxyurea. *J. Biol. Chem.* **2004**, *279* (39), 40723-40728.
325. Han, W.-G.; Noodleman, L., DFT calculations for intermediate and active states of the diiron center with a tryptophan or tyrosine radical in Escherichia coli ribonucleotide reductase. *Inorg. Chem.* **2011**, *50* (6), 2302-2320.
326. Lee, W.; Minnihan, E.; Stubbe, J., Probing conformational change during radical propagation in the E. coli class 1a RNR using 3-aminotyrosine as a radical "sink". *The FASEB Journal* **2015**, *29* (1 Supplement).
327. Jin, F.; Leitich, J.; von Sonntag, C., The superoxide radical reacts with tyrosine-derived phenoxyl radicals by addition rather than by electron transfer. *Journal of the Chemical Society, Perkin Transactions 2* **1993**, (9), 1583-1588.
328. Sjödin, M.; Irebo, T.; Utas, J. E.; Lind, J.; Merényi, G.; Åkermark, B.; Hammarström, L., Kinetic effects of hydrogen bonds on proton-coupled electron transfer from phenols. *J. Am. Chem. Soc.* **2006**, *128* (40), 13076-13083.
329. Johannissen, L. O.; Irebo, T.; Sjödin, M.; Johansson, O.; Hammarström, L., The kinetic effect of internal hydrogen bonds on proton-coupled electron transfer from phenols: A theoretical analysis with modeling of experimental data. *J. Phys. Chem. B* **2009**, *113* (50), 16214-16225.
330. Irebo, T.; Johansson, O.; Hammarström, L., The rate ladder of proton-coupled tyrosine oxidation in water: A systematic dependence on hydrogen bonds and protonation state. *J. Am. Chem. Soc.* **2008**, *130* (29), 9194-9195.
331. Chen, J.; Kuss-Petermann, M.; Wenger, O. S., Distance dependence of bidirectional concerted proton-electron transfer in phenol-Ru(2,2'-bipyridine)<sub>3</sub><sup>2+</sup> dyads. *Chemistry – A European Journal* **2014**, *20* (14), 4098-4104.
332. Rizzato, R.; Kaminker, I.; Vega, S.; Bennati, M., Cross-polarisation edited ENDOR. *Mol. Phys.* **2013**, *111* (18-19), 2809-2823.
333. Denysenkov, V. P.; Prisner, T. F.; Stubbe, J.; Bennati, M., High-field pulsed electron-electron double resonance spectroscopy to determine the orientation of the tyrosyl radicals in ribonucleotide reductase. *Proc. Natl. Acad. Sci. U. S. A.* **2006**, *103* (36), 13386-13390.
334. Weingarth, M.; Baldus, M., Solid-state NMR-based approaches for supramolecular structure elucidation. *Acc. Chem. Res.* **2013**, *46* (9), 2037-2046.
335. Sengupta, I.; Nadaud, P. S.; Jaroniec, C. P., Protein structure determination with paramagnetic solid-state NMR spectroscopy. *Acc. Chem. Res.* **2013**, *46* (9), 2117-2126.
336. Seyedsayamdost, M. R.; Yee, C. S.; Stubbe, J., Site-specific incorporation of fluorotyrosines into the R2 subunit of e-coli ribonucleotide reductase by expressed protein ligation. *Nat. Protoc.* **2007**, *2* (5), 1225-1235.

337. Kühlbrandt, W., The resolution revolution. *Science* **2014**, 343 (6178), 1443-1444.
338. Fischer, N.; Neumann, P.; Konevega, A. L.; Bock, L. V.; Ficner, R.; Rodnina, M. V.; Stark, H., Structure of the E. coli ribosome-EF-Tu complex at <3 Å resolution by cryo-EM. *Nature* **2015**, 520 (7548), 567-570.
339. Moughal Shahi, A. R.; Domratcheva, T., Challenges in computing electron-transfer energies of DNA repair using hybrid qm/mm models. *J. Chem. Theory Comput.* **2013**, 9 (10), 4644-4652.
340. Pinto, G. P.; Ribeiro, A. J.; Ramos, M. J.; Fernandes, P. A.; Toscano, M.; Russo, N., New insights in the catalytic mechanism of tyrosine ammonia-lyase given by QM/MM and QM cluster models. *Arch. Biochem. Biophys.* **2015**, 582, 107.
341. Bernini, C.; Arezzini, E.; Basosi, R.; Sinicropi, A., In silico spectroscopy of tryptophan and tyrosine radicals involved in the long-range electron transfer of cytochrome c peroxidase. *J. Phys. Chem. B* **2014**, 118 (32), 9525-9537.

---

## 8 APPENDICES

APPENDIX 1: PREVIOUS EPR RESULTS FOR  $\text{NH}_2\text{Y}\bullet$ 

		$\alpha - \text{ND}_2\text{Y}_{730}\bullet$ $\alpha - \text{NH}_2\text{Y}_{730}\bullet$			$\alpha - \text{ND}_2\text{Y}_{731}\bullet$ $\alpha - \text{NH}_2\text{Y}_{731}\bullet$			$\beta - \text{ND}_2\text{Y}_{356}\bullet$ $\beta - \text{NH}_2\text{Y}_{356}\bullet$		
		$ A_{xx} $	$ A_{yy} $	$ A_{zz} $	$ A_{xx} $	$ A_{yy} $	$ A_{zz} $	$ A_{xx} $	$ A_{yy} $	$ A_{zz} $
<b>Hyperfine couplings</b>	$\text{C}_\beta\text{-H}_1$	30.8	28.0	30.5	23	22	21	29	24.5	27
	$\text{C}_\beta\text{-H}_2$	-	-	-	13	8	7	-	-	-
	$^{14}\text{N}$	2.4	1.6	30.5	2.4	1.6	30.5	2.4	1.6	30.7
	$\text{NH}_2\text{(H2)}$	13	4.4	27.6	18.2	4.4	25.7	13	4.4	27.6
	$\text{NH}_2\text{(H1)}$	6.7	8.0	18.0	6.7	8.0	21.8	4.8	15	16
<b>Euler angles</b>	<b>Nucleus/ Euler angle</b>	$\alpha$	$\beta$	$\gamma$	$\alpha$	$\beta$	$\gamma$	$\alpha$	$\beta$	$\gamma$
	$^{14}\text{N}$	$60^\circ$	$ 5^\circ $	-	$60^\circ$	$ 5^\circ $	-	$60^\circ$	$ 5^\circ $	-
	$\text{NH}_2\text{(H2)}$	-	$ 126^\circ  \pm 10^\circ$	$-60^\circ \pm 5^\circ$	-	$ 126^\circ  \pm 10^\circ$	$-60^\circ \pm 5^\circ$	-	$ 126^\circ  \pm 10^\circ$	$-60^\circ \pm 5^\circ$
$\text{NH}_2\text{(H1)}$	$0^\circ\text{ (-}40^\circ\text{)}$	$ 50^\circ $	-	$0^\circ\text{ (-}40^\circ\text{)}$	$ 50^\circ $	-	$0^\circ\text{ (-}40^\circ\text{)}$	$ 50^\circ $	-	
<b>g-values</b>	<b><math>g_x</math></b>	<b><math>g_y</math></b>	<b><math>g_z</math></b>	<b><math>g_x</math></b>	<b><math>g_y</math></b>	<b><math>g_z</math></b>	<b><math>g_x</math></b>	<b><math>g_y</math></b>	<b><math>g_z</math></b>	
	2,0052	2,0042	2,0022	2,0052	2,0042	2,0022	2,0050	2,0041	2,0021	

Table A. 1: Summary of EPR parameters from  $\text{NH}_2\text{Y}\bullet$  by simulation of 94 GHz EPR spectra in  $\text{D}_2\text{O}$  and  $\text{H}_2\text{O}$  buffer at position  $\beta\text{-356}$ ,  $\alpha\text{-731}$  and  $\alpha\text{-730}$  on the PCET of *E. coli* RNR. T. Argirević presented these hyperfine couplings, Euler angles and g values in his thesis (2011).<sup>92</sup> The large couplings were additionally in agreement with 34 GHz  $^1\text{H}$  Davis ENDOR spectra.<sup>92</sup>

## APPENDIX 2: APPENDIX TO CHAPTER 4 ( $\text{NH}_2\text{Y}_{730/731}\bullet$ )

The 263 GHz spectrum in  $\text{H}_2\text{O}$  buffer was recorded at a different reaction time point of 2 min, but still shows the  $g$  values as demonstrated by the simulations. However, one should note, that due to the absence of sharp features beside  $g_y$  the accuracy of the  $g$  value determination is lower.

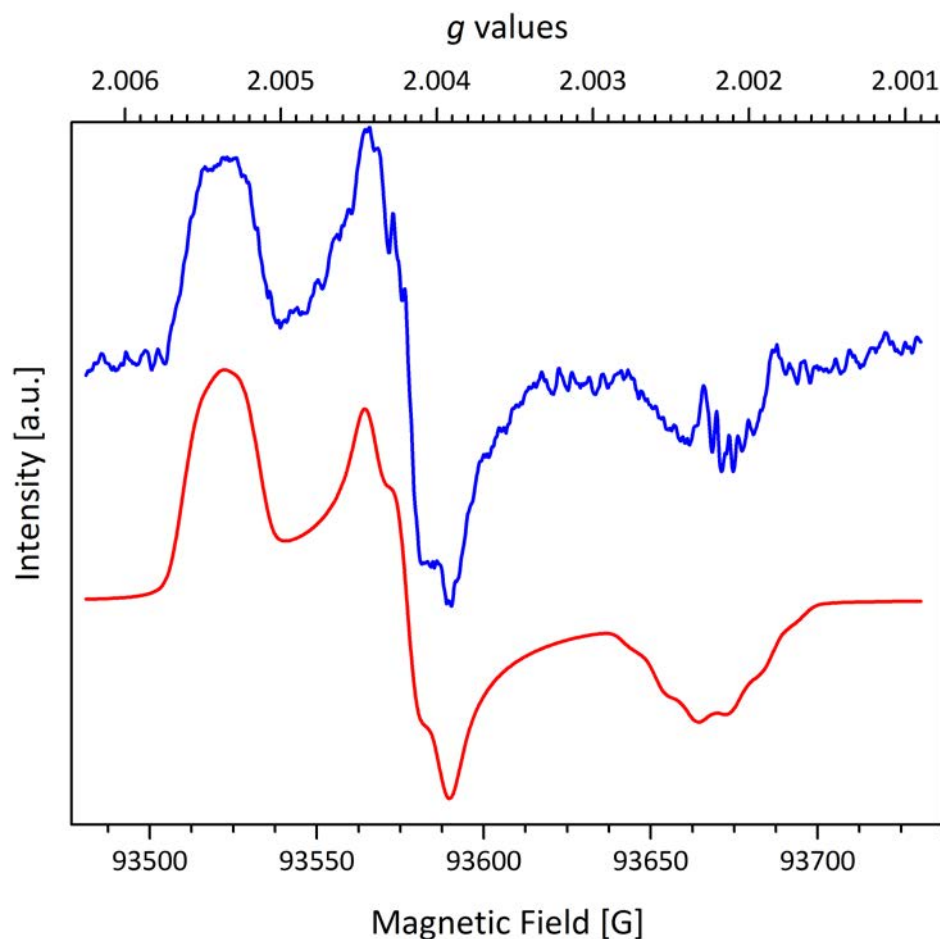


Figure A - 1: 263 GHz ESE Spectrum of  $\text{Y}_{730}\text{NH}_2\bullet$  2 min at 70 K. Blue shows derivative (obtained by 5 points 2<sup>nd</sup> order Savitzky-Golay filter) and red shows the simulation. Exp. details: ESE,  $\pi/2=64$  ns,  $\tau=270$  ns, SRT= 6 ms, SPP=500, 200 scans.



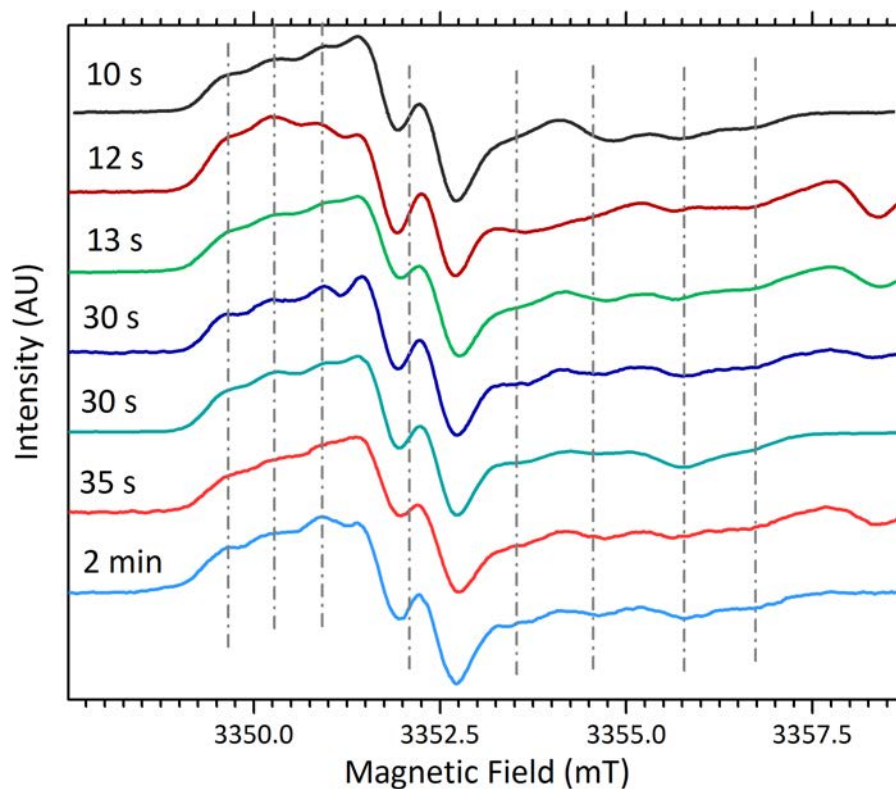


Figure A - 2: 94-GHz EPR spectra at various reaction times (10 s- 2 min) of  $\text{ND}_2\text{Y}_{731}\bullet$ . Exp. details: ESE,  $T = 70$  K,  $\tau = 240$  ns, SRT = 5 ms, SPP= 50-100, scans=100-200. The derivative was built by a 5–10 points second order Savitzky-Golay filter.

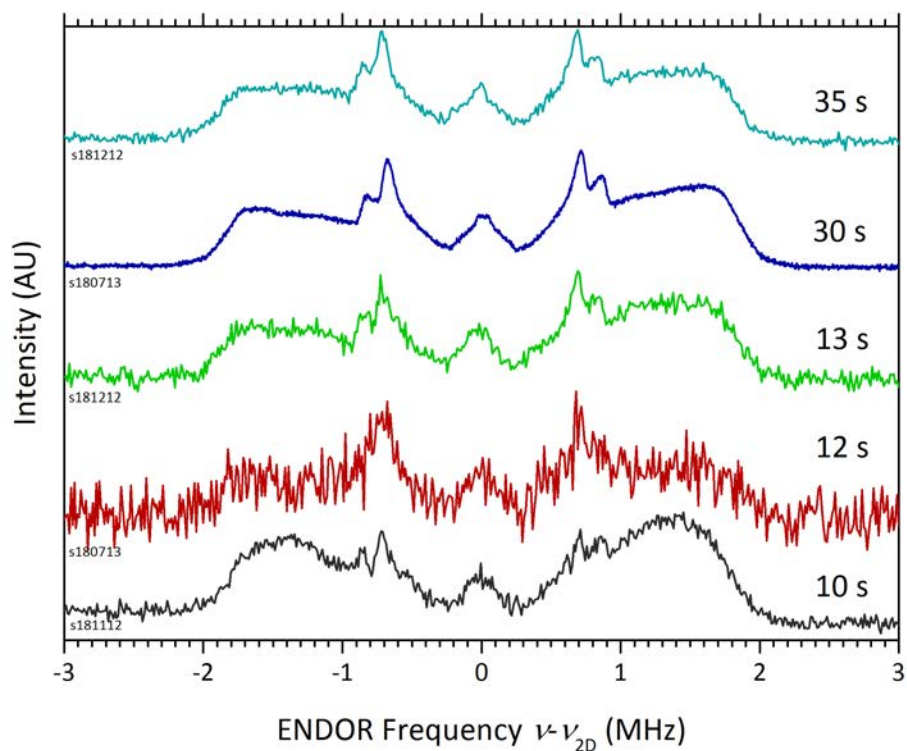


Figure A - 3: ENDOR spectra of  $\text{ND}_2\text{Y}_{731}$  at  $g_y$  from three preparations and from reaction time points ranging from 10-35 s. All spectra show within S/N the same features. Exp. details:  $^2\text{H}$  Mims ENDOR,  $T = 10 \text{ K}$ ,  $\tau=200 \text{ ns}$ ;  $\pi/2=20 \text{ ns}$ , SRT= 150-200 ms; number of averages from top to down: 450 (2 h), 2800 (11 h), 150 (0.6 h), 300 (1.2 h), 50 (12 min), 3000 (12 h); Exp. details of the 30 s trace can be found in Figure 4-7 (p.83).

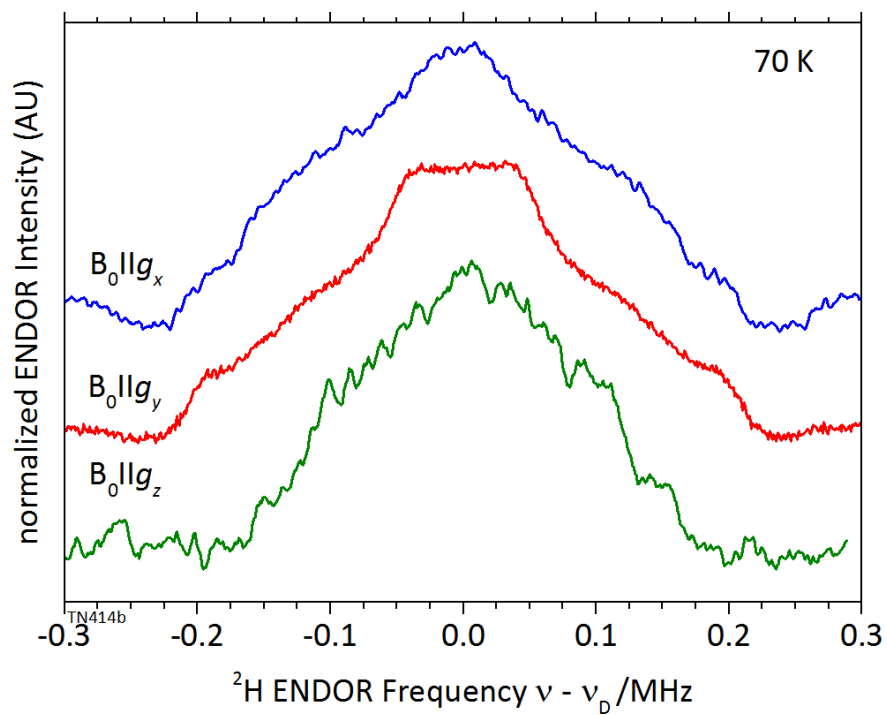


Figure A - 4: Orientation selective  $^2\text{H}$  Mims ENDOR spectrum of the central line of  $\text{NH}_2\text{Y}_{731}\bullet$ . Spectral range between -0.3 to 0.3 MHz shows weak couplings. Exp. details:  $T = 70\text{ K}$ ,  $\pi/2 = 20\text{ ns}$ ,  $\tau = 360\text{ ns}$ ,  $\text{SRT} = 10\text{ ms}$ , acquisition time 5 h (3000 scans).

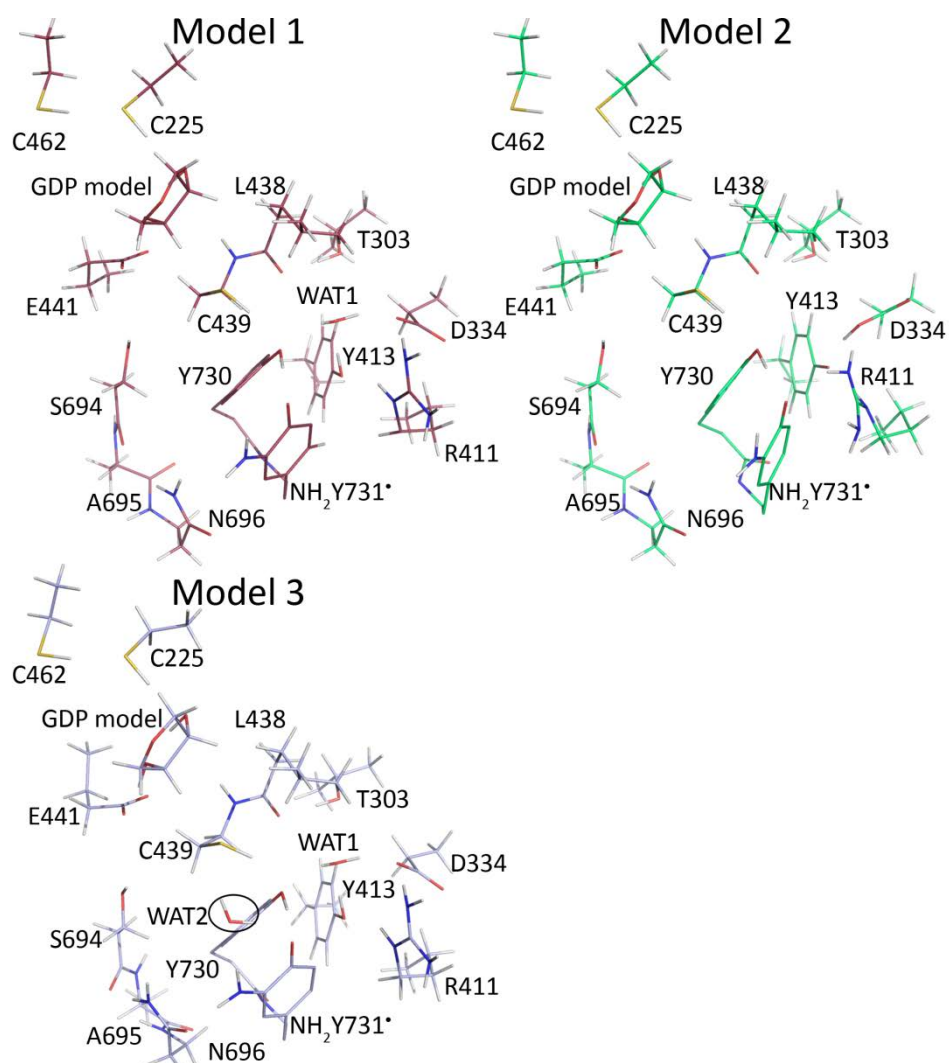


Figure A - 5: Large DFT models for  $\text{NH}_2\text{Y}_{731}^\bullet$ . The 210 to 216 atoms large Model 1 (wine red), Model 2 (green) and Model 3 (purple) are depicted. The GDP is modeled by an (3*R*, 4*S*)-tetrahydrofuran-3,4-diol.

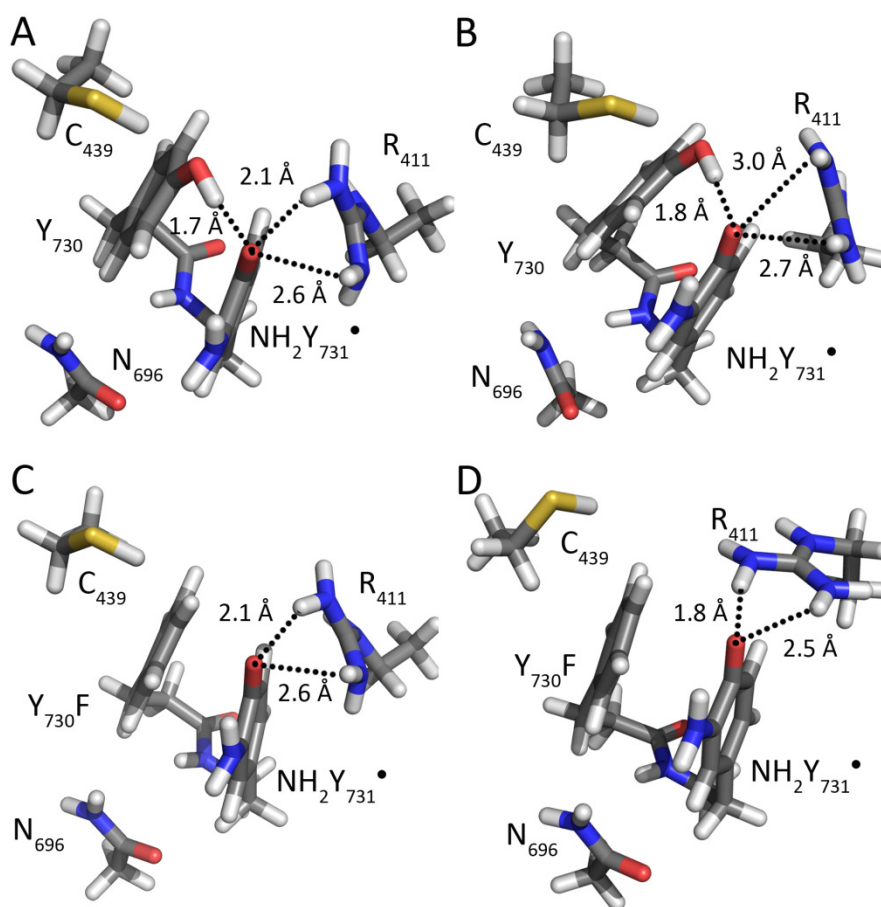


Figure A - 6: Small DFT models for  $\text{NH}_2\text{Y}_{731}^\bullet$ . Small models were constructed from DFT Model 2 in order to check for the effect of individual amino acid residues on the  $g$  values of  $\text{NH}_2\text{Y}_{731}^\bullet$ . For geometry optimization the functional (B3LYP) and the Aldrich's' TZVPP basis set of triple- $\zeta$  quality were used. For deriving the EPR parameters, the EPR II basis set was used (Online Methods). Solvent effects were taken into account by a conductor like screening model (COSMO) with the polarizability of ethanol. A) This first small model is built from Model 2 by considering residues only in the first interaction sphere. No further geometry optimization was carried out. The  $g$  tensor with  $\text{R}_{411}$  is  $g_{xyz} = [2.0050, 2.0041, 2.0022]$ . If  $\text{R}_{411}$  is removed the  $g$  tensor becomes  $g_{xyz} = [2.0055, 2.0044, 2.0021]$ , i.e., the  $g_x$  value shifts by  $\Delta g_x = +0.5$  ppt. B) Small model A after additional geometry optimization,  $g_{xyz} = [2.0052, 2.0042, 2.0022]$ . C) Small model which mimics the double mutant  $\text{NH}_2\text{Y}_{731}^\bullet/\text{Y}_{730}\text{F}$ . The  $g$  tensor results to  $g_{xyz} = [2.0060, 2.0046, 2.0023]$ . D) Small model C after geometry optimization. The  $g$  tensor is  $g_{xyz} = [2.0052, 2.0043, 2.0023]$ , i.e., the computed  $g_x$  lowers by 0.8 ppt.

### APPENDIX 3: APPENDIX TO CHAPTER 4 ( $\text{NH}_2\text{Y}_{356}\bullet$ )

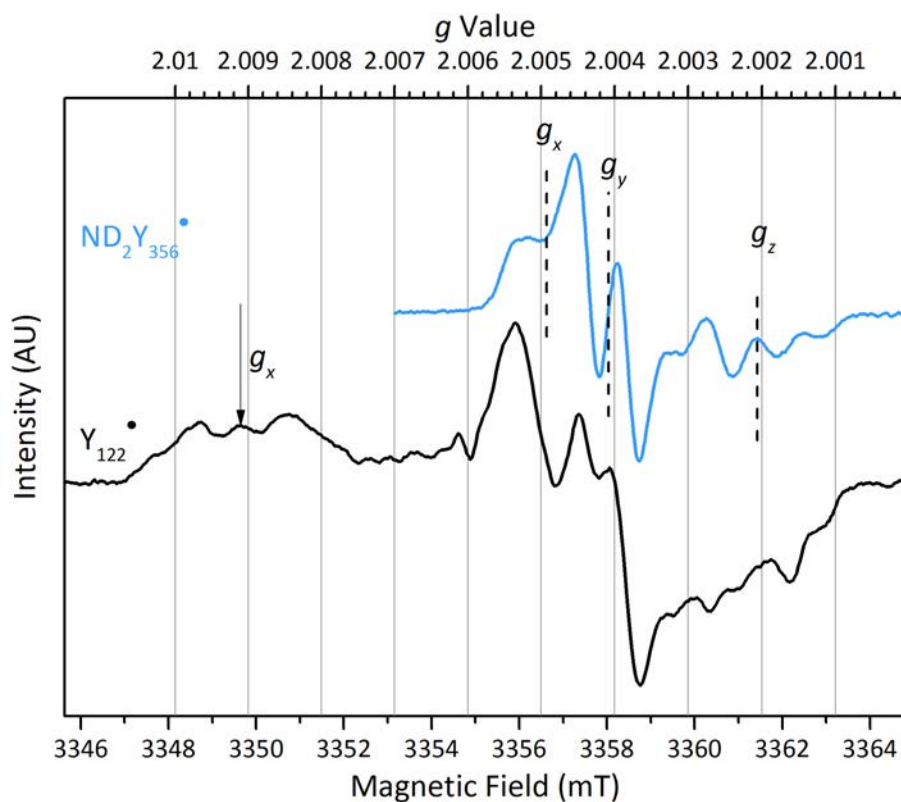


Figure A - 7: 94 GHz field calibration of  $\beta\text{-ND}_2\text{Y}_{356}\bullet$  (blue line) by internal  $\beta\text{-Y}_{122}\bullet$  (black line). The  $g$  values were aligned on  $\text{Y}_{122}\bullet$  with  $g_x=2.00912$ .<sup>157</sup> Exp. details (blue/black): ESE, 13 s reaction time,  $T = 70 \text{ K} / 10 \text{ K}$ ,  $\pi = 30 \text{ ns}$ ,  $\tau=275 \text{ ns}$ , SRT = 5 ms/ 50 ms, SPP= 100/10, scan= 62/1. The derivative was built by a 10 point second order Savitzky-Golay filter.  $\text{NH}_2\text{Y}_{356}\bullet$  yield was 13%, estimated by the integral with and without subtraction resting state of  $\beta_2\text{-Y}_{122}\bullet$ .

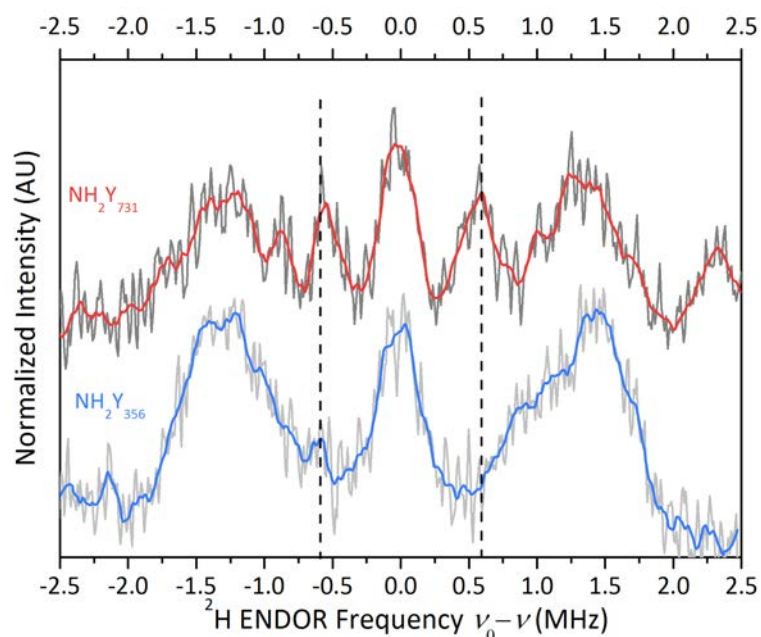


Figure A - 8:  $^2\text{H}$  Mims ENDOR spectrum of  $\text{ND}_2\text{Y}_{356}\bullet$  compared to  $\text{ND}_2\text{Y}_{731}\bullet$  at 35 GHz. Exp. details (blue/red):  $T = 10\text{ K}$ ,  $\pi/2 = 20\text{ ns}$ ,  $\tau = 200\text{ ns}$ ,  $\pi_{\text{RF}} = 30/40\ \mu\text{s}$ ,  $\text{SRT} = 30/150\text{ ms}$ ,  $\text{SPP} = 1$ , averaging time = 11 h. 20 point Savitzky-Golay second order filter was used to obtain blue and red from the corresponding gray spectrum. Data courtesy belongs to Bejenke and Argirević for blue and red, respectively.

## APPENDIX 4: APPENDIX TO CHAPTER 5

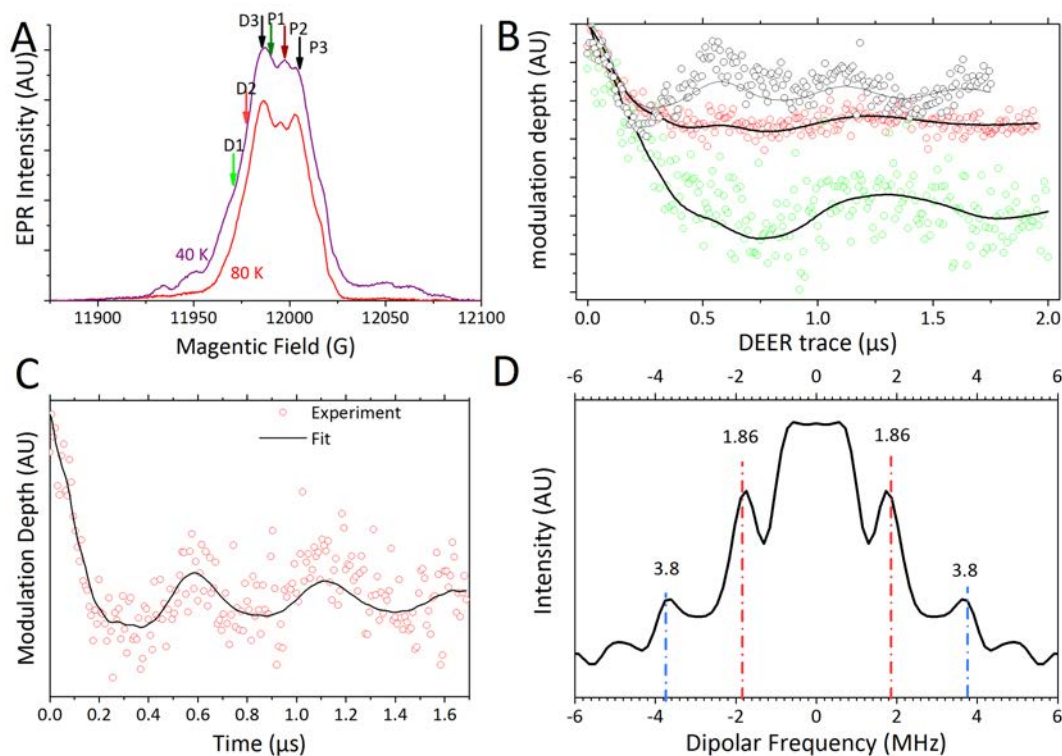


Figure A - 9: Diagonal distance measurement of pathway radical produced with  $\alpha_2$ -2,3,5- $F_3Y_{122};\beta_2$ -wt. ESE spectrum at 40 K (violet) and spectrum of pathway radical alone at 70 K (red) are shown together with the pump and detect positions of the PELDOR measurements. From pump ( $\pi = 56$  ns) and detect ( $\pi = 46$  ns) separated by 54 MHz the dipolar oscillation (B) is obtained after background subtraction and normalization. DEER Analysis using Tikonov regularization gives a fit (black line) to the individual (B) and summed (C) dipolar oscillation. This oscillation can be Fourier transformed to a Dipolar pake pattern (D). The perpendicular component with  $\pm 1.86$  MHz can be read out. From Eq. (2-19) the dipolar distance is obtained with  $3.0 \pm 0.1$  nm. The inner part of the pake pattern also show another contribution with  $\pm 0.6$  MHz, but the length of the recorded time trace is too short to resolve this contribution.